博士論文

Non-centrosymmetric Two-dimensional Layered Materials for Piezoelectric and Ferroelectric Device Applications

（圧電・強誘電デバイス応用に向けた
中心対称性の破れた二次元層状物質の研究）

東垂水 直樹

Non-centrosymmetric Two-dimensional Layered Materials for Piezoelectric and Ferroelectric Device Applications

by

Naoki Higashitarumizu

Submitted to the Department of Materials Engineering
on February 20, 2020, in partial fulfillment of the
requirements for the degree of
Doctor of Philosophy in Materials Engineering

Abstract

Non-centrosymmetric two-dimensional (2D) layered materials are explored toward the piezoelectric and ferroelectric applications. Monolayer tin sulfide (SnS), an emerging 2D material with a purely in-plane spontaneous polarization, is investigated from material synthesis to device applications. The objective of this work is to demonstrate piezoelectric and ferroelectric devices based on 2D SnS, and investigate their mechanisms.

Since the discovery of graphene and other 2D materials, van der Waals (vdW) materials have attracted a great deal of interests on their unique properties at the atomic-thick scale, from the perspectives of science and engineering. Especially, the research fields of their electrical and optical applications have been rapidly growing after the first demonstration of graphene field-effect transistors (FETs) in 2004. Although graphene has no piezoelectricity due to its centrosymmetric atomic structure, some 2D materials lack the centrosymmetry, which gives a birth of piezoelectricity. In 2014, the first experimental demonstration was reported for piezoelectric nanogenerators based on a monolayer molybdenum disulfide (MoS_2). This achievement has given a new insight to the researches on 2D materials into the piezoelectric applications, enabling self-generated functional devices for the Internet of Things (IoT). However, the mechanism of 2D piezoelectric materials is unidentified, and the output power density is still at the order of several hundred nW/cm^2, much smaller than the required power for the IoT devices.

Monolayer SnS has been theoretically expected to have a large piezoelectric constant $d = 145$ pm/V, which is two order larger than that of MoS_2 ($d \sim 4$ pm/V) and comparable to that of PZT ($d \sim 300$ pm/V), owing to the puckered structure with quite a small Young's modulus. Given that PZT and other piezo-ceramics are breakable due to their brittle fracture, 2D SnS is superior to these conventional piezoelectric for the sake of wearable device applications. Furthermore, SnS has been theoretically expected to exhibit a ferroelectricity unlike MoS_2, suggesting a potential for applications such as nonvolatile memory and nonlinear optoelectronics. Despite the novel characteristics of monolayer SnS, experimental demonstrations are still challenging

due to the difficulty of monolayer fabrication.

Unlike other vdW materials of graphene and MoS_2, it is difficult to isolate the monolayer SnS *via* mechanical exfoliation due to the ionic interlayer interactions along with vdW forces. This strong interlayer force is found to be caused by the lone pair electrons in Sn atoms, which also contribute to the puckered structure of Sn along the armchair direction. These lone pair electrons constitute the top of the valence band of SnS, resulting in a favorable bonding with oxygen. Thus, the SnS surface is easy to be oxidized during the thinning process, though this oxidation is self-stopping owing to a robust feature of SnO_x layer, and a steep interface is identified at SnO_x/SnS. When a bulk SnS is treated by an oxygen annealing intentionally, a self-passivated hetero-structure SnO_x/monolayer-SnS is achieved.

Together with the top-down process, bottom-up crystal growth is proposed, where he SnS adsorption/desorption is precisely controlled. For the first time, micrometer-size SnS crystal down to the monolayer has been grown *via* physical vapor deposition (PVD) on mica substrate, whose surface is atomically flat. Monolayer SnS grown *via* PVD reveals high crystalline quality better than that obtained *via* top-down methods: peculiar Raman peaks are observed only for the PVD grown monolayer. Further strikingly, PVD-SnS exhibits a strong interaction with mica substrate: x-ray diffraction measurement confirmed that the lattice orientation of SnS tends to aligned for that of mica. These results suggest that mica is a promising platform for 2D SnS.

An electromechanical response of 2D SnS is described. Flexible devices are demonstrated on mica, which is used as a platform throughout the whole process from crystal growth to the device fabrication. This approach leads to the highly sensitive electromechanical response of SnS, with a gauge factor of approximately 130 much higher than that of metal strain gauges and graphene sheets.

Note that 2D piezoelectric materials (SnS and MoS_2) are semiconductor materials, different from the typical piezoelectric insulators. For the piezoelectric generator, Schottky contact is necessary at the metal/semiconductor interface to prevent the carrier injection from electrode to semiconductor. When the piezoelectric charges are generated, they are expected to be accumulated at the Schottky barrier contact. Although the piezoresistive effect have no polarity at source/drain, the piezoelectric effect modulates the Schottky barrier height (SBH) asymmetrically at the source/drain (S/D). To clarify this asymmetric modulation of the SBH, static I_D–V_D curve is measured under an external strain for MoS_2 as a model material. In this work, metal electrodes are fabricated with a transfer process, because a strong Fermi level pinning is crucial at the metal/MoS_2 interface when the metals are evaporated. When bilayer MoS_2 with different stacking sequences are investigated, transport characteristics of AA-parallel and AB-antiparallel stacked MoS_2 are found to be dominated by piezoresistive and piezoelectric effects, respectively. These results suggest that piezoelectricity can be preserved in the stack-controlled multilayer MoS_2, so that the output power density per unit area can be improved overcoming the monolayer limit. For further understanding, top-gated MoS_2 FETs are fabricated *via* the defect-free transfer method. Under the positive gate bias accumulating the channel region, a polarity of conductivity is observed reflecting the asymmetric SBH modulation at S/D.

Finally, an in-plane ferroelectric device is demonstrated for a micrometer-size monolayer SnS grown *via* PVD. Polarized Raman spectroscopy for monolayer SnS indicates high crystalline quality and strong anisotropy, and second harmonic generation (SHG) spectroscopy reveals that monolayer SnS is non-centrosymmetric unlike bulk SnS. Ferroelectric switching is successfully demonstrated for the monolayer device at room temperature. Remarkably, for thin SnS below a critical thickness ($\sim$ 15 layers), the SHG signal and ferroelectric switching are observed in both odd- and even-number layers, thus overcoming the odd–even effect, which suggests that ultra-thin SnS is grown in an unusual stacking sequence lacking centrosymmetry. A cross-sectional TEM observation of multilayer SnS directly proves the transition of staking sequence from AA to AB staking. Given that SnS is the semiconductor with multiferroicity, innately exhibiting pyroelectricity and piezoelectricity, this first demonstration of the ferroelectricity in SnS will open up possibilities of providing novel multifunctionalities in vdW heterostructure devices.

Thesis Supervisor: Kosuke Nagashio
Title: Associate Professor of Materials Engineering

Acknowledgments

First of all, I would like to thank my supervisor Prof. Kosuke Nagashio. Nagashio-sensei gave me the greatest and hardest opportunity to struggle with a new material: SnS. Nagashio-sensei's support and insightful advises lead me to the deep understading. Nagashio-sensei can do a magic making us believe that the impossible is possible. Actually, the monolayer SnS was far from us at the beginning. But we did it. Thank you so much for giving me a chance.

I would also like to thank Prof. Yuji Suzuki, Prof. Satoshi Watanabe, Prof. Ken Uchida, and Prof. Koji Kita for their help on my doctoral dissertation committee. The discussion with them improved my research and let me thoroughly reconsider the experimental results.

Secondly, I would like to thank Dr. Tomonori Nishimura for his help to understand ferroelectric and interface. Without Nishimura-san's help, I couldn't reach a deep understanding on the ferroelectric and Fermi level pinning of the 2D materials. I would like to thank Hayami Kawamoto, one of the largest collaborator in SnS-project, for his great contribution on the PVD growth of SnS. I also feel very luck to work with Masaya Umeda and Yih-Ren Chang. A part of measurement setup for nanogenerators in this work was built by Umeda-kun. And Chang's ideas for growth mechanism helped me to understand the experimental results. I hope for your further success.

There are so many other collaborators: I also thank Prof. Wen-Hao Chang, Dr. Chien-Ju Lee, Bo-Han Lin, and Fu-Hsien Chu (NCTU, Taiwan), for their nice data of SHG measurement. For the collaborate on first-principle calculation of phonon modes of SnS, I really thank Prof. Katsunori Wakabayashi and Itsuki Yonemori (Kwansei Gakuen Univ.). Prof. Keiji Ueno (Saitama Univ.), Dr. Masaru Nakamura, Dr. Naoki Ohashi, and Prof. Kiyoshi Shimamura (NIMS) provided us SnS crystals. Prof. Ryo Kitaura and Zhao Chen (Nagoya Univ.) provided us MoS_2 crystals. Prof. Takeshi Momose and Dr. Tae-Woong Kim (UTokyo) supported me for the Auger measurments. I also thank the support by Dr. Naoka Nagamura (NIMS) for nano-ESCA measurements. I was really happy to work with Prof. Toshiya Sakata and

Shoichi Nishitani (UTokyo), who kindly supported and encouraged me to try the SnS Bio-sensors.

In Nagashio group, I also thank Mrs. Kyoko Ogawa for her supporting our lab life. I really thank Prof. Yoshiaki Hattori for his help in the experiments. Dr. Nan Fang is a good teacher and friend for me. He always encourages me and gives me a new insights. There are so many others to thank: Dr. Teerayut Uwanno, Taro Sasaki, Junyang He, Koki Taniguchi, Syunya Sekizaki, Kohei Maruyama, Satoshi Toyoda, Keigo Nakamura, Yuichiro Sato, Masahiro Kobayashi, Shuhong Li, Ryoichi Kato, and Wataru Nishiyama. Thanks for all the fun memories. These past three years are more valuable than PhD degree. I wish all of you the best of luck.

Finally, I would like to express my deepest gratitude to my parents and family. You have encouraged me more than you will ever know. I would not have come here without your help. This thesis is dedicated to all of you.

Contents

List of Figures

List of Tables

Chapter 1

Introduction

In the past decade, cost-effective and environmentally friendly electronic devices has become increasing important for a sustainable society. To realize a low carbon society, ultra-low power electronic devices are required. Moreover, high-efficient energy harvesting technology is an urgent issue to satisfy the growing up demands of internet of things (IoT). A great deal of enthusiasm has been given in diverse fields of circuit design, mechanical system, and softwares, in order to realize Trillion Sensor Universe. Also new material platforms have been anticipated for a game-changing breakthrough. Two-dimensional (2D) layered material is one of the promising candidate for multifunctional device applications. Some non-centrosymmetric 2D materials posses piezoelectricity, pyroelectricity, and ferroelectricity, which can be applied to non-volatile memories or energy harvesters that can constitute self-powered IoT devices. This chapter is dedicated to brief introductions of the IoT, fundamental principles of piezoelectricity and ferroelectricity, and historical reviews of non-centrosymmetric materials.

1.1 Internet of Things

The word *Internet of things* is now a common word that people use in the various fields of engineering, economics, and industry. Not a few people believe it is a fashionable term and gives us new insights for the future world, though the origin of this word

goes even further to 30 years ago, and it has been often misunderstood away from its original definition and implication. As far back as September 1985, Peter T. Lewis coined the term Internet of Things (IoT) in a speech to the Congressional Black Caucus Foundation 15th Annual Legislative Weekend (Washington, D.C.). Lewis defined IoT as "The integration of people, processes and technology with connectable devices and sensors to enable remote monitoring, status, manipulation and evaluation of trends of such devices." This definition includes three important features of IoT as follows:

- IoT enables us to get to know about the status of things remotely.
- We can manipulate and communicate with the devices.
- Things can communicate with each other interactively and seamlessly.

Even now, these concepts are regarded as the fundamental significances of IoT. However, IoT had not been featured for over 10 years after it was firstly coined, because it was too early for the internet to be far reaching in 1980's.

The internet widely spread all over the world with a remarkable development of optical fibers in 1990's. Fig. 1-1 shows the information-carrying capacity with time [1]. Back to 1880's that the telephone line was firstly constructed, the relative information capacity was $\sim$1 bit/s. From 1980 to 2000, the information-carrying capacity had grown up remarkably, owing to the development of technologies such as communication satellite and optical fiber systems. In the early 2000's, the information-carrying capacity increased to $\sim 10^{12}$ bit/s. Based on the Cisco VNI Global IP Traffic Forecast, the global internet protocol traffic is reaching to 3.0 zettabytes (ZB) per year in 2020 ($1\,\text{zettabyte} = 1\,\text{trillion}\,\text{GB} = 10^{21}\,\text{B}$), as shown in Fig. 1-2.

IoT had to wait to be widely recognized until 1999, when Kevin Ashton had a presentation titled as "Internet of Things" at Procter & Gamble (MIT Auto-ID Labs). Together with the fundamental features that Lewis mentioned, Kevin implied the importance of *things* rather than *information*. Actually the information technology was reaching maturity at that time, though it left the physical world including human

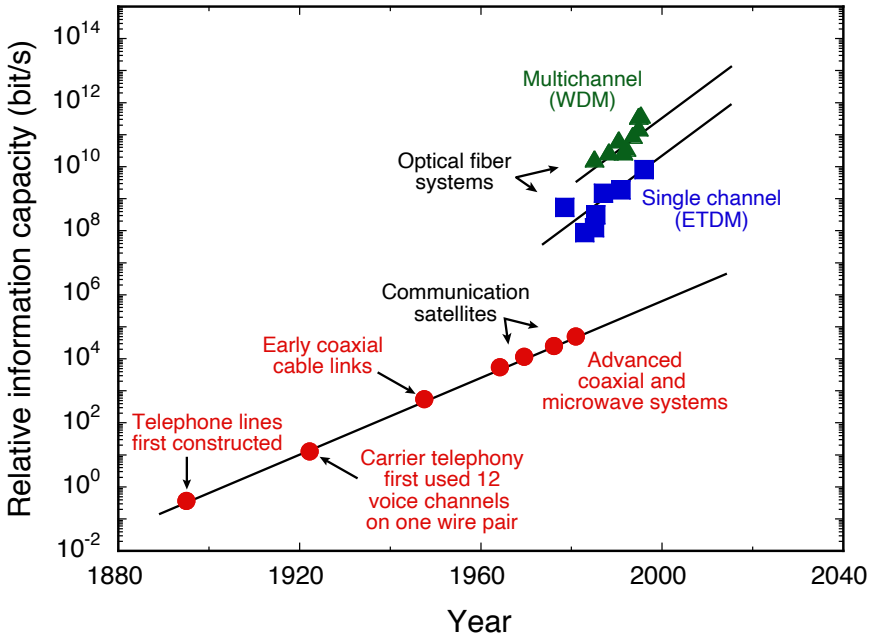

Figure 1-1: Progress of the in information-carrying capacity of a single line [1].

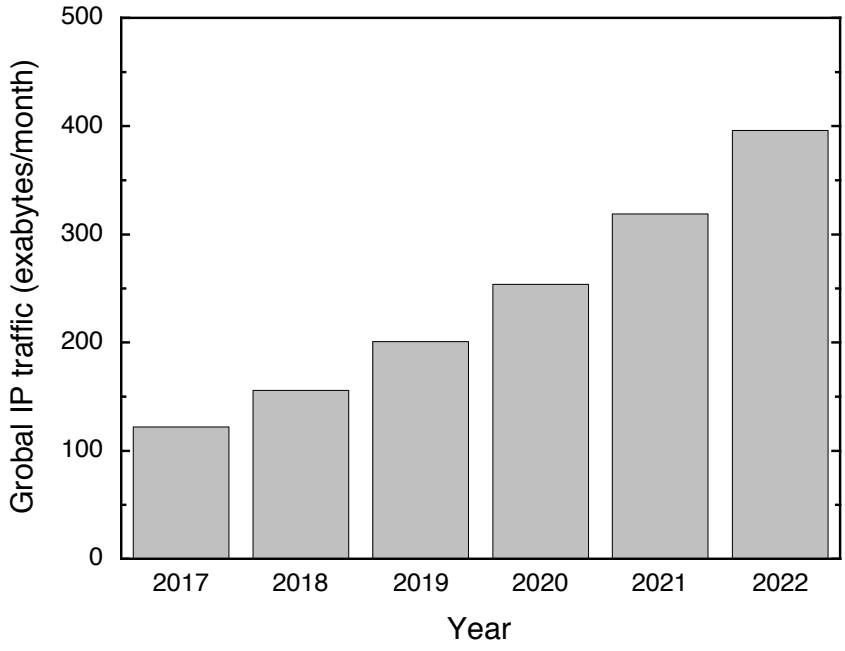

Figure 1-2: Global IP traffic forecast (Cisco).

beings behind. Kevin's suggestion was a paradigm shift from *Internet for Information* to *Internet for Things*, which gathers the information of whole things without any help from people so that we can know everything as the physical world is [2]. Despite of his prospect, IoT had been misunderstood to be a mere digitalization or distribution of things, in the early 2000's. But its potential to make the world better became gradually recognized in various fields.

Since around 2010, IoT is taking on reality with the development of technology in sensors and wireless communications [3, 4]. In 2009, IBM proposed "Smarter Planet" framework, where the physical things are monitored and processed intelligently [3]. Recently, In the last few years, the emerging technologies of artificial intelligence, machine learning, and 5G networks, has been boosting the IoT area [5, 6]. A massive amount of data and high-speed data analysis of it will enable us to realize the veiled information that difficult to extract directly from the real world.

This section exclusively focuses on the current statuses of two key technologies for IoT; low power consumption and energy harvesting devices.

1.1.1 Trillion Sensor Universe

In the developed IoT society, sensors will be embed in an enormous number of physical things, and all of them are connected to the internet [7]. The demand of sensors per year has been predicted to be scaled up to trillion by 2021 or more a few years later, as whon in Fig. 1-3 [8]. This phase was coined as "Trillion Sensor (TSensor)" universe by Janusz Bryzek, who is the Chairman and CEO of TSensors Summit. In his TSensor vision, the number of sensors will exceed over 10 trillion in the next 15 years [8]. From the World Population Prospect (by United Nations, 2019), the total world population is expected to be approximately 7.79 billions in 2020, which means that people use $\sim$128 sensors per person and per year in the one trillion sensor universe. The TSensors initiative has been pursuing the possibility of solving worldwide problems from environmental, food, education and medical problems. However, there are still lot of issues to to solve. With increasing the number of sensors people use, it is no realistic to operate them *via* power supply wiring or on batteries. In such

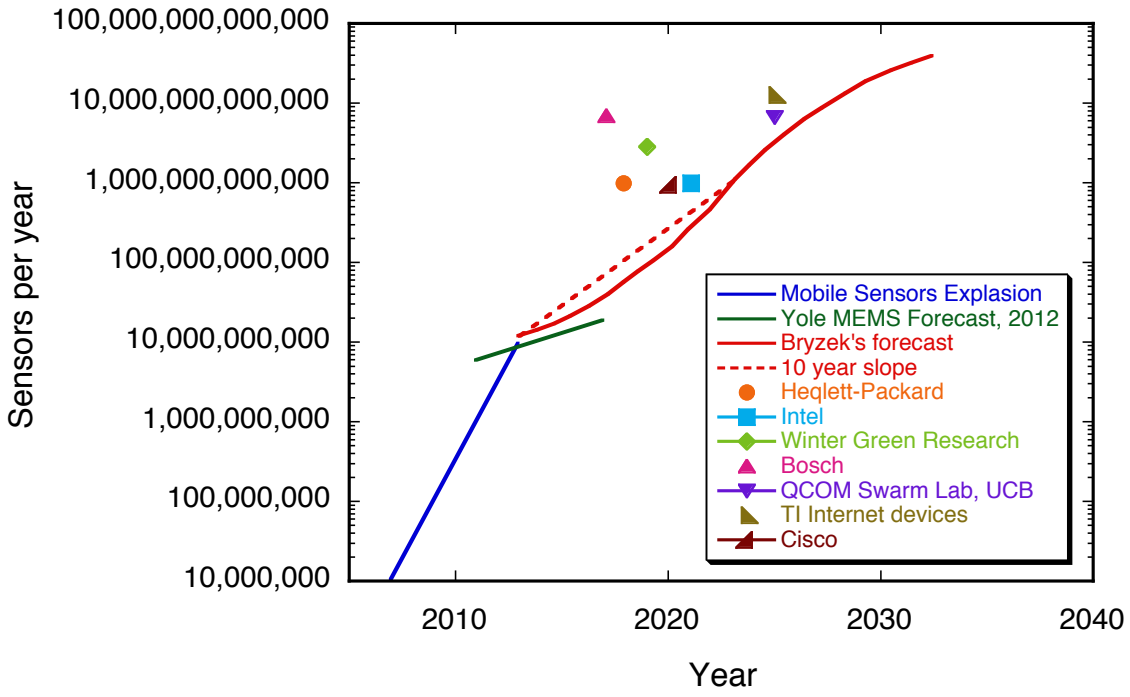

Figure 1-3: Forecast of the number of sensors demand per year [8].

a situation, the IoT devices has to be wireless and self-powered. Actually, EnOcean has been producing self-powered wireless switches and sensor modules since 2002 [9]. In these devices, power generators are embed, witch are based on electromagnetic induction, solar cells, or thermoelectric generators. Also EnOcean focuses on the one-channel wireless communication with randomized signals to prevent mixing multiple signals. These devices has been already utilized in the building automation for over one million buildings all over the world [9], though their application region and functionalities would further improve if further low power consumption, high efficient power generation, and miniaturization are realized.

1.1.2 Power Consumption and Supply

Fig. 1-4 shows trend and forecast of power consumption and supply in the electronic devices. There are three phases:

1. Intermittent operated closed devices without wireless communication, for health care and body-iplanted device applications.

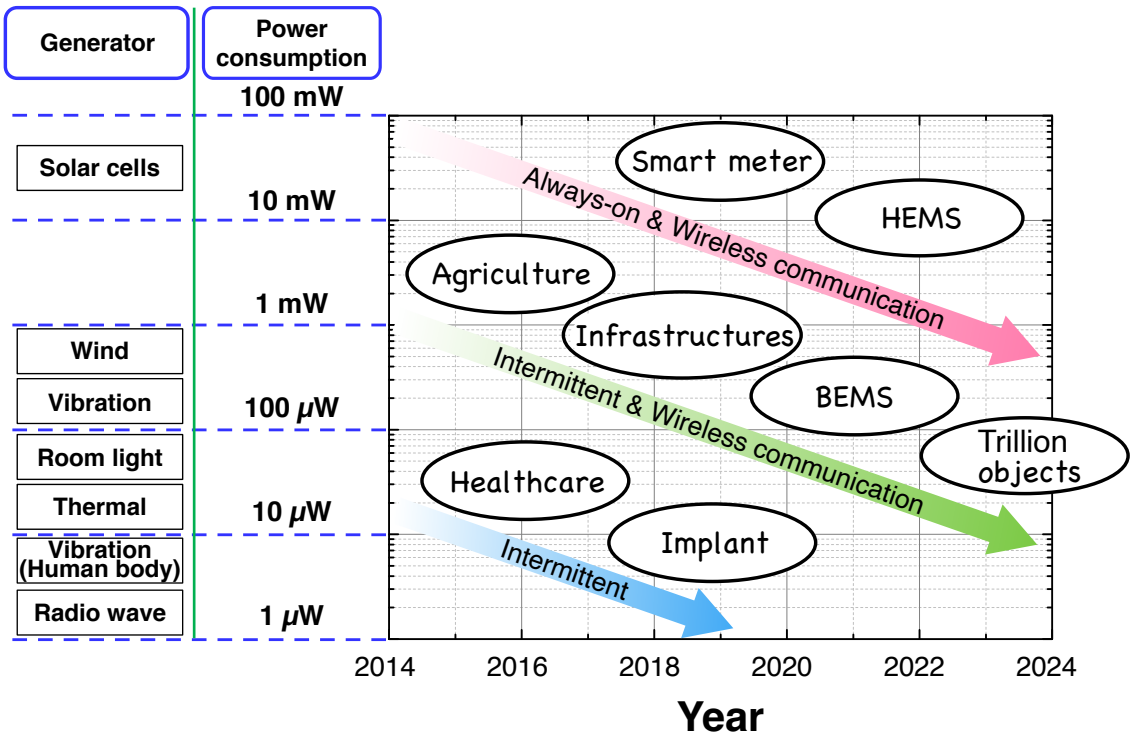

Figure 1-4: Worldwide trend of power consumption and supply for the electrical devices (IEICE-ICD, Japan).

2. Intermittent operated IoT device, for monitoring agricultural and infrastructural objects.

3. Always-on IoT devices, for smart meters and home energy management systems.

The power consumption of these IoT devices is decreasing and larger power is required for the upper phase. It is expected that the power consumption of single IoT device will decrease down to at the order of 100 µW even at the Phase 3 (Fig. 1-4). Currently, the power consumption of commercially available intermittent devices is several-tens mW per device: 52 mW on average for Apple Watch (Apple), and 60 mW at maximum for ZigBee (Texas Instrument). For the always-on devices, the average power consumption is below 100 µW: 33 µW for a heart pace maker Medtronic Advisa MRI A3DR01 (Medtronic), and 88 nW for a timer IC TPL5010/TPL5110 (Texas Instruments). As an end-of-phase goal of this work, 100 µW class of ultra-low power consumption functional devices and energy harvesters are focused.

1.2 Low Power Consumption Devices

Fig. 1-5 shows an example of memory hierarchy in an information and communication technology (ICT) system (LEAP, Japan). For the data processing and computations, there are four types of functions: high capacity data storage, high speed storage for data transfer, main memory, and logic circuit such as transistor or switching devices. Here, this work focuses on a non-volatile memory (NVM) for the main memory. NVM is a memory that can retain the data even at the off-state, and composing the present electronics. For example, Flash Memory is one of the NVMs, which is widely used as memory card, USB, and SSD.

In this section, various kinds of researches on the NVM are reviewed. Especially, the mechanism and perspective of random access memories (RAM) based on ferroelectric materials are discussed.

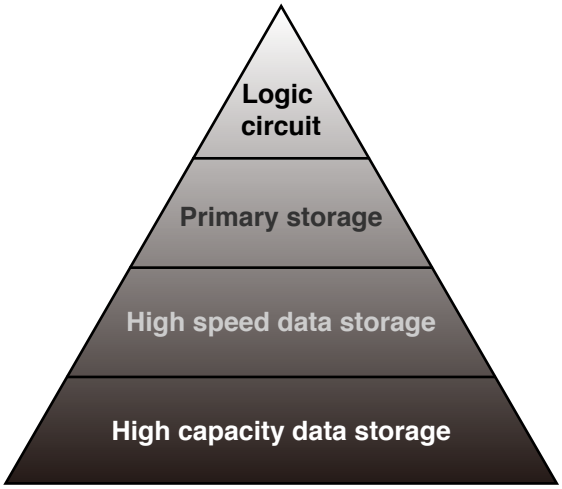

Figure 1-5: Example of memory hierarchy in an ICT system (LEAP, Japan).

1.2.1 Non-volatile Memories

Currently, NVMs are used for secondary/external storages. For most of main storage, a volatile RAM is usually used, which means that all the data will be erased when it is shut down. That is why we have to take a sequence of shutdown PC in order to save all the tasks, otherwise main memory has to be always on-state. NVM have an advantage

of low-power operation, however, it has not reached the industrial application because it is still expensive and unstable for the main memories. Table 1.1 shows the typical figure of merits and market situations for the volatile and non-volatile memories [10]. The volatile memories of static RAM (SRAM) and dynamic RAM (DRAM) are usually used for the main memory. SRAM has an advantage of high-speed operation, though its device structure is complicated so that SRAM is more expensive than DRAM. There are various kinds of NVMs such as NAND flash memory, resistive RAM (ReRAM), ferroelectric RAM (FeRAM), phase-change memory (PCM), and spin-transfer torque RAM (STT-MRAM) [11, 10]. From the point of view of the writing time, energy consumption, retention, and endurance, FeRAM is a promising candidate for the NVMs, owing to its operation mechanism as discussed later (see details in Section 1.2.2). However, it is more expensive and has much smaller data capacity, compared to other NVMs.

Table 1.1: Typical FoM values and market readiness for established and emerging memory technologies [10].

FoM	SRAM	DRAM	Flash NAND	ReRAM	FeRAM	PCM	STT-MRAM
Density (bytes per chip)	$\approx$ 10 MB	1–10 GB	$\approx$ 10 GB	$\approx$ 1 GB	$\approx$ 1 MB	1–10 GB	10–100 MB
Cell size (F^2)	>100	6–10	4–5	6–20	15–40	6–20	35–40
Write time	<10 ns	$\approx$ 10 ns	$\approx$ 100 μs	10–100 ns	$\approx$ 100 ns	10–100 ns	$\approx$ 10 ns
Program energy per bit	1–10 pJ	1–10 pJ	$\approx$ 10 nJ	$\approx$ 10 pJ	1 pJ	0.1–1 nJ	<1 pJ
Retention	Volatile	Volatile 10–100 ms	Nonvolatile >10 years	Nonvolatile >10 years	Nonvolatile >10 years	Nonvolatile >10 years	Nonvolatile >10 years
Endurance (cycles)	$>10^{15}$	$>10^{15}$	10^2–10^5	10^6–10^9	$>10^{15}$	10^6–10^9	$>10^{15}$
Maturity	Product	Product	Product	Early product	Product	Early product	Early product
Merket price ($ per GB)	10–100 k	$\approx$ 10	$\approx$ 1	$\approx$ 1 k	10–100 k	10–100	1–10 k

1.2.2 FeRAM

FeRAM's fundamental mechanism is the spontaneous polarization in the ferroelectric materials. If a polarization is formed in a dielectric under an external electric field and the polarization disappear without the electric field, this dielectric is not a ferroelectric, but just a paraelectric. For the ferroelectricity, rigid characteristics of structural non-centrosymmetricity and switchable spontaneous polarization are required. In this case, the polarization formed under the external electric field will be maintained as a remanent polarization even after the electric field becomes zero. Ferroelectricity has an advantage in the durable polarization switching, which is owing to the ionic displacement at an atomic scale, as shown in Table 1.1. Though it has been a critical issue that ferroelectric materials is difficult to be thinned down due to a size effect [12, 13, 14], especially a depolarization field [15] (see details in Section 4.1). Due to the limitation of thickness and footprint for FeRAM, the data capacity per unit are is much smaller than other NVMs. For further progress in FeRAM, material breakthrough is necessary overcoming the depolarization field and other issues.

1.3 Energy Harvesting

Table. 1.2 shows the list of energy sources and their power densities. Among the environmental energies, vibrational energy has a high power density 10–1000 times larger than other energy sources: optical, thermal, electromagnetic energies [16]. Also the vibrational energy is less influenced by the change of environment, while solar and thermal power usually have preferences of the location. Therefore, this study focuses on the vibrational energy harvesting toward the self-generated IoT devices.

Up to date, the high-efficiency and ultra-low energy consumption devices have been developed not only in the laboratory, but also commercially. For example, 100 μW is enough to work the temperature and humidity sensors. However, most of the energy harvesters are still low-efficiency, and their power density is below several $\mu W/cm^2$. A game-changing generator has been expected in order to change the IoT devices form wired/battery-powered to self-generated.

Table 1.2: Power densities of different energy sources [16].

Energy source	Examples	Power density (W/cm^2)
Vibrational	Walking, motors, bridge	10^{-3}–10^{-4}
Light	Room light, solar	10^{-4}
Thermal	Human body, automobile	10^{-5}
Electromagnetic	Micro wave, wireless LAN	10^{-6}

1.3.1 Approaches for Mechanical Energy Harvesting

Table 1.3 summarize different approaches for energy harvesting from the mechanical energy. Each method has both advantages and disadvantages, thus it prefer the device application and environment. To satisfy a demand of huge and stable power supply for the modern society, basically electromagnetic induction is used in the thermal and wind power generation systems. Electromagnetic induction is composed of a heavy magnet and bundled coils, which are rotated by steam or wind turbines. These large systems can stably produce megawatts electricity per single unit, though elec-

Table 1.3: Comparison of the principles for mechanical energy harvesting [19].

Approaches	Electromagnetic	Electrostatic	Piezoelectric	Triboelectric
Principles	Electromagnetic induction	Electrostatic induction	Piezoelectric effect and Electrostatic induction	Contact electrification and Electrostatic induction
Impedance type	Resistive	Capacitive	Capacitive	Capacitive
Pros	High efficiency, easy to scale up	Light weight	Easy scale down to nanoscale	High efficiency, cost effective
Cons	Heavy magnet required, low output for small-scale devices	Pre-charge required, low output, high matched impedance	Low output, low efficiency, pulsed output, high matched impedance	Pulsed output, high matched impedance

tromagnetic induction is unfavorable for the small-scale devices due to a fundamental principle of miniaturization (see discussions in the next Section 1.3.2).

In the point of view of miniaturization that is necessary for the energy harvester on IoT devices, electrostatic, piezoelectric, and triboelectric generators are superior to electromagnetic method. These three energy harvester's output power density per unit volume increase with decreasing the device size unlike as the electromagnetic induction. This difference can be clearly understood with using Trimmer's equation [17], as discussed in Section 1.3.2. Also, the classification, electromagnetic versus the others, are originated from a simple Maxwell's equation [18, 19], as described in Section 1.3.3. Complementing these different principles, hybrid energy harvesters have been investigated with an integration of solar cells and piezoelectric generators [20]; and triboelectric, pyroelectric, and piezoelectric generators [21].

1.3.2 Miniaturization of Generators

When an object is scaled-down or scaled-up, the world looks different from the human being's life. For example, a typical ant can easily lift up a bait weighted several times heavier than its body weight, and never die even if it falls freely from the height

of 100 m. This is because the forces and weight changes in the different way with scaling; the weight increases cubically with size, while the muscle strength and air resistance increase quadratically with size. This kind of concept can be generalized to the scaling laws for the power density of mechanical energy harvesters with different methods. The scaling principle was postulated by W. Trimmer in 1989 [17].

As a first step, a matrix formalism is introduced to describe the scaling results. Here, a scale variable s represents the linear scale of system. As an assumption, all dimensions of the system are changed in the same factor as s. When s is changed from 1 to 10, all the dimensions are scaled-up by 10 times. The forces such as electrostatic, pressure, and electromagnetic forces, scale in different ways: $[s^1]$, $[s^2]$, $[s^3]$, $[s^4]$ [17].

- $[s^1]$: electrostatics where $\boldsymbol{E} = [s^{-0.5}]$.
- $[s^2]$: piezoelectric and electrostatics where $\boldsymbol{E} = [s^0]$, electromagnetics where $\boldsymbol{J} = [s^{-1}]$.
- $[s^3]$: electromagnetics where $\boldsymbol{J} = [s^{-0.5}]$.
- $[s^4]$: electromagnetics where $\boldsymbol{J} = [s^0]$.

These four different force laws can be shown in one equation as follows:

$$F = \begin{bmatrix} s^1 \\ s^2 \\ s^3 \\ s^4 \end{bmatrix} \tag{1.1}$$

The scaling of the acceleration a and transit time t can be given,

$$a = F/m = [s^F][s^{-3}] \tag{1.2}$$

$$t = (2x/a)^{1/2} = (2xm/F)^{1/2} = ([s^1][s^3][s^{-F}])^{1/2} \tag{1.3}$$

When the scalings of force is given as Eq. 1.1, a and t can be transformed,

$$a = \begin{bmatrix} s^{-2} \\ s^{-1} \\ s^{0} \\ s^{1} \end{bmatrix} \tag{1.4}$$

$$t = \begin{bmatrix} s^{-1.5} \\ s^{1} \\ s^{0.5} \\ s^{0} \end{bmatrix} \tag{1.5}$$

The power P, amount of work per unit time can be expressed as

$$P = Fx/t = \begin{bmatrix} s^{1} \\ s^{2} \\ s^{3} \\ s^{4} \end{bmatrix} \begin{bmatrix} s^{1} \\ s^{1} \\ s^{1} \\ s^{1} \end{bmatrix} \begin{bmatrix} s^{-1.5} \\ s^{-1} \\ s^{-0.5} \\ s^{0} \end{bmatrix} = \begin{bmatrix} s^{0.5} \\ s^{2} \\ s^{3.5} \\ s^{5} \end{bmatrix} \tag{1.6}$$

Thus the power density per unit volume can be extracted as

$$\frac{P}{V} = \begin{bmatrix} s^{0.5} \\ s^{2} \\ s^{3.5} \\ s^{5} \end{bmatrix} \begin{bmatrix} s^{-3} \\ s^{-3} \\ s^{-3} \\ s^{-3} \end{bmatrix} = \begin{bmatrix} s^{-2.5} \\ s^{-1} \\ s^{0.5} \\ s^{2} \end{bmatrix} \tag{1.7}$$

Eq. 1.7 means that when the scaling factor of force is $F = [s^1], [s^2]$, the power density increases with miniaturizing the device; while for $F = [s^3], [s^4]$, scaling-up is necessary to increase the power density. When the external electric field $\boldsymbol{E} = 0$, whose scaling factor is $\boldsymbol{E} = [s^0]$, the power density of piezoelectric and electrostatic generators has a negative scaling factor $[s^{-1}]$, resulting in the benefit of scaling down for the sake of efficiency. In contrast, the power density of electromagnetic generators has a positive scaling factor, thus scale down has no benefit for its efficiency.

In conclusion, mechanical energy harvesters based on the principles, electrostatic induction, piezoelectricity, and triboelectricity, have advantages in the miniaturization.

1.3.3 Maxwell's Displacement Current Giving Birth of Piezoelectricity

The fundamental theory of the nanogenerators starting from the Maxwell equations were postulated in Ref. [19, 22]. The first and second terms in the Maxwell's displacement current, $\epsilon_0 \frac{\partial \boldsymbol{E}}{\partial t}$ and $\frac{\partial \boldsymbol{P}}{\partial t}$, are the origin of electromagnetic wave and piezo/triboelectric generator, respectively, as discussed below. The Maxwell's equations are shown below:

$$\nabla \cdot \boldsymbol{D} = \rho_f \quad \text{(Gauss's Law)} \tag{1.8}$$

$$\nabla \cdot \boldsymbol{B} = 0 \quad \text{(Gauss's Law for magnetism)} \tag{1.9}$$

$$\nabla \times \boldsymbol{E} = -\frac{\partial \boldsymbol{B}}{\partial t} \quad \text{(Faraday's Law)} \tag{1.10}$$

$$\nabla \times \boldsymbol{H} = \boldsymbol{J}_f + \frac{\partial \boldsymbol{D}}{\partial t} \quad \text{(Ampere's law with Maxwell's addition)} \tag{1.11}$$

where $\boldsymbol{D}$ is the displacement field, $\boldsymbol{B}$ is the magnetic field, $\boldsymbol{E}$ is the electric field, $\boldsymbol{H}$ is the magnetizing field, ρ_f is the free electric charge density, and $\boldsymbol{J}_f$ is the free electric current density. The displacement field can be written as,

$$\boldsymbol{D} = \epsilon_0 \boldsymbol{E} + \boldsymbol{P} \tag{1.12}$$

where $\boldsymbol{P}$ is the polarization field and ϵ_0 is the dielectrics permittivity. J.C. Maxwell has introduced the Maxwell's displacement current defined as [18]

$$\boldsymbol{J}_D = \frac{\partial \boldsymbol{D}}{\partial t} = \epsilon_0 \frac{\partial \boldsymbol{E}}{\partial t} + \frac{\partial \boldsymbol{P}}{\partial t} \tag{1.13}$$

The first term in Eq. 1.13 $\epsilon_0 \frac{\partial \boldsymbol{E}}{\partial t}$ generates the electromagnetic wave, thus is the fundamental law for the wireless communication devices, which are necessary technology

nowadays. Here, the latter term $\frac{\partial \boldsymbol{P}}{\partial t}$ is featured because it determines the polarization induced current, which is the fundamental mechanism for the piezoelectric or triboelectric generators. The piezoelectric equation and constituter equations can be written as follows [23]:

$$P_i = (\boldsymbol{e}_{ijk})(\boldsymbol{s}_{jk}) \tag{1.14}$$

where $\boldsymbol{e}_{ijk}$ is the piezoelectric tensor and $\boldsymbol{s}$ is the mechanical strain. From Eq. 1.13 and 1.14, the displacement current from the piezoelectric polarization is:

$$J_{Di} = \frac{\partial P_i}{\partial t} = (\boldsymbol{e})_{ijk} \left(\frac{\partial \boldsymbol{s}}{\partial t} \right)_{jk} \tag{1.15}$$

This relationship indicate displacement current density is proportional to the variation rate of the strain. When the external electric field is assumed to be zero, and the polarization is along the x-axis, the polarization vector is:

$$D_x = P_x = \sigma_p(x) \tag{1.16}$$

where $\sigma_p(z)$ is the surface density of piezoelectric polarization charges. Thus the variation rate of surface polarization charge density directly means the piezoelectric output current. The open circuit voltage V_{OC} can be give as follows:

$$V_{OC} = z\sigma_p(x)/\epsilon \tag{1.17}$$

1.4 2D Materials

In 2004, Andre Geim and Konstantin Novoselov (Manchester Univ. in England) has investigated the graphene field-effect transistors (FET), for the first time [24] (Fig. 1-6a). The mechanical exfoliation method by the Scotch tape, which they proposed to isolate a single layer from bulk graphite, has been commonly used all over the world for graphene, transition metal dichalcogenides (TMDCs), and other two-dimensional (2D) layered materials. In 2011, Kis's group (EPFl in Switzerland) has demonstrated FETs based on monolayer MoS_2, a member of TMDC family, for the first time [25] (Fig. 1-6b). Before that, MoS_2's advantage of layered structure was used only in the very limited applications such as solid lamella lubricants [26]. Owing to these discoveries of the potentials in 2D layered materials at the atomic thickness, lots of novel research areas in science and engineering have been emerging. However, their device application has been limited to the electronic and optical devices.

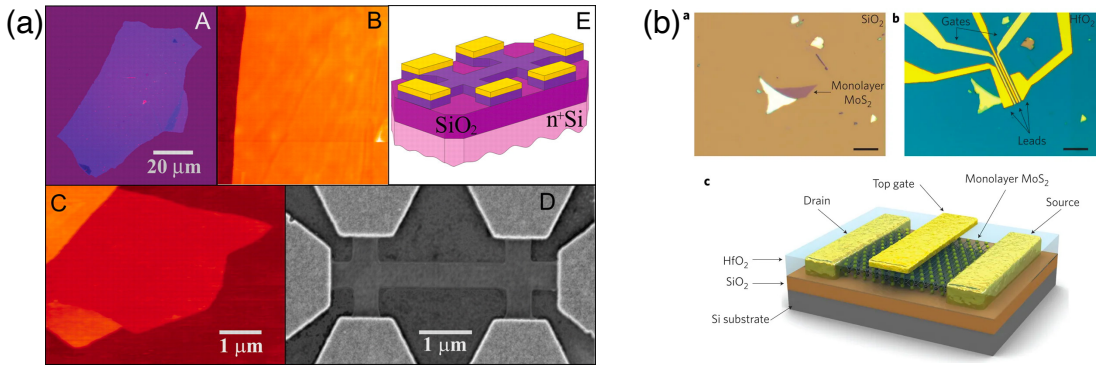

Figure 1-6: FET devices based on (a) graphene and (b) monolayer MoS_2 [24, 25].

Although the crystal structure of graphene is centrosymmetric, monolayer and odd-number-layer MoS_2 lacks the centrosymmetry, resulting in a piezoelectric effect. In 2014, Z.L. Wang's group (Georgia Tech in US) has demonstrated piezoelectric generators based on 2D MoS_2 [27]. Fig. 1-8 shows the thickness dependence of piezoelectric response under the repeated strain. The current is generated only in the odd number layers $(1, 3, 5...)$, though even number layers have no piezoelectricity due to an odd–even effect, as discussed later. The piezoelectric coefficient d_{11} of MoS_2 is maximized in the monolayer [28] and its power density was experimentally

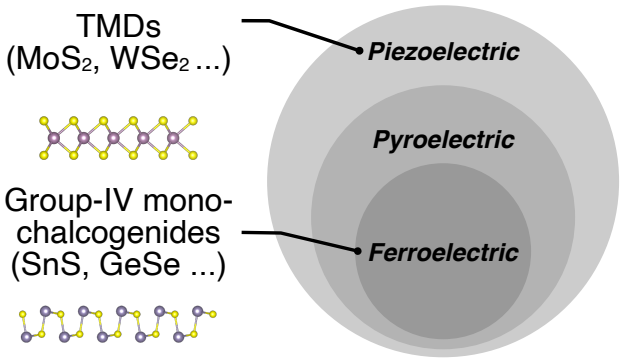

Figure 1-7: Non-centrosymmetric 2D materials. Piezoelectricity and pyroelectricity are innate property of ferroelectricity.

determined to be ~200 nW/cm^2 [27], which is still insufficient to make present low-power consumption IoT devices work. To improve the power density beyond 100 μW/cm^2, which is enough large to operate the IoT devices, a breakthrough of material is necessary.

2D layered tin sulfide (SnS), one of the group-IV monochalcogenides (MX), is theoretically expected to have a large piezoelectric coefficient two order larger than MoS_2 and comparable to conventional piezo-ceramics [29]. Moreover, ferroelectricity is expected in monolayer SnS in addition to the piezoelectricity and pyroelectricity [30, 31].

In this section, literature reviews are summarized for graphene and other 2D materials. As non-centrosymmetric 2D materials, TMDCs and MXs are discussed with previous theoretical and experimental references.

1.4.1 Graphene and TMDCs

The first demonstration of graphene FET by Geim and Novoselov has boosted the research and industrial interests for graphene and other layered materials [24]. Graphene has advantages in high mobility over 200,000 cm^2/Vs (at room temperature) [32] and quite high in-plane and stiffness [33, 34]. Although some fabrication procedures of graphene have been reported, remarkably, especially a high-quality graphene is obtained *via* a simple mechanical exfoliation method, which utilize a commercially

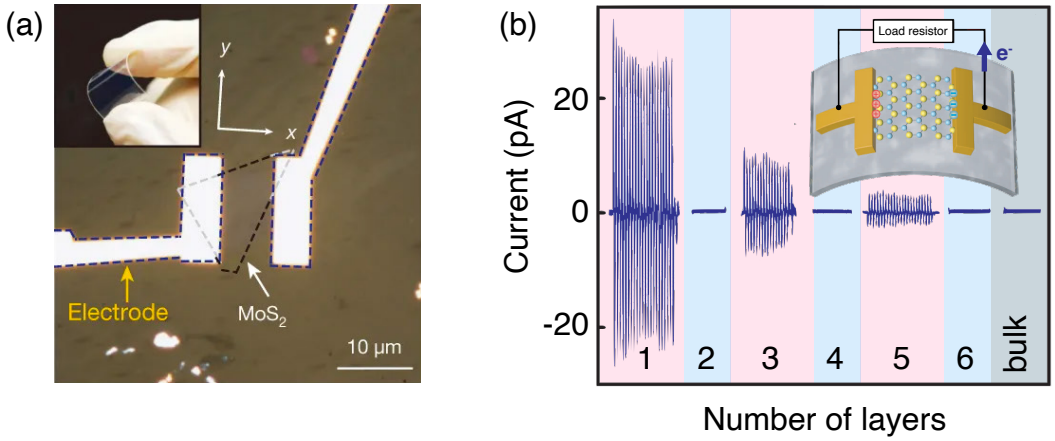

Figure 1-8: The first demonstration of piezoelectric generators of MoS_2 [27]. (a) A typical flexible device with single-layer MoS_2 flake and electrodes at its zigzag edges. Inset: optical image of the flexible device. (b) Evolution of the piezoelectric outputs with increasing number of atomic layers in MoS_2 flakes.

available Scotch tape to exfoliate a single layer from a bulk graphite [24]. Different from other semiconductors, graphene have the linear energy dispersion and carriers with zero mass, which attribute to its high mobility [35]. A single layer graphene has no bandgap, which can be an issue for electrical application because off-state is inevitable; while it is possible to open a bandgap in bilayer graphene with applying an external field [36]. Even recently, new physics are still unveiled in graphene and bilayer graphene, for example, superconductivity in a twisted bilayer graphene with a magic angle [37].

2D materials have also attracted much attention with their unique electrical, optical, and mechanical characteristics. Their monolayer can also be isolated from bulk materials in the same way as exfoliation of graphene. As a representative of 2D materials, TMD has been a hot topic in science and engineering for these ten years [25, 38]. MoS_2, a member of TMDs family, is an indirect semiconductor in bulk and down to bilayer, while transit to direct bandgap in monolayer [39]. These properties of non-zero bandgap and layer number dependence are reasons why MoS_2 is expected to be a promising candidate in the application to electrical [40] and optical [41] applications.

1.4.2 Non-centrosymmetric 2D Materials

One of the fundamental feature that monolayer MoS_2 has but graphene does not is a structural non-centrosymmetry [42]. The definitions of "centrosymmetric" and "non-centrosymmetric" are as follows [43]: a centrosymmetric material has points of inversion symmetry throughout its volume, and a material that does not is said to be non-centrosymmetric. The non-centrosymmetry is required for the piezoelectricity, pyroelectricity and ferroicities. Here, note that a non-centrosymmetric material is not always piezoelectric (Class 432 is a non-centrosymmetric but not a piezoelectric [43]), and piezoelectric effect requires non-zero bandgap. To clarify how many and which materials have non-centrosymmetric, Evan J. Reed's group (Stanford Univ. in US) has investigated over 50,000 inorganic materials with using a data mining method: among non-zero bandgap materials, 325 materials were found to be non-centrosymmetric materials [44]. They have also theoretically investigated piezoelectric 2D layered materials in 2012: a series of TMDs and *h*-BN was calculated, and found to show an intrinsic piezoelectricity [28]. For example, the theoretical piezoelectric coefficient d of monolayer MoS_2 is $d = 3.73$ pm/V, comparable to that of bulk α-quartz [28].

Two years later, following Evan's theoretical works, Z.L. Wang's group has experimentally demonstrated MoS_2 piezoelectric nanogenerators [27]. One more year later, for further investigation, Qi *et al*. reported a work on piezoelectric charge polarization-induced electric field in a monolayer MoS_2 by atomic force microscope (AFM) probe [45]; and Zhu *et al*. reported an electromechanical actuation of free standing monolayer MoS_2 sheet [46]. Moreover, Sang-Woo Kim's group (SKKU in Korea) has been exploring monolayer WSe_2 and bilayer WSe_2 with different stacking sequences, and demonstrated their piezoelectric generators [47].

In another approach, surface modification methods has been investigated to induce a piezoelectricity into centrosymmetric materials, black phosphorus (BP) [48, 49] and graphene [50], which are non-piezoelectric itself.

Among intrinsically piezoelectric material, group-IV monochalcogenide (MX: M

= Sn, Ge and X = S, Se) is theoretically expected to have a remarkable piezoelectric coefficient [29]. For SnS, SnSe, GeSe, and GeS, the piezoelectric coefficient is expected to be approximately $d = 251, 145, 212, 75$ pm/V, respectively [29]. Fig. 1-9 shows a comparison of piezoelectric coefficients d and g for SnS, MoS_2, and conventional piezoelectric materials [28, 29, 51]. Each coefficients correspond to the energy conversion efficiency from mechanical to electrical, and from electrical to mechanical, for g and g, respectively (also see the discussion in Section 3.1). These values of SnS are almost two order larger than MoS_2 and comparable to the conventional. Thus, SnS is a promising platform for the piezoelectric generator. Furthermore, the crystal structure of monolayer SnS exhibits a spontaneous polarization, and theoretically expected to be a ferroelectric (Fig. 1-7).

1.4.3 2D SnS

Bulk SnS has been investigated as a semiconductor with moderate band gap $E_g = 1.1 - 1.3$ eV [52, 53, 54, 55, 56], for the application of solar cells [57], thermoelectric [58], and p-type FETs [59, 60, 61]. As different phases of *tin sulfide*: SnS, Sn_3S_4, Sn_2S_3, and SnS_2, have been studied theoretically and experimentally [62, 63]. Only for the SnS, multiple phases have been predicted and discovered [64, 65]; in this work, the orthorhombic SnS is focused that belongs to $Pnma$ in bulk ($Pmn2_1$ in monolayer) and shows piezoelectricity in odd-number layers. All the notations SnS shown below means the orthorhombic SnS unless otherwise noted.

With a lots of works on various properties in 2D SnS, mostly focusing on monolayer, SnS is expected to be a promising candidate for functional device applications such as FETs [59, 66], optical [67, 68, 69, 70], energy harvesting [29, 71], memories [72, 73, 74], gas sensing [75, 76, 77], and medical applications [78, 79].

In this work, piezoelectric and ferroelectric properties of 2D SnS is investigated toward nanogenerator and FeRAM applications in TSensor universe. Given that SnS is composed of Sn and S, both of which are earth-abundant and eco-friendly material, it has much potential to be a game-changing material.

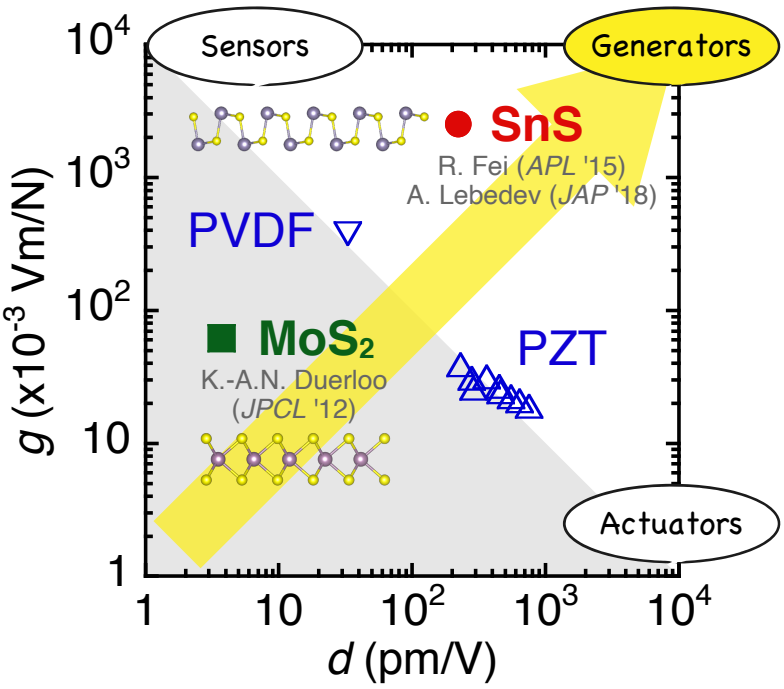

Figure 1-9: Piezoelectric coefficients of 3D and 2D materials.

1.4.4 Odd–even Effect

The piezoelectric effect in MoS_2 and SnS appears when they are thinned down to odd-number few-layer, while disappears in even number layers and bulk states. This effect is called odd–even effect in this thesis. Fig. 1-10 illustrate the origin of odd–even effect. In an energetically ground state, bilayer MoS_2 and SnS are stacked in anti-parallel direction, as shown in Fig. 1-10, which cancel out the piezoelectric effect. As in the same way, the ferroelectricity in SnS is expected only in the odd-number few-layer. These situation is opposite to that of conventional piezoelectric and ferroelectric 3D materials, whose ferroelectricity disappears in the nanoscale owing to the depolarization field or interfacial effects [15, 80, 81] (see details in Section 4.3). The downscaling property in MoS_2 and SnS means that nanogenerators and FeRAMs based on these 2D materials can be achieved at an ultimate atomic thickness along with the remarkable flexibility, which can be applied to wearable devices and shape memories in soft robots.

This odd-even effect is not applied to all the non-centrosymmetric 2D materials. There are some materials, whose multilayers also posses the non-centrosymmetry:

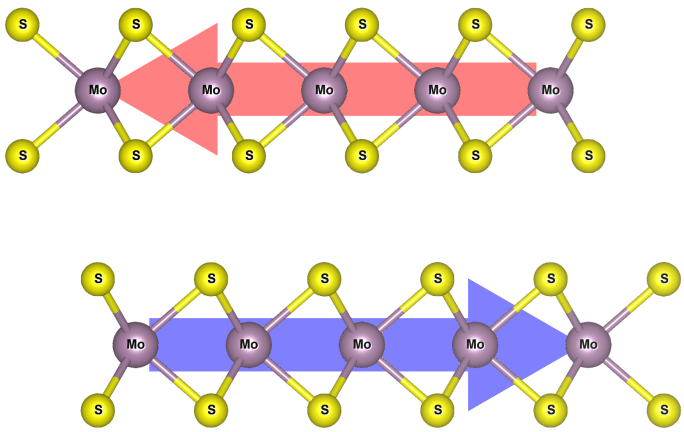

Figure 1-10: Schematic illustration of odd–even effect in the MoS_2

tellurene [82], In_2Se_3 [83], and SnTe [73]. Moreover, in a parallel stacking sequence, multilayer MoS_2 or WSe_2 can be piezoelectric even in the even number layers and bulk [84, 47, 85]. These results suggest that it can be possible to realize a piezo/ferroelectricity in SnS regardless of the number of layers, if we can control the stacking sequences. In Chapter 3 and 4, stacking-controlled multilayer MoS_2 and SnS will be discussed.

1.5 Thesis Goal and Outline

The goal of this thesis work is to understand the mechanism of 2D piezo/ferro-electric materials, and demonstrate piezo/ferro-electric devices based on the monolayer SnS. As will be seen, the fundamentals of piezo/ferro-electricity in 2D materials, fabrication methods for monolayer SnS, characterization of electromechanical response of SnS, and the first demonstration of purely in-plane ferroelectricity in few-to-monolayer SnS will be described.

In Chapter 2, the origin of strong interlayer forces in SnS is discussed starting from its structural configuration. A significant role of lone pair electrons in Sn atoms are portrayed to explain the structural distortion, interlayer interaction, and chemical/thermal stabilities of 2D SnS. Fabrication methods of monolayer SnS are investigated from a top-down thinning to bottom-up crystal growth. Comparing each fabrication procedures, structural, optical, and electrical characterizations will be discussed to evaluate the crystalline quality. A monolayer SnS is achieved *via* surface oxidation thinning method, with forming a robust self-passivation of SnO_x. Also, bottom-up crystal growth is studied with physical vapor deposition (PVD). The PVD grown monolayer SnS exhibits higher crystalline quality and less extrinsic defects than monolayer *via* top-down thinning. As a key technology of monolayer growth, important roles in mica substrate will be discussed.

In Chapter 3, fundamentals and experimental results for the piezoelectric devices are described. Modulation of Schottky barrier height at the interface between metal and SnS are found to be critical, for applying it to the piezoelectric and ferroelectric devices. A fundamental mechanism for the piezoelectric effect in the 2D materials is investigated with using 2D MoS_2 as a model material. An important techniques in the device fabrication, metal transfer method to create the van der Waals gap between metal/MoS_2 free from Fermi level pinning, is discussed in detail. The origin and of piezoelectricity in 2D materials are found to be an asymmetric modulation of Schottky barrier height at the 2D/metal interface. Furthermore, an electromechanical response of 2D SnS is investigated, under both static and dynamic external

strains. As an analogy of the piezoelectric effect, the piezoresistive effect is precisely distinguished from the piezoelectricity. Piezoresistive and piezoelectric effects are characterized with a symmetric and asymmetric change of Schottky barrier height at source and drain. A novel approach in characterizing piezoelectric charge at the 2D/metal interface, transport measurement of top-gated field effect transistor under the strains, is describes. As an important finding, the piezo-charge can be unveiled by modulating channel property.

In Chapter 4, the first demonstration of room temperature (RT) ferroelectricity is shown. As a prerequisite property for ferroelectricity, a structural non-centrosymmetry is confirmed for the monolayer by second harmonic generation (SHG) measurement. A angular resolved SHG and Raman measurements are also performed to reveal a strong anisotropy in SnS. Also, a dependence of SHG intensity on the number of layers is investigated. A remarkable finding for the layer number dependence that the intrinsic property of odd–even effect in 2D SnS is broken for the few-to-monolayer SnS PVD grown on mica substrate, is discussed in detail. An electrical transport characterization of a two-probe device with modulating the Schottky barrier height is described, as a direct proof for the ferroelectricity in SnS. A ferroelectric resistive switching under an external electric field is demonstrated at RT and 1 Hz. The layer number dependence of ferroelectric switching will be discussed in comparison with the results of SHG measurement.

Finally, a summary with knowledge and findings in the 2D SnS are given. Future outlooks for the functional nano-devices based on 2D SnS are also be shown.

Appendixes contain fabrication methods, theoretical analyses, and other additional experimental results.

Chapter 2

Fabrication and Characterization of 2D SnS

Two-dimensional tin sulfide (SnS), one of the group-IV monochalcogenides (MXs; M = Sn/Ge and X = S/Se, has recently attracted interests in the application to flexible piezoelectric generator, because it is theoretically predicted that SnS has a large piezoelectric coefficient $d_{11} = 145$ pm/V that is comparable to conventional lead zirconate titanate (PZT, $d_{33} \sim 300$ pm/V) [29]. For MXs, the piezoelectricity exists only in the odd-number layers, since the broken inversion symmetry disappears in the even-number layers. The piezoelectric coefficient increases with decreasing the layer number, and is maximized in the monolayer [27]. However, the fabrication of monolayer SnS has only been achieved by liquid phase exfoliation with smaller lateral size than 500 nm [52]. Although relatively large SnS layers can be fabricated by mechanical exfoliation and thin film growth methods, SnS layers thinner than 5.5 nm have not been realized yet [86]. This is probably due to the strong interlayer interaction by lone pair electrons in Sn atoms [87].

In this chapter, fundamental characteristics of 2D SnS is discussed structurally, chemically, optically, and electrically, starting from the crystal structure of SnS. To realize the monolayer fabrication, different approached were performed from mechanical exfoliation to crystal growth.

2.1 Fundamentals of Group-IV Monochalcogenides

2.1.1 Distortion from NaCl Structure

Fig. 2-1 shows top and cross-sectional views of crystal configuration of SnS (monolayer and bilayer SnS are shown for top and side view, respectively). The crystal orientation, b and c here, are commonly called as zigzag and armchair directions, which represent the shapes of atomic configuration at the edge. Also, the crystal structure along armchair direction is called puckered structure in this thesis, expressing rows of two orthogonally coupled hinges similar to black phosphorus (BP). The piezoelectricity and ferroelectricity in SnS are expected along the armchair direction prominently [29], owing to the remarkable flexibility of puckered structure.

Fig. 2-2 shows nine combinations of group-IV atoms (Ge, Sn, Pb) and group-VI atoms (S, Se, Te). Among them, only the combination of (Ge, Sn) and (S, Se) can be a layered materials, which are called as group-IV monochalcogenides (MXs). The other combinations of GeTe, SnTe, PbS, PbSe, and PbTe has a NaCl structure as shown in Fig. 2-2. The puckered structure of MXs are originated from a distortion from NaCl structure [88, 89]. This phase transition will appear in Section 4.1 to explain the ferroelectric switching in SnS. Distorting from NaCl to puckered structure, lone pair electrons are created in Sn atoms (Fig. 2-3), as a result of broken covalent bondings in NaCl structure. The lone pair electrons are responsible for not only the structural distortion from NaCl structure, but also a strong interlayer forces and oxidizable features, as discussed in the following sections.

BP is regarded as a very unstable materials due to an oxygen favorable features of lone pair electrons [90, 91]. There are common characteristics between BP and SnS, as being the puckered structure and lone pair electron materials, however, SnS is expected to be more stable than BP because SnS has lone pair electrons only in Sn atoms but all P atoms have lone pair electrons for BP [92] (see details in Fig. 2-6).

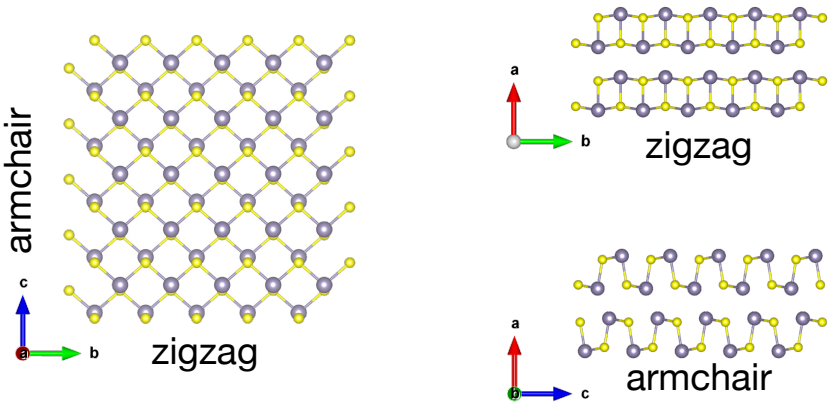

Figure 2-1: Crystal structure of orthorhombic group-IV monochalcogenides. Sn and S atoms are shown in gray and yellow, respectively.

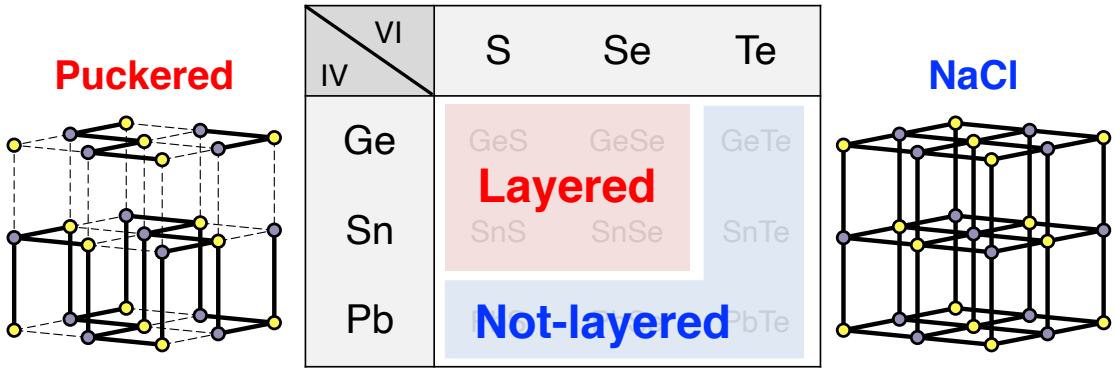

Figure 2-2: Combinations of group-IV metals and chalcogenides.

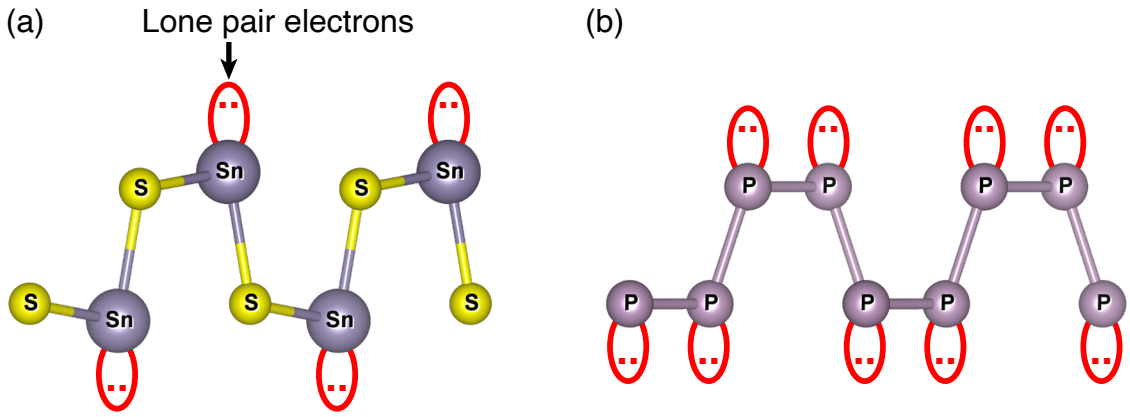

Figure 2-3: Schematic illustration of the lone pair electrons in Sn atoms: (a) SnS and (b) BP.

2.1.2 Strong Interlayer Force

For graphene and MoS_2, it is not difficult to isolate a single layer from bulk materials due to a weak van der Waals (vdW) interlayer force [24]. In the case of SnS and other MXs, however, the monolayer isolation is quite difficult [87]. As shown in Fig. 2-4, the thinnest μm-size SnS is 5.5 nm *via* growth [86], and 64 nm *via* mechanical exfoliation [59], thus the properties of few-to-monolayer SnS has been unveiled. To visualize the interlayer forces in MX and TMDs, Song *et al*. investigated density functional theory (DFT) calculations [87]. In Fig. 2-4, electron density distributions are illustrated for MoS_2 and $SnSe_2$. Compared to MoS_2, larger distribution can be seen in the SnSe, resulting in strong ionic bonding in addition to vdW bonding. As discussed above, the strong interlayer interaction originated from the lone pair electrons has been a bottleneck for the experimental researches on 2D SnS.

2.1.3 Oxidizable Features

Fig. 2-5 shows calculated electronic-structure of SnS [94]. As illustrated, the lone pair electrons forms the top of the valence band, which dominantly contribute to the chemical reactions. Owing to this chemical favorability, SnS is easy to be oxidized, compared to other stable layered materials of graphene and MoS_2. Figure 2-6(a) shows the relationship between the activation energy barrier for O_2 molecule to chemisorb on the monolayer MXs or black phosphorus (BP) [92], and the elastic energy barrier of these materials which is related to the order-disorder transition [95]. The order-disorder transition indicates the structural stability. There is a trade-off between the structural stability and the resistance against oxidation. In MXs, GeS is the only material which is structurally stable at room temperature (RT), but is the most oxidizable material. In contrast, SnS is the most structurally unstable material in MXs, while has the largest resistance against oxidation. Figure 2-6(b) shows melting temperatures of two-dimensional materials (SnS, GeS, BP and MoS_2) and their oxides (SnO_2, GeO, P_2O_5 and MoO_3). For the Ge oxides, GeO is known to easily desorb at low temperature of 400–600°C [96, 97]. SnS, GeS and BP are more unstable than

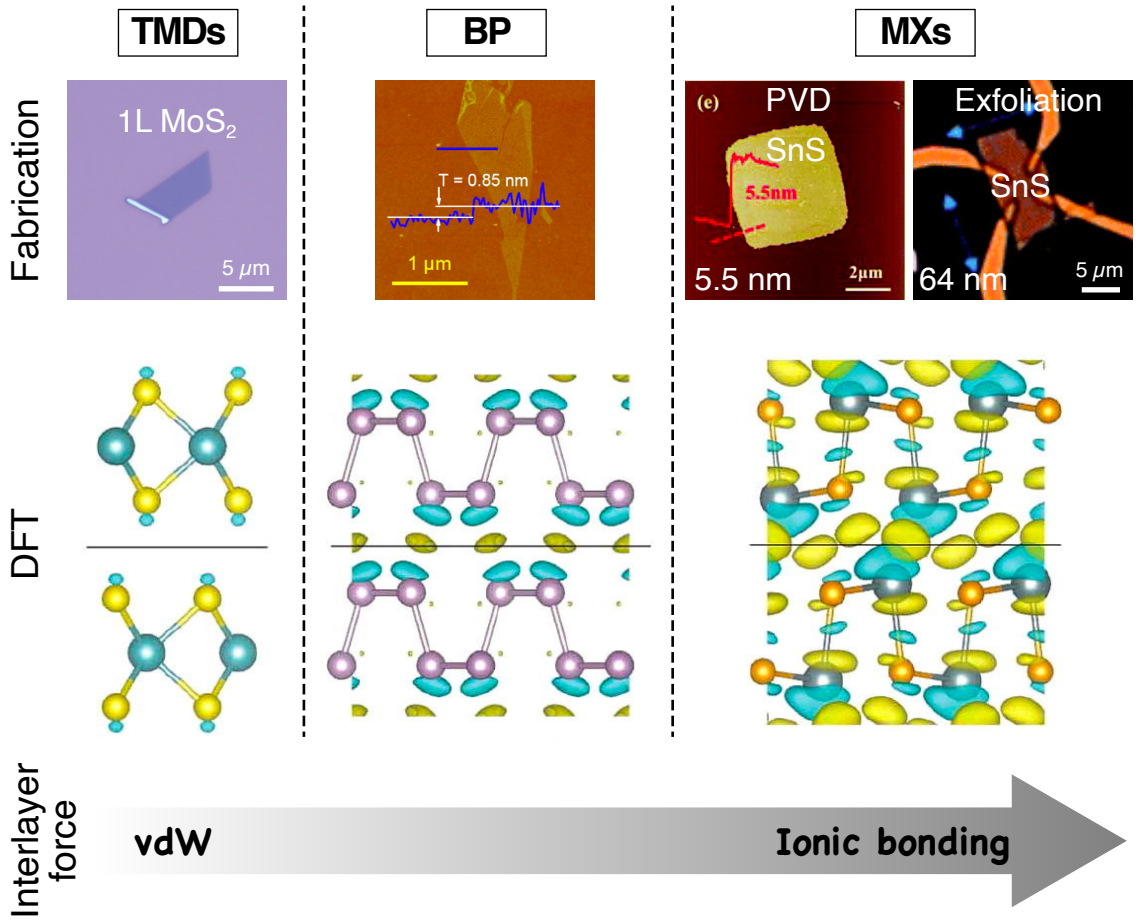

Figure 2-4: Comparison of MXs and other 2D materials: TMDs and BP. (Upper) Fabrication of monolayer MoS_2, BP [93], and SnS [86, 59]. (Middle) Electron density difference of bulk MoS_2, BP and SnSe, calculated by DFT [87]. The yellow part means positive and cyan means negative. (Bottom) Trend of interlayer force.

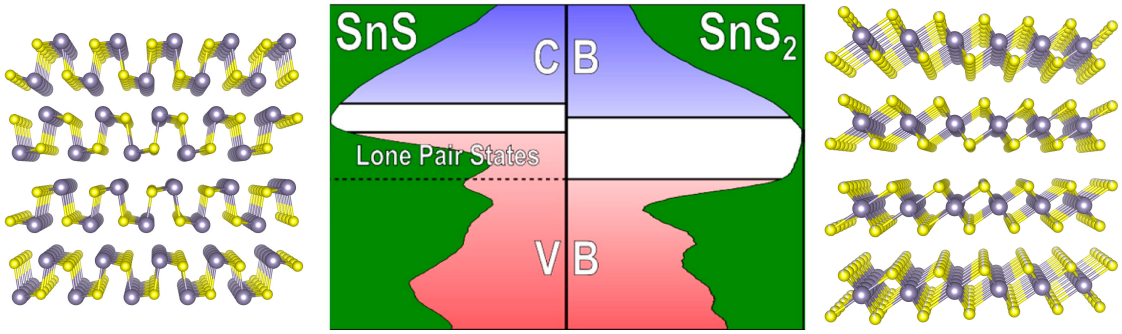

Figure 2-5: Calculated electronic-structure of SnS and SnS_2 [94].

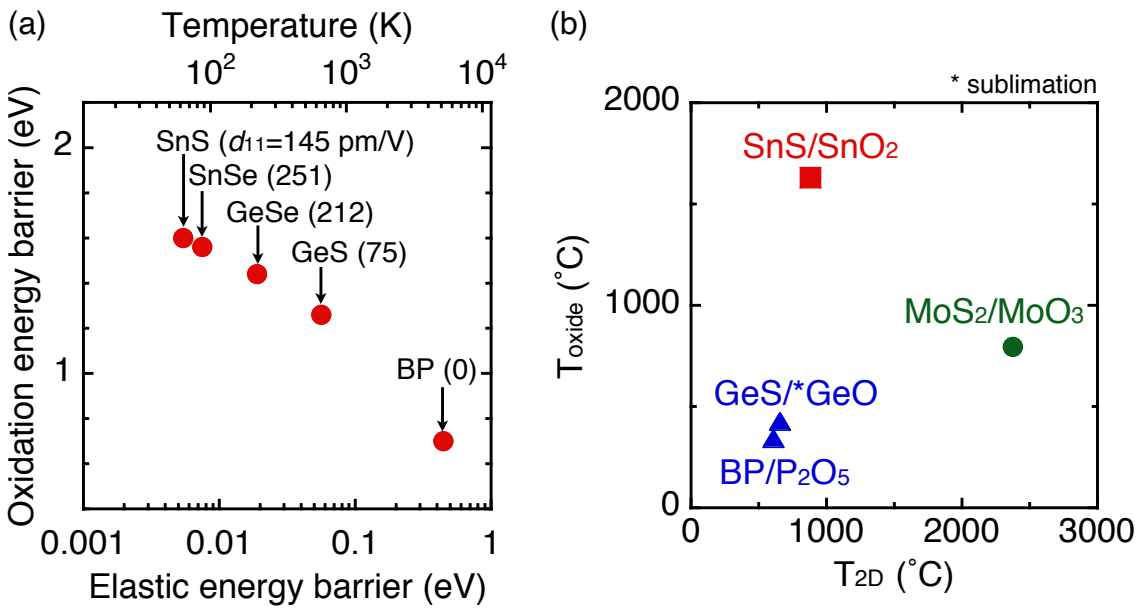

Figure 2-6: (a) The relationship between activation barrier energy for O_2 molecule to chemisorb on the material surface [92] and elastic energy barrier (E_e) which is related to the order-disorder transition [95] for monolayers of group-IV monochalcogenides and black phosphorus. The top transverse axis is obtained by dividing E_e by the Boltzmann constant. Calculated piezoelectric coefficients d_{11} (pm/V) [29] are also shown. (b) Melting temperatures of two-dimensional materials (T_{2D}) and oxide materials (T_{oxide}).

MoS_2, though SnO_2 is more stable than any other oxide materials. Thermally unstable materials tend to be easily decomposed with chemical reaction even at RT owing to the weak bonding energy between constituent elements. On the other hand, it can be expected that SnO_2 works as a stable passivation layer for SnS layers. The thermal and the chemical stabilities of SnS and SnO_x, however, have not been investigated experimentally. Fundamental understanding is required on the stability of ultrathin SnS layers toward the realization of its piezoelectric device.

2.2 Mechanical Exfoliation

Mechanical exfoliation is performed to fabricate ultrathin SnS layers, and chemical/thermal stability of SnS layers is discussed in comparison with GeS, toward piezoelectric nanogenerator application. Both SnS and GeS are difficult to be exfoliated under 10 nm using tape exfoliation due to strong interlayer ionic bonding by lone pair electrons in Sn or Ge atoms. Au-mediated exfoliation enables to fabricate larger-scale ultrathin SnS and GeS layers thinner than 10 nm owing to strong semi-covalent bonding between Au and S atoms, but GeS surface immediately degrades during Au etching in an oxidative KI/I_2 solution. Although the surface of SnS after the Au-mediated exfoliation reveals several-nm oxide layer of SnO_x, the surface morphology retains the flatness unlike the case of GeS. The SnS layers are more robust than GeS against the thermal annealing as well as the chemical treatment, suggesting that SnO_x works as a passivation layer for SnS. Self-passivated SnS monolayer can be obtained by a controlled post-oxidation.

2.2.1 Gold-mediated Exfoliation

In this study, Au-mediated mechanical exfoliation is used to fabricate ultrathin SnS layers. For MoS_2, Au-mediated exfoliation has been found to be effective to fabricate a large-scale monolayer owing to the strong semi-covalent bonds between Au and S atoms [98]. In the Au-mediated exfoliation process, a KI/I_2 oxidative solution is used to etch the Au residue, which might oxidize the SnS surface. In order to evaluate the chemical/thermal stabilities of SnS layers, effects of the chemical oxidation and laser annealing are studied on SnS layers in comparison with GeS.

SnS and GeS thin layers were transferred on 90-nm SiO_2/n^+-Si substrates by the tape exfoliation and the Au-mediated exfoliation. In the Au-mediated exfoliation, the Au residue was etched in the KI/I_2 solution for 5 min, followed by a rinse in deionized water. The thickness and surface morphology were measured by atomic force microscopy (AFM). In order to investigate the effect of the Au etchant on the surface oxidation of exfoliated thin layers, Auger electron spectroscopy (AES) and

X-ray photoelectron spectroscopy (XPS) were used.

Micro-Raman spectra of the tape-exfoliated bulk SnS and GeS were measured in air at RT. The excitation laser wavelength and power were 488 nm and 5.3 µW, respectively. Magnification of the objective lens to irradiate sample surface was ×100, and the laser diameter on the surface ($1/e^2$ intensity in the Gaussian-shaped spatial distribution) was normally 1 µm. The laser annealing (LA) was performed in air for the tape-exfoliated bulk SnS and GeS to evaluate the thermal stability. The laser was irradiated in air for 1 min with the same system of the Raman measurement. The power of LA was changed between 5.3 and 5.9×10^3 µW. After the LA, a Raman spectrum at the annealed spot was measured with the laser power of 5.3 µW.

Figure 2-7(a) shows an optical image of tape-exfoliated SnS flakes. The typical size and thickness were several µm and several tens of nm, respectively, as shown in Figure 2-7(e). By the Au-mediated exfoliation, much larger SnS flakes were obtained, compared to the tape exfoliation, as shown in Figure 2-7(b). The flake thickness exhibits a wide distribution down to 1.1 nm, which is close to the thickness of monolayer SnS (∼0.6 nm), as shown in Figure 2-7(e). This relatively larger ultrathin SnS flake can be attributed to the strong semi-covalent bonding between Au and S atoms. AFM images of thin flakes by the tape exfoliation and the Au-mediated exfoliation are shown in Figures 2-7(c) and 2-7(d), respectively. Atomically flat surfaces were obtained for thin flakes with both exfoliation methods. Typical RMS roughness of the bulk flakes by tape exfoliation and Au-mediated exfoliation were 0.07 and 0.13 nm, respectively.

2.2.2 Chemical and Thermal Stability

Au-mediated exfoliation was not applicable to GeS unlike SnS due to the surface degradation as described below. In order to investigate the effects of the Au etchant on the surface of SnS and GeS, tape-exfoliated layers were dipped in the Au etchant for 5 min. Figures 2-8(a–d) compare the morphology of bulk SnS and GeS flakes before and after the Au etchant treatment. Even after the Au etchant treatment, the SnS flake maintained a flat surface as shown in Figure 2-8(c), while the GeS surface

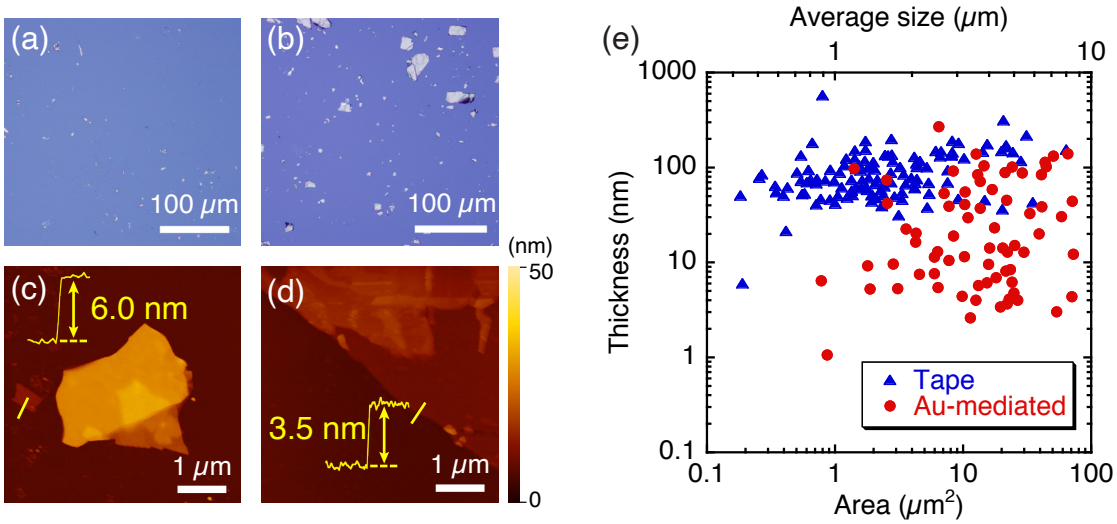

Figure 2-7: Optical images of SnS flakes obtained by (a) tape exfoliation and (b) Au-mediated exfoliation, and AFM topographic images of SnS flakes obtained by (c) tape exfoliation and (d) Au-mediated exfoliation. (e) The relationship between thickness and surface area of exfoliated SnS flakes. Average size is calculated as the square root of the surface area.

was etched ununiformly as shown in Figure 2-8(d). Typical Raman spectra of the tape-exfoliated bulk SnS and GeS are shown at the bottom of Figures 2-8(f) and 2-8(g), respectively. For SnS, two Raman peaks are observed at 162.0 and 191.2 cm−1. These values agree with the reported values [99]. Although other specific peaks of SnS at around 96 and 220 cm^{-1} [99] were not observed due to the detection limit at the excitation power of 5.3 μW, those peaks were certainly observed under the strong excitation at 500 μW. On the other hand, for GeS, four Raman peaks were observed at 111.7, 213.7, 237.3, and 269.9 cm^{-1}. These values agree with the reported values [100]. After the Au etchant treatment, there was no change in the spectrum shape of SnS, whereas for GeS, an additional broad peak was clearly observed at ∼370 cm^{-1}, as shown in Figures 2-8(f) and 2-8(g). The additional peak is very similar with the Raman spectrum of GeO_xS_y [101], indicating the existence of an oxide layer. The chemical etching of GeS in Figure 2-8(d) is probably attributed to the low oxidation energy barrier and the chemical instability of GeO_x as shown in Figure 2-5(b). Additionally, GeO_2 dissolves in the water even at RT. When the Au-mediated exfoliation was used for GeS, worm-eaten thin layers were obtained as

shown in Figure 2-8(e).

Compared with GeS, it is evident that SnS is chemically stable. To further investigate the origin of the chemical stability of SnS in detail, AES measurements were carried out for bulk and 3.5nm-thick flakes obtained by the Au-mediated exfoliation. As shown in Figure 2-9(a), the Auger signals of Sn and S were detected for the bulk SnS, while for the 3.5nm-thick flake, only the Sn signal was observed and the S signal was missing. In this measurement, the probe acquisition depth is deeper than flake thickness since the signal from SiO_2 substrate was detected. AES results suggest that the flakes thinner than 3.5 nm obtained by the Au-mediated exfoliation are totally oxidized. Figure 2-9(b) shows typical XPS spectra of bulk SnS obtained by the tape exfoliation and the Au-mediated exfoliation. For the tape-exfoliated SnS, a clear Sn $3d_{5/2}$ peak was observed with slight asymmetry. The asymmetric shape is caused by the surface oxidation due to air exposure or/and residual oxygen in the XPS chamber. By Gaussian fitting with binding energies of Sn-S (486.6 eV) and Sn-O (487.4 eV) from the reference values [102], the intensity ratio $I_{\mathrm{SnO}}/I_{\mathrm{SnS}}$ for the raw data was determined to be 0.1. For the Au-mediated exfoliation, a strong additional peak was observed at 487.4 eV, which corresponds to the binding energy of Sn-O. The ratio $I_{\mathrm{SnO}}/I_{\mathrm{SnS}}$ for the raw data was determined to be 3.2, which is much larger than that of the tape-exfoliated SnS. Although the SnS surface was oxidized after the Au-mediated exfoliation, the Sn $3d_{5/2}$ peak from Sn-S was still observed as well as the peaks of S $2p_{3/2}$ ($\sim$162 eV) and S $2p_{1/2}$ ($\sim$163 eV), indicating that the oxidized layer was limited within the escape depth of photoelectrons; several nm in thickness. These results suggest that the surface oxidation of SnS is self-limited unlike the case of GeS.

Figure 2-10(a) shows typical Raman spectra of SnS after the LA at different laser powers between 5.3 and 5.9×10^3 µW. With increasing the LA power, the peak intensity and the full-width at half maximum (FWHM) were constant up to 1.2×10^3 µW. However, the peak intensity decreased over 1.7×10^3 µW as shown in Figure 2-10(c), with increased FWHM. After the LA at 5.9×10^3 µW, the peak intensity decreased to $\sim$20% of 5.3 µW and the Raman peak from the Si substrate was observed

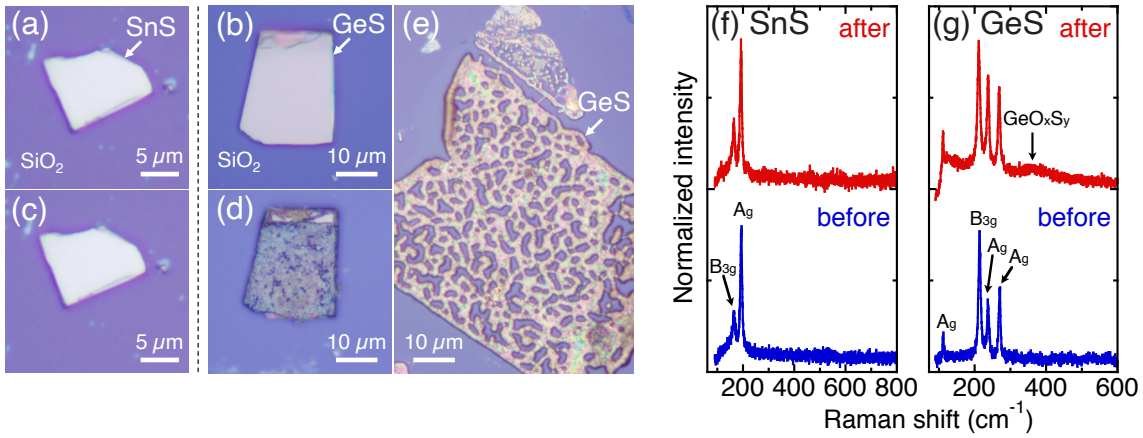

Figure 2-8: (a, b) Optical images of tape-exfoliated bulk flakes of SnS and GeS. (c, d) Optical images of SnS and GeS treated in the Au etchant for 5 min. (e) Optical image of GeS after Au-mediated exfoliation. (f, g) Typical Raman spectra of tape-exfoliated bulk SnS and GeS before/after the Au etchant treatment for 5 min.

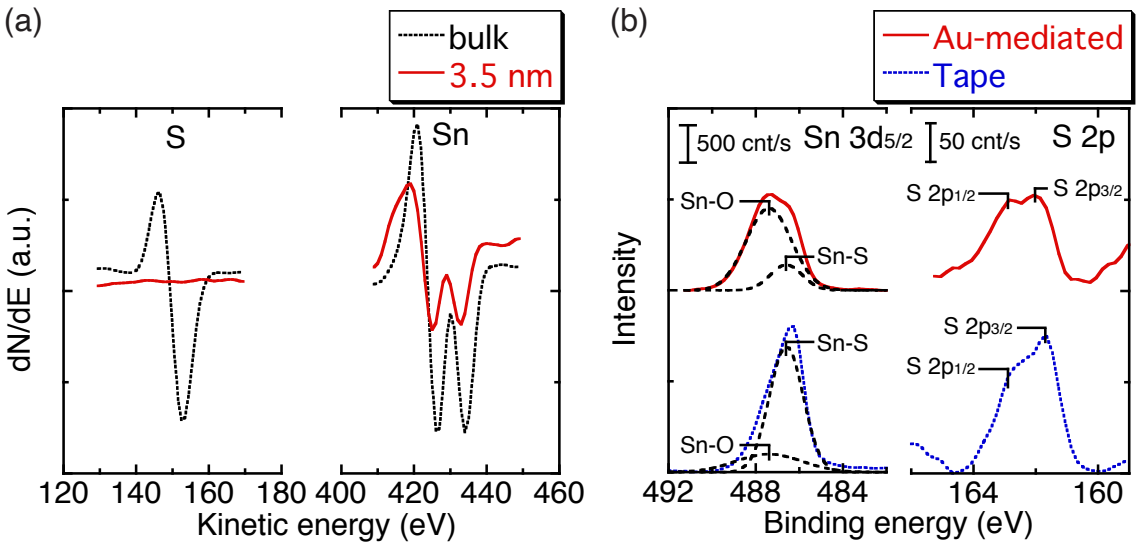

Figure 2-9: (a) Typical differential AES spectra for bulk and 3.5nm-thick SnS after the Au-mediated exfoliation. (b) Typical XPS spectra of Sn 3d and S 2p for bulk SnS after the tape and Au-mediated exfoliation. Dashed lines represent Gaussian fits to the data, with the binding energies of SnS and SnO [102].

at ∼518 cm^{-1}. These results indicate that the upper layers of bulk SnS evaporated due to the excess heating with the stronger LA power than 1.7×10^3 µW.

On the other hand, the Raman spectrum of GeS was found to be easily degraded after the LA; the Raman intensity decreased over 57.7 µW, which is much lower than the critical LA power for SnS; 1.7×10^3 µW. After the LA at 5.9×10^3 µW, Raman peaks from GeS disappeared as shown in Figure 5(b). In addition to the narrow Si peak at ∼518 cm^{-1}, a sharp peak at ∼299 cm^{-1} appeared, which is possibly from the Ge-Ge bond. Moreover, a peak of GeO_xS_y was observed at ∼376 cm^{-1} in the same way as the GeS oxidized in the Au etchant (Figure 2-8(g)).

Based on these results, SnS is revealed to be chemically and thermally stable. The key feature is the formation of the SnO_x passivation layer on the SnS flake, which is chemically and thermally stable because of its high melting temperature of 1630°C (SnO_2) or 1080°C (SnO) [103]. This is completely opposite situation from GeS, where GeO is quite unstable. So far, in the case of BP and WSe_2, layer-by-layer oxidations have been realized by oxygen plasma [104] and ozone treatment [105], respectively, since the oxidation rate is limited by the oxygen diffusion in the oxide layer when the oxide thickness is moderately increased. Therefore, monolayer SnS self-passivated with the SnO_x layer will be realized by precisely controlling the surface oxidation.

Au-mediated exfoliation of SnS and GeS, and chemical/thermal stability of exfoliated flakes were investigated. The Au-mediated exfoliation enabled relatively large SnS layers thinner than 10 nm, but is not applicable for GeS due to unstable surface oxides during the Au etching process. Although the SnS surface is also oxidized, SnO_x is much stable and the oxidation is self-limited. As well as the chemical stability, SnS also shows thermal stability owing to the robust SnO_x layer that works as the passivation layer. The present findings indicate that SnO_x/SnS hetero-structure is a promising candidate for the nanogenerator.

2.2.3 Surface oxidation of SnS layers

Fig. 2-11a shows an optical image of SnS flakes fabricated *via* Au-exfoliation. From the AFM image (Fig. 2-11b), the flake thicknesses were determined to be 13.8, 10.5

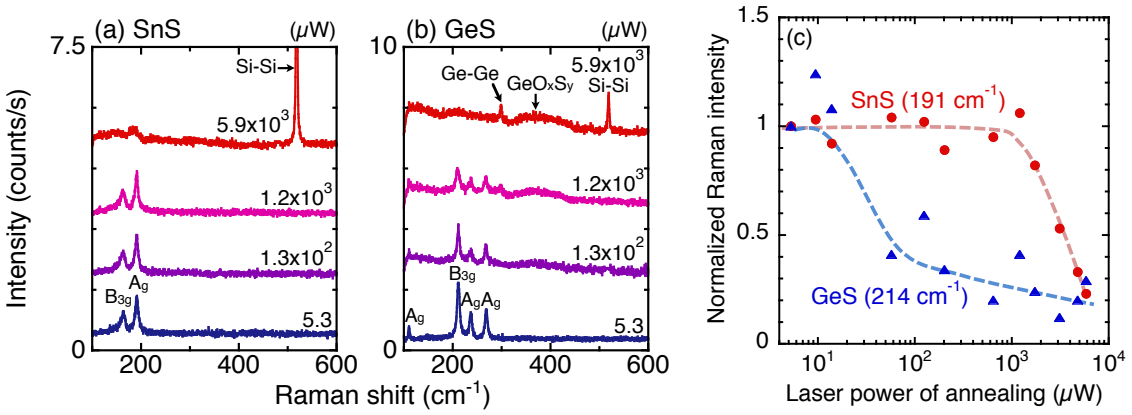

Figure 2-10: (a, b) Typical Raman spectra of laser-annealed bulk SnS and GeS flakes. The laser annealing was performed in air under different laser powers between 5.3 and 5.9–10^3 μW. The laser power for Raman measurement was fixed at 5.3 μW. (c) Normalized Raman intensity versus laser power of annealing for bulk SnS and GeS. The dashed lines are guides to the eye.

and 4.3 nm at the points A, B, and C, respectively. With decreasing the flake thickness, the Raman spectrum from SnS suddenly disappeared below a critical thickness of 4.3 nm owing to the surface modification, as shown in Fig. 2-12.

To investigate the surface modification of Au-exfoliated SnS in detail, Fig. 2-11c shows the cross-sectional HAADF-STEM image along the dashed line in Fig. 2-11b. For the point A (13.8 nm), combined with the EDS analysis in Fig. 2-11d, the formation of amorphous SnO_x (a-SnO_x) is revealed at the surface of the intrinsic SnS single crystal during the Au-exfoliation process. Moreover, the a-SnO_x/SnS heterostructure was also observed for the point B (10.5 nm), whereas only the a-SnO_x layer was observed for the point C (4.3 nm), lacking apparent crystallinity, as shown in Fig. 2-13. These behaviour is consistent with the Raman data. This chemical instability of SnS originates from the lone pair electrons in Sn atoms, which favor the oxygen bonding [92, 106]. The sharp a-SnO_x/SnS interface suggests that the oxidation is a self-limiting layer-by-layer process [104, 105]. This is different from GeS, whose oxide layers (GeO and GeO_2) are chemically/thermally unstable and successive oxidation degrades GeS rapidly and non-uniformly [71]. Once the SnS surface is oxidized, excess oxidation is limited by the oxygen diffusion in the SnO_x layer, which is supported by

the similar thicknesses of SnO_x layers at the points A and B. These results indicate that SnO_x can function as a self-passivation layer for the SnS layer underneath.

In the Raman spectra of the bulk flake (∼432 nm thick) at RT, as shown in Fig. 2-12, specific peaks of SnS were observed at 161.7, 189.6 and 218.3 cm^{-1}, which are consistent with the reported values [86, 99, 107]. With a reduction in the thickness from bulk to A to B, the sharp spectrum became broader with a redshift. The broadening and redshift are considered to be due to a phonon confinement owing to the thinning effect [52, 108]. When the flake thickness further decreased to 4.3 nm (point C), Raman spectrum suddenly disappeared at RT and was not recovered even at 3 K. In contrast, a clear spectrum was observed for the bulk SnS with a smaller full-width at half-maximum and larger intensity at 3 K, compared with that at RT. These results indicate that the disappearance of Raman peaks below a critical thickness of 4.3 nm originates from the surface modification rather than the detection limit of Raman measurement.

The a-SnO_x/SnS hetero-structure was also observed for the point B (10.5 nm), as well as point A (13.8 nm), whereas only the a-SnO_x layer was observed for the point C (4.3 nm), lacking apparent crystallinity. Notably, the HAADF-STEM image of the point B is more ambiguous than that of the point A, because it was difficult to obtain a clear electron diffraction image with the decrease in the flake thickness owing to the in-plane fluctuation, which originates from the surface roughness of the SiO_2/Si substrate. As shown in Fig. 2-13c, the atomic configurations of SnS layers correspond to those of 2D SnS grown *via* physical vapor deposition and bulk SnS along the armchair c axis direction [86, 103, 107, 59, 109, 110, 111], where the largest carrier mobility can be obtained [53, 112].11,12 The lattice constants were determined to be a = 10.7 Å and c = 4.2 Å, consistent with the reported values[103, 110, 111]. The numbers of SnS layers at the points A and B were determined to be 17 and 11 (17L and 11L), respectively.

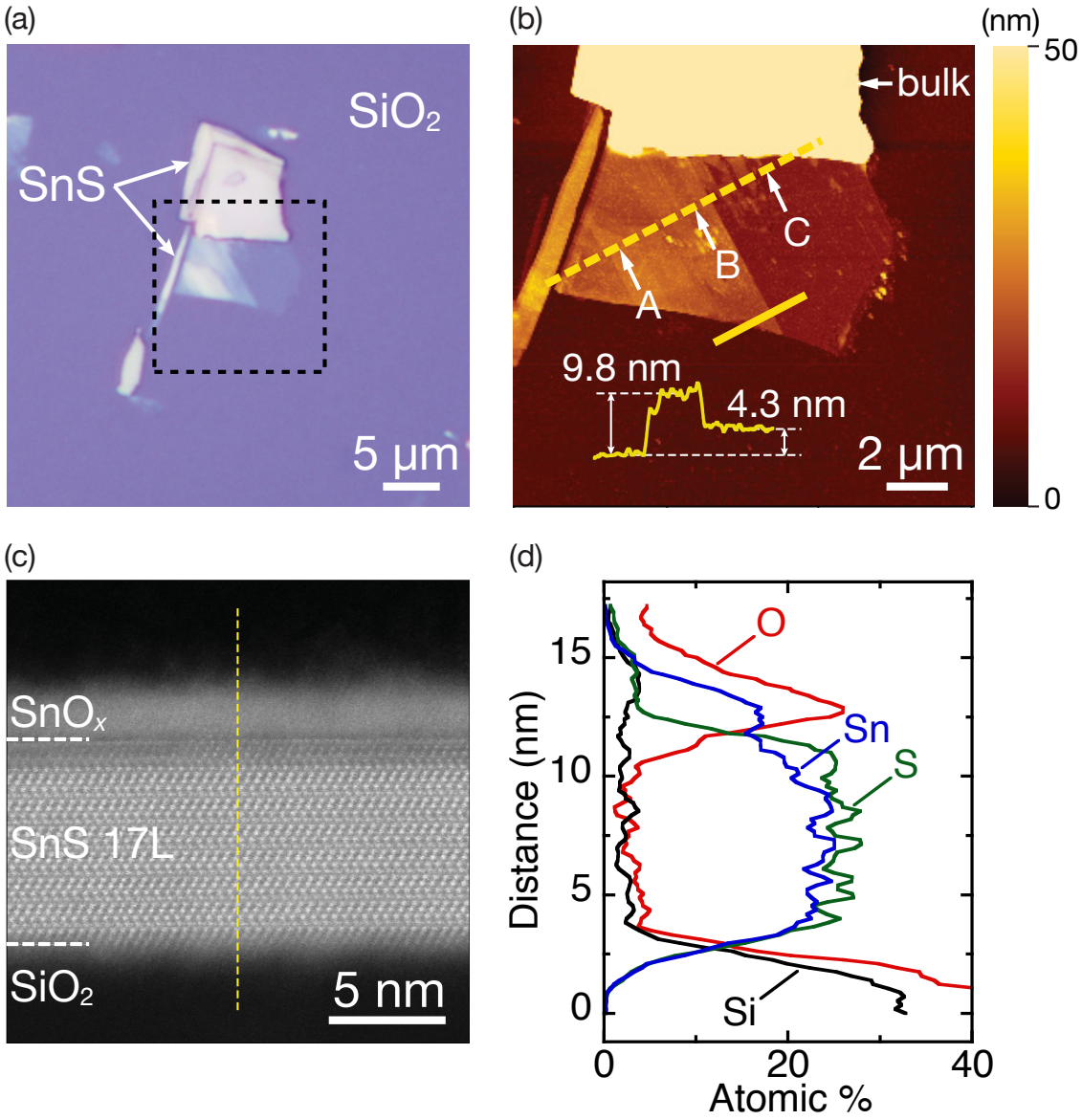

Figure 2-11: (a) Optical image of SnS flakes *via* Au-exfoliation. (b) AFM topographic image of selected area in Fig. 2-11a. The height profile along the solid line is shown in the inset. (c) Cross-sectional HAADF-STEM images of SnS flakes at the points A in Fig. 2-11b. (d) EDS depth profiles of SnS flake along the dashed lines in Fig. 2-11c.

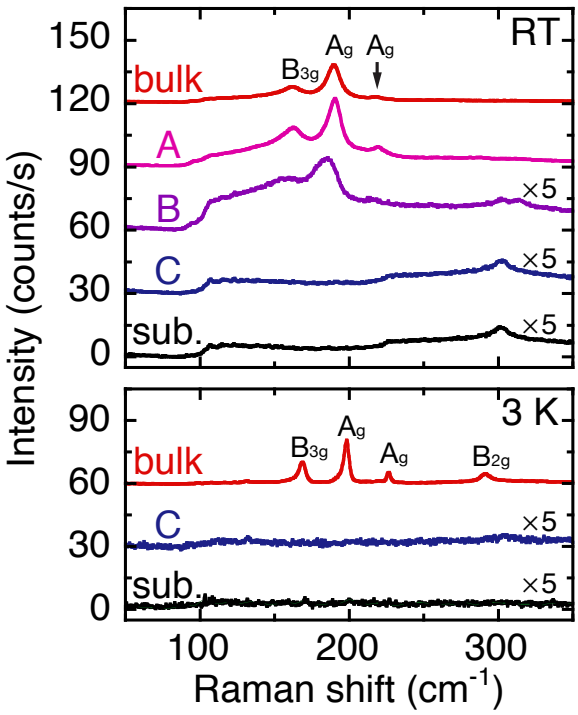

Figure 2-12: Raman spectra measured at the points A, B, and C in Fig. 2-11b. The Raman spectrum of the SiO_2/Si substrate is also shown.

2.2.4 Electrical Characteristics

To investigate the electrical characteristics of the SnO_x/SnS hetero-structure obtained *via* Au-exfoliation, two-probe FET devices were fabricated for various numbers of SnS layers. Note that the transport characteristics of SnO_x/SnS hetero-structure were measured without removing the SnO_x layer, as shown in Fig. 2-14. The number of SnS layers (N_L) was estimated as $N_L = (d_{total} - d_{oxide})/d_{1L}$, where dtotal is the flake thickness, doxide is the thickness of SnO_x, and d_{1L} is the monolayer thickness of SnS. The values of doxide and d_{1L} were determined to be 4.3 nm and 5.4 Å, respectively, from HAADF-STEM images. Fig. 2-15a shows the I_d–V_d curves of 9 layers (9L) SnS at different temperatures. At RT, the I_d–V_d curve exhibited a linear characteristic, but it became nonlinear at temperatures below 150 K, which indicates that the contact barrier height is approximately as small as the thermal energy at 150 K, i.e., ∼13 meV. Fig. 2-15b shows the electrical transport characteristics as a function of the back-gate voltage at V_d = 1 V, for different SnS thicknesses: 9L, 12L,

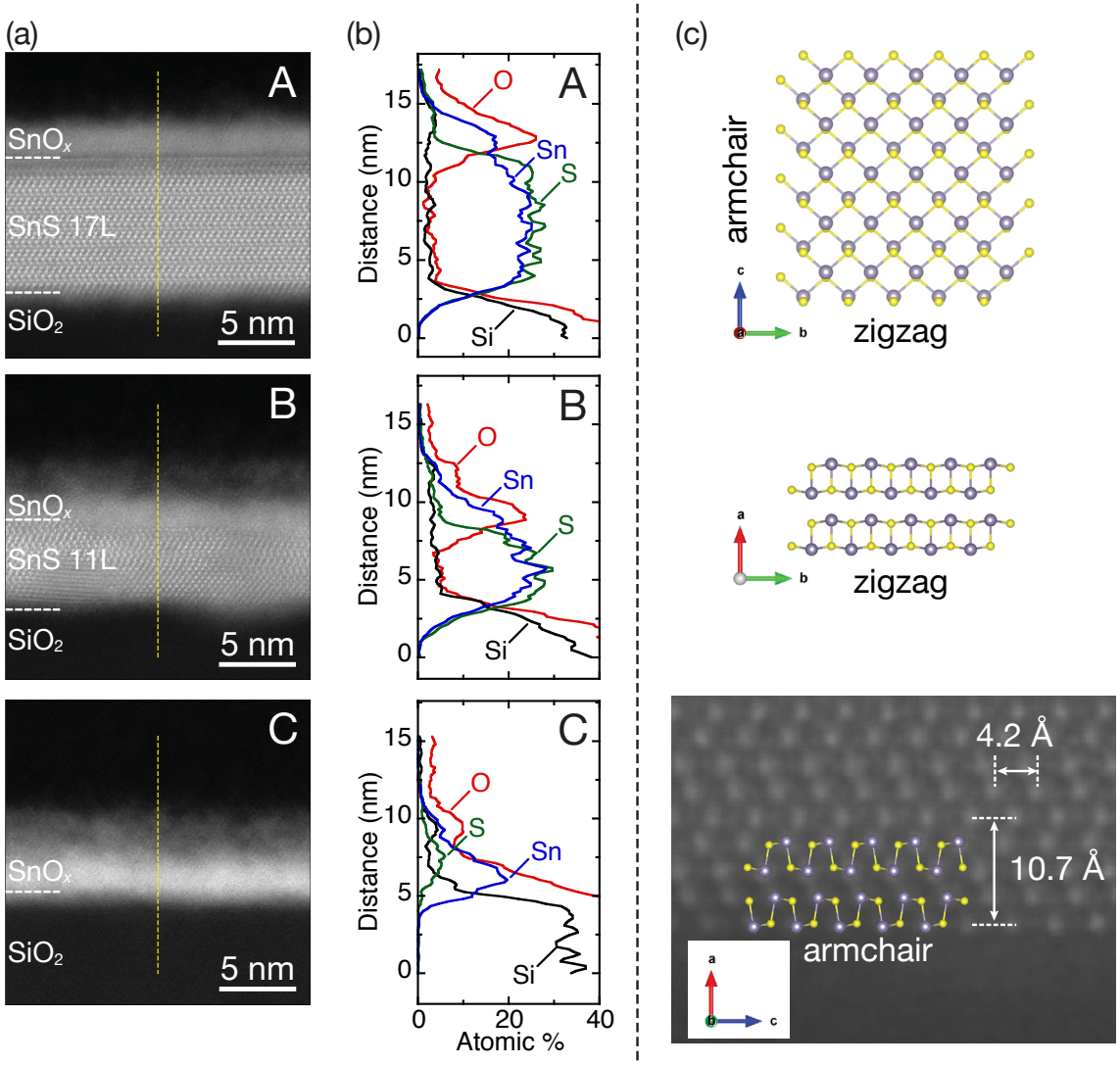

Figure 2-13: (a) Cross-sectional HAADF-STEM images of SnS flakes at the points A, B, and C in Fig. 2-11b. (b) EDS depth profiles of SnS flakes along the dashed lines in Fig. 2-13a. (c) Crystal structure of SnS from a, b, and c axis. Enlarged cross-sectional HAADF-STEM image at the point A is also shown in comparison with a crystal structure model along the armchair direction. Sn and S atoms are shown in grey and yellow, respectively.

and 16L. Although all FET devices showed p-type characteristics, the device was not turned off with the back-gate modulation even for 9L. So far, owing to the difficulties associated with substitutional doping of 2D materials, the electron transport in most 2D-FETs with a global back gate and metallic contacts is claimed to be governed by the gate control of the Schottky barrier (SB) [113, 114]. However, a recent study has suggested that accumulation-depletion mode at the channel is dominant especially for highly doped 2D materials as the metal/2D channel contact does not control the transport properties owing to narrow SB width [115]. Therefore, this poor gate-tuning characteristic is due to heavy doping in SnS, resulting in a limited depletion width [109, 59, 116, 115]. To estimate the acceptor density of SnS, a simple calculation was performed using the depletion width W_{D} as follows:

$$W_{\mathrm{D}} = \sqrt{\frac{4\varepsilon k_{\mathrm{B}} T ln\left(\frac{N_{\mathrm{A}}}{p_{\mathrm{i}}}\right)}{e^2 N_{\mathrm{A}}}} \tag{2.1}$$

where k_{B} is the Boltzmann constant, e is the elementary electron charge, N_{A} is the acceptor density of SnS, and p_{i} is the intrinsic carrier concentration. Furthermore, ε is the dielectric constant of SnS, roughly estimated using the relative dielectric constant $\varepsilon_{\mathrm{r}} \sim 10$ of bulk SnS [54, 117]. The pi of thin SnS is estimated using the equation $p_{\mathrm{i}} = 10^{18}\mathrm{exp}(-E_g/2k_{\mathrm{B}}T)$ [118] with the bandgap $E_g = 1.1$ eV [52, 53, 54, 55, 56], where $T = 300$ K yields a value of $p_{\mathrm{i}} = 5.8 \times 10^8$ cm^{-3}. In Fig. 2-16c, the relationship between W_{D} and N_{A} of SnS at 100 K is shown. In the I_{d}–V_{g} curves at 100 K, the off-state was observed for 9L and 12L, but not for 16L (see Fig. 2-15c, 2-16a and 2-16b). Therefore, by equating W_{D} to these SnS thicknesses, N_{A} is roughly estimated to be of the order of 10^{19} cm^{-3}, which is consistent with the previous estimation [119, 109]. but larger than other experimental/theoretical values (10^{16}–10^{18} cm^{-3}). This heavy doping level originates from Sn vacancies ($\mathrm{V_{Sn}}$) [120, 121, 67]. The field-effect mobility μ was estimated using the following equation:

$$\mu = \frac{L}{W}\frac{g_{\mathrm{m}}}{C_{\mathrm{ox}}V_{\mathrm{d}}}, \qquad \text{where} \quad g_{\mathrm{m}} = \frac{dI_{\mathrm{d}}}{dV_{\mathrm{g}}} \tag{2.2}$$

where L and W are the length and width of the channel, respectively, and C_{ox} is the gate capacitance. The typical μ values for 9L, 12L, and 16L SnS at RT were determined to be 0.47, 0.18, and 0.05 $\mathrm{cm^2V^{-1}s^{-1}}$, respectively, which are comparable to the reported μ values for ∼10-nm-thick SnS ranging from 0.2 to 1.1 $\mathrm{cm^2V^{-1}s^{-1}}$ [66]. For the completely oxidized 3.5-nm-thick flake, the current flow was not observed, indicating that the I_{d}–V_{g} observed for the a-SnO_x/SnS hetero-structure results from the current flow through SnS channel, but not through the a-SnO_x layer. Moreover, the non-conductive SnO_x layer existing between SnS and metal electrode could work as a depinning layer for the Fermi level pinning observed typically for 2D/metal contact [122, 123], resulting in the ohmic characteristics of I_{d}–V_{d}.

As N_{A} was determined, let us now obtain the activation energy of the acceptor level for V_{Sn}. Fig. 2-15d shows the Arrhenius plot of conductivity for 9L SnS at V_g = -30, -15, 0, 15, 30 V. The activation energies (E_{a}) were determined to be in the range 43–239 meV. The off-state appeared only when the temperature was decreased, as shown in Fig. 2-15c, which is in contrast to that of typical 2D channels, such as MoS_2. This is because the carrier concentration is significantly reduced by the freeze-out of holes from acceptors, but not because the nearest-neighbor hopping is suppressed. Therefore, the estimated E_{a} indicates a shallow acceptor level, which is consistent with that obtained from experimental/theoretical works (E_{a} = 42–300 meV) [109, 120, 67, 124].

When the low temperature range 150–80 K is applied for 9L SnS, Fig. 2-15e shows the so-called metal–insulator transition (MIT) at ∼10 nS (also see Fig. 2-17). As recent studies have suggested that the MIT in monolayer MoS_2 FET is extrinsic [125, 126], the origin of MIT is not discussed here. Experimentally, the extrinsic MIT can be observed intuitively by the combination of (i) the increase of the mobility and (ii) positive (for n-type) or negative (for p-type) shift of the threshold voltage with the decrease in the temperature. For MoS_2, the extrinsic MIT is only observed for the samples with high mobility, i.e., high crystallinity [127, 128]. The observation of extrinsic MIT in the present a-SnO_x/SnS FET suggests that the SnS layer underneath possesses high crystallinity, as supported by the TEM image in Fig. 2-11c. In the

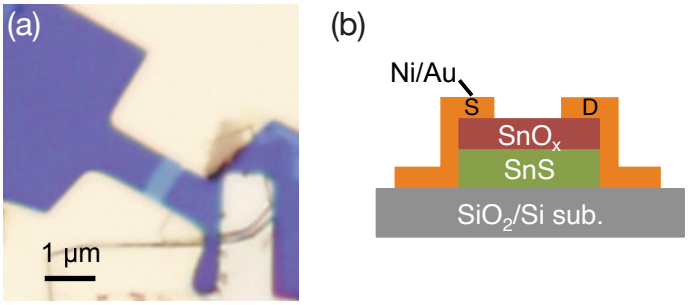

Figure 2-14: (a) Typical optical image and (b) cross-sectional illustration of back-gated SnO_x/SnS FET.

temperature range 300–150 K, the electrical transport characteristic can be explained by the temperature dependence of carrier concentration, whereas, in the range 150–80 K, μ could be limited by the phonon scattering; $\mu \propto T^{-\gamma}$ where γ is approximately 2.1 for 9L SnS (see Fig. 2-15f).

As discussed above, after the Au-exfoliation, a ∼4-nm-thick self-passivation SnO_x layer is formed on the surface of SnS, and the SnS layer underneath has high crystallinity down to 9L at least. The monolayer SnS should have been obtained *via* surface oxidation; however, it was not obtained after Au-exfoliation. All flakes thinner than 5.3 nm (∼2L SnS with SnO_x) were inactive optically and electrically. One of the possible reasons for this is that the monolayer SnS is more unstable than the thicker one and degenerates in the Au etchant even though the a-SnO_x layer protects the SnS layer to some extent. A more moderate oxidation method than the use of the KI/I_2 solution is required to realize SnO_x/monolayer-SnS.

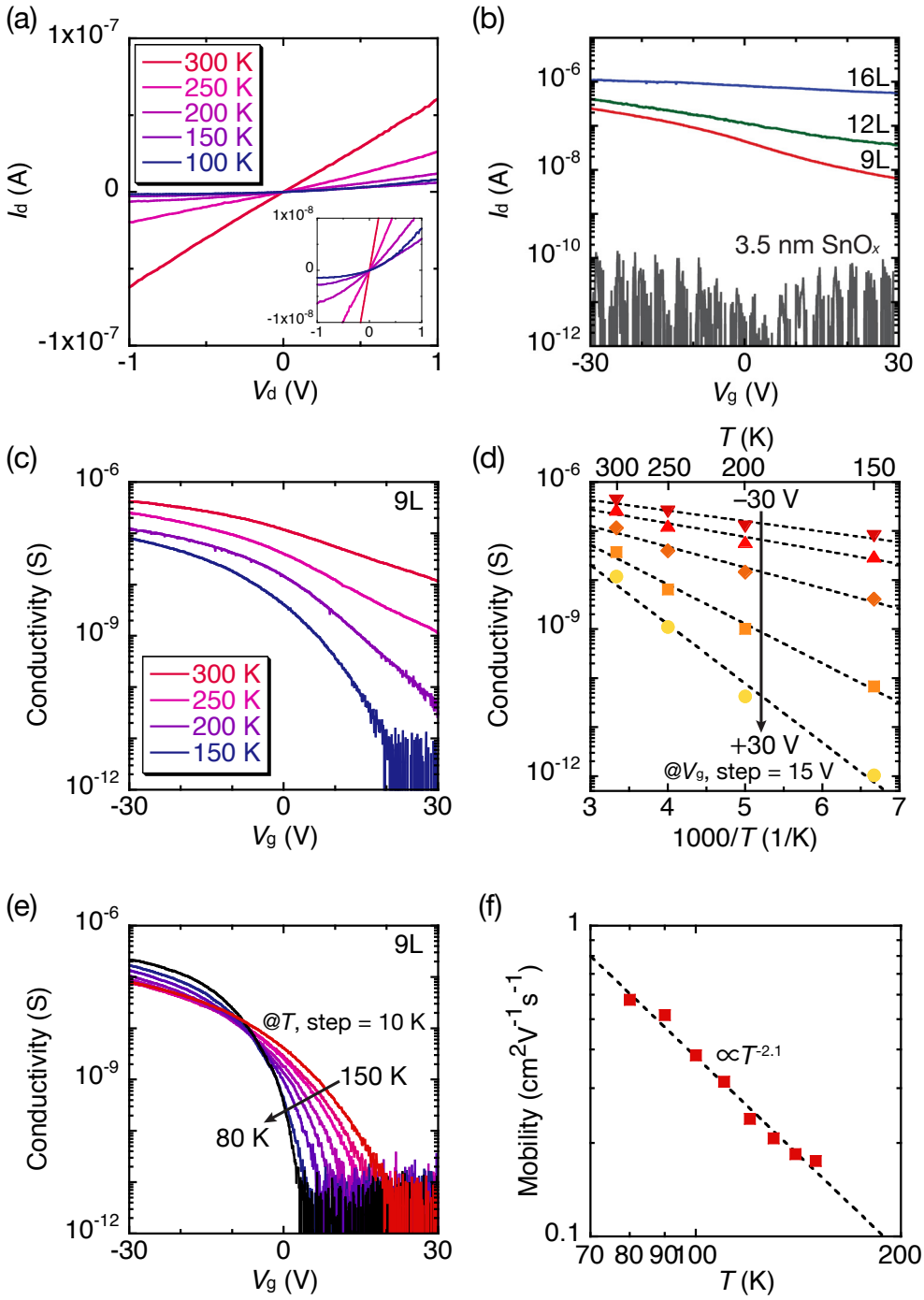

Figure 2-15: (a) I_d–V_d plots of 9L SnS at $V_g = 0$ V in the temperature range 300–100 K. Inset: Enlarged I_d–V_d plots. (b) I_d–V_g plots of SnS flakes with the different number of layers at RT and $V_d = 1$ V. The non-conductive characteristic of 3.5-nm-thick SnO_x is also shown. (c,e) Two-probe conductivities as a function of V_g in the temperature range (c) 300–150 K and (e) 150–80 K. (d) Arrhenius plot of conductivity for 9L SnS from Fig. 2-15c at $V_g = -30$, -15, 0, 15, 30 V. (f) Field-effect mobilities of 9L SnS in the temperature range 150–80 K.

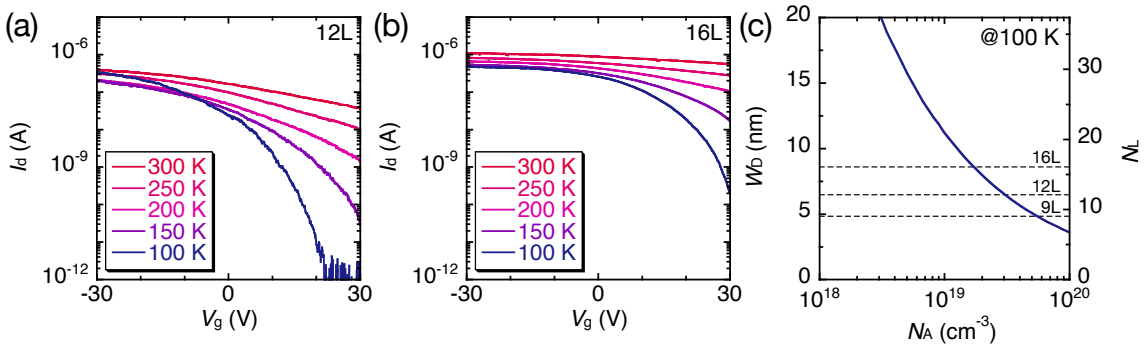

Figure 2-16: I_d–V_g plots of (a) 12L and (b) 16L SnS FETs in the temperature range 300–100 K. (c) Relationship between depletion width W_D and acceptor density N_A at 100 K. N_L is the number of SnS layers, which corresponds to W_D. The highlighted region shows the estimated N_A of SnS.

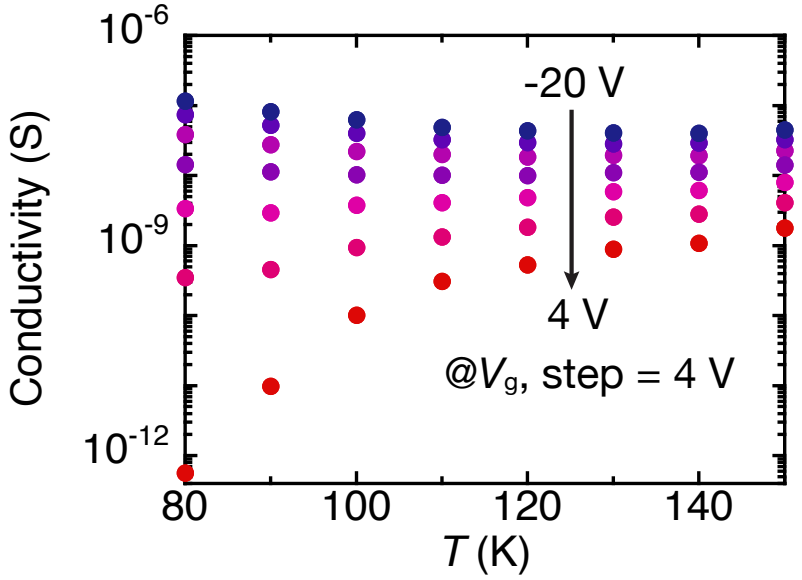

Figure 2-17: Two-probe conductivity as a function of temperature for the 9L SnS fabricated *via* Au-exfoliation.

2.3 Post-thinning *via* Oxygen Annealing

Remarkable optical and electrical features are expected in two-dimensional group-IV monochalcogenides (MXs; M=Sn/Ge and X=S/Se) with a uniquely distorted layered structure. The lone pair electrons in the group-IV atoms are the origin of this structural distortion, while they also cause a strong interlayer force and high chemical reactivity. The fabrication of chemically stable few-to-monolayer MX has been a significant challenge. We have observed that, once the SnS surface is oxidized, the SnO_x top layer works as a passivation for the SnS layer underneath. In this work, the SnO_x/SnS hetero-structure is studied structurally, optically, and electrically. When a tape-exfoliated bulk SnS is oxygen-annealed under a reduced pressure at 10 Pa, surface oxidation and SnS sublimation proceed simultaneously, resulting in a monolayer-thick SnS layer with the SnO_x passivation layer. The field-effect transistor of nine-layer SnS prepared *via* mechanical exfoliation exhibits a *p*-type characteristic because of intrinsic Sn vacancies, whereas ambipolar behavior is observed for the monolayer-thick SnS obtained *via* oxygen annealing probably owing to the additional *n*-type doping by S vacancies. This work on monolayer-thick SnS fabrication can be applied to other unstable lone pair analogues and can facilitate future research on MXs.

Two-dimensional (2D) orthorhombic group-IV monochalcogenides (MXs; M=Sn/Ge and X=S/Se), which are compound analogues of black phosphorus (BP), possess significant features such as strong optical/electrical anisotropies [86, 129, 130, 59, 109, 107, 131, 132], noncentrosymmetry in the odd-layers [29], and native *p*-type conductivity with a high theoretical carrier mobility over 10,000 $cm^2V^{-1}s^{-1}$ [67, 53, 112]. These properties are theoretically expected to appear in monolayer MXs distinctively. The orthorhombic MXs belong to the space group $Pnma$ in bulk and even-number layers, and $Pmn2_1$ in odd-number layers, which are distorted from the NaCl structure. Stereochemically active lone pair electrons in Sn 5s or Ge 4s play an important role in this structural distortion, resulting in the anisotropic and layered structure [89, 72, 133]. In the past decade, 2D MXs and related materials have been investi-

gated for various applications, such as field-effect transistor (FET) [59, 66, 61], photonic [67, 68, 69, 70], piezoelectric [29, 71], thermoelectric [131, 132, 112, 134], and ferroelectric devices [72, 135, 73]. So far, however, there have only been a few reports on few-to-monolayer MXs [136, 52, 55, 137, 138] because the isolation of monolayer is prevented by a strong interlayer force owing to the lone pair electrons, which generate a large electron distribution and electronic coupling between adjacent layers [87, 139]. Song *et al.* calculated the interlayer binding energy of SnSe as 146 meV/atom, which is much larger than those of graphite (24 meV/atom) and MoS_2 (38 meV/atom) [87]. As a representative MX, SnS with fewer than 10 layers has not been obtained either *via* tape exfoliation [59, 71] or crystal growth [86, 107, 132, 137, 109, 140]. The fabrication of few-layer SnS down to monolayer has been achieved only *via* liquid phase exfoliation, and its lateral size is usually too small for it to be applied to devices owing to the harsh exfoliation process with prolonged ultrasonication [52, 136, 55]. A reliable fabrication process of large-scale few-to-monolayer MXs will uncover their undemonstrated diverse properties.

For other 2D materials (graphite, MoS_2, WSe_2, BP, etc.), monolayer has been successfully obtained by using post-thinning techniques such as plasma treatment [104, 141, 142, 143, 144], ozone treatment [105], thermal annealing [145, 146], and laser annealing [147]. For MXs, in contrast, only a few cases of successful post-thinning of micrometer-sized monolayer SnSe and GeSe have been reported by using thermal annealing [137] and laser annealing [138], respectively.

Alternatively, Desai *et al.* reported an Au-mediated exfoliation method (Au-exfoliation) to fabricate monolayer MoS_2, whose lateral size is much larger than that of the tape-exfoliated one owing to the strong semi-covalent bonds between Au and S atoms [98]. Recently, we demonstrated that Au-exfoliation is effective for the thinning of bulk SnS with micrometer-size, but Au-exfoliated flakes thinner than $\sim$4 nm were completely oxidized [71]. In the Au-exfoliation, the Au residues are etched in a KI/I_2 oxidative solution, which is inactive for MoS_2 but easily causes the surface oxidation of SnS. In the electronic band structure of SnS, the lone pair electrons constitute the top of the valence band, resulting in favorable bonding with oxygen [92, 94]. In spite of the oxi-

dizable feature of SnS, the bulk SnS flake obtained after the Au-exfoliation shows an atomically flat surface and chemical/thermal stabilities, which are different from the instability of GeS, GeSe, and BP [92, 104, 71, 138, 106, 90]. This difference originates from the following advantages of SnX and its oxide. From the previous calculation studies by Guo *et al.*, the oxidation energy barriers of SnS and SnSe were 1.60 and 1.56 eV, respectively, which are larger than those of GeS (1.26 eV), GeSe (1.44 eV), and BP (0.70 eV) [92]. The lowest energy barrier of BP can be explained by the existence of the lone pair electrons in all the P atoms of BP, but only in the constituent atoms of M in MXs. In addition to the relatively large oxidation resistance of SnX, the well-known transparent conductive SnO_x ($1<x<2$) [148] has robust stability with high melting points, e.g., 1080°C (SnO) and 1630°C (SnO_2), much higher than those of GeO, GeO_2, and P_2O_5 [103]. Once the SnX surface is oxidized, the SnO_x layer can work as a passivation layer. Therefore, reliable monolayer SnX self-passivated with an SnO_x layer will be realized *via* the post-thinning techniques mentioned above because more precise control is possible owing to the stable surface oxidation.

In this paper, an SnO_x/SnS hetero-structure is studied structurally, optically, and electrically. The SnO_x/SnS structure exhibits a sharp interface after the Au-exfoliation and the ultra-thin SnS layer down to nine layers present underneath is characterized as a well-defined crystal. To further reduce the SnS thickness, a post-thinning method is performed for the bulk SnS using oxygen annealing. The sublimation of SnS layers occurs along with the formation of SnO_x, resulting in a successful thinning down to 0.7 nm, close to the monolayer thickness [103, 111, 110]. The electrical transport properties of SnS FETs with the thickness ranging from bulk to 0.7 nm are systematically discussed.

2.3.1 Experimental Procedure

Mechanical exfoliation of SnS layers: High-quality SnS single crystals were grown *via* the horizontal gradient freeze method [110] and chemical vapor transport method using iodine as the transport agent [149]. Although these bulk SnS crystals exhibited comparable crystallinity, SnS grown *via* the horizontal gradient freeze method was

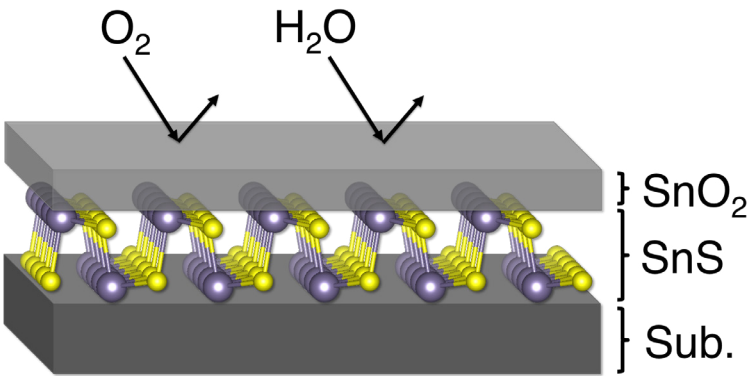

Figure 2-18: SnS layer with the monolayer thickness was realized with a stable SnO_x passivation layer *via* mechanical exfoliation, followed by moderate oxygen annealing.

mainly used because relatively large flakes were exfoliated. SnS thin flakes were fabricated from bulk SnS *via* tape exfoliation and Au-exfoliation [98, 71]. The SnS flakes were transferred onto 90-nm SiO_2/n^+-Si substrates. In the Au-exfoliation, the Au residue was etched in an oxidative KI/I_2 solution for 5 min, followed by rinsing with deionized water for 10 min.

Post-thinning method: Post-annealing of the tape-exfoliated bulk SnS (∼100 nm thick) was performed in an O_2/N_2 mixture gas (O_2 : N_2 = 1 : 4) at 10 Pa. The samples were heated in a home-made tube furnace, which was first preheated at 100°C for 10 min, and thereafter heated to target temperatures in the range 300–900°C for 10 min. The furnace was maintained at the target temperature for 5 min to 12 h. Subsequently, the furnace was naturally cooled to room temperature (RT). In this method, oxidation and sublimation are expected to be moderate and controllable with a well-crystallized SnO_x passivation layer formed at the high temperature.

Characterization: Atomic force microscopy (AFM) was used to identify the flake thickness and surface morphology. Raman spectra were measured using a 488-nm excitation laser. An optimal laser power of 0.5 mW was used to avoid degradation of SnS owing to laser heating [71]. Moreover, X-ray photoelectron spectroscopy (XPS) was used to investigate the surface modification. The sample structure, crystallinity and chemical composition were determined using high-angle annular dark-field scanning transmission electron microscopy (HAADF-STEM) and energy-dispersive X-ray

spectroscopy (EDS).

Device fabrication and electrical characterization: Back-gated FET devices were fabricated with electrode patterning using the standard electron beam lithography and Ni/Au electrode formation *via* thermal evaporation. As a contact metal, Ni was used for ohmic contacts owing to its high work function [150]. Au was used to prevent the oxidation of Ni. Electrical transport measurements were performed at different temperatures in the range 80–300 K.

2.3.2 Optimization of Annealing Condition

As post-thinning methods, three kinds of oxidation processes were tested at different temperatures: O_2 plasma, ozone treatment, and oxygen annealing. In the case of the former two processes, a rougher surface was obtained after the oxidation (see details in Section A), compared with that obtained with oxygen annealing, suggesting localized oxidation owing to the high oxidation rate [90, 144]. Therefore, oxygen annealing was selected as a moderate post-thinning method. Table 2.1 shows typical etching rate of oxygen annealing with different temperatures. Fig. 2-19a shows a typical optical image of the tape-exfoliated bulk SnS (∼100 nm thick) with a bright contrast to the substrate. Notably, an SnS surface freshly cleaved in air is intrinsic unlike the oxidized SnS surface after the Au-exfoliation [71]. Fig. 2-19b, c, and d show the optical images after oxygen annealing at 380°C, 410°C, and 430°C for 6 h, respectively. At 380°C, most of the flakes were light blue in color. At 410°C, a dark-blue flake with a similar contrast to the substrate was observed in addition to the light-blue flakes. In contrast, at temperatures greater than 430°C, all the flakes were almost transparent, similar to those observed after oxygen annealing at 900°C above the melting point of SnS (880°C [103]). This indicates that SnS layers were completely oxidized to SnO_x with high melting points [103], which is transparent owing to the wide bandgap (E_g = 3.6–4.0 eV [151, 152]). It has been reported that the oxidation of SnS to SnO_x through the reaction $SnS + (1 + x/2)O_2 \rightarrow SnO_x + SO_2$ occurs at temperatures above 325°C [148].

To investigate the change in flake color systematically and quantitatively, optical

Table 2.1: Typical etching rates of SnS in the early stage of annealing (<20 min) at different temperatures.

Temperature (°C)	350	380	410	430
Eting rate (nm/min)	<0.1	0.9	2.0	>10

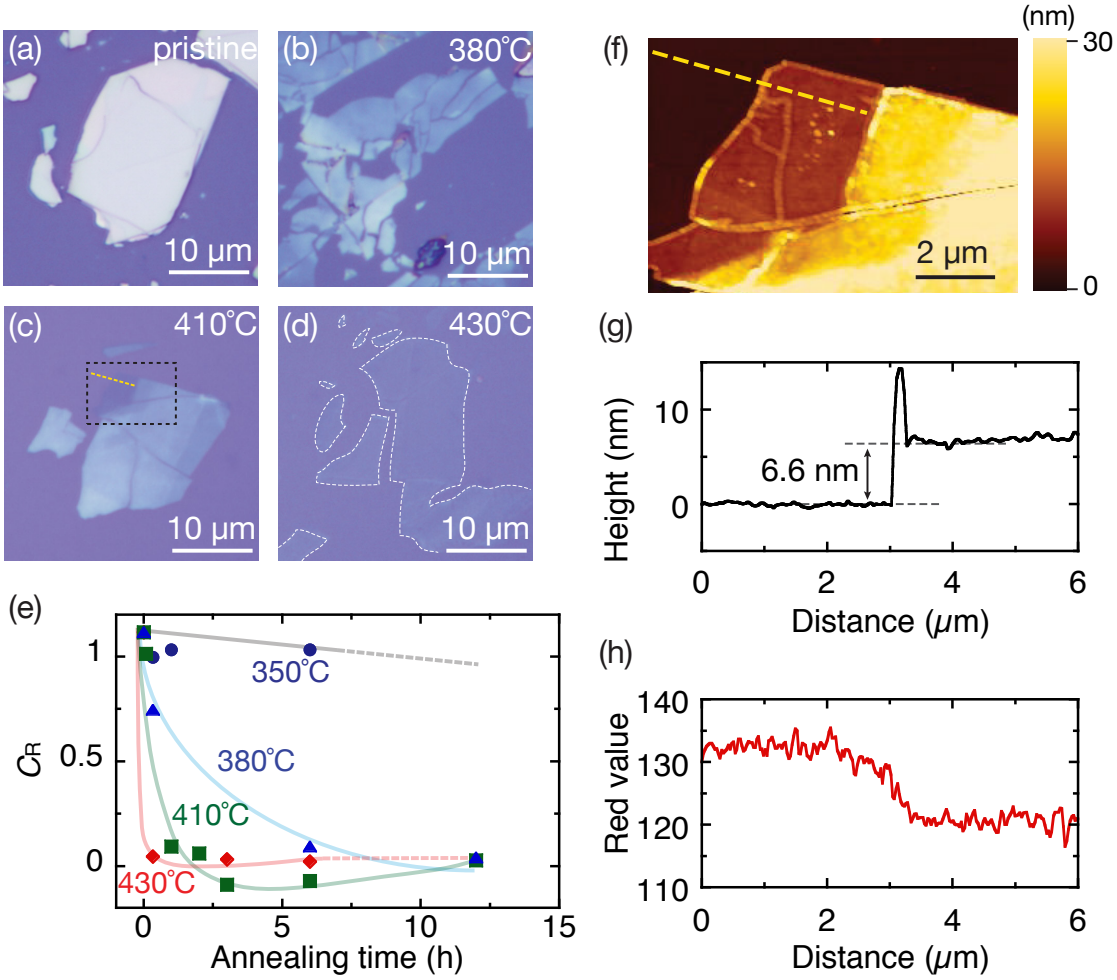

Figure 2-19: (a–d) Optical images of the tape-exfoliated SnS flakes (a) before oxygen annealing, and after oxygen annealing at (b) 380°C, (c) 410°C, and (d) 430°C for 6 h. (e) Optical contrast versus annealing time at different annealing temperatures. (f) AFM topographic image of selected area in Fig. 2-19c. (g) AFM height profile for the annealed SnS along the dashed line in Fig. 2-19f. (h) Red value profile for the annealed SnS along the dashed line in Fig. 2-19c.

contrasts were calculated for each color scheme–red, green and blue (RGB)–using

$$C_{\mathrm{i}} = \frac{I_{\mathrm{flake}} - I_{\mathrm{sub}}}{I_{\mathrm{sub}}} \qquad (\mathrm{i} = \mathrm{R},\ \mathrm{G},\ \mathrm{B}) \tag{2.3}$$

where I_{flake} and I_{sub} are the RGB values of the annealed SnS and the substrate, respectively. By comparing the RGB images, $\mathrm{C_R}$ was observed to be preferable to recognize the annealed flakes. Fig. 2-19e shows the time evolutions of $\mathrm{C_R}$ at different temperatures for the thinnest flake on the substrate. At temperatures below 350°C, $\mathrm{C_R}$ was almost constant within the range 1.00–1.12 even after 6 h. With the increase in the annealing temperature, the $\mathrm{C_R}$ value tended to change rapidly and significantly. At the temperature of approximately 410°C, negative $\mathrm{C_R}$ values were obtained over the large time window of ∼3–6 h. This negative $\mathrm{C_R}$ corresponds to the dark-blue flake in Fig. 2-19c. At temperatures above 430°C, $\mathrm{C_R}$ suddenly dropped at 5 min and was thereafter saturated to the value of fully oxidized SnO_x, i.e., 0.03. It can be expected that the negative $\mathrm{C_R}$ is a footprint of the non-transparent monolayer SnS (E_g = 1.5–2.4 eV [52, 53, 55]), which can survive over a long lifetime at the moderate temperature of ∼410°C. This is supported by a previous report, which indicated that the interaction between the substrate and monolayer materials stabilizes the monolayer during the post-thinning process [137]. To further examine the thinned SnS with negative $\mathrm{C_R}$, an AFM image was obtained for the selected area in Fig. 2-16c. As shown in Fig. 2-16f and g, the surface of annealed SnS was atomically flat; the typical root-mean-square surface roughness was 0.28 nm. The total thickness of the flat area was 6.6 nm, including the thicknesses of SnS and SnO_x. As the initial thickness of SnS flakes was ∼100 nm, it is suggested that the oxidation and sublimation of SnS occur simultaneously and the thickness of SnO_x will remain constant during the post-thinning process. Elevated regions at the edge and throughout the flake are probably the thick oxide, as the defective edges and grain boundaries are much easily oxidized than the surface without any dangling bonds. Fig. 2-19h shows the optical line profile at the position corresponding to the height profile. Along with a uniform height profile, the thinned flake showed optical uniformity, suggesting the uniformity

of thickness of the SnS layer below SnO_x.

To investigate the surface oxidation of SnS, surface-sensitive XPS measurement was performed. Fig. 2-20a shows the XPS spectra before/after oxygen annealing at 410°C. For the pristine SnS immediately after tape exfoliation, a peak of Sn $3d_{5/2}$ was observed at 486.6 eV, which is consistent with the reference value for the intrinsic SnS [102]. In addition, a peak was observed at approximately 162 eV, which can be decomposed into two peaks: S $2p_{1/2}$ and S $2p_{3/2}$ at 162.5 and 161.5 eV, respectively. After oxygen annealing for 5 min–3 h, the Sn $3d_{5/2}$ peak shifted to the higher binding energy of 487.4–487.5 eV, which corresponds to the binding energy of Sn-O [102]. However, the S 2p peaks were not observed after oxygen annealing for over 5 min. Thus, it can be concluded that the SnS surface was completely oxidized with a thickness at least several nanometers, which is the escape depth of photoelectrons [153, 154]. To evaluate the effect of oxidation on the crystallinity of SnS layers underneath, Raman spectra were obtained for the bulk flakes after tape exfoliation, Au-exfoliation, and oxygen annealing at 410°C for 6 h, as shown in Fig. 2-20b. In this measurement, the bulk thicknesses were much larger than the penetration depth of ∼20 nm for the excitation wavelength of 488 nm, and hence the crystallinity near the surface can be estimated from the Raman spectrum. For the tape-exfoliated SnS, Raman peaks were observed at 94.6, 161.7, 190.0, and 218.4 cm^{-1}, which corresponded to the reported peaks of A_g and B_{3g} modes for SnS [86, 107, 99]. These peaks were observed even after the surface oxidation *via* Au-exfoliation and oxygen annealing, indicating that the SnS layers underneath retain their high crystallinity. Although the Raman peaks of SnO_x (SnO, Sn_3O_4, Sn_2O_3, and SnO_2) have been reported to exist in the range 50–800 cm^{-1} in theoretical and experimental works [155, 156, 157], there were no other peaks than those of SnS and SiO_2/Si substrate for the oxidized SnS after Au-exfoliation and oxygen annealing. The discrepancy between the results of Raman and XPS measurements regarding the existence of an oxide layer is possibly due to the very small thickness of SnO_x and the detection limit of Raman measurement.

To investigate the thinned SnS with the negative CR, a cross-sectional TEM image was obtained along the dashed line in Fig. 2-19f. As shown in Fig. 2-21a, a hetero-

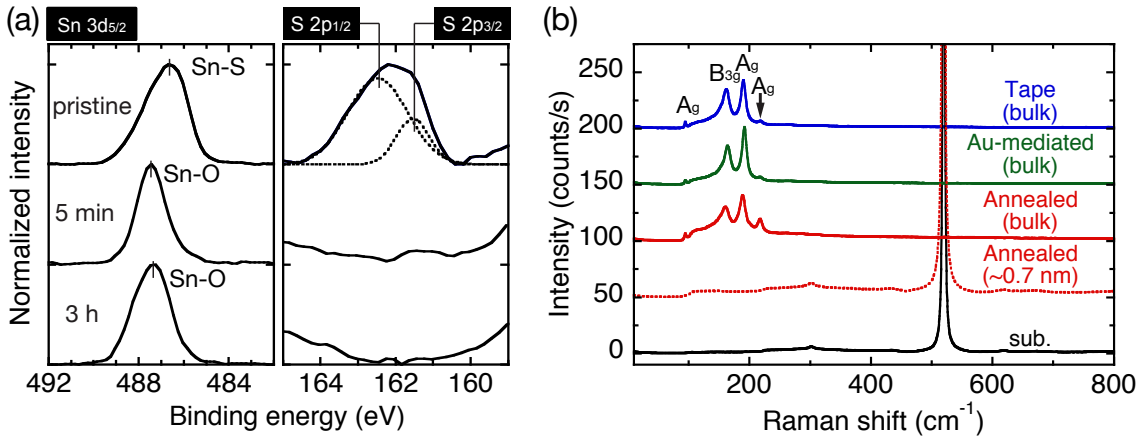

Figure 2-20: (a) Typical XPS spectra of Sn 3d and S 2p for the tape-exfoliated SnS before/after oxygen annealing at 410°C for 5 min and 3 h. (b) Typical Raman spectra of pristine bulk SnS *via* tape exfoliation and Au-exfoliation, and bulk and 0.7-nm-thick SnS obtained after oxygen annealing at 410°C for 6 h. The Raman spectrum of the SiO_2/Si substrate is also shown.

structure was observed: an ultrathin underlayer on the SiO_2/Si substrate and an upper SnO_x layer with a thickness of ∼6 nm. The thickness of the underlayer was determined to be ∼0.7 nm, very close to that of monolayer SnS [103, 111, 110]. To verify the existence of Sn and S atoms in the underlayer, EDS measurement was performed. Although S atoms were undetectable in the 0.7-nm-thick underlayer, both Sn and S were observed in the 2.3-nm-thick underlayer obtained after oxygen annealing, as shown in Fig. 2-21b. In addition to the Sn and S atoms, Ni and Au contaminations were detected, which were used for the metal marks on the substrate. In addition, other elements such as C, O, Si, and Ga were detected owing to the signals from the substrate and contamination during the focused ion beam process and electron beam irradiation. From the quantitative analysis, the atomic % ratio was estimated to be S : Sn = 1 : 7.2. Although one of the main reasons for the much larger content of Sn atoms than that of S atoms is that the signals from SnO_x are included, the existence of S defects induced during annealing cannot be excluded. As shown in Fig. 2-20b, specific Raman peaks were not observed for the 0.7-nm-thick SnS. The absence of Raman signals has been reported for the SnSe layers thinner than 9 nm and monolayer SnSe [132, 137]. Therefore, the Raman signal from 0.7-nm-thick SnS is probably under the detection limit. The SnO_x layer was partially

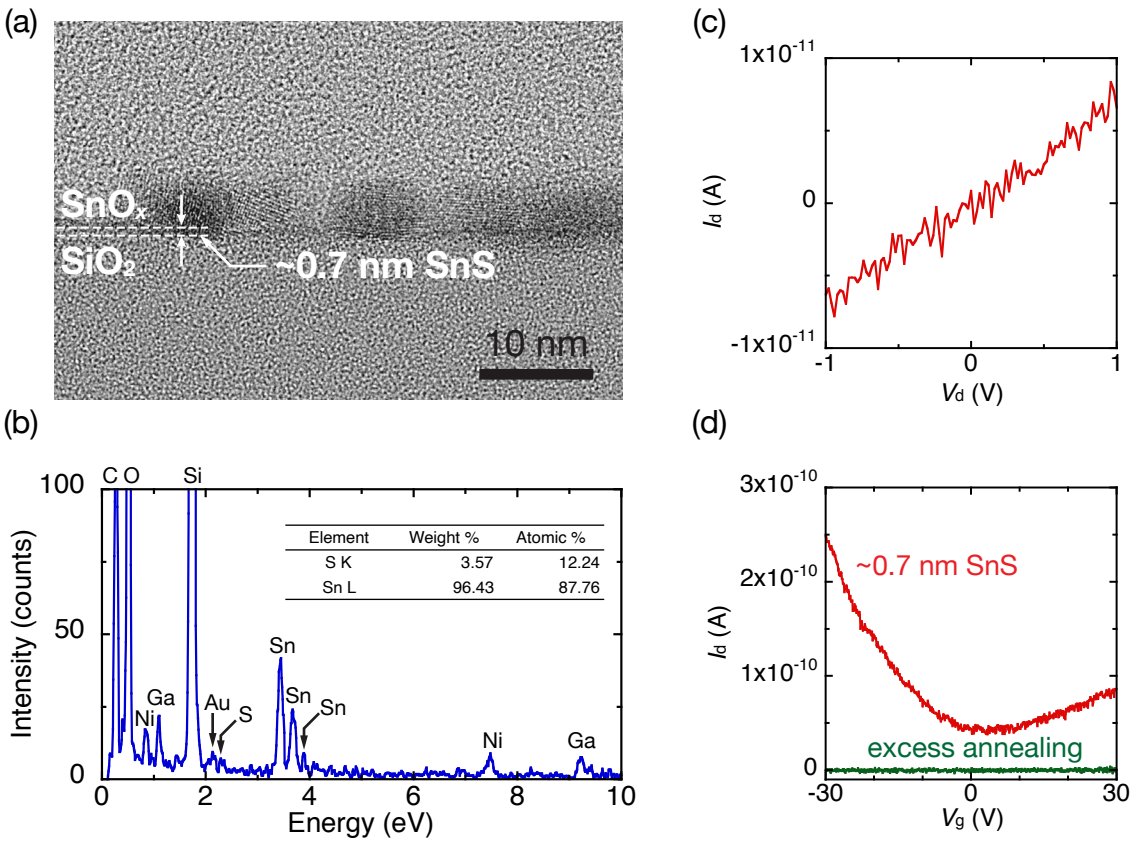

Figure 2-21: (a) Cross-sectional TEM image of 0.7-nm-thick SnS along the dashed line in Fig. 2-19f, obtained *via* oxygen annealing at 410°C for 6 h. (b) Typical cross-sectional EDS spectrum of 2.3-nm-thick SnS obtained *via* oxygen annealing at 410°C for 6 h. (c) I_d–V_d at $V_g = 0$ V and (d) I_d–V_g at $V_d = 3$ V for the 0.7-nm-thick SnS. The non-conductive characteristic of 0.7-nm-thick SnS after the excess annealing at 410°C for 40 min is also shown. The channel length and width were 0.65 µm and 2.16 µm, respectively.

crystalized, as shown in Fig. 2-21a. This is in contrast to the wet oxidation at RT during Au-exfoliation process. With oxygen annealing, the quality of crystallized SnO_x (c-SnO_x) should be better than that obtained with the RT oxidation; hence, moderate oxidation/sublimation were realized.

2.3.3 Electrical Characterization of Monolayer SnS

To investigate the electrical characteristics of 0.7-nm-thick SnS, a two-probe FET device was investigated. Fig. 2-21c shows the I_d–V_d curve of 0.7-nm-thick SnS at RT and $V_g = 0$ V. Notably, the TEM image in Fig. 2-21a was obtained for this device after

the transport measurement. Although the SnS layer was indirectly contacted with the metal through the c-SnO_x layer, the I_d–V_d curve exhibited a linear characteristic indicating an ohmic contact because the Fermi level pinning observed commonly in any 2D/metal contacts [122, 123] is possibly released due to the c-SnO_x layer. Fig. 2-21d shows the I_d–V_g curves at $V_d = 3$ V. The 0.7-nm-thick SnS exhibited ambipolar behavior, even though the SnS FETs thicker than 9L exhibited *p*-type characteristic as shown in Fig. 2-16b. When the dark-blue 0.7-nm-thick SnS flake was annealed excessively for 40 min, it became transparent and non-conductive, as shown in Fig. 2-21d. These results indicate that the ambipolar characteristic of annealed SnS is attributed to the transport characteristic of 0.7-nm-thick SnS. The same situation has been reported for the monolayer SnSe obtained *via* N_2 annealing [137] in spite of the *p*-type nature of bulk SnSe [121]. For both cases of SnS and SnSe, the native *p*-type characteristics originate from V_{Sn}, whereas the S/Se vacancies might be the origin for the *n*-type conduction [158].

Conculusion The structure distortion caused by the lone pair electrons produces unique anisotropic structural/optical/electrical properties in MXs. The lone pair electrons also cause a strong interlayer force and high chemical reactivity, which prevent the isolation of the monolayer MX *via* simple mechanical exfoliation. In this study, the SnS layer with the monolayer thickness was realized with a stable SnO_x passivation layer *via* mechanical exfoliation, followed by moderate oxygen annealing. The field-effect transistor of monolayer-thick SnS exhibited ambipolar behavior probably owing to the combined *p*- and *n*-type doping with Sn and S vacancies, respectively. This work on the monolayer-thick SnS fabrication can be applied to other unstable lone pair analogues and can facilitate future research on MXs.

2.4 Physical Vapor Deposition

As described in Section 2.3, the top-down thinning methods including the oxygen annealing, oxygen plasma, and ozone treatment, has been revealed to be difficult to fabricate a high-quality monolayer SnS due to the external defects. The self-passivated SnO_x/SnS heterostructure has been succeeded *via* the oxygen annealing, however, its FET behavior exhibited the extrinsic defects of V_{Sn}.

For further improvement of the crystalline quality of monolayer SnS, a bottom-up fabrication process is proposed in this Section. Fig. 2-22 shows a conceptual illustrations of top-down and bottom-up fabrication processes. So far, the bottom-up material syntheses of 2D SnS have been reported, though no reliable method for monolayer growth has been established [109, 86, 107, 159]. The present oxygen annealing method in this work, moderate SnS desorption has been achieved at the reduced pressure of 10 Pa and the optimized temperature at around 410°C (Fig. 2-19). Considering an analogy between the desorption-like conditions in the top-down thinning and bottom-up growth methods. In this section, a physical vapor deposition (PVD) is investigated, where SnS adsorption and desorption are precisely balanced based on the findings in the thinning *via*oxygen annealing. For the PVD growth of SnS, the thinnest thickness has been 5.5 nm (>10 layers) [86], which was realized under the growth pressure of 10^4 Pa. Here, the pressure is reduced to 10 Pa, which has been found to be effective to decompose the SnS.

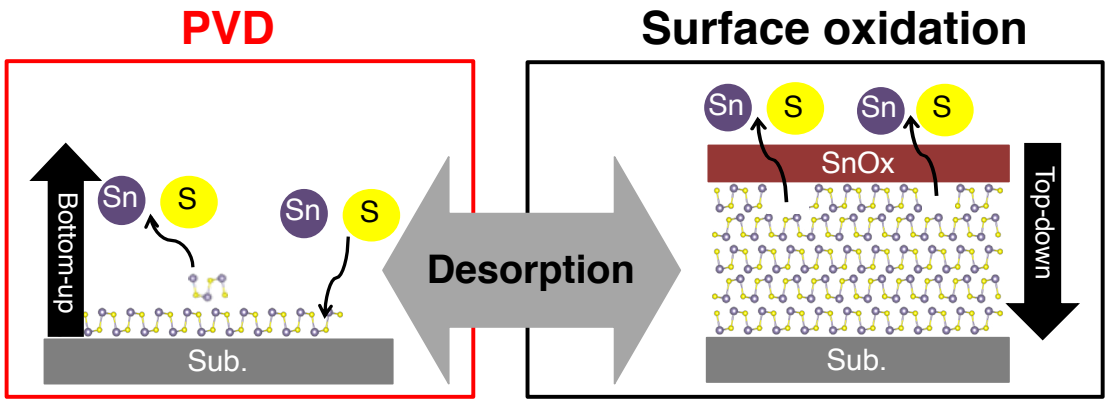

Figure 2-22: Conceptual illustration of bottom-up/top-down fabrication methods for the monolayer SnS.

2.4.1 Growth Procedure

Fig. 2-23a shows the schematic illustration of a home-built three-zone PVD growth system. A SnS source, powder or grains, was placed at the high temperature and a growth substrate was set at the downstream. A N_2 gas was used as a carrier gas. Each heaters were independently controlled to make a gentle temperature gradient. Detailed preparation and growth procedure is described as follows.

1. Preparation of Sn sources: two types of SnS source was used. One is a commercially available SnS powder (99% up). The other is an amorphous bulk SnS, which was obtained *via* a purification of sulfur sources [110]. The amount of SnS source was fixed at 0.1 g. As the bulk SnS has a small specific surface area, it was crushed by a mortar.

2. Preparation of substrate: SiO_2/Si and mica substrates were used as a growth substrate. The SiO_2/Si substrate was treated in diluted HF solution, followed by a rinse in deionized water, to eliminate contaminations at the surface. While mica's top layers were mechanically exfoliated with the Scotch tape instead of a solution treatment. Mica is a 2D layered material so that a fresh surface can be obtained with cleaving the top layers.

3. Both SnS source and substrate were set at upstream and downstream, respectively.

4. N_2 purge was performed for three times to minimize the oxygen and H_2O residues.

5. A growth recipe was operated. Fig. 2-23b shows a typical time evolution of temperatures. Initially, the source and substrate were heated at 100°C to eliminate the H_2O physically adsorbed on the substrate surface. After that, substrate was preheated at the growth temperature beforehand, followed by a heat up of source to the target temperature. The typical growth time was ranged between 2–10 min.

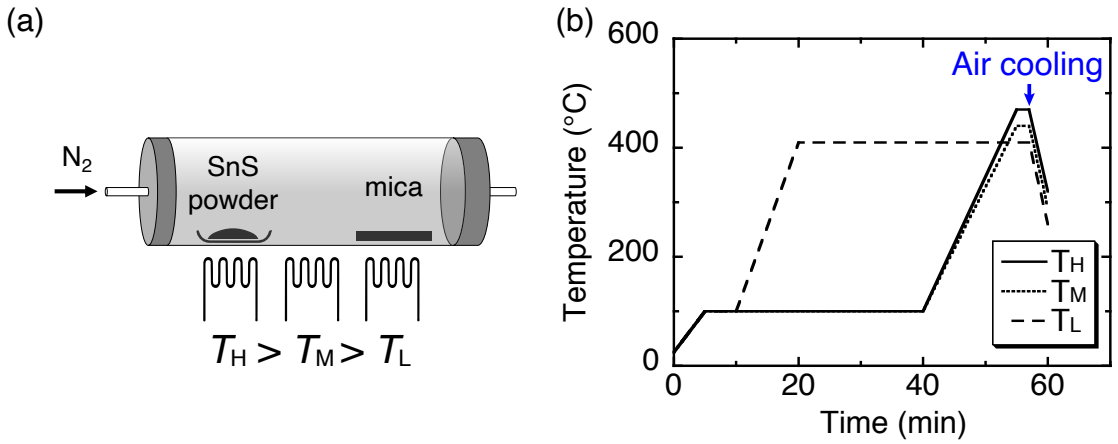

Figure 2-23: Growth conditions for monolayer SnS. (a) Schematic diagram of three-zone PVD chamber by separately controlling the heaters at high, middle, and low temperatures (T_H, T_M, and T_L). (b) Typical temperature profiles for monolayer growth. After the growth, the chamber was air-cooled at the rate of ~50 °C/min.

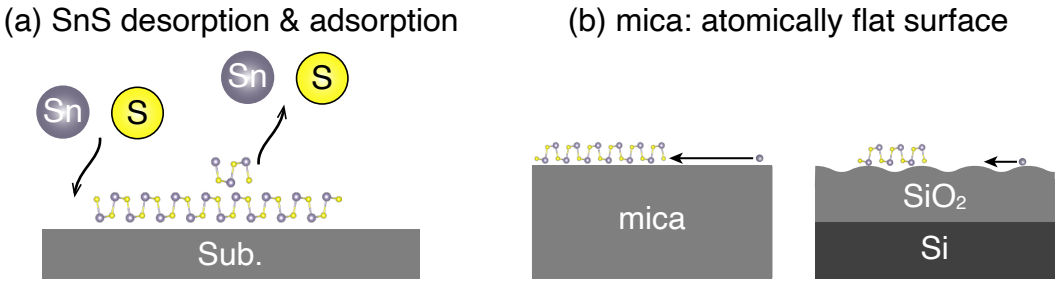

Figure 2-24: Strategies of monolayer growth: (a) control of SnS adsorption and desorption during the growth, (b) mica substrate with atomically flat surface.

6. An air-forced cooling was operated down to RT. Then the sample was took out from the chamber.

7. To clean-out the growth tube (quartz), a baking was operated at 900°C with the source boat and substrate stage.

As shown in Fig. 2-24, the mica substrate has an atomically flat surface enhancing the atomic migration during the growth, compared to the SiO_2/Si substrate. Thus a lateral growth rate is expected to be enhanced for the mica substrate.

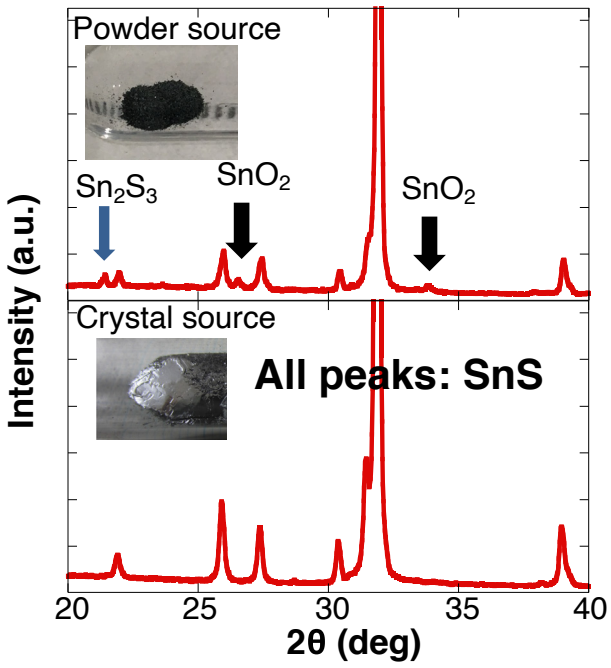

Figure 2-25: Powder XRD of different SnS sources: (Upper) high-purity crystal and (Bottom) commercially purchased SnS powder (>99.9%)

2.4.2 Purity of SnS Source

Fig. 2-25 shows typical results of XRD measurement for the powder and bulk SnS. For the powder source, additional peaks were observed except for the specific peaks from SnS. Each peaks were determined to belong to SnO_2 and Sn_2S_3. In contrast, for the purified bulk SnS, only SnS's peaks were observed. These results agree with previous works on the SnS growth *via* EB or thermal evaporations toward the solar cells applications [160, 57]. The purchased SnS powder sources usually contains multiphase contaminations (SnS_2, Sn_2S_3). In Ref. [57], a 3.88% efficient SnS solar cells were achieved by eliminating the S-rich contaminations with post annealing.

Generally, the *contamination* are regarded to be obstacles for the high-quality growth. Interestingly, however, the Sn_2S_3 *contamination* plays an important role in the monolayer growth of SnS, as discussed blow.

2.4.3 Surface Morphology of SnS Crystals

Here, SnS growth is discussed based on the crystals grown from the SnS powder. The surface morphology of SnS crystals were categorized into two types: 2D nucleation growth and stepped growth. Fig. 2-26 shows the series of AFM morphologies with changing the source/growth temperature. The SnS surface was flat and no step/terrace was found. When the temperatures of source (T_{sub}) and substrate (T_{SnS}) were set at 590 and 530°C, the crystal shape showed a very clear diamond-shape (Fig. 2-26e). With decreasing T_{sub} and T_{SnS}, the SnS thickness was modulated down to 0.8 nm, which is close to the monolayer thickness [161] (Fig. 2-26b). For the SnS crystals with step/terrace, monolayer-thick steps were observed for the different SnS thicknesses, as shown in Fig. 2-27. Similar morphology was found in the MBE growth of SnS; Bao *et al*. observed the wedding-cake shaped SnS multilayers [159], while Sutter *et al*. determined the screw dislocation assisted spiral growth [162]. For both growth mechanism, their SnS thickness tends to be thicker than 10 layers, probably due to a high perpendicular growth rate. Also in this work, no few-layer SnS with stepped structure was obtained. These results suggest that the 2D nucleation is necessary for the growth of few-to-monolayer SnS.

The AFM topography of monolayer usually included some tiny holes with a diameter below 1 µm, which becomes apparent when a post-growth annealing was performed. Fig. 2-28 shows AFM images for the SnS annealed at 440 and 410°C. Square-shaped etch pits were clearly observed, which are probably reflecting the atomic configuration of SnS. This result indicate that the thin SnS crystals posses a uniform crystal orientation in the micro scale despite of their rounded shapes. Furthermore, this uniformity was determined for the different growth mechanisms: 2D nucleation (Fig. 2-28a) and stepped growth (Fig. 2-28b).

Interestingly, from the purified bulk SnS source, few-to-monolayer SnS was not realized below ∼2 nm thickness. Fig. 2-29 compares AFM images of the thinnest SnS crystals. For the bulk source, a SnS crystal was surrounded by flat mica surface, while for the powder source, µm-size monolayer SnS was surrounded with sub-micron

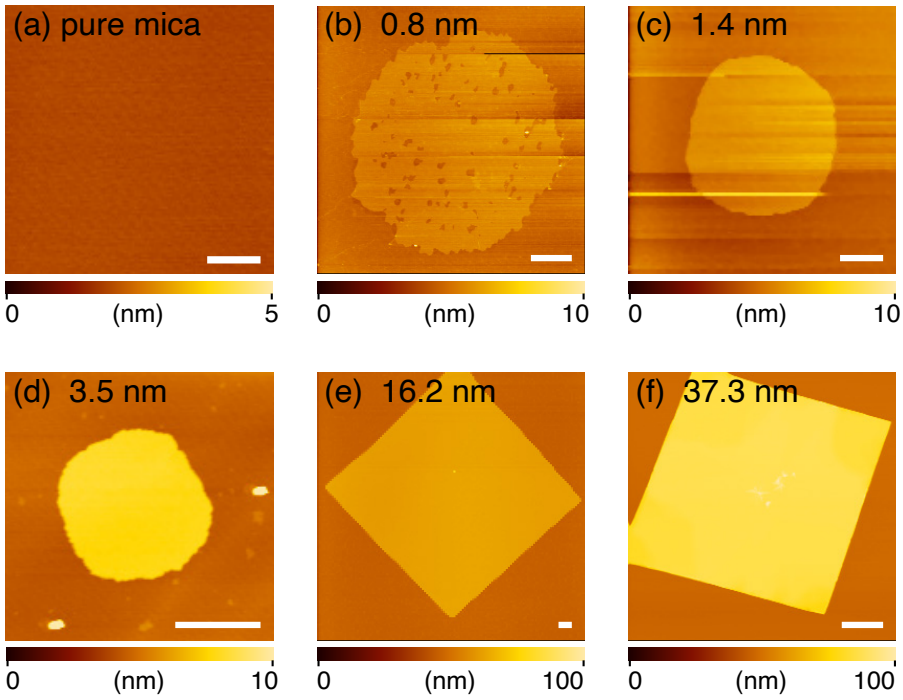

Figure 2-26: Evolution of crystal morphology for different SnS thicknesses. (a) pure mica, (b) 0.8 nm, (c) 1.4 nm, (d) 3.5 nm, (e) 16.2 nm, and (f) 37.3 nm. The scale bars represent 1 µm.

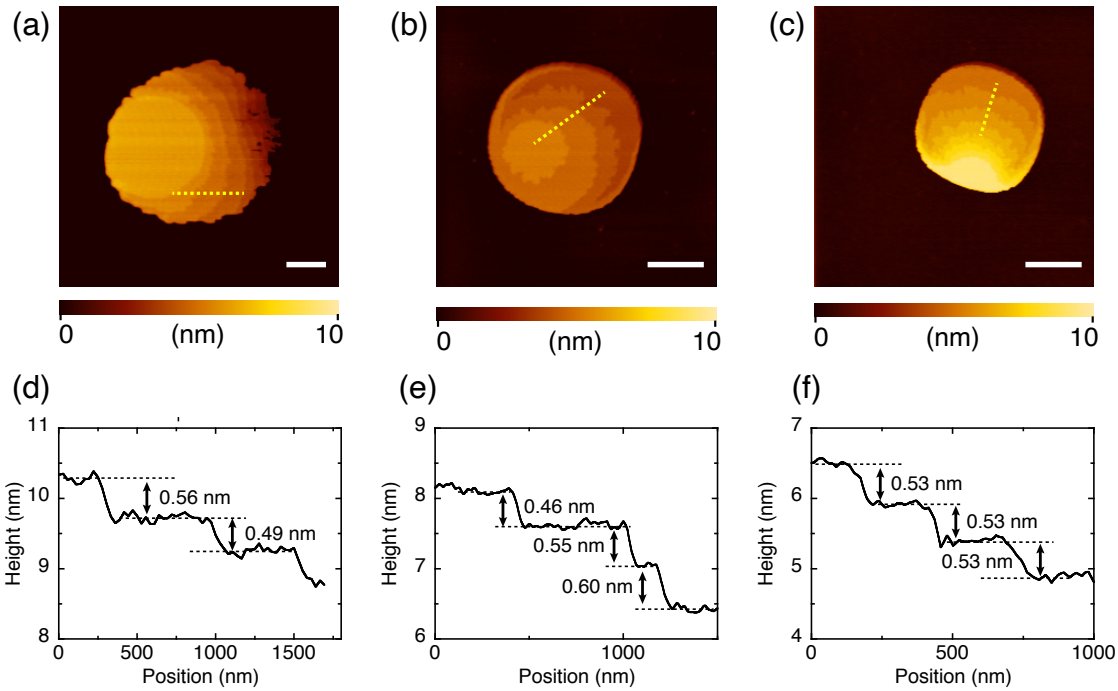

Figure 2-27: Wedding-cake morphology of SnS multilayers. The scale bars represent 1 µm.

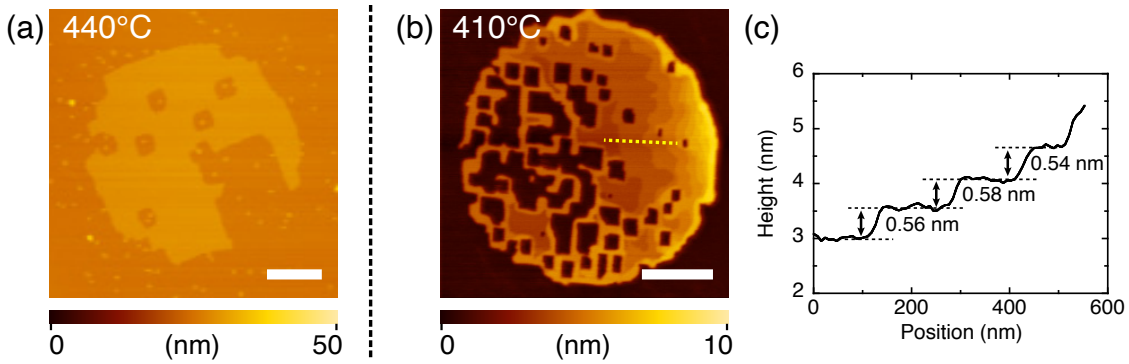

Figure 2-28: AFM topographic images of multilayer SnS after post-growth annealing in N_2 atmosphere at (a) 440 °C and (b) 410 °C. The scale bars represent 500 nm. (c) Height profile along the dashed line in Fig. 2-28b.

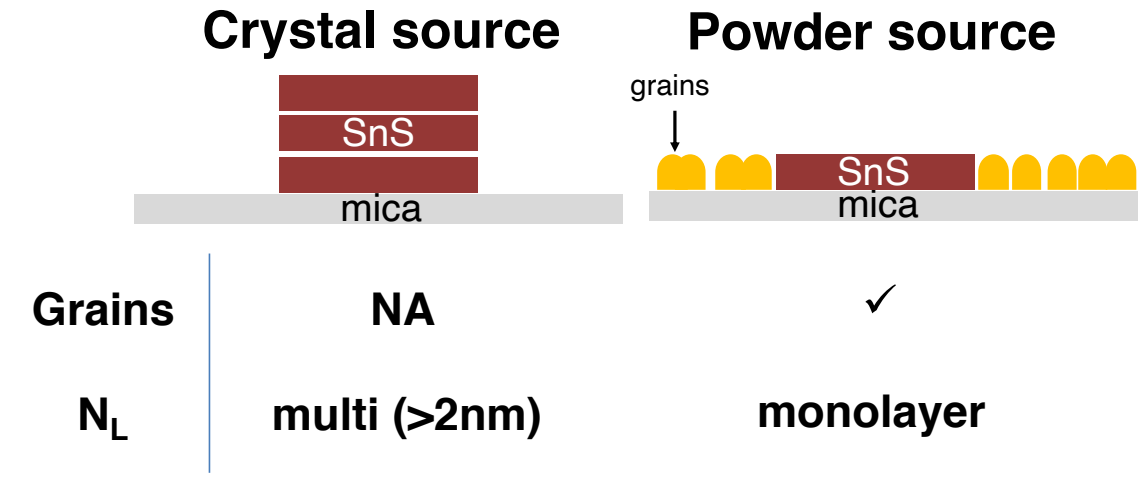

Figure 2-29: Comparison between SnS crystals grown from powder and purified bulk SnS sources.

grains, whose size is approximately 100 nm or below and which tends to be triangle-shaped.

2.4.4 Composition evaluation of SnS

For further characterization of SnS crystals and sub-micron grains, EDS spectra were measured for them. In Fig. 2-30a, typical cross-sectional EDS spectra for trilayer SnS crystal and sub-micron grains are shown. Clear EDS peaks from Sn and S were confirmed. The other additional signals are from the contaminations of substrates and owing to the FIB/EB irradiation processes. The ration of atomic% was determined

to be 1 : 0.81 for Sn : S, excluding other possibility of S-rich phases such as SnS_2 and Sn_2S_3. On the other hands, for the sub-micron grains, the ratio of Sn : S was determined to be 1 : 1.36, suggesting that these grain is different from the SnS crystals. Considering that the sub-micron grains were peculiar to the PVD growth with powder source, which initially contains S-rich phases; the existence of S-rich states possibly contribute the monolayer growth. One of the possible explanation is that the S-rich grains cover the mica substrate at first and then they increase the wettability of SnS molecules against the substrate. Otherwise they would work as a precursors of SnS.

In order to prove the difference of composition between the large SnS monolayer crystal and small grains around SnS for powder source, nanoscale electron spectroscopy for chemical analysis (nano-ESCA) was performed. Figs. 2-31 shows the optical and AFM topographic images for the SnS/mica sample. In order to prevent the charge-up on mica insulator during the ESCA measurement, Ni/Au electrodes were fabricated *via* a standard EB lithography and metal evaporator. Comparing the optical images before and after the electrode, optical contrast of SnS crystal turned to be transparent near the bottom-right edge after the metal liftoff. This change of optical contrast is probably due to the chemical modification of SnS into SnO_x: the bandgap of SnO_x is larger than that of SnS. As shown in Fig. 2-31c, the surface roughness for the transparent region is larger than the inner intrinsic region.

Figs. 2-32a,b show the System setup of 3D nano-ESCA (SPring-8). This system enable the nanoscale spatial resolution three-dimensionally. The earth wire was extended with Ag paste and Cu wire as shown in Fig. 2-32c. Figs. 2-33a,b shows the AFM topographic and phase shift images, respectively. At the bottom-right region, phase shift image indicated the larger phase shift compared to the inner intrinsic region. This should be caused by the change of adhesion property due to the oxidation, which agree with the optical change. Fig. 2-33c shows intensity mapping image with using the Sn 3d peak intensity. The intensity difference is probably both owing to the inhomogeneous composition and thickness. In Fig. 2-33d, ESCA spectra at different points as shown in Fig. 2-33a-c are shown: (A) inner intrinsic SnS region, (B) oxidized edge region, and (C) small grains outside the SnS crystal. With using

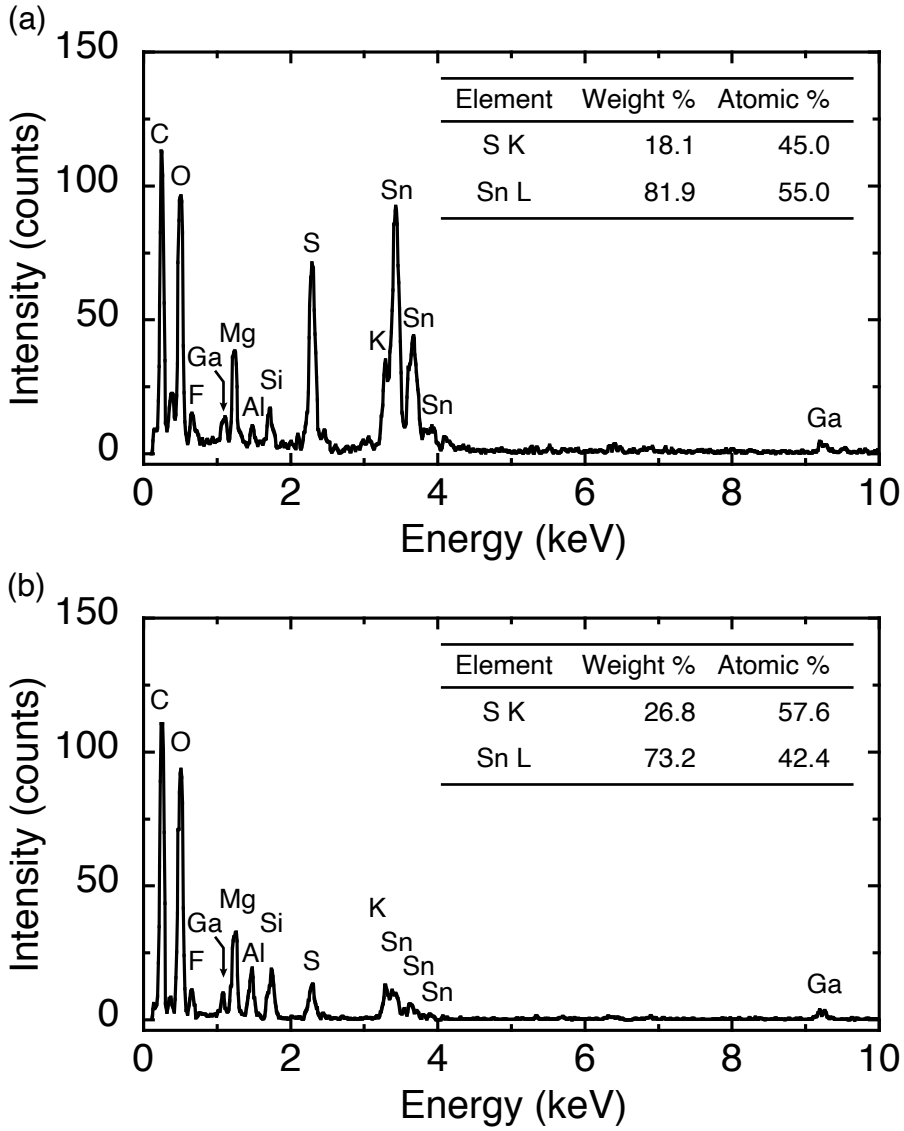

Figure 2-30: Typical cross-sectional EDS spectrum of (a) trilayer SnS and (b) grains.

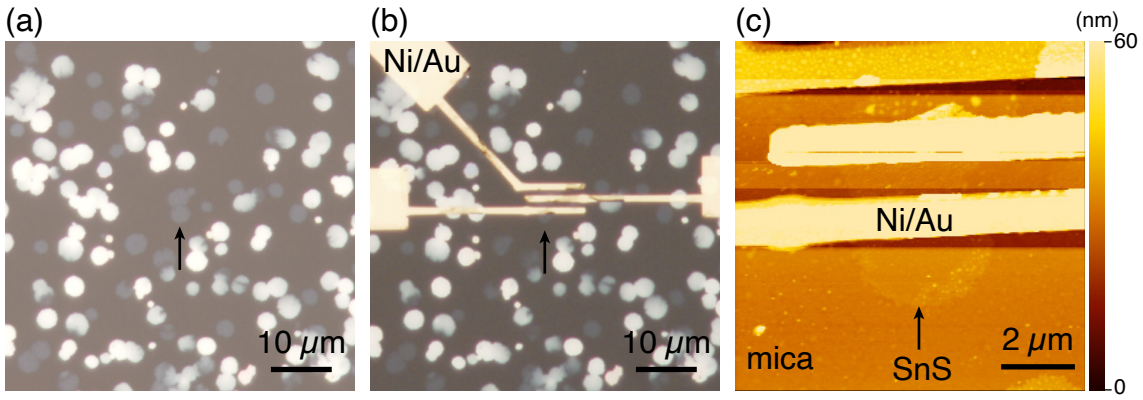

Figure 2-31: Optical images of SnS samples (a) as grown, and (b) after the device fabrication. (c) AFM topological image for the monolayer-thickness SnS with electrode.

multi-curve fitting, single main peak and small sub peak were found for the point A. The peak position for the main peak was around 485.9 eV, which corresponds to the Sn $3d_{5/2}$ peak position for Sn^{2+}. This main peak was also confirmed at the point B and C. In addition to the Sn^{2+} peak, main peak at around 486.5 eV was found for the point B and C, which corresponds to the Sn^{4+} peak. For bulk SnS and SnS_2, single peak has be observed at 485.6 and 486.5 eV; and two main peaks have been observed at 485.8 and 486.4 eV for Sn_2S_3[94]. These results indicate that the inner region of large crystal (point A) is SnS, while the outside region (point C) is Sn_2S_3. For the degraded edge region of large crystal (point B), further investigation is necessary to determine the composition, though it is possibly SnO_x, considering together with the optical contrast change [161].

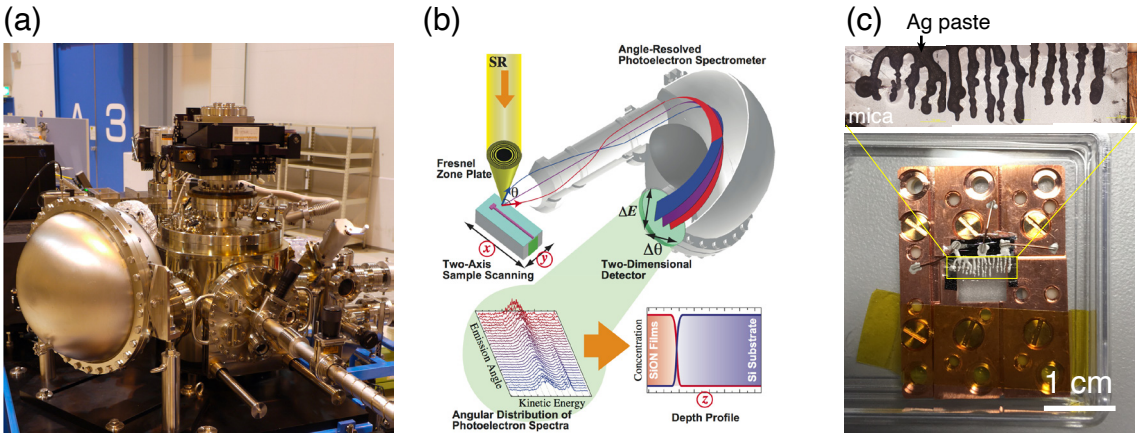

Figure 2-32: (a,b) System setup of 3D nano-ESCA (SRRO, University of Tokyo). (c) Sample preparation for nano-ESCA measurement.

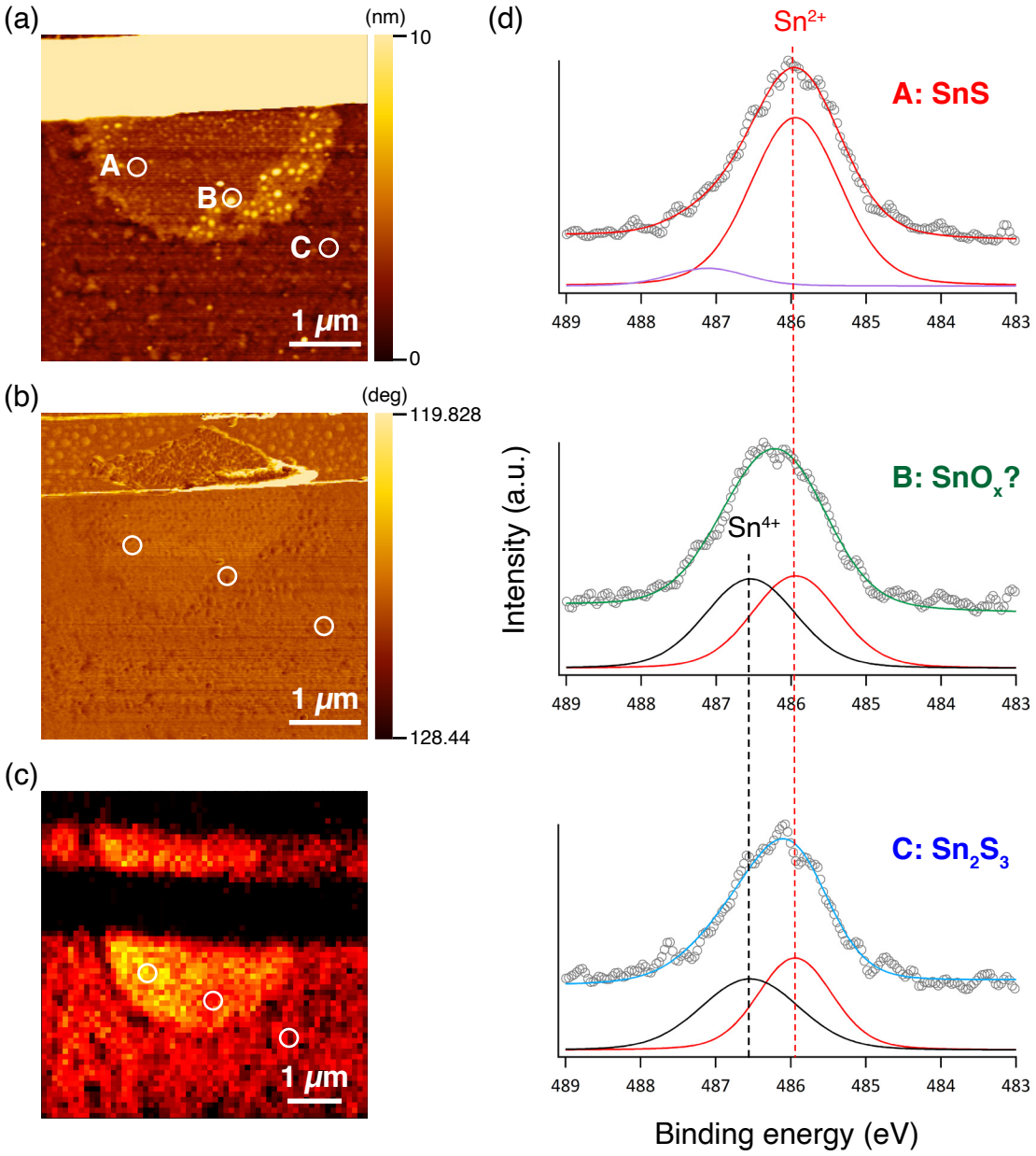

Figure 2-33: AFM (a) topological, and (b) phase shift images for the sample. (c) Intensity mapping of Sn 3d peak. (d) ESCA spectra for each point A, B, and C in Fig. 2-33a–c.

2.5 Characterization of Monolayer SnS *via* PVD

In this section, optical and electrical characterizations are described for the few-to-monolayer SnS prepared *via* PVD growth in order to evaluate the crystalline qualities. For optical measurement, Raman spectrum is studied. With focusing the excitation laser in a micro-meter diameter, light-induced heat sometimes cause the sample modification [71]. For electrical measurements of SnS on the mica insulator, FET devices require the fabrication of top-gates or transferring SnS from mica to the global back-gated substrates such as SiO_2/Si. As discussed in Section 2.1, SnS is easy to be oxidized due to the oxygen favorability of lone pair electrons that constituting the top of the valence band [94]. Therefore, negative effects of the optical measurements and device fabrication processes have to be carefully considered.

In this work, for the optical measurement, the SnS samples are measured in vacuum to prevent the surface oxidation during the measurement. Moreover, top-gated FETs are investigated rather than the transfer method, for the sake of utilizing the mica substrate as a straightforward platform from crystal growth to the flexible devices, as will be discussed in Section 3. For the top-gate insulator, atomic layer deposition (ALD) has been commonly used with an assistance of buffer layers [163, 164, 165]. However, ALD process usually requires high temperature deposition at around 200°C, which might degrade SnS. To prevent the thermal effect on the channel, TG fabrication *via* *h*-BN transfer below 90°C [166] will be effective, though it takes quite a bit of care. In this works, Er_2O_3 deposition at RT is examined as a damage-less and efficient TG fabrication method.

2.5.1 Raman Measurement

μ-Raman spectrum was measured in vacuum with using a 488-nm excitation laser. The optimal laser power below 0.5 mW was used to avoid degradation of SnS owing to laser heating [71]. A 40× objective lens was used, whose nominal $1/e^2$ spot diameter on the sample surface is 2.5 μm. Fig. 2-34a shows typical RT Raman spectrum of PVD grown SnS from bulk to monolayer thickness. There are overlaps between the

Raman peaks from SnS and mica at around 120, 190, and 270 cm^{-1}. For bulk SnS, specific Raman peaks from SnS were observed at around 150, 180, and 220 cm^{-1}. With decreasing the thickness, the Raman peaks between 120–190 cm^{-1} become ambiguous, while the peak at 220 cm^{-1} can be clearly found down to the monolayer. To increase the Raman intensity, the temperature was decreased, as shown in Fig. 2-34b. At 3K, Raman peaks were observed apparently even at 120–190 cm^{-1}. For the monolayer, specific peaks were observed at around 150, 220, and 290 cm^{-1}. This result guarantees the high-quality of SnS crystals. For further understanding, polarized Raman measurements and Ab initio Simulation of phonon modes are investigated, as will be discussed later 4.

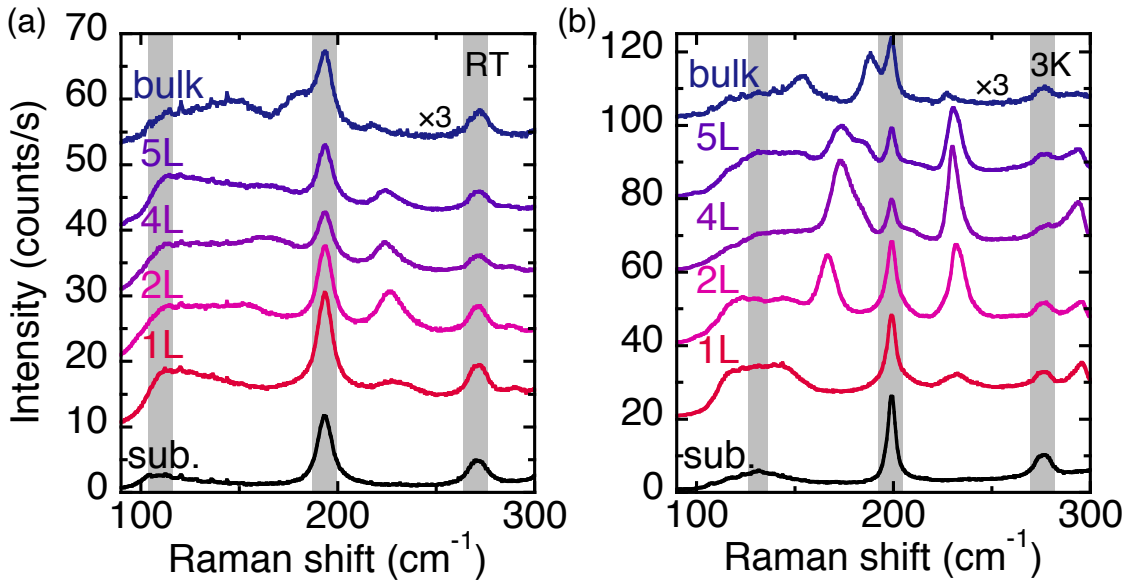

Figure 2-34: Typical Raman spectra for SnS with different thicknesses from bulk to monolayer, measured at (a) RT and (b) 3K.

2.5.2 Fabrication Procedure of Top-gated FETs

In order to deposit the insulating materials, a home-built oxygen pressure controlled thermal evaporator was used [167]. A schematic illustration of system setup is shown in Fig. 2-35. The feed source and deposition chamber are separated by an aperture of $\phi = 5$ mm and can be evacuated independently. Here, Er_2O_3 is selected as a gate

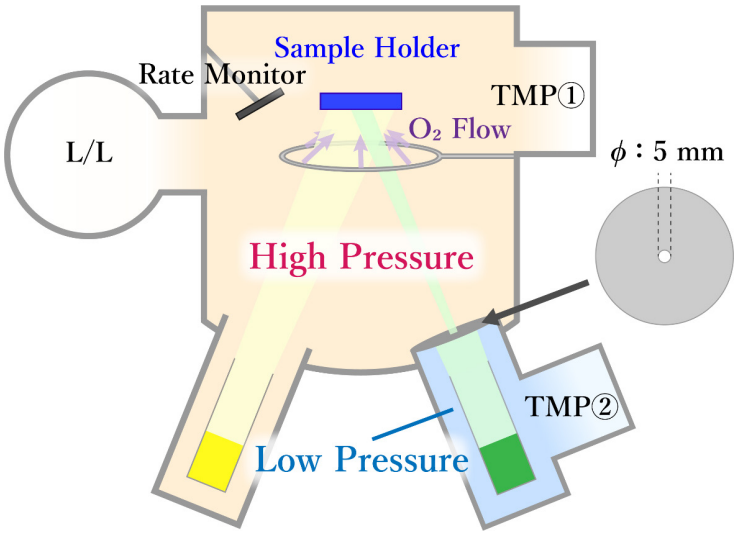

Figure 2-35: Schematic illustration of Er_2O_3 deposition at room temperature [167].

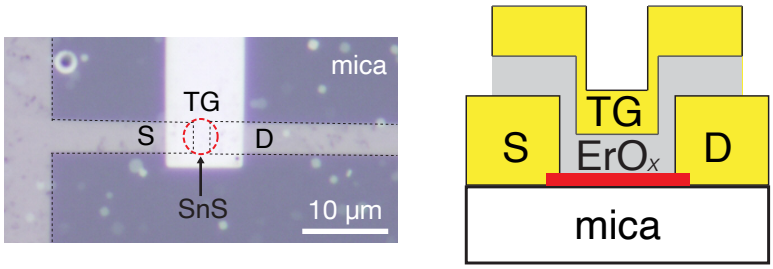

Figure 2-36: (a) Optical image and (b) Device structure of TG-gated FETs.

insulator, whose effective dielectric constant is $\varepsilon = 4.5 - -6.0$ and vapor pressure is relatively higher than other metals such as Y. After SnS crystals were grown *via* on mica substrate, source/drain electrodes were fabricated with using Ni/Au. Then top-gate patterns were drawn by EB lithography, followed by an Er_2O_3 deposition. The temperatures of source and sample stage was set at 1090°C and RT, respectively. The thickness of Er_2O_3 layer on SnS was estimated from a x-ray reflectivity measurement of Er_2O_3 on a dummy Si substrate, which was placed next to the target samples. After depositing a dielectric layer, Al top-gate electrode was deposited *via* a standard resistance heating evaporator. Finally, all the Er_2O_3 and Al layers were lifted off in acetone solution. As a results, top-gated FET was obtained, as shown in Fig. 2-36.

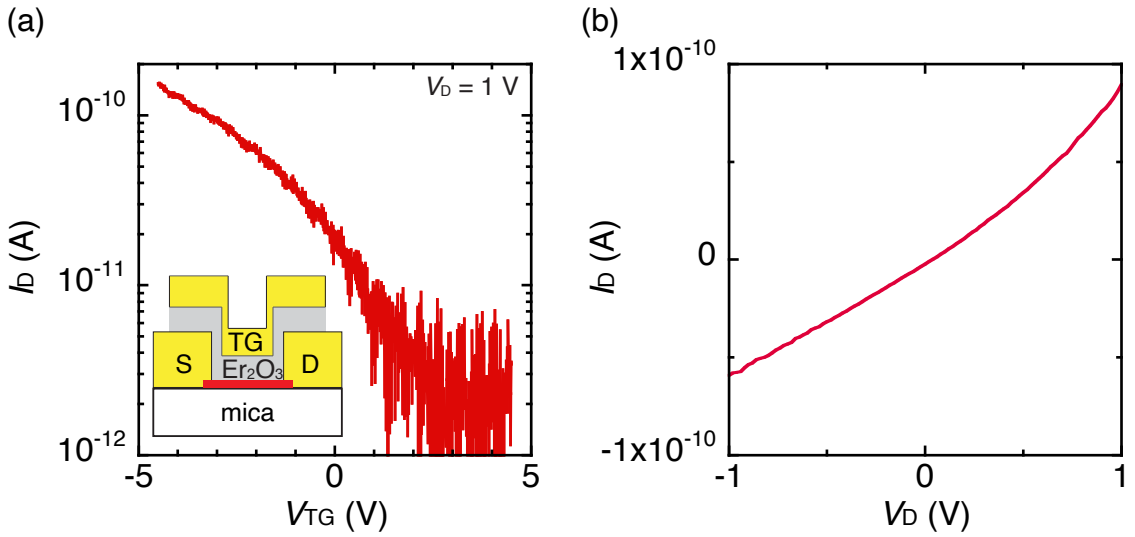

Figure 2-37: (a) I_D–V_{TG} plot at VD = 1 V and (b) I_D–V_D plot at V_{TG} = 0 V of 5L SnS at RT.

2.5.3 Electrical Characterization of Few-to-monolayer SnS

Fig. 2-37 shows the electrical transport characteristics of PVD grown 5L SnS as a function of the top-gate voltage at RT and V_D = 1 V. In contrast to the thick SnS (>9L, Fig. 2-15), 5L SnS exhibited the off-state at RT. Herein, for the first time, the intrinsic *p*-type and fully depleted FETs was demonstrated for few-to-monolayer SnS. Given that the few-to-monolayer SnS *via* showed ambipolar FET behavior due to the extrinsic defects V_{Sn} (see details in Section 2.3), the intrinsic *p*-type behavior of PVD grown few layer SnS indicates the highly crystalline quality. This is probably because of the continuous supply of SnS sources during the PVD growth.

Fig. 2-38a summarizes the SnS thickness dependence of current modulation I_{ON}/I_{OFF} from this work, including PVD grown and mechanically exfoliated SnS, and the reported thinnest SnS FET [66]. The transition occurs at ~5 nm, which is much smaller than MoS_2 FETs (48–55 nm [115]), suggesting the heavy doping in SnS to limit the depletion width W_D. To estimate the acceptor density N_A of SnS, a simple calculation was performed using the maximum depletion width W_D as following Eq. 2.1. In Fig. 2-38b, the relationship between W_D and N_A of SnS at RT is shown. By equating W_D to these SnS thicknesses, N_A is estimated to be of the order of 10^{19} cm^{-3}, which is consistent with the previous estimation [67]. Although

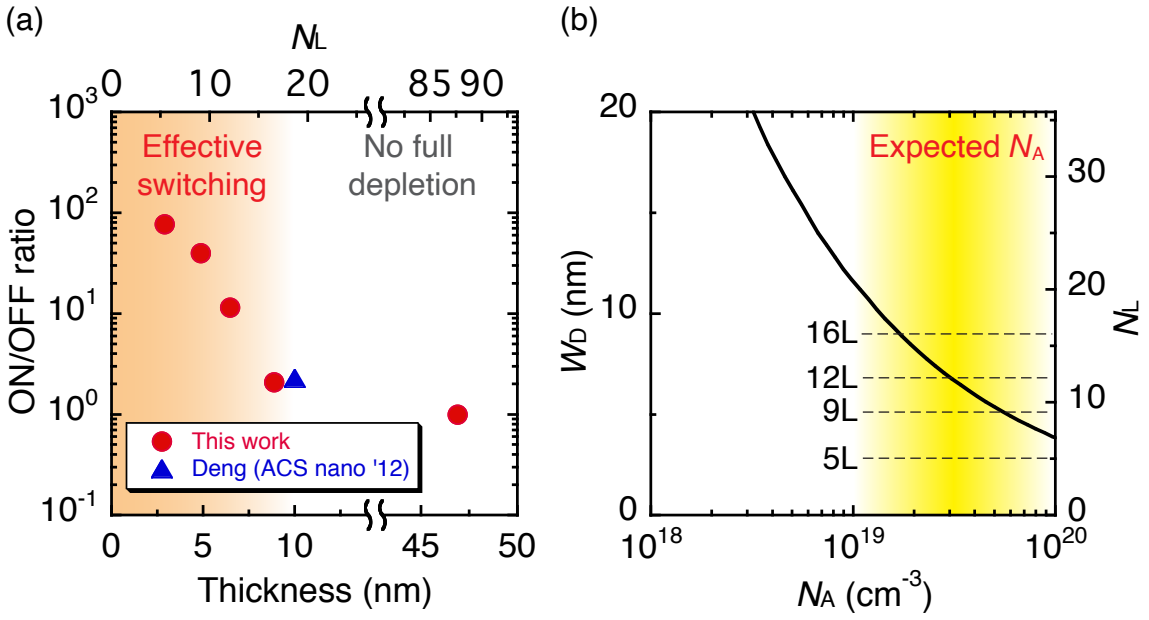

Figure 2-38: (a) Current modulation I_{ON}/I_{OFF} versus thickness. (b) Relationship between depletion width W_D and acceptor density N_A.

$I_{ON}/I_{OFF} \sim 10^2$ of 5L was much higher than thicker ones, further performance can be expected since the high-crystallinity for as-grown crystals has been confirmed by Raman measurement. Improvement of device fabrication process enables to extract original features of few-to-monolayer SnS.

SnS has been recently attracted attention for its strong anisotropy and p-type conductivity with a high theoretical carrier mobility over 10,000 $cm^2V^{-1}s^{-1}$, which is comparable to the high mobility of BP [53]. Compared with MoS_2 with large effective mass due to Mo-d orbital, SnS and BP have small effective mass due to S-p and P-p orbitals, respectively. Furthermore, the deformation potential of SnS is smaller than that of BP, which results in higher mobility along the armchair direction [53]. Despite of the outstanding theoretical estimation, the present 2D SnS FETs showed much poor conductivity than the theoretical value even at the accumulated region. One of the possible reason is the extrinsic defects induced during the source/drain electrode deposition even though the damage due to the insulator formation was prevented with RT deposition. Also the kinetic energy of Er vapor is decreased by a collision with oxygen molecules. Fig. 2-39 summarize the melting points (T_m) and theoretical carrier

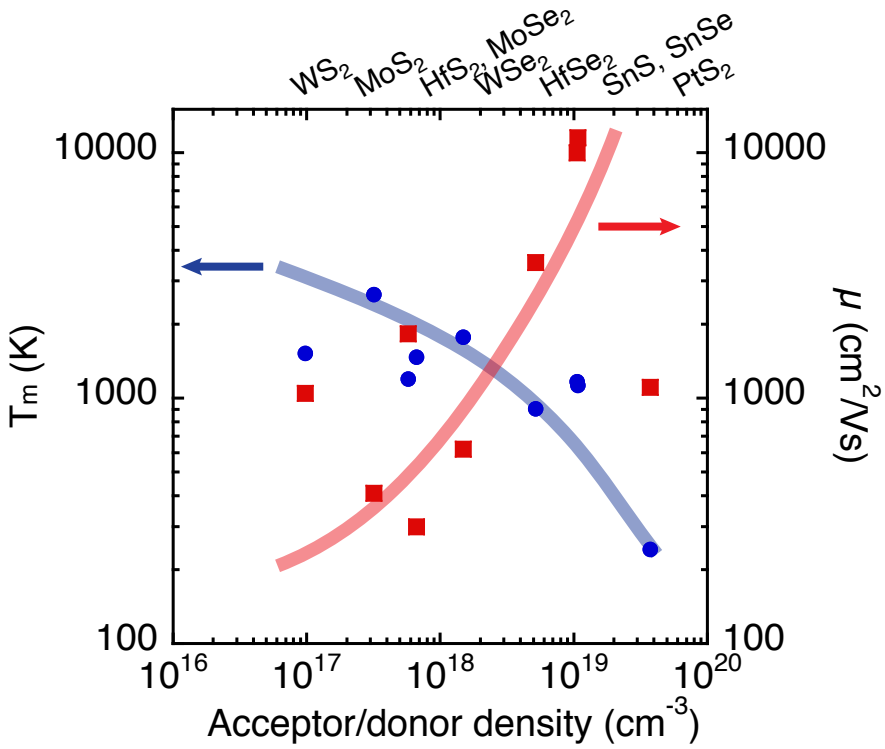

Figure 2-39: Melting point and theoretical carrier mobility versus donor/acceptor density.

mobility for variable 2D materials. With increasing the acceptor/donor density, the mobility tends to increase, while T_{m} decreases. In the case of monolayer SnS, T_{m} is 880°C [103], much lower than TMDCs, suggesting the relatively lower stability among 2D material family.

In order to minimize the damage during the deposition of source/drain metal, a gentle deposition method has been investigated. As shown in Fig. 2-40a, metal deposition was performed in the Ar atmosphere (P = 0.6 Pa). At P = 0.6 Pa, the mean free path is 1.19×10^{-2} m, enough smaller than the length of evaporator ($L \sim 0.25$ m). Fig. 2-40b shows I_{D}–V_{D} characteristics of ~5L-thick SnS with different ways of source/drain fabrication. Ni electrodes were deposited in vacuum at 4×10^{-4} Pa and in Ar (P = 0.6 Pa). The gentle deposition in Ar successfully increased the conductivity compared to the vacuum evaporation.

For further understanding of the electrical stability of 2D SnS, the effect of air exposure was investigated. Fig. 2-41 shows the time evolution of surface morphology

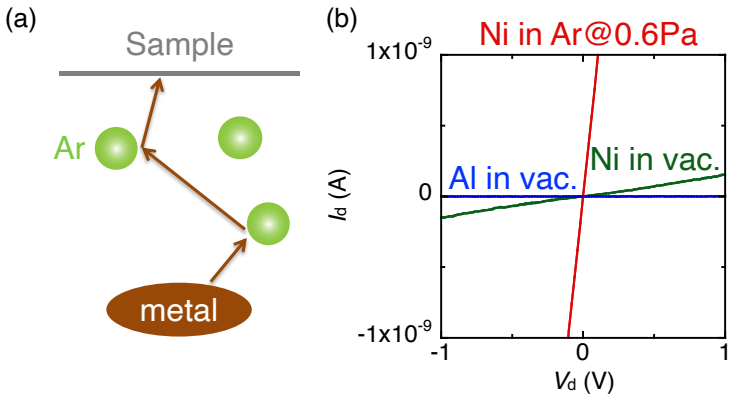

Figure 2-40: (a) Schematic view of metal deposition in Ar. (b) I_{d}–V_{d} characteristics.

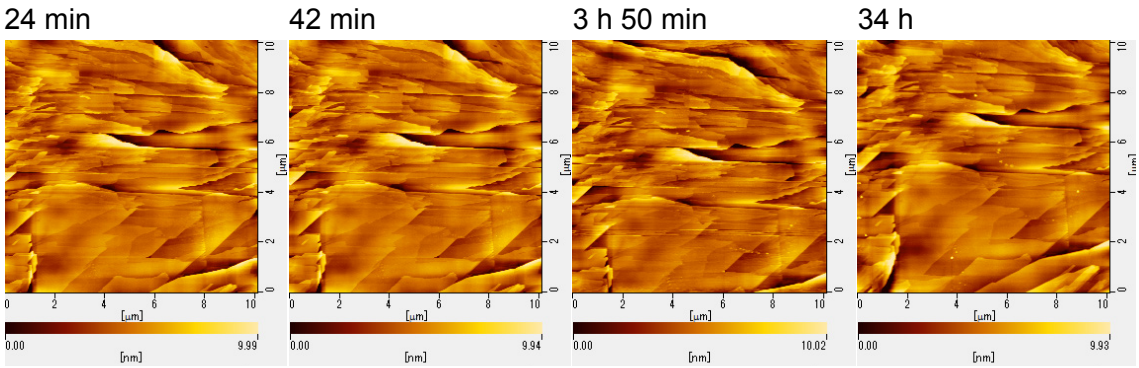

Figure 2-41: Time evolution of AFM image for the bulk SnS surface.

of bulk SnS mechanically exfoliated *via* a Scotch tape. The relative humidity was stabilized at around 27%. When the AFM measurements were performed 24 min to 34 h after the mechanical exfoliation, there was no surface modification. When the similar experiment is performed for BP, an analogous of SnS, it is well known that BP's surface immediately oxidized in air, resulting in the increase of RMS [90, 91]. These facts indicate that SnS is much more stable than BP.

To investigate the effects of air exposure on the electrical transport characteristics, I_{D}–V_{D} curves were measured befor and after the air exposure with relative humidity at 35% for 24 h. Note that the device structure was without a top-gate, thus only source/drain electrodes. Fig. 2-42a shows typical change of ∼5L-thick SnS. Even though the initial measurements in vacuum before the air exposure exhibit a good reproducibility of I_{D}–V_{D} curve, the conductivity dramatically decreased after the air exposure. Fig. 2-42b shows thickness dependence of the I_{D} value under $V_{\mathrm{D}} = 10$ mV.

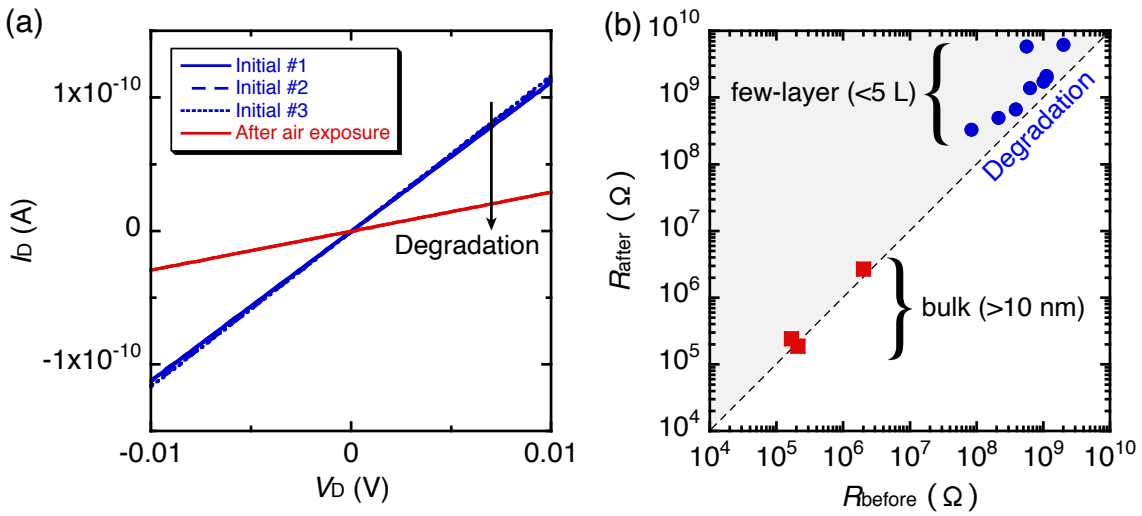

Figure 2-42: (a) I_D–V_D characteristics of bilayer SnS, and (b) change of resistance for bulk and few-layer SnS, measured in air before and after the air exposure for 24 h with the relative humidity at 35%.

For the bulk SnS thicker than 10 nm showed similar I_D before/after the air exposure, however, that of SnS thinner than 3 nm revealed a significant decrease by up to one order. These results indicate that the few-to-monolayer SnS is more unstable than bulk SnS, so that we have to carefully treat and measure the 2D SnS, and crucially a surface passivation is necessary to achieve high mobility and highly efficient piezoelectric generators or ferroelectric memories operating in the atmosphere.

Chapter 3

Mechanism of Piezoelectric Devices Based on 2D Materials

In this chapter, 2D piezoelectric materials are investigated toward the generator application. Firstly, the discussion starts from the fundamentals of piezoelectricity: origin, coefficients, and equivalent circuit for the piezoelectric generators. From the analysis on equivalent circuit, an equation for the out-put power will be extracted. Secondly, Schottky barrier height modulation is discussed as a key engineering to demonstrate the high-efficient nanogenerators based on 2D piezoelectric materials. A new methodology of metal transfer is proposed instead of deposition in order to form a Schottky contact at metal/piezoelectric interface. Finally, experimental results for the electromechanical responses are shown. A key finding is that the piezoresistive effect is also observed together with the piezoelectric effect. These two effects are characterized from the modulation of Schottky barrier height at source and drain. The dynamic electromechanical responses will be also discussed for the sensor and generator applications.

3.1 Fundamental of Piezoelectricity

3.1.1 Origin of Piezoelectricity

Piezoelectric materials are widely applied to the generator, microphone, and surface acoustic wave filter applications (Fig. 3-1). Not only for the electronic devices, the piezoelectric effect also exists in human body: bones [168]. The piezoelectric effect originate from the ionic displacement in the non-centrosymmetric materials under an external strain, as shown in Fig. 3-2. Also, the piezoelectric can deform with applying electric field. The former is called as direct piezoelectric effect, and the latter is converse piezoelectric effect. A similar phenomenon can be observed in the flexoelectricity, which does not require the non-centrosymmetry [169, 170].

Fig. 3-2 shows the displacements of each ions in $BaTiO_3$ at room temperature. When a positive (Ti^{4+}, Ba^{2+}) ions and negative ion (O^{2-}) are displaced like as Fig. 3-2, the direction of polarization is defined as a vector from negative to positive charge. The electric displacement for the dielectric materials is

$$D = \varepsilon_0 E + P \tag{3.1}$$

$$= \varepsilon_0 \varepsilon_r E \tag{3.2}$$

where E is the electric field, and P is the polarization charge. Eq. 3.1 can be

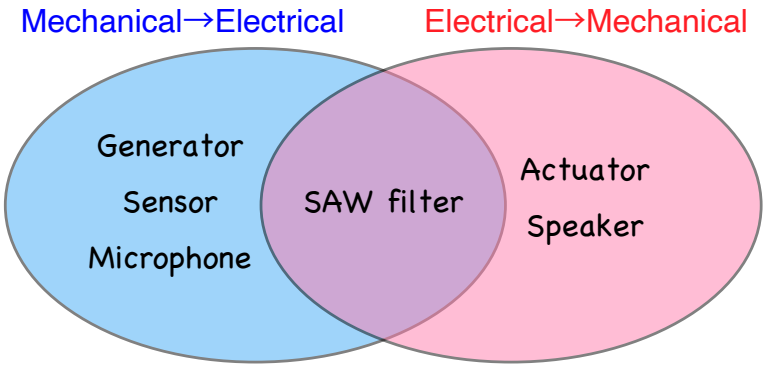

Figure 3-1: Applications of piezoelectric materials.

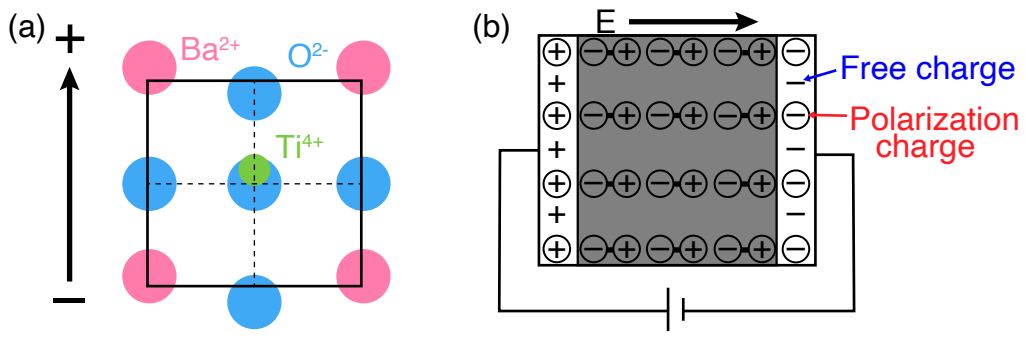

Figure 3-2: Origin of piezoelectricity and the definition of polarization direction ($BaTiO_3$).

transformed as

$$E = \frac{D - P}{\varepsilon_0} \tag{3.3}$$

This equation means that a net electric field is formed with subtracting the polarization charge P form the total amount of charge D.

3.1.2 Piezoelectric Constants

The piezoelectric effect includes both electrical and mechanical properties: the electric displacement D, the electric field E, strain S, and stress T. Firstly, a non-piezoelectric dielectric materials is assumed. Under $S = 0$ or $T = 0$, the electric displacement is proportional to the electric field,

$$\delta D = \frac{\partial D}{\partial E}\delta E = \varepsilon \delta E \tag{3.4}$$

where ε is the dielectric constant. Note that the value of ε will different for the different boundary conditions, $S = 0$ or $T = 0$. In such a manner, there is a relationship:

$$\delta S = \frac{\partial S}{\partial T}\delta T = s \delta T \tag{3.5}$$

where s is the elastic compliance.

For the piezoelectric materials, the piezoelectric basic equation in d-form is written

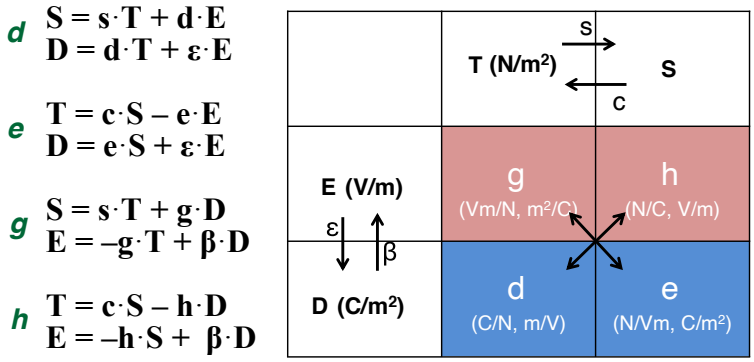

Figure 3-3: Basic equations of piezoelectric materials.

as follows:

$$\delta S = \frac{\partial S}{\partial T}\delta T + \frac{\partial S}{\partial E}\delta E = s^E \delta T + d\delta E \tag{3.6}$$

$$\delta D = \frac{\partial D}{\partial T}\delta T + \frac{\partial D}{\partial E}\delta E = d\delta T + \varepsilon^T \delta E \tag{3.7}$$

where d is the piezoelectric coefficient;

$$d = \frac{\partial S}{\partial E} = \frac{\partial D}{\partial T} \tag{3.8}$$

These equation is called as a basic piezoelectric equation in d-form. there are also other forms with ε, β (the inverse dielectric constant), s, and c (the elastic stiffness). A summary of basic equations are summarized in Fig. 3-3. The d-form will be exclusively focused in the discussion below.

In three dimensional structure, the basic equation is expressed as follows:

$$\begin{pmatrix} S_1 \\ S_2 \\ S_3 \\ S_4 \\ S_5 \\ S_6 \end{pmatrix} = \begin{pmatrix} s_{11}^E & s_{12}^E & s_{13}^E & s_{14}^E & s_{15}^E & s_{16}^E \\ s_{21}^E & s_{22}^E & s_{23}^E & s_{24}^E & s_{25}^E & s_{26}^E \\ s_{31}^E & s_{32}^E & s_{33}^E & s_{34}^E & s_{35}^E & s_{36}^E \\ s_{41}^E & s_{42}^E & s_{43}^E & s_{44}^E & s_{45}^E & s_{46}^E \\ s_{51}^E & s_{52}^E & s_{53}^E & s_{54}^E & s_{55}^E & s_{56}^E \\ s_{11}^E & s_{12}^E & s_{13}^E & s_{14}^E & s_{15}^E & s_{16}^E \end{pmatrix} \begin{pmatrix} T_1 \\ T_2 \\ T_3 \\ T_4 \\ T_5 \\ T_6 \end{pmatrix} + \begin{pmatrix} d_{11} & d_{21} & d_{31} \\ d_{12} & d_{22} & d_{32} \\ d_{13} & d_{23} & d_{33} \\ d_{14} & d_{24} & d_{34} \\ d_{15} & d_{25} & d_{35} \\ d_{16} & d_{26} & d_{36} \end{pmatrix} \begin{pmatrix} E_1 \\ E_2 \\ E_3 \end{pmatrix} \tag{3.9}$$

$$\begin{pmatrix} D_1 \\ D_2 \\ D_3 \end{pmatrix} = \begin{pmatrix} d_{11} & d_{12} & d_{13} & d_{14} & d_{15} & d_{16} \\ d_{21} & d_{22} & d_{23} & d_{24} & d_{25} & d_{26} \\ d_{31} & d_{32} & d_{33} & d_{34} & d_{35} & d_{36} \end{pmatrix} \begin{pmatrix} T_1 \\ T_2 \\ T_3 \\ T_4 \\ T_5 \\ T_6 \end{pmatrix} + \begin{pmatrix} \varepsilon_{11}^T & \varepsilon_{12}^T & \varepsilon_{13}^T \\ \varepsilon_{21}^T & \varepsilon_{22}^T & \varepsilon_{23}^T \\ \varepsilon_{31}^T & \varepsilon_{32}^T & \varepsilon_{33}^T \end{pmatrix} \begin{pmatrix} E_1 \\ E_2 \\ E_3 \end{pmatrix} \quad (3.10)$$

These equation might be complicated to analysis, however, they can be simplified with considering the crystal symmetry in a practical case. For example,

$$S_3 = s_{33}^E T_3 + d_{33} E_3 \quad (3.11)$$

$$D_3 = d_{33} T_3 + \varepsilon_{33}^T E_3 \quad (3.12)$$

for $BaTiO_3$. In ceramic and polymer piezoelectric materials, usually d_{33}, d_{31}, and d_{14} are considered, while d_{11} is important for 2D piezoelectric materials (e.g. SnS and MoS_2).

Fig. 3-4 shows the relationship between the relative permittivity ε_r and the piezoelectric coefficients d, g for PZT, quartz and $BaTiO_3$ [171]. In the long history of piezo-ceramics, most of efforts forcused on controlling ε_r. There are tradeoff between d and g, which means that it is difficult to increase both d and g with the improvement of dielectric constants. This is because d and g are ideally proportional to $\sqrt{\varepsilon}$ and $\sqrt{1/\varepsilon}$, respectively. From Eq. 3.8, d can be expressed with using the dielectric constant ε, the Young's modulus σ, the lattice strain ϵ:

$$d = \frac{\partial D}{\partial \sigma} = \frac{\varepsilon \partial E}{\sigma \partial \epsilon} \quad (3.13)$$

Although large ε was necessary for large d, this is not true for SnS. As shown in Fig. 1-9, for monolayer SnS, both d and g show outstanding values owing to the structural flexibility (small σ) and relatively small relative permittivity $\varepsilon_r \sim 10$ [172].

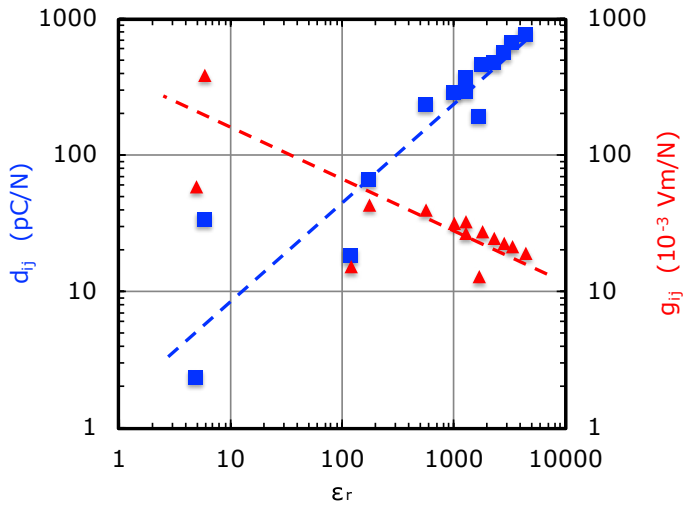

Figure 3-4: Tradeoff between piezoelectric d and g constant for PZT, PVDF, and quartz [171].

Assuming $T = 0$ (no external force), Eq. 3.6 and 3.7 can be

$$S = dE \tag{3.14}$$

$$D = \varepsilon^T E \tag{3.15}$$

Total input energy U_{in} is quall to the electrical energy,

$$U_{in} = \int_0^D EdD = \int_0^D \frac{D}{\varepsilon^T} dD = \frac{D^2}{2\varepsilon^T} = \frac{\varepsilon^T E^2}{2} \tag{3.16}$$

On the other hand, output mechanical energy is written as,

$$U_{out} = \int_0^S TdS = \int_0^S \frac{S}{s^E} dS = \frac{S^2}{2s^E} = \frac{s^2 E^2}{2s^E} \tag{3.17}$$

Then the electromechanical coupling factor k can be defined as,

$$k^2 = \frac{U_{out}}{U_{in}} = \frac{d^2 E^2 / 2s^E}{\varepsilon^T E^2 / 2} = \frac{d^2}{\varepsilon^T s^E} \tag{3.18}$$

This mean the energy conversion efficiency between electrical and mechanical energies.

3.1.3 Equivalent Circuit of Piezoelectric Devices

An equivalent circuit for the piezoelectric nanogenerator can be extracted, starting from Eq. 3.6 and 3.7 [173]. Under the boundary condition $T = 0$, as shown in Fig. 3-5,

$$D = \varepsilon^T E = \left(\varepsilon^S + \frac{d^2}{s^E}\right) E \tag{3.19}$$

The total charge Q is

$$Q = abD = ab\left(\varepsilon^S + \frac{d^2}{s^E}\right) E = \varepsilon^S \frac{ab}{l} El + ab\frac{d}{ls^E} El \tag{3.20}$$

$$= \varepsilon^S \frac{ab}{l} V + \frac{d^2(ab)^2}{(s^E)^2 l^2} \frac{s^E l}{sb} V = \left(C_d + A^2 \frac{1}{K}\right) V \tag{3.21}$$

where

$$K = \frac{1}{s^E}\frac{ab}{l} \quad : \text{spring constant} \tag{3.22}$$

$$El = V \tag{3.23}$$

$$C_d = \varepsilon^S \frac{ab}{l} \quad : \text{damper capacitor} \tag{3.24}$$

$$A = \frac{dab}{s^E l} \quad : \text{force factor} \tag{3.25}$$

Eq. 3.21 means that the piezoelectric device, which is composed of electrical and mechanical prats, can be expressed in an simple electrical circuit, as shown in Fig. 3-6. In this equivalent circuit, the maximum out-put power can be extracted as [173, 174],

$$P_{max} = \frac{V^2}{R_L} = \frac{\omega AdT)^2}{1 + (\omega C_d R_L)^2} \propto d \times g \tag{3.26}$$

Thus, both d and g is necessary to be large for the high-efficiency piezoelectric generators. In this perspective, SnS is a promising candidate because of its large d and g (Fig. 1-9).

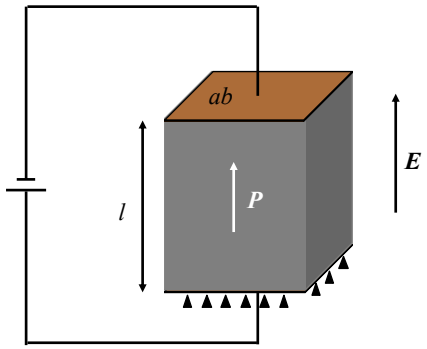

Figure 3-5: Schematic illustration of piezoelectric device under the external electric field.

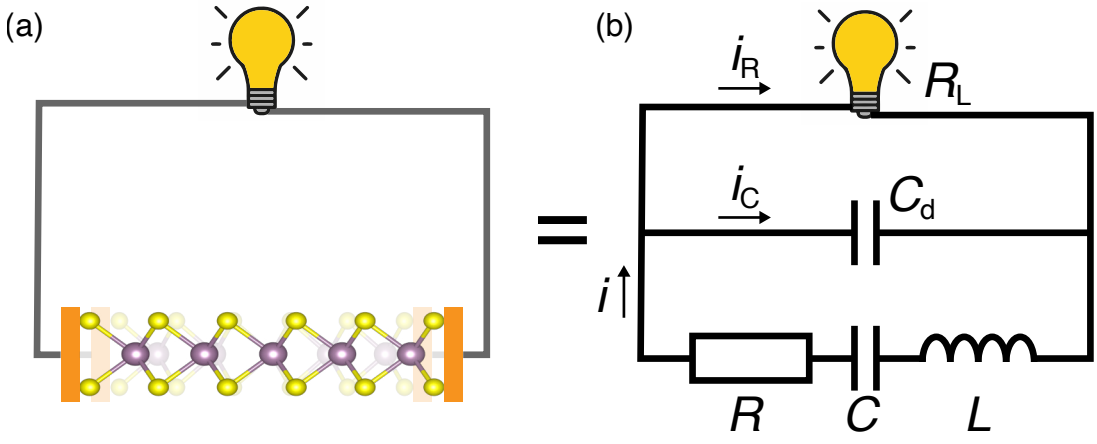

Figure 3-6: Equivalent Circuit of Piezoelectric Devices.

Table 3.1: Comparison between piezoelectricity and piezoresistivity [175].

Piezoresistive effect	Piezoelectric effect
• Linear IV curve	• Non-linear "rectifying" IV curve
• Symmetric effect in end-contacts	• Asymmetric effect on end-contacts
• No polarity	• With strong polarity
• "Volume" effect	• "Interface" effect
• No stitch function	• Switch function

3.1.4 Literature Review of MoS_2 Piezoelectric Devices

Fig. 3-7 shows the first demonstration of piezoelectricity in monolayer MoS_2 by Wu *et al*. [27]. They used the Pd as electrodes in order to create Schottky contacts at the metal/MoS_2 interface. Considering that MoS_2 is a semiconductor, carrier injection from electrode into the channel is crucial for accumulating the polarization charges at the interface. Assuming the ideal condition: the Schottky barrier height (SBH) at source and drain is same under no strain (Fig. 3-7a). When an external strain is applied into the monolayer, polarization will appear at the interface, resulting in an asymmetric change of SBH at source/drain. SBH increase at drain, and decrease at source in this case. This characteristic can be observed in the I_D–V_D curve under the static strains. As shown in Fig. 3-7b, for monolayer, the resistance changes asymmetrically in the negative and positive drain bias. This rectification means that the contact resistance is different at source and drain as a result of piezoelectric charges. In contrast, for bilayer MoS_2, I_D–V_D changes symmetrically under a strain. The resistance decrease with increasing the strain, which is caused by the piezoresistive effect in the channel region. These characteristics are summarized in Table 3.1.

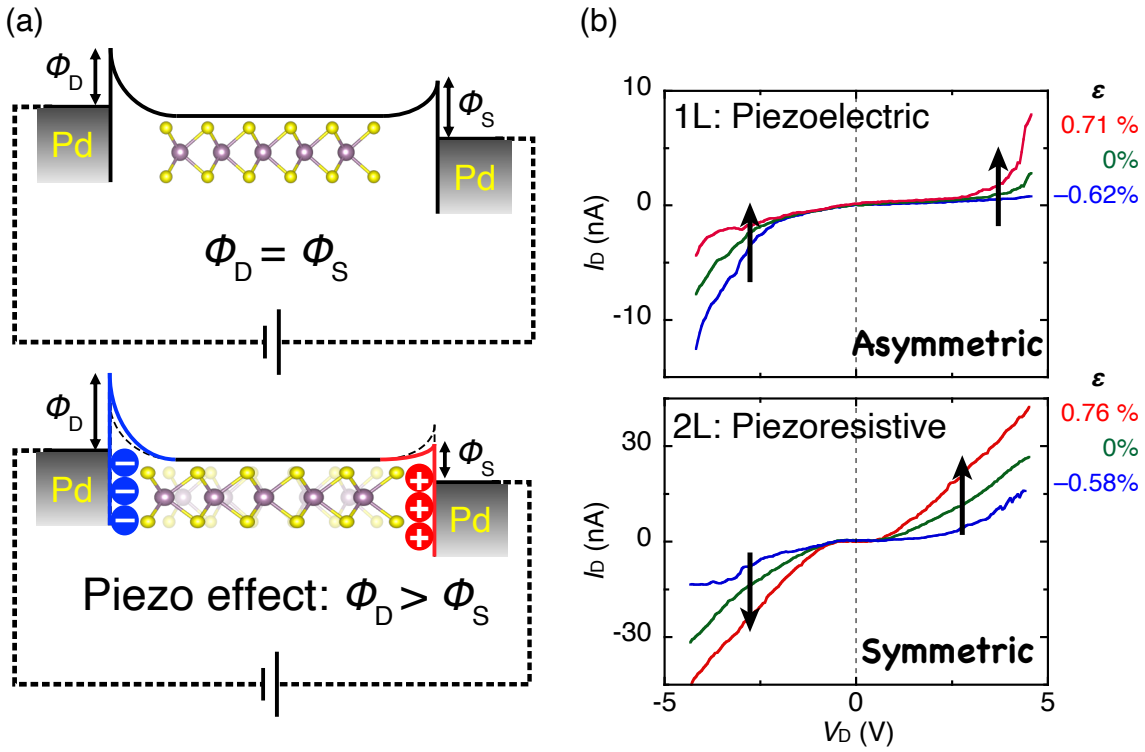

Figure 3-7: Experimental demonstration of piezoelectric device based on 2D MoS_2. (a) Schottky barrier height modulation. (b) Static I_D–V_D measurement for mono- and bi-layer MoS_2 [27].

3.2 Interface Engineering at Metal/Semiconductor Interface

Fig. 3-8 shows a temperature dependence of MoS_2 FET at 100–400 K. In the high temperature region, the conductivity is high even under the depletion region, which means a thermionic emission current. With decreasing the temperature, the resistance is very high unless the assist of positive gate bias. At low temperature, the voltage drop only occurs at the metal/MoS_2 contact, and a flat band is formed in the channel region. These results indicate that the transport in 2D MoS_2 is dominated at the contact.

Among the 2D materials, MoS_2 is relatively stable, chemically and thermally. However, not a few defects are induced when we deposit a metal to fabricate the electrode. In Fig. 3-9, a cross-sectional TEM image is observed for the metal deposited MoS_2. Even for the "stable" MoS_2, defects, glassy region, and metal diffusion into MoS_2 are created, resulting in a strong Fermi level pinning (FLP). For MoS_2, the S factor is known to be ~ 0.1 [113, 176], which is smaller than Si and Ge [177].

In order to prevent the FLP, Liu *et al*. utilized a metal transfer method in the same manner of transfer method for layered materials. Strikingly, very steep, completely defect-free, interface is formed as shown in Fig. 3-9. The S factor for the metal transfer was determined to be 0.96. Even now, it is a mystery the origin of FLP in metal/2D system, disorder induced gap state (DIGS) [178], metal-induced gap states (MIGS) [179], or anything else; though the metal transfer method will reduce both DIGS and MIGS owing to the defect-free and vdW gap.

In this work, the metal transfer method is investigated for the piezoelectric characteristic in MoS_2 as a model material.

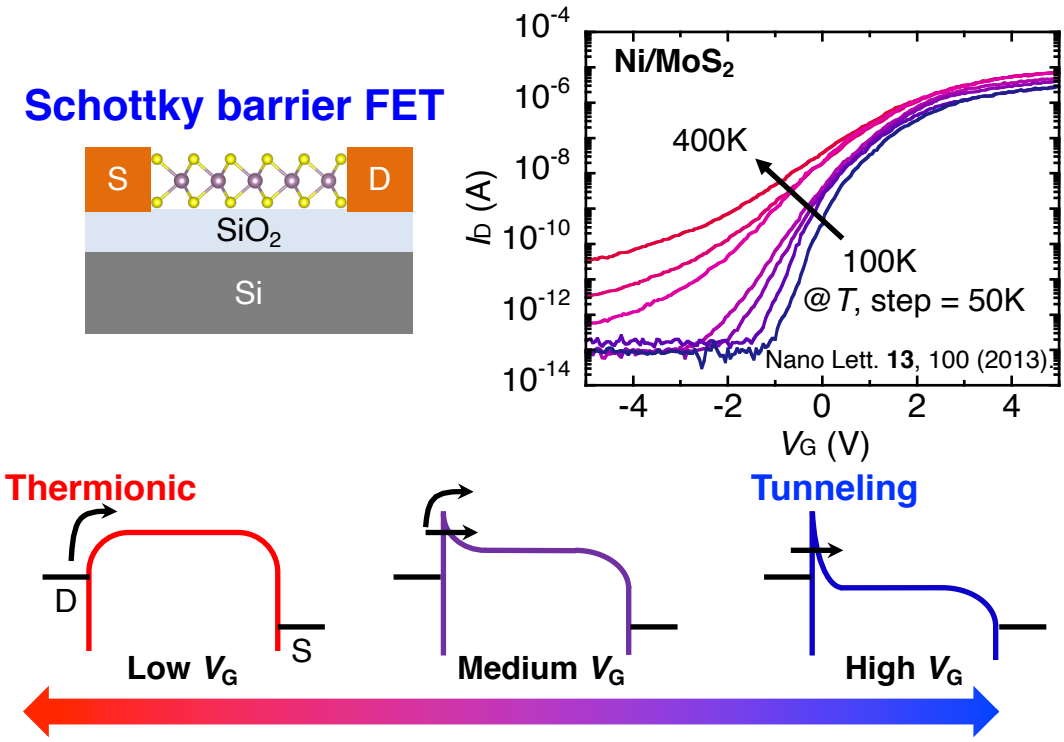

Figure 3-8: Electrical transport in 2D materials is contact limited [113].

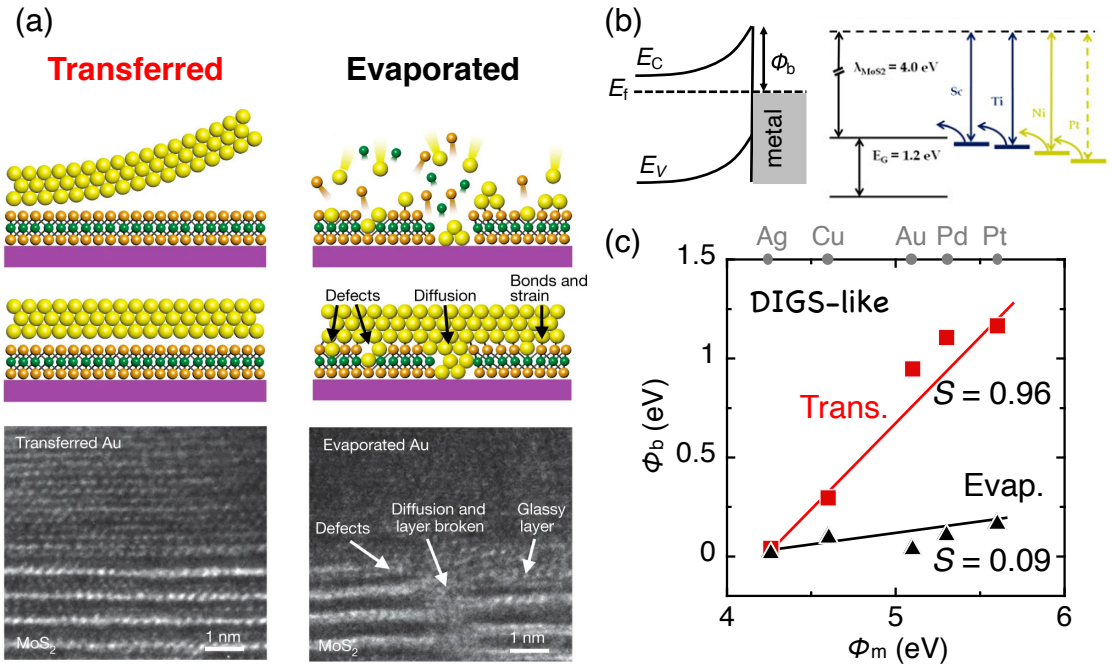

Figure 3-9: Metal deposition versus transfer for MoS_2 [176]. (a) Illustrations and TEM images for metal/MoS_2 interface. (b) Strong Fermi level pinning for MoS_2 [113]. (c) Depinning of Fermi level by metal transfer method [176].

3.3 Experimental Methods of Electromechanical Characterization

3.3.1 System Setup

For the sake of electromechanical characterization, two kinds of measurement systems were built-up. Firstly, a picture of static electromechanical measurement system is shown in Fig. 3-10. In this system, I_D–V_D and I_D–V_G characteristics were investigated with bending the sample by vise. The sample and probes were placed in an electromagnetic shield to reduce unexpected signals. The relative humidity was reduced to 40% by a standard dehumidifier in order to prevent the sample oxidation assisted by a Joule heating during the transport measurement. The other measurement system is designed for a measurement under a dynamic strain, as shown in Fig. 3-11. Instead of linear actuator, rotated actuators was used to apply a strain uniformly on the substrate. Also, the present system enable it to switch tensile/compressive strains easier than the linear actuator. To minimize background noises, electromagnetic shield was used. Without the shield, the noises exceed several-hundred pA (Fig. 3-12a). This value is has to be reduced to several pA, given that the maximum output from single device of monolayer MoS_2 and WSe_2 are several-tens pA [27, 47]. When the shield is used, the noise was successfully reduced below ~5 pA (Fig. 3-12d).

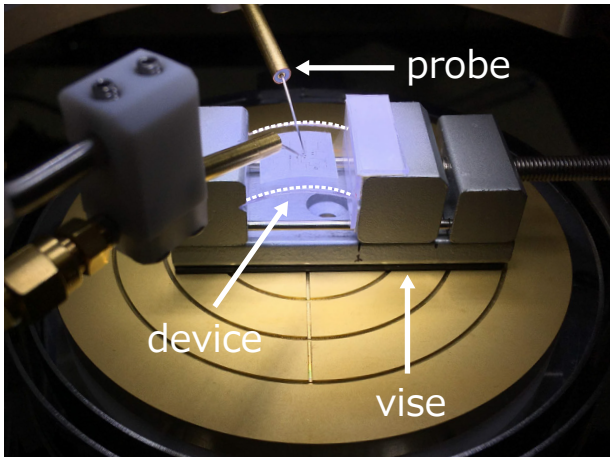

Figure 3-10: Electrical measurement under static strains.

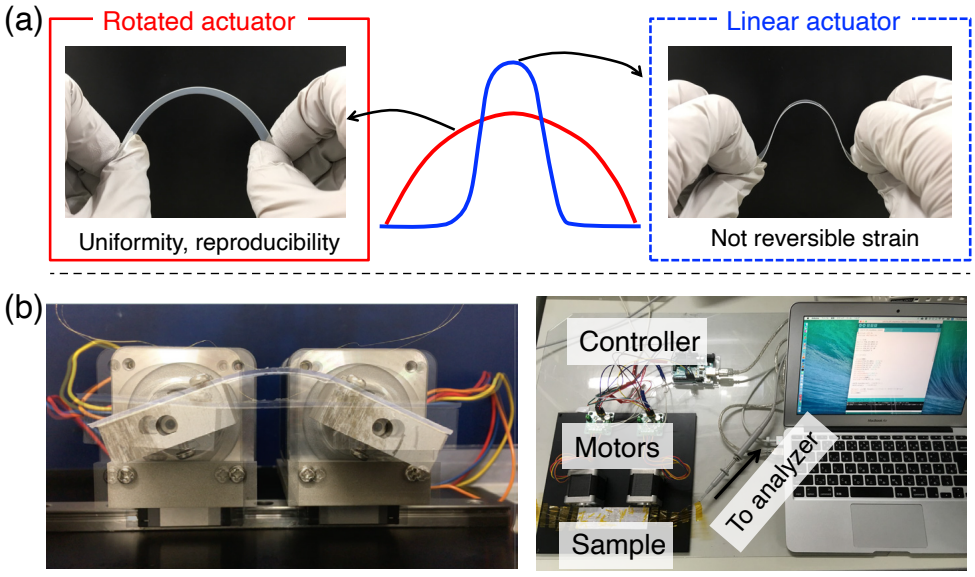

Figure 3-11: Electrical measurement setup for electromechanical response under dynamic strain.

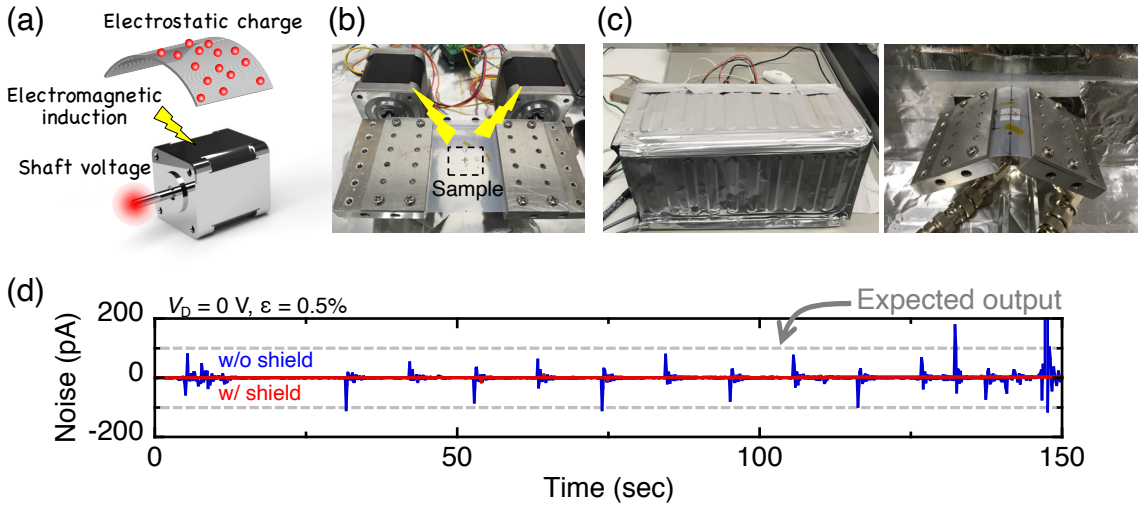

Figure 3-12: Reducing background noise. (a) Variety of causes of the noise. Measurement setup (b) without and (c) with electromagnetic shield and earth wires. (d) Back ground noise applying a repeated external strain.

3.3.2 Fabrication of Flexible Devices

The mica substrate, which is used for the 2D growth of SnS as described in Section 2.4, is also a 2D layered materials. When the mica thickness is thinned, it becomes flexible and thus can be directly applied to a flexible device without any process of SnS transfer from mica to other platforms. After the growth of 2D SnS on mica substrate (600 µm thickness), mica was thinned to 10–50 µm, which is flexible and easy to treat by tweezers. To thin the mica below 50 µm, a knife was used to exfoliate the top surface with ∼100 µm thickness, followed by Scotch tape exfoliations for a few times to exfoliate the bottom mica. The mica thickness was measured by micrometer. The electrodes was fabricated by a standard electron beam lithography and metal deposition. Initial electronic transport characteristics was measured in vacuum at 10^{-3}–10^{-2} Pa to compare with the characteristics in the atmosphere, where the electromechanical measurements are performed. Some effects of air are expected such as a material degradation due to oxidation, charge transfer from the adsorbed molecules, and mechanical destruction during bending.

In order to apply a strain in SnS and mica, PET substrate was used (Fig. 3-13). They were stacked with commercially available double sided tape after fabricating electrodes. The strain ε applied in SnS was assumed to be

$$\varepsilon = \pm d/2r \tag{3.27}$$

where d is the thickness of mica, r is the curvature radius of mica substrate. When the substrate is bent as shown in Fig. 3-13b, tensile and compressive strains are applied on the top and bottom sides, respectively; they can be reversed when the substrate is bent toward the opposite direction (Fig. 3-13a). Here, a strain on the PET surface is assumed to be totally relaxed due to the existent of soft double sided tape. The stress was applied by a vise, as shown in Fig. 3-14. The curvature radius r was measured with the arch-shaped cross-sectional image of the flexible device, as shown in Fig. 3-14. The image was analyzed in the digitizer software (PlotDigitizer X, macOS) to extract the shape of bent substrate. This digitized curve was fitted

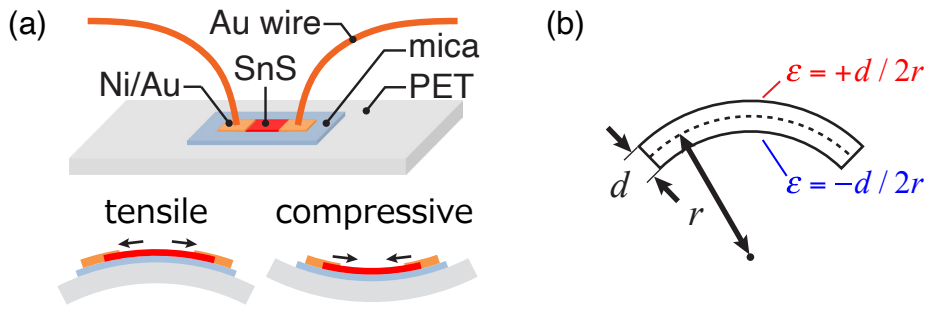

Figure 3-13: Schematic views of flexible device.

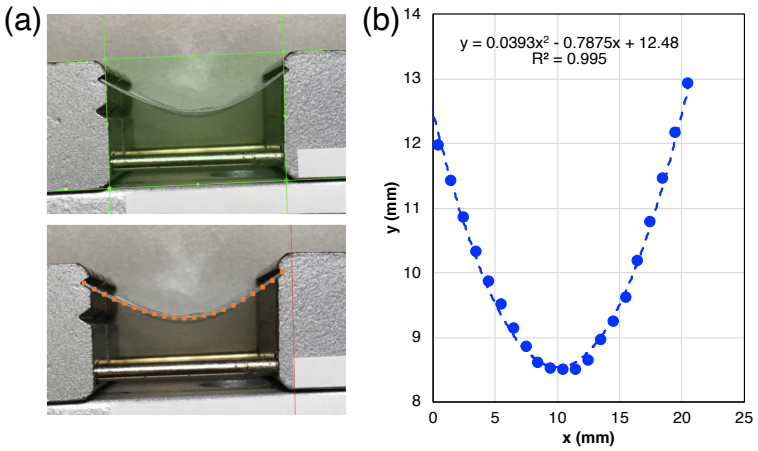

Figure 3-14: Estimation of applied strain. (a) Desitization of the curvature. (b) Curve fitting with quadratic function.

with parabolic function written as,

$$f(x) = ax^2 + bx + c \tag{3.28}$$

The curvature radius $r(x)$ at the point of $(x, f(x))$is calculated by the following equation:

$$r(x) = \frac{(1 + f'(x)^2)^{\frac{3}{2}}}{|f''(x)|} \tag{3.29}$$

Especially at the vertex of the parabola, where the SnS is located, the curvature radius is simplified to be $r(-b/2a) = 1/|2a|$.

3.4 Piezoresistivity in 2D Materials

In this section, electromechanical response of 2D SnS is studied. Especially, the piezoresistive strain gauge is demonstrated as a preliminary step for the piezoelectric application. As discussed in Section 3.1, piezoelectricity and piezoresistivity co-exist when the piezoelectric material is strained. Especially, for the piezoelectric 2D materials SnS and MoS_2, piezoresistivity should be more effective than the conventional piezo-ceramics because they are semiconductors. The purposes of this section are;

1. Demonstration of piezoresistive strain gauge to verify the operation of electromechanical measurement system and flexible device.

2. Characterization of piezoresistivity in 2D SnS to distinguish it from the piezoelectricity.

The flexible devices were fabricated with few-to-monolayer SnS, as described in Section 3.3.2. In this section, Ni was used as a contact metal for SnS because it has an ohmic contact and preferable to observe the change of resistivity caused by the piezoresistivity. Actually, Schottky barrier height at the metal/piezoelectric contact is critical to observe the piezoelectric charge accumulated at the contact, as will be discussed later (in Section 3.5). Moreover, modulating Schottky barrier height is also important for ferroelectric devices, as discussed in Chapter 4.

3.4.1 Optical Characterization of Strained SnS

After fabricating source/drain electrodes for ∼10 layers SnS, μ-Raman spectrum was measured at the channel region (Fig. 3-15a). The electrodes were designed along the armchair direction, identified by a polarized Raman measurement, as shown in Fig. 3-15b,c (see details in Section 4).Fig. 3-16 shows a typical Raman spectrum before and after applying a tensile strain at 0.5%. Under a flat condition ($\varepsilon = 0\%$), Raman peaks were observed at around 160 and 230 cm^{-1}, which agree with the Raman modes of bulk SnS along out-of-plane and armchair directions, respectively [107]. The other peaks at around 140 and 190 cm^{-1} are from the substrate. When the tensile strain

was applied along the armchair direction, Raman peaks at 160 and 230 cm^{-1} shifted toward positive and negative, respectively; indicating that tensile strain was applied along the in-plane direction, while compressive strain was applied along the out-of-plane direction. This result suggest that the crystal structure transformed elastically like as the inset of Fig. 3-16.

3.4.2 Piezoresistive Response under a Static Strain

To investigate the pirzoresistive response of bulk SnS, static I_D–V_D measurements were performed in air under an external strain applied by the vice. Fig. 3-17a shows I_D–V_D characteristics of ∼10 layers SnS under tensile and compressive strains ±1.7%. When the tensile strain was applied, the conductivity decreased indicating the increase of resistivity. In contrast, the resistivity decreased under the compressive strain. These results agree with the theoretical estimation of the bandgap against the lattice strain; the bandgap increases with increasing the strain in the strain region of ±3% (Ref. [180]). Interestingly, the sensitivity under the compressive was much larger than the tensile strain. In Fig. 3-17, a systematic strain dependence of I_D at the fixed drain bias $V_D = 0.1$ V. Although, in the negative strain region (compressive), the conductivity linearly decreased with increasing the strain; in the positive region, the current saturated at around 590 nA. This significant discrepancy was not observed for metal strain gauge, which was strained in the same vice as for SnS and revealed almost the same sensitivity at tensile/compressive strains (see details in Section 3.3). This difference is probably owing to a smaller influence of the tensile strain on the electronic band structure of SnS due to a decreased charge transfer from Sn to S, compared to the compressive strain [180].

3.4.3 Anisotropy of Gauge Factor in SnS

In order to investigate the effect of lattice orientation on the piezoresistive response, two sets of source and drain electrodes were orthogonally aligned, as shown in Fig. 3-18. The orientation was determined before designing the electrodes pattern, from a

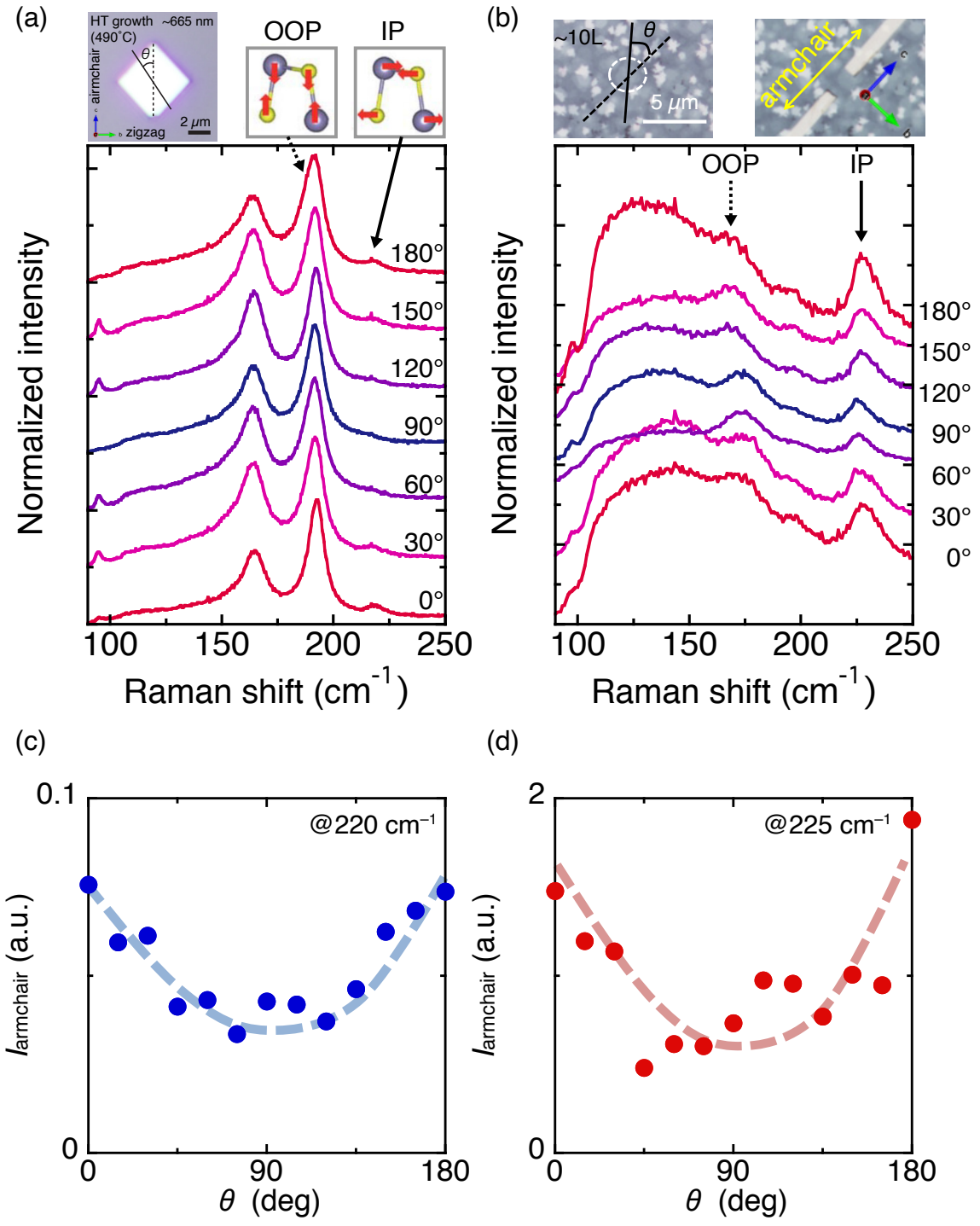

Figure 3-15: Angular dependence of Raman spectra from (a,c) bulk (∼665 nm) and (b,d) ∼10 layers SnS.

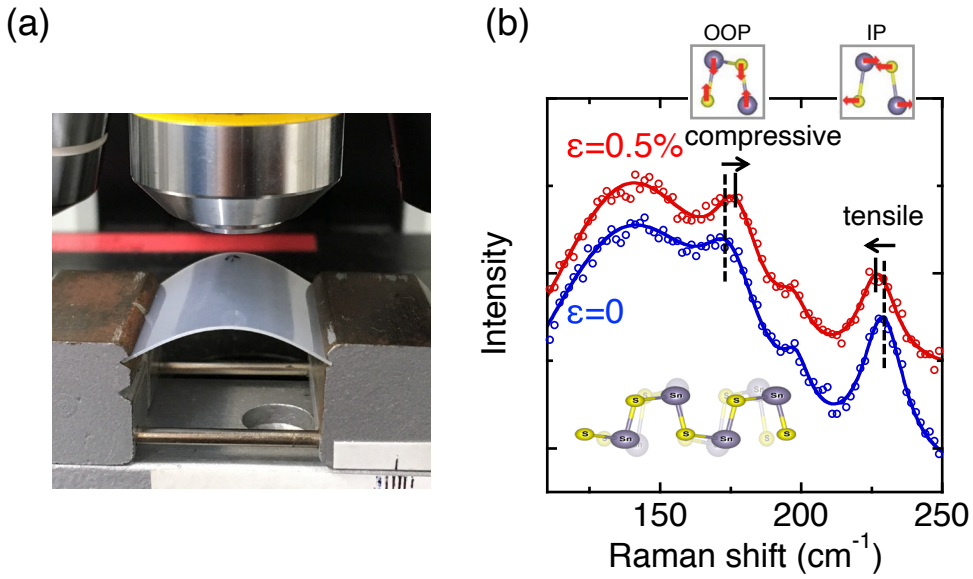

Figure 3-16: Typical Raman spectrum from ∼10 layers SnS with strains $\varepsilon = 0$ and 0.5%.

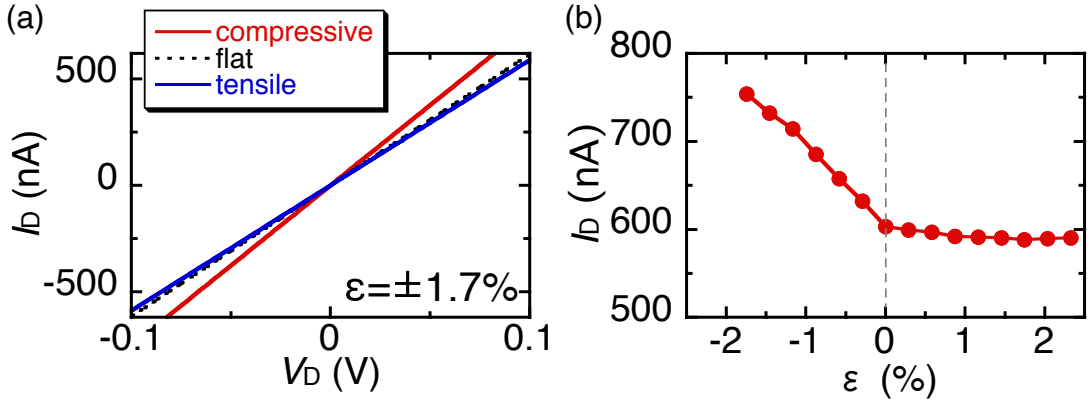

Figure 3-17: Piezoresistive response of ∼10 layers SnS under tensile and compressive strains. (a) I_D–V_D. (b) I_D value at $V_D = 0.1$ V.

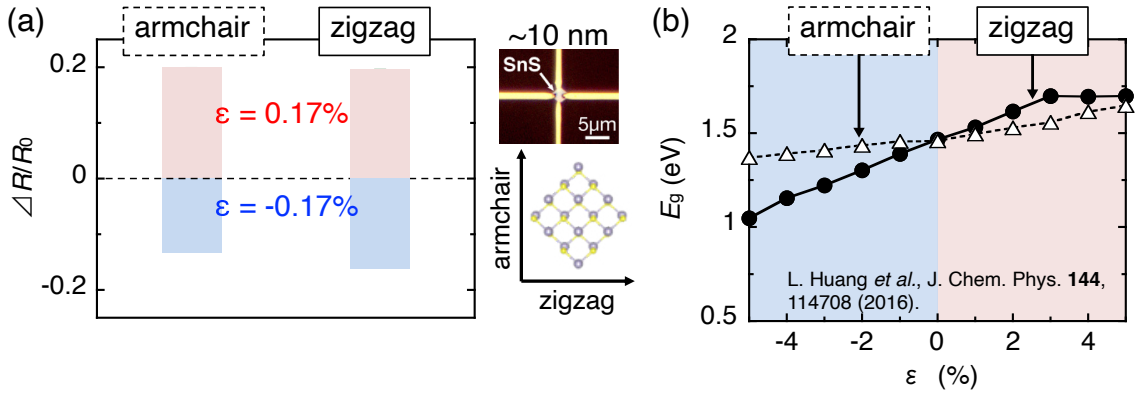

Figure 3-18: Anisotropy of piezoresistivity in bulk SnS, along armchair and zigzag directions: (a) experiment in this work and (b) theory in Ref. [180].

distorted diamond shape of SnS crystals reflecting the atomic structure. The I_D–V_D characteristic was measured in air under tensile and compressive strains at ±0.17%. The piezoelectric sensitivity was quantified with $\Delta R/R_0$, where R_0 is an initial resistivity and ΔR is a change of resistivity after applying strain. For 1∼10 nm SnS, $\Delta R/R_0$ was approximately 0.2 both for armchair and zigzag direction under the tensile strain, while larger value was obtained along zigzag direction under the compressive strain. This is probably because of the anisotropy of band structure dependence on the lattice strain. In Ref. [180], the relationship between bandgap E_g and lattice strain ε; stronger dependence was determined along the zigzag direction than the armchair direction due to an anisotropic in-plane elastic stiffness.

3.4.4 Gauge Factor

Gauge factor (GF) is usually used to compare the strain gauges between different materials and measurement conditions. GF is defined as follows:

$$GF = \frac{\Delta R/R_0}{\varepsilon} \tag{3.30}$$

Table 3.2: Calculated Poisson's ration of monolayer SnS [181].

	ν_{21}	ν_{31}	ν_{12}	ν_{32}	ν_{13}	ν_{23}
monolayer	0.097	0.277	0.025	0.861	0.067	0.419

When the crystal structure is regarded to be isotropic, Eq. 3.30 can be written as the total of geometric effect and resistivity effect.

$$GF = \frac{1}{\varepsilon}\left(\frac{\Delta L}{L} - \frac{\Delta A}{A} + \frac{\Delta \rho}{\rho}\right) \tag{3.31}$$

$$= 1 + 2\nu + \frac{\Delta\rho/\rho}{\varepsilon} \tag{3.32}$$

where L is the channel length, A is the cross-sectional area of channel, ρ is the resistivity, and ν is the Poisson's ratio. The GF can be approximated to be the geometric terms $GF = 1 + 2\nu$ for some metals, whose piezoresistive effect is very small. This geometric piezoresistivity is very small because ν is usually below 0.5 for most of metals, thus the GF is limited below 2. For Si, ν is 0.28 comparable to metals, though the GF exceeds 200 owing to the resistivity effect $\Delta\rho/\rho$. For the piezoelectric material, GF sometimes includes not only the piezoresistive effect, but also the piezoelectric effect [27], though the later effect is absent in this measurement because the bulk SnS is not a piezoelectric.

Based on the relationship between strain and resistance, the GF are determined. From the results of bulk SnS as shown in Fig. 3-17, the GF was determined to be 12.4 and 1.3 for compressive and tensile strains, respectively. Table 3.2 shows calculated Poisson's ratios for bulk and monolayer SnS with x, y, z axises along out-of-plane, zigzag, and armchair directions, respectively. The value of ν is 0.861 at maximum, thus the geometric effect contribute to the GF as large as 1–2. The large GF in the compressive region is probably owing to the change of resistivity $\Delta\rho/\rho$.

For further understanding, thickness dependence was investigated. Although the I_{D}–V_{D} curve of bulk SnS (>10 layers) was measured in air, that was measured in vacuum to minimize the surface modification because few-to-monolayer SnS electrically

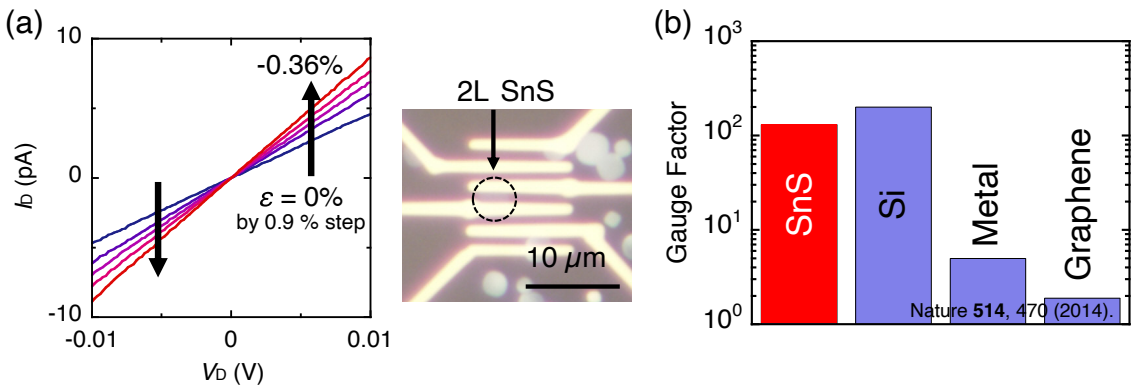

Figure 3-19: Typical piezoresistive characteristic of few-to-monolayer SnS. (a) I_D–V_D curves under different strains. (b) Gauge factor for SnS and other materials [27].

measured in air is easy to be degraded in air (Fig. 2-42). For each measurements, SnS surface was cleaned by IPA solution to eliminate the H_2O molecules physically absorbed on it. In Fig. 3-19, I_D–V_D curves under different strains are shown. The strain was changed systematically from 0 to 0.36% of compressive strain, which has a larger effect on the electrical properties than tensile strain [180]. Similar with bulk SnS, resistivity of bilayer SnS decreased under the compressive strain. The maximum GF $\sim$ 130 was obtained at bilayer, which is much larger than metals and graphene sheet, and comparable to crystal Si. This improvement from the bulk SnS as discussed above (see details in Section 3.4.2), should be owing to the single grain of SnS crystal rather than multi-grained bulk SnS (Fig. 3-15). Fig. 3-20a shows strain versus I_D at V_D = 10 mV for different few-to-monolayer SnS (N = 7). The gauge factor varied from 51 to 130. This dispersion is probably caused by the crystalline quality and number of layers. In Fig. 3-20 shows the relationship between GF and SnS thickness. In the region between monolayer to trilayer, the maximum GF was 131, and comparable value was also obtained at 13.1 nm (GF = 122). In this experiment, the lattice orientation of SnS was unidentified before designing electrodes, thus the large distribution in thin layers should also suggests the orientation dependence. For further investigation, the crystal orientation has to be determined preliminary to the fabrication of electrodes, by using polarized SHG or Raman measurements.

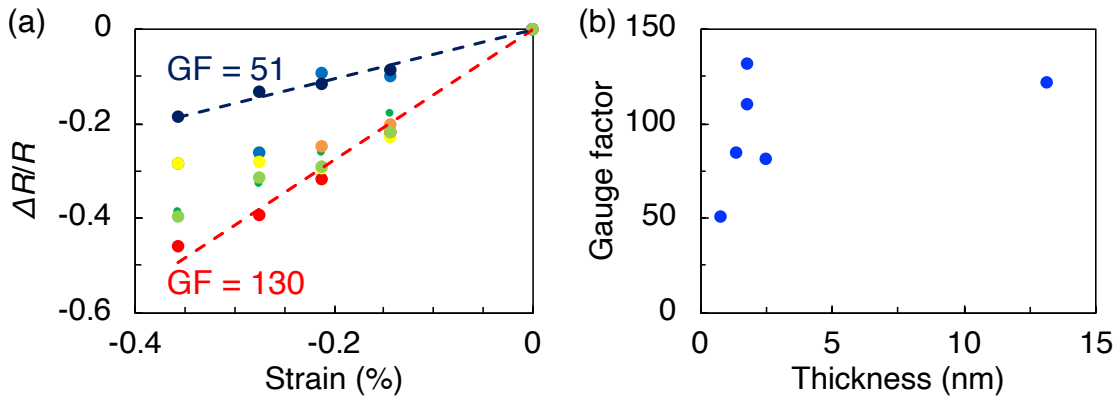

Figure 3-20: (a) Variation of GF for few-to-monolayer SnS. (b) Number of layer dependence of GF of SnS.

3.4.5 Piezoresistive Response under a Dynamic Strain

In order to investigate a time-resolved piezoresistive response of SnS, electromechanical response was measured under a dynamic strain. The SnS was the bulk SnS (∼10 layers) exactly same as the sample measured in Section 3.4.2. The I_D–time measurement was performed in air by the rotated actuator (FIg. 3-11). As shown in Fig. 3-21, tensile and compressive strains at $\varepsilon = \pm 0.58\%$ were applied repeatedly with a time interval of 5 sec. When the drain bias was fixed at $V_D = 1$ V, the drain current was approximately $I_D = 560$ nA. Under the tensile strain, the channel resistance increased due to the increased bandgap, and vice versa. These results are consistent with the piezoresistive characteristics of SnS under the static strain. The resistivity changed reproducibly with time, indicating the stability of the sample and measurement setup. However, when the strain exceeded over 1%, it became less reproducible. One of the possible reasons is plastic deformation of the mica and PET substrates.

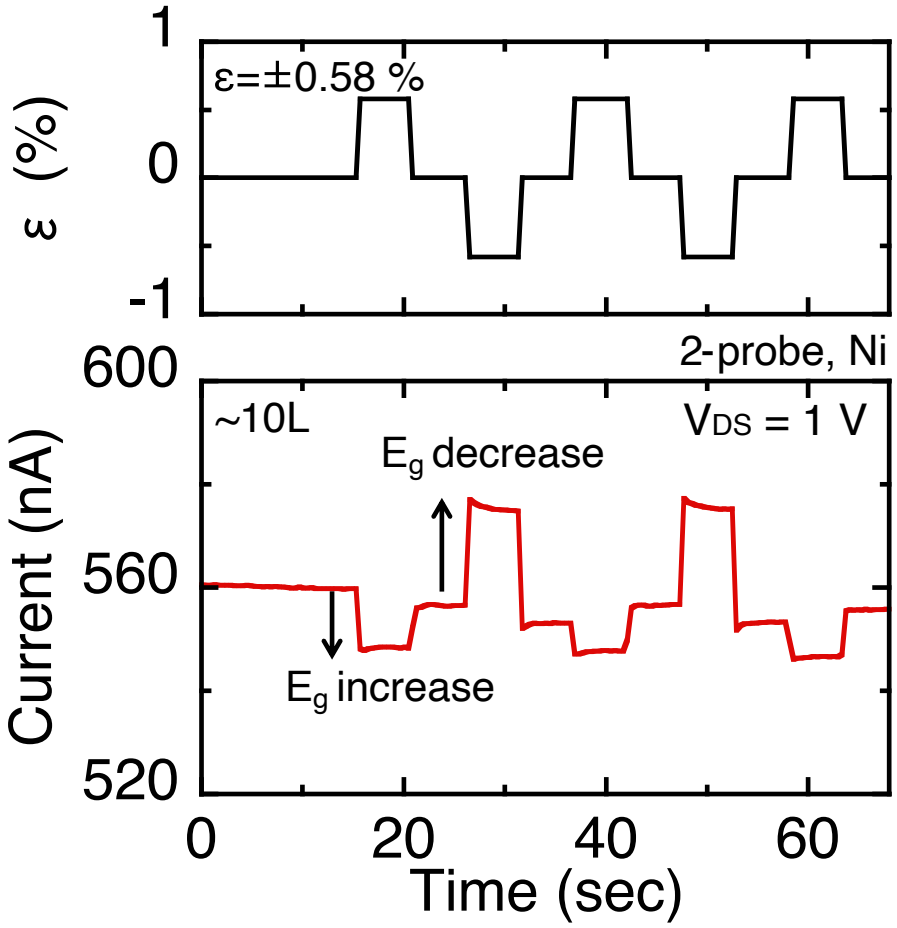

Figure 3-21: Time-resolved piezoresistive response under the repeated bending.

3.5 Piezoelectricity in 2D Materials

When the piezoelectric materials are strained, piezoelectric charges are accumulated near the contact metals. For two-dimensional materials, piezoelectric generators based on MoS_2 and WSe_2 have been reported [27, 47]. Most of the conventional ferroelectrics such as PZT or $BaTiO_3$ are insulators, however, 2D piezoelectric materials (SnS, MoS_2, and WSe_2) are semiconductor. Given that the generated current can flow in the conductive channel, Schottky barrier height is necessary to prevent the carrier injection from the contact metals [182, 183]. Wu *et al.* used Pd as a contact metal for MoS_2 to form a Schottky barrier [27]. With applying an in-plane strain into monolayer MoS_2, positive and negative piezoelectric charges are accumulated at source and drain. Owing to the charge polarity, the Schottky barrier height at source and drain changes asymmetrically. Actually, it has been reported that the Schottky-like I_D–V_D curve changes asymmetrically at negative and positive drain bias, under the lattice strains [27]. In contrast, in the case of bilayer MoS_2, only the symmetric change is observed because bilayer is not piezoelectric, but just piezoresistive [27]. These characteristics can be determined by a static I_D–V_D measurement under the strain [184], as discussed in Section 3.1. This model of the Schottky barrier height modulation has originally been proposed to explain the piezoelectric properties of zinc oxide (ZnO) nanowires [184]. The mechanism of piezoelectricity in ZnO is valid and reproducible, however, the piezoelectric generators based on 2D materials has been reported only by a few groups and there is still a room to discuss the mechanism of 2D piezoelectric devices.

One of the considerable concerns is the place where piezoelectric charges are accumulated. There has been a theoretical investigation of the piezoelectric charges for Pd/MoS_2 system [185, 186]. In their calculation, the Pd contact was assumed to half-cover MoS_2 edges. There are two possible regions where the charge is accumulated; the MoS_2 edge, and the metal edge near MoS_2 channel. Just under the Pd electrodes, electronic characteristics of MoS_2 is totally different from the intrinsic MoS_2, so that the piezoelectric charges are absent in these regions. As a results, the charges are

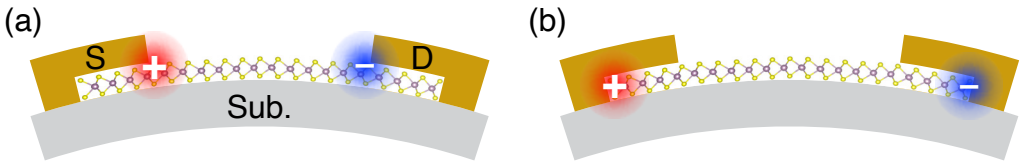

Figure 3-22: Schematic illustrations of accumulated region for the piezoelectric charges: (a) metal edges and (b) MoS_2 edges.

theoretically expected to be mainly accumulated near the metal edges, where the MoS_2 preserves its electronic property [186]. If this model is authentic, it is possible to improve the power density by shortening the channel length and increasing the density of electrode edges, though there has not been reported any experimentally direct proof for the piezoelectric charge model.

In this section, mechanism of 2D piezoelectric device is discussed for MoS_2 as a model material. For metal/MoS_2, there is a strong Fermi-level pinning near the conduction band minimum. Therefore, it is difficult to form a large Schottky barrier height even if the metal work function is changed. In order to overcome the Fermi level pinning, metal transfer method was utilized [176].

3.5.1 Material Preparation: Non-centrosymmetric Multilayer MoS_2

Fig. 3-23 shows typical optical images of bilayer MoS_2 grown by chemical vapor deposition (CVD) on SiO_2/Si substrate. There are two kind of stacking sequences; 3R and 2H structures. The triangle shape reflects the atomic configuration of MoS_2, and the second layer are grown on the first layer in anti-parallel and parallel direction for 2H and 3R structures, respectively. As the bilayer 2H MoS_2 has the centrosymmetricity due to the anti-parallel stacking sequence, it has no piezoelectricity. In the bilayer 3R MoS_2, top and bottom MoS_2 layer keep the piezoelectricity owing to the parallel stacking. Here, these 2H and 3R staking are called as AA and and AB stacking for simplicity.

So far, the largest output power density of monolayer MoS_2 is approximately 200 nW/cm^2 [27]. With using the AA stacked multilayer MoS_2, the power density

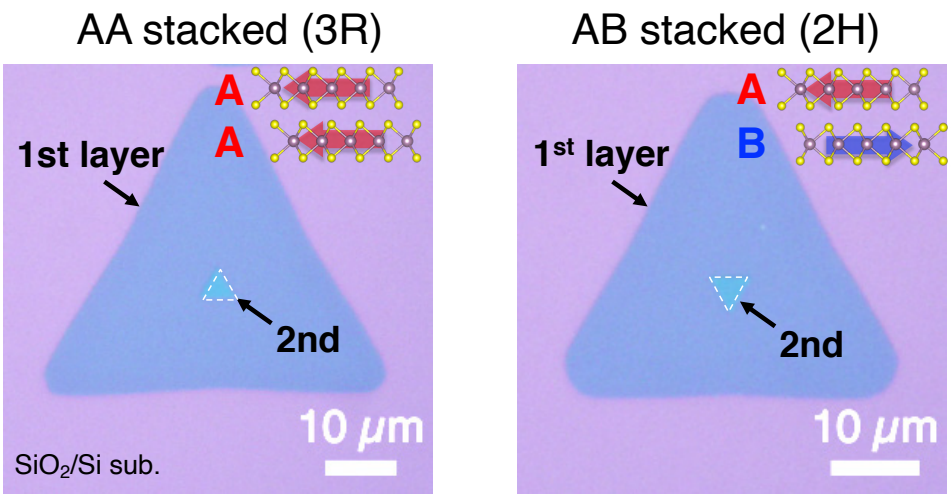

Figure 3-23: Optical images of CVD grown bilayer MoS_2 with different stacking sequence: AA (3R) and AB (2H) stackings.

should increase with the number of layers, beyond the monolayer limit [84, 85]. In this work, AA and AB stacked MoS_2 were used to investigate the stacking effect on the piezoelectric property, and to improve the power density of 2D piezoelectric generators.

3.5.2 Metal Transfer and Deposition Procedures

Firstly, MoS_2 flakes were transferred on the mica from SiO_2/Si in order to fabricate a flexible device. The transfer procedure is described as follows:

1. CVD growth of MoS_2 with solid sources, sulfur and MoO_3 powders. SiO_2/Si was used as a growth substrate.

2. Spin coating PMMA on the substrate MoS_2 was grown, followed by a baking at 120°C for 10 min.

3. Preparing a home-made PDMS film (2–5 mm thickness) with a hole, which is for the sake of releasing the strain in PMMA film. If the PMMA is fully covered with PDMS, large strain is induced in MoS_2 flakes during a following wet process; finally cracks and wrinkles are formed in MoS_2. Transferring PDMS on PMMA for the easy handling.

4. Etching SiO_2 layers by KOH solution (KOH : DIW = 3 : 2). The upper layers will be lifted off [128].

5. Rinsing with DIW to remove KOH residue, followed by drying in vacuum at RT.

6. Transfer the dried MoS_2 on mica substrate. To improve the adhesion, the sample was heated at 120°C for 10 min. The hole of PDMS was filled with PDMS hollowed out at Step. 3, and it was pressed with an 100 g weight.

7. Liftoff the PMMA and PDMS in acetone for ∼12h. After the liftoff, MoS_2 flakes remain on mica. Rinsing the sample in IPA, followed by N_2 blow. To minimize the deformation due to the blowing, its flow rate should be gentle.

Secondly, source and drain electrodes are prepared as flowing procedures:

1. Fabricating electrodes on a sacrificial substrate of SiO_2/Si substrate by using standard EB lithography and metal deposition. Gold was selected as an electrode because of its chemical stability during the following wet process or transfer process in atmosphere.

2. Spin coating PMMA and transferring PDMS in the same way as for MoS_2 transfer. Here, windows for measurement probes were fabricated on PMMA by EB lithography.

3. Liftoff and cleaning process in the same method, as described above.

4. Transferring metals in atmosphere by a home-built transfer system. The source and drain electrodes were aligned towards the armchair direction of MoS_2, where the piezoelectric effect is maximized. During the transfer, the mica substrate was heated at 120°C, which can reduce an adhesion between PMMA and PDMS, so that finally a two-probe device can be obtained sandwiched with mica and PMMA (Fig. 3-24).

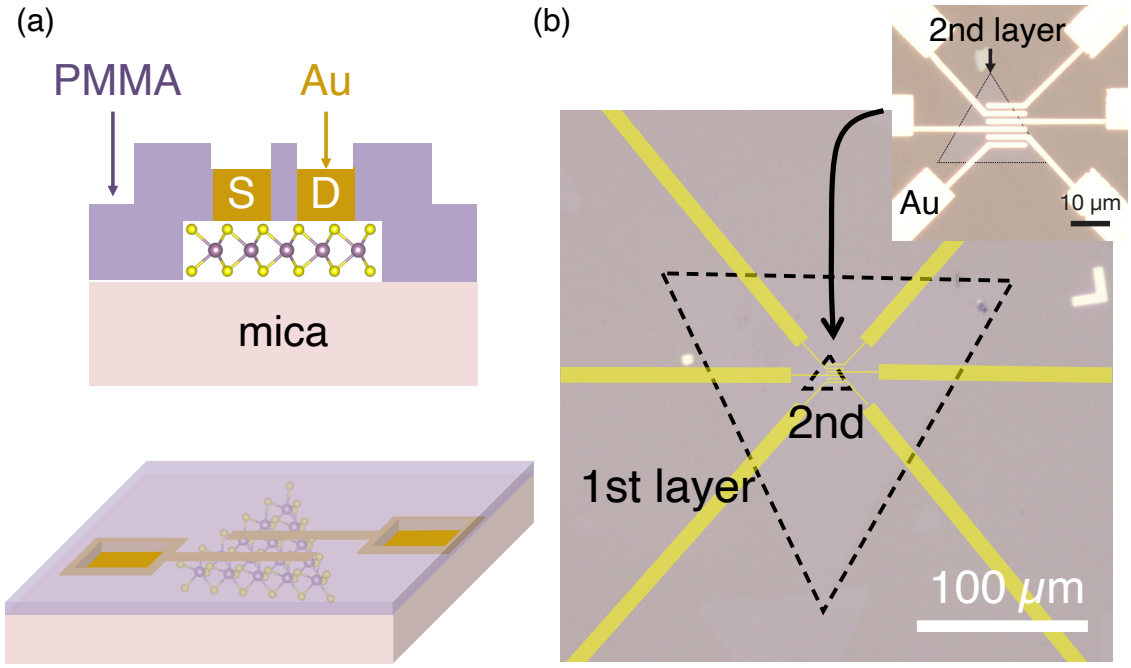

Figure 3-24: (a) Schematic illustration and (b) Optical image of two-probe device *via* metal transfer.

The transferred metals located at the MoS_2 surface and had no overlap with MoS_2 edge. The strain was applied toward the armchair direction, then the piezoelectric charges are expected to be accumulated at the source/drain electrodes.

3.5.3 Electromechanical Response of MoS_2 with Metal Deposition

When the Au electrodes were fabricated for monolayer MoS_2 *via* deposition instead of transfer method, the symmetric change of I_D–V_D curve was observed under the tensile and compressive strain, as shown in Fig. 3-25a. Even if the contact metal was replaced to Ni, Pd, and Cr, the I_D–V_D curve changed symmetrically as like Au. For the AA and AB stacked bilayer MoS_2, symmetric changes were obtained like as monolayer. The piezoelectricity is absent in the AB stacked bilayer, thus the symmetric change is apparently caused by the piezoresistive effect. Although the monolayer and AA stacked bilayer are ideally piezoelectric, the asymmetric change of Schottky barrier height at source/drain probably have a small effect on the electronic

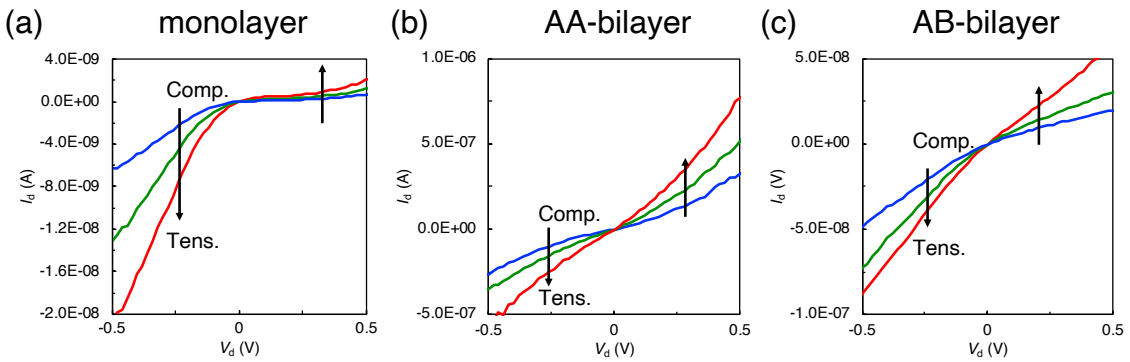

Figure 3-25: I_D–V_D under strains for (a) monolayer, and (b,c) AA/AB bilayer MoS_2. The electrodes were fabricated *via* evaporation.

transport characteristics due to a strong Fermi level pinning [176]. These results suggest that the piezoresistive effect is more dominant than the piezoelectric effect for MoS_2 with deposited metal electrodes.

3.5.4 Piezoelectric Response of Two-probe MoS_2 Device *via* Metal Transfer

Fig. 3-26 shows I_D–V_D characteristics for AA and AB stacked bilayer MoS_2 under compressive strain. For the AB stacked, symmetric change due to the piezoresistive effect was obtained as similar as the results of MoS_2 with deposited metal. In contrast, for the AA stacked, I_D–V_D curve changed asymmetrically in the negative and positive drain bias. This is probably because of the piezoelectric effect; a strong Schottky contact was formed as a results of Fermi level depinning owing to a defect-free van der Waals gap between metal electrode and MoS_2 [176]. The piezoelectric behavior was achieved for the AA stacked bilayer, indicating the piezoelectric property in the monolayer can be preserved with AA stacking sequence even though it is stacked with other monolayer.

For the monolayer, however, the asymmetric change was not observed unlike as the bilayer. This is probably because the piezoelectric charge in the monolayer is smaller than the bilayer and piezoresistivity is still dominant for the carrier transport characteristic.

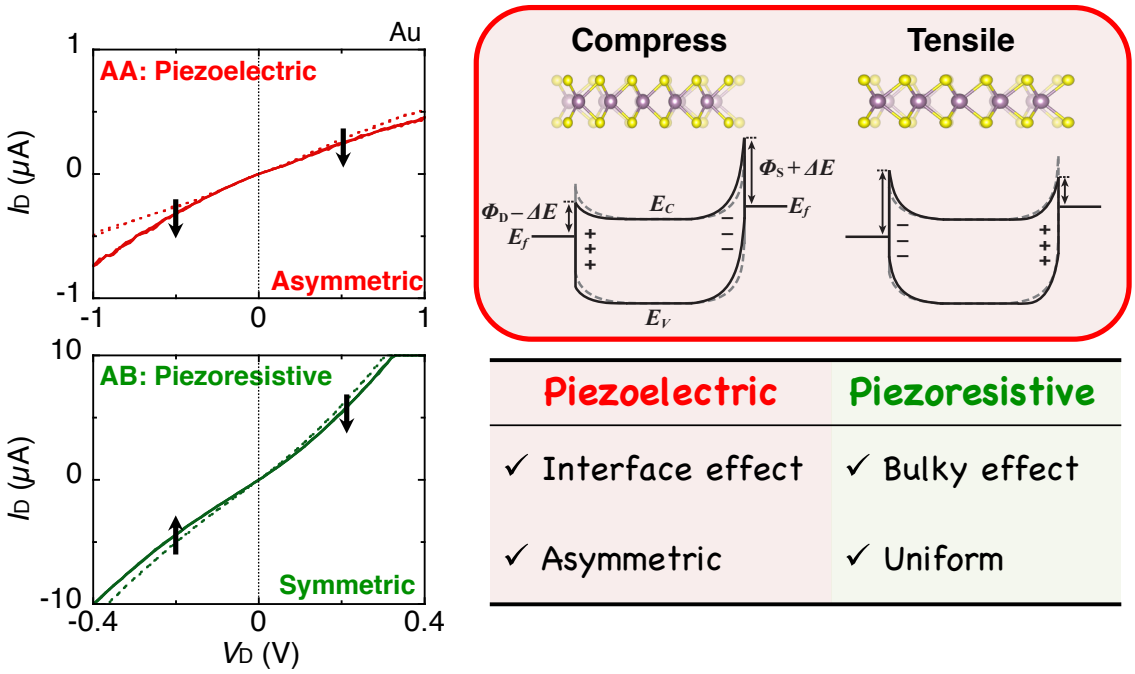

Figure 3-26: Asymmetric and symmetric change of I_D–V_D curves for AA and AB stacked MoS_2, respectively.

3.5.5 Electromechanical Response under a Top-gate Modulation

For further investigation of the piezoelectric charge in the monolayer MoS_2, top-gated field-effect transistors were fabricated with the metal transfer method. The source/drain and top-gate electrodes were fabricated on the sacrificial SiO_2/Si substrate as follows:

1. As a gate insulator, 2D *h*-BN (several-tens-nm thickness) was used. *h*-BN was transferred on the sacrificial substrate *via* the Scotch tape and a commercially available PDMS film. To improve the adhesion, the substrate was heated at 180°C for 10 min.

2. To eliminate the tape and PDMS residues, the sacrificial substrate was treated in UV ozon for 5 min.

3. Selecting a BN flake with a suitable size for the MoS_2 crystal, the top-gate and source/drain Au electrodes were fabricated at the same time with using EB

lithography and metal deposition.

4. All the layers were transferred from the sacrificial substrate to the mica substrate in the same, as described in Section 3.5.2.

5. Transport characteristics were measured with an external strain, applied toward the armchair direction.

Fig. 3-27 shows the I_{D}–V_{TG} at $V_{\mathrm{D}} = 10$ mV with and without the tensile strain of 0.15%. Under the flat condition, this FET exhibited an n-type behavior, which is the intrinsic property of MoS_2. When the source and drain was reversed, usually the I_{D}–V_{TG} curve is different from the initial curve before reversing the source/drain. This means that the contact resistance is not the same at source/drain, probably due to the geometric difference of electrodes or fluctuation of fabrication processes. To simplify the analysis, a sample that has the almost same contact resistance at source and drain, as shown in Fig. 3-27. Under the tensile strain, a discrepancy was found in the accumulated region when the source/drain were reversed. In contrast, in the depletion region, these two curves traced almost the same line. The total resistance of this FET device can ve written as $R = R_c + R_{ch}$ where R_c and R_{ch} are contact and channel resistances, respectively. When the negative TG bias is applied, the R_{ch} increase and is more dominant for the carrier transport than the R_c. For the positive bias, the R_{ch} and the transport characteristic is dominated by the R_c, in other words, the asymmetric change of SBH can be effectively detected as a polarity, as shown in the inset of Fig. 3-27.

3.5.6 Origin of Piezoelectric Charge in Metal/MoS_2

The asymmetric modulation of SBH due to the piezoelectric effect has been determined by the static transport measurement for monolayer and AA-stacked bilayer MoS_2, as described above. In the present experiments, the source/drain electrodes were transferred onto the MoS_2 surface, without overlapping at the MoS_2 edge, as shown in Fig. 3-28a. Thus the piezoelectric charges induced by the strain are accumulated at the metal/MoS_2 interface rather than the MoS_2 edge. When the drain

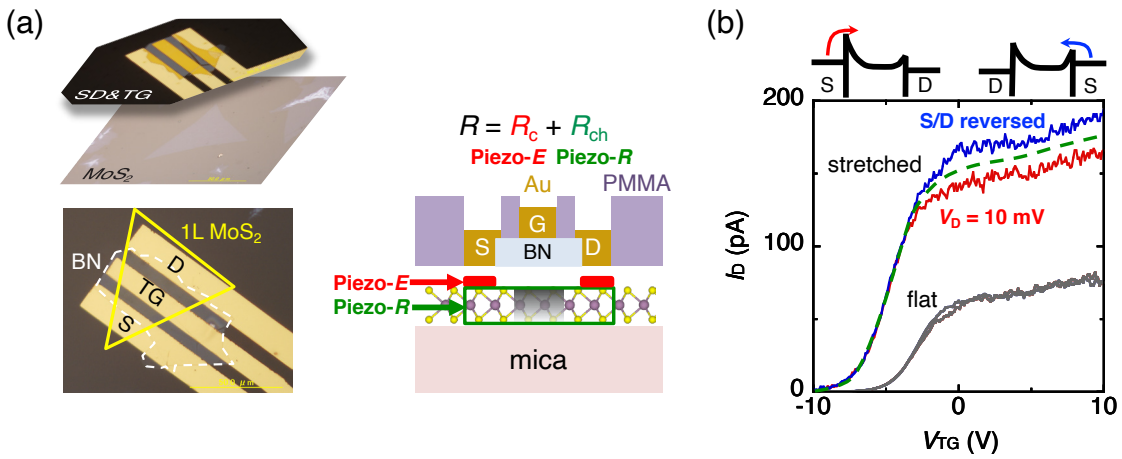

Figure 3-27: (a) Optical image and cross-sectional illustration of TG/SD transferred device. (b) I_{D}–V_{TG} characteristics of monolayer MoS_2 with applying the tensile strain along the armchair direction.

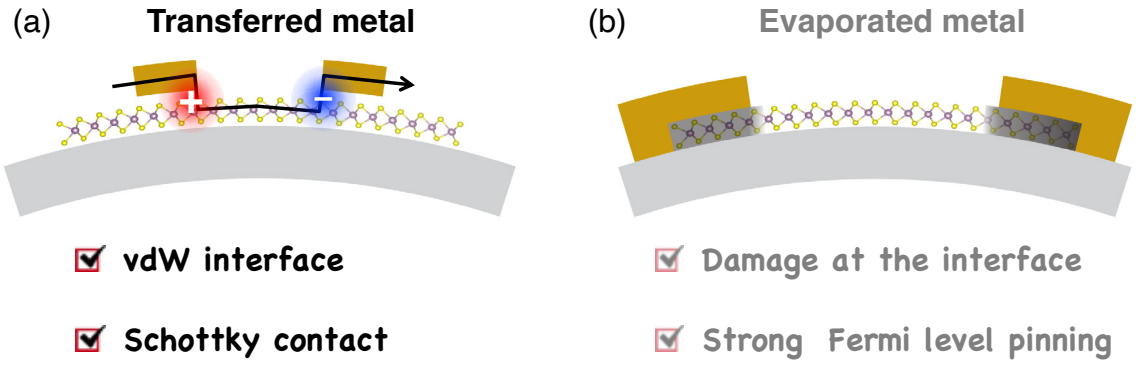

Figure 3-28: Schematic illustrations of (a) transferred and (b) deposited metal electrodes.

voltage is applied, the current flow should be through the metal edge near the channel, so that the piezo-charge accumulated at the interface between the MoS_2 channel and source/drain metal edge has been detected in Figs. 3-26,3-28. These experimental results agree with the theoretical estimation [185, 186].

Given that the piezoelectric effect in 2D materials appears at the interface between contact metal and 2D material, their power density can be improved with the methods as suggested below,

- Post-fabrication SBH engineering: although the SBH at the facial interface between metal and 2D material's surface, the metal edge near the channel can be modified. For MoS_2, Ti has an ohmic contact, though a Schottky contact

is formed when Ti is oxided to TiO_2 [187]. This Schottky contact is owing to the increase of SBH from $\Phi_m = 4.33$ eV (Ti [188]) to $\Phi_m = 4.9 - 5.5$ eV (TiO_2 [189]). Even if the electrodes are fabricated *via* a deposition, the effect of strong Fermi level pinning will be neglected in the channel region and Schottky contact at the metal edge should be realized.

- Refinement of electrodes: the output current is proportional to the channel width. With minimizing the cannel length, the number of devices per unit area increase. Conpared to the conventional piezoelectrics, which has to be sandwiched by electrodes because of the out-of-plane polarization, the refinement of electrodes on MoS_2 is much easier because of its in-plane piezoelectricity.

In order to investigate the piezoelectric generator based on MoS_2, two-probe device was fabricated, as shown in Fig. 3-29a,b. For this generator, Ti electrodes were fabricated *via* metal evaporation. The sample was exposed in air after the metal deposition to oxidize Ti into TiO_x, probably resulting in a strong Schottky barrier contact. Fig. 3-29c shows the short circuit output current of MoS_2 monolayer with applying compressive strain repeatedly. The output current was approximately 30 pA, which is comparable to that of Pd/MoS_2 system [27]. In the first demonstration of piezoelectric generator of monolayer MoS_2, the source and drain electrodes were fabricated with the channel length of ∼10 µm, and its power density was approximately ∼200 nW/cm^2. When the channel length is minimized, the power density can be larger than 1 µW/cm^2. For further understanding, it is necessary to investigate the relationship between piezoelectric output and channel length. Also, defect treatment in the ferroelectric material will be effective to improve the piezoelectric property. For MoS_2, sulfur vacancies are the origin of its n-type property. S. Han *et al*. has demonstrated the improvement of piezoresponse in the monolayer MoS_2 by sulfur treatment [190].

Moreover, if the piezoelectric material is replaced with SnS, whose piezoelectric coefficient is 10–100 times larger than MoS_2, its generator will exceed over 10–100 µW/cm^2.

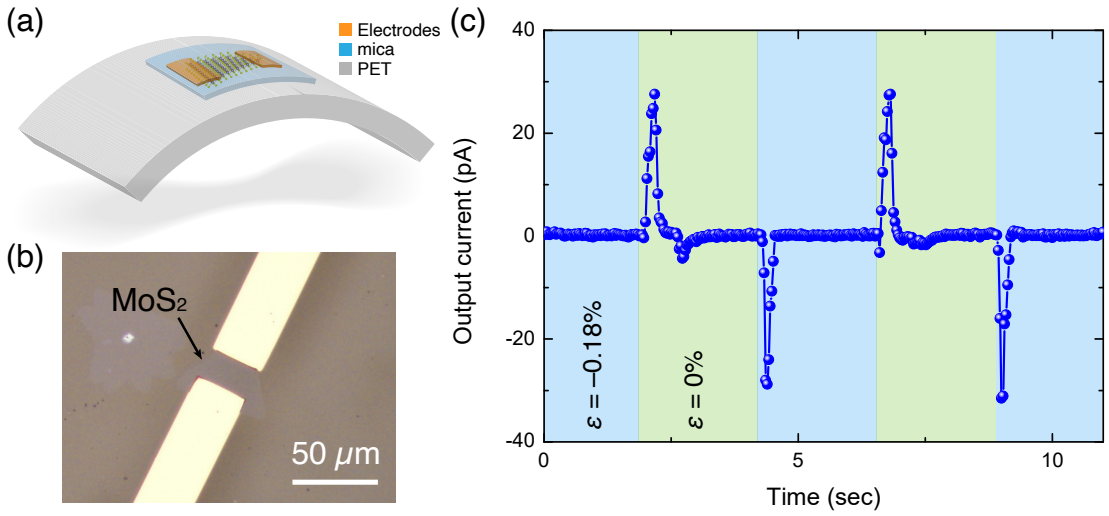

Figure 3-29: (a) Schematic illustration of a piezoelectric generator based on MoS_2. (b) Optical image of two probe device. (c) Piezoelectric output current for monolayer MoS_2 under the repeated external strain.

Chapter 4

Ferroelectricity in SnS

2D van der Waals ferroelectric semiconductors have emerged as an attractive building block with immense potential to provide multifunctionality in nanoelectronics. Although several accomplishments have been reported in ferroelectric resistive switching for out-of-plane 2D ferroelectrics down to the monolayer, a purely in-plane ferroelectric has not been experimentally validated at the monolayer thickness. Herein, a micrometer-size monolayer SnS is grown on mica by physical vapor deposition, and in-plane ferroelectric switching is demonstrated with a two-terminal device at room temperature (RT). SnS has been commonly regarded to exhibit the odd–even effect, where the centrosymmetry breaks only in the odd-number layers to exhibit ferroelectricity. Remarkably, however, a robust RT ferroelectricity exists in SnS below a critical thickness of 15 layers with both an odd and even number of layers. The lack of the odd–even effect probably originates from the interaction with the mica substrate, suggesting the possibility of controlling the stacking sequence of multilayer SnS, going beyond the limit of ferroelectricity in the monolayer. This work will pave the way for nanoscale ferroelectric applications based on SnS as a new platform for in-plane ferroelectrics.

4.1 Fundamental of Ferroelectrics

In this section, the fundamental principles of the ferroelectricity and the literature review of ferroelectric downscaling are described. The mechanism of ferroelectric effect is discussed with the conventional 2D materials as a model material. The significance of Schottky barrier for the ferroelectric semiconductor is shown. Also, the strategy for the Schottky contact at 2D/metal interface will be discussed.

4.1.1 Origin of Spontaneous Polarization

As discussed in Chapter 1, ferroelectricity requires non-centrosymmetricity and spontaneous polarization. The spontaneous polarization directly means that the positive and negative ions are displaced in the material despite the zero electric is zero. Considering the elastic energy, this displacement will give a birth of unsuitability, though actually the spontaneous polarization is stable, as will be discussed below [171].

Fig. 4-1a shows an initial state of cubic crystal structure for perovskite. Figs. 4-1b–d show the different state as a result of normal lattice vibration. There are no dipole moment in (d), though (c) and (d) have dipole moments and these modes are called as acoustic and optical modes, respectively. If these modes are stabilized, they correspond to the state of (c) ferroelectricity and anti-(d) ferroelectricity. At the Currie temperature T_c, the frequency of these phonon modes becomes zero and increase above T_c.

The local field E^{loc} induced by surrounding polarization$P$ can be written as,

$$E^{loc} = \frac{\gamma}{3\epsilon_0} P \tag{4.1}$$

where γ is the Lorentz term (e.g. $\gamma = 1$ for the isotropic cubic crystals), ϵ_0 is the dielectric constant of vacuum. If the ionic polarizability is α, the dipole moment per crystal unit cell μ can be written as,

$$\mu = \frac{\alpha\gamma}{3\epsilon_0} P \tag{4.2}$$

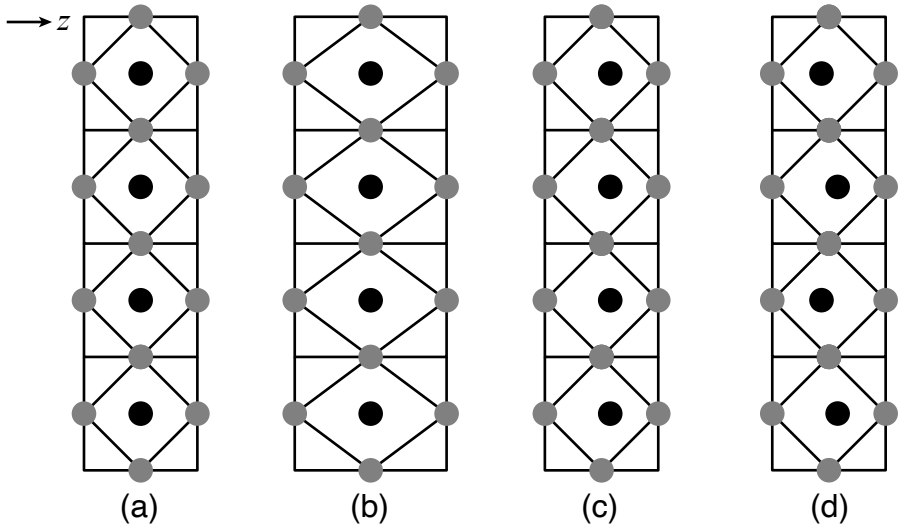

Figure 4-1: Normal modes of vibration in perovskite crystal.

Thus, the energy of dipole moment is

$$w_{dip} = -\mu E^{loc} = -\frac{\alpha\gamma^2}{9\epsilon_0^2}P^2 \tag{4.3}$$

$$W_{dip} = -Nw_{dip} = -\frac{N\alpha\gamma^2}{9\epsilon_0^2}P^2 \tag{4.4}$$

$$\tag{4.5}$$

where N is the number of atoms per unit volume.

For the elastic energy, the increase of energy per unit volume is [191]

$$W_{elas} = N\left(\frac{k}{2}u^2K + \frac{k'}{4}u^4\right) \tag{4.6}$$

where k and k' are force factors and u is a displacement. The displacement can be transformed with electrical charge q as follows:

$$P = Nqu \tag{4.7}$$

Thus, the total energy W_{tot} can be extracted as,

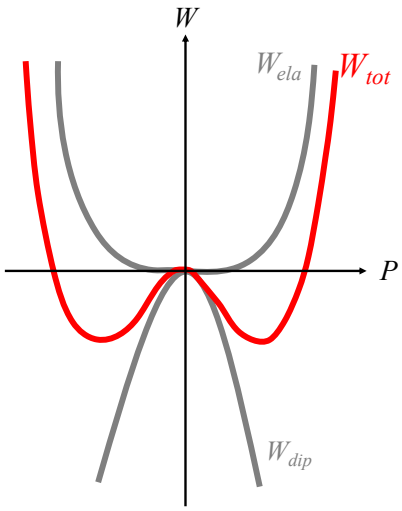

Figure 4-2: Origin of the spontaneous polarization.

$$W_{tot} = W_{dip} + W_{elas} \tag{4.8}$$

$$= \left(\frac{k}{2Nq^2} - \frac{N\alpha\gamma^2}{9\epsilon_0}\right) P^2 + \frac{k'}{4N^3q^4} P^4 \tag{4.9}$$

This relationship is illustrated in Fig. 4-2, indicating that the spontaneous polarization is stabilized where $\partial W_{tot}/\partial P = 0$.

4.1.2 Downscaling Ferroelectrics

Fig. 4-3 shows the thickness dependence of the ferroelectricity in SnS and $BaTiO_3$ [12, 80]. For $BaTiO_3$, the ferroelectric polarization is along the out-of-plane direction (Fig. 4-4), so that it has to be sandwiched with contact metals for the device application. In other words, the ferroelectric makes no sense when the electric field is applied perpendicular to its polarization. When the thickness of ferroelectric layer decrease below several-tens nm, the depolarization field is dominant and the ferroelectricity disappears. In contrast, monolayer SnS is a purely in-plane ferroelectric, as shown in Fig. 4-4. For the in-plane ferroelectrics, electrodes will fabricated aligned toward in-plane direction. With an enough space between source and drain, the intrinsic region of ferroelectric can be preserved even at the atomic thickness. From the theoretical

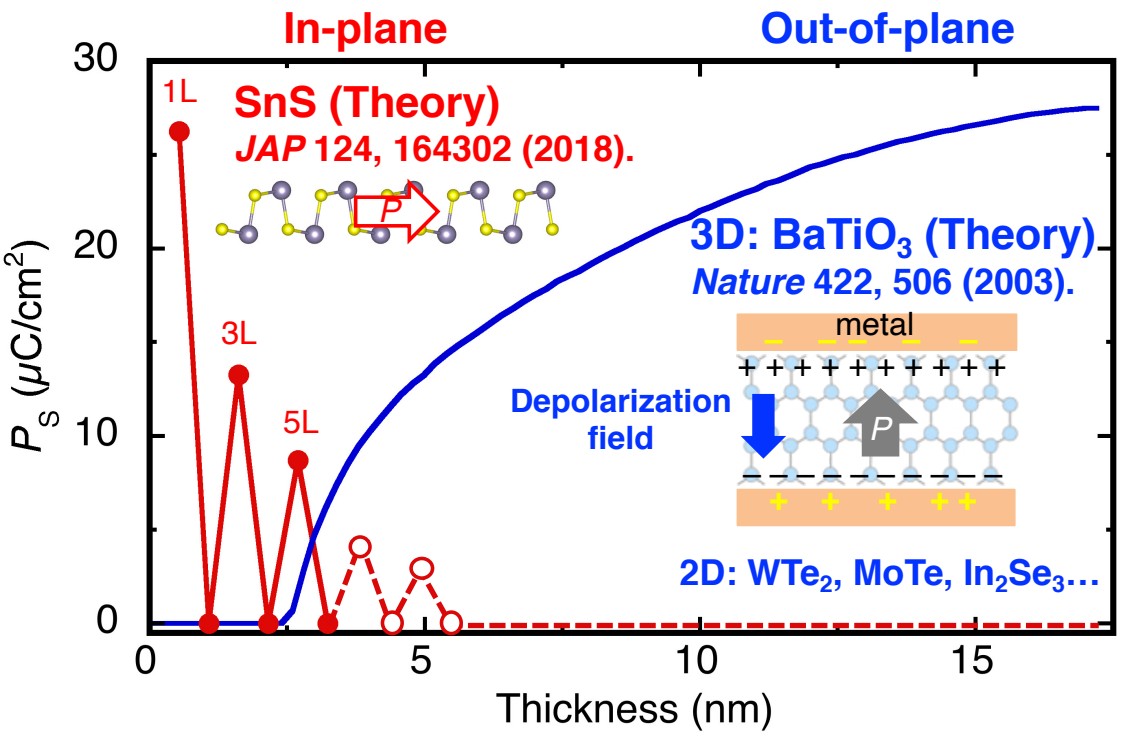

Figure 4-3: Downscaling of ferroelectric materials [12, 80].

calculation the spontaneous polarization P_s of 2D SnS is expected to increase with decreasing the number of layers, and be maximized at monolayer with a large P_s comparable to $BaTiO_3$ [51]. Also, it is a unique property that the ferroelectricity can be only observed in the monolayer and odd-number layers, as discussed in Section 1.4.4.

Not only the polarization direction, there are another difference between SnS and the conventional ferroelectrics. As shown in Fig. 4-4, the polarization switching of SnS is in the way of bond-switching unlike as the $BaTiO_3$ and most of other ferroelectrics, which change the polar direction with the ionic displacement. The switching mechanism in SnS can be also explained the phase transition between NaCl and puckered structure (Fig. 2-2): SnS has to take a step to transform into the NaCl structure in order to switch the polarization.

As discussed above, SnS is a promising material to realize a robust ferroelectricity at the atomic scale. Although not a few 2D ferroelectrics have been discovered and demonstrated, most of 2D ferroelectrics have an out-of-plane vector for its polarization

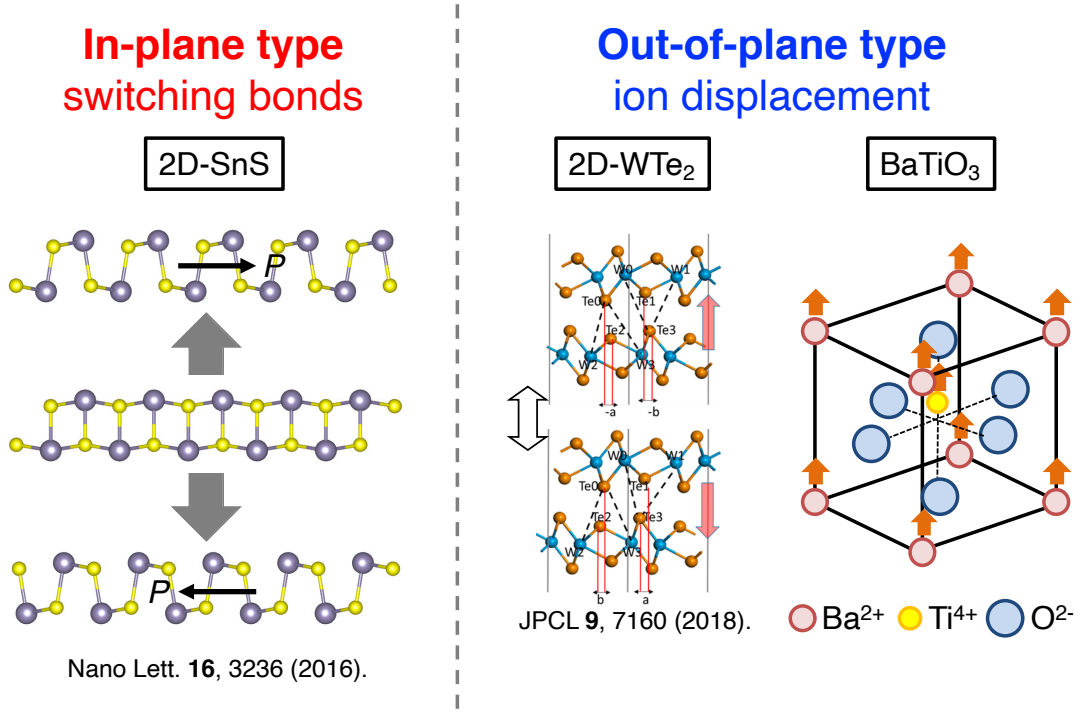

Figure 4-4: Schematic illustration of ferroelectric polarizations: in-plane versus out-of-plane.

[192, 193, 194, 195, 196, 197, 198, 199, 73, 200, 201, 202, 203, 204]. One of the advantage of 2D layered materials is it has no dangling bond on the surface, which reveals an ideal interface at the interface of heterostructure. However, this advantage does not work well for the ferroelectric downscaling. As in the same way of out-of-plane 3D ferroelectrics, out-of-plane 2D ferroelectrics are also suffered from the depolarization field when they become thin [83]. These difference between the in-plane and out-of-plane 2D ferroelectrics can be understood like as the conceptual illustration in Fig. 4-5. 3D materials has two kind of characteristics, interface and bulk, due to the existence of dangling bonds at the surface. The out-of-plane 2D ferroelectrics inherits the "interface" properties from the two-faced feature of 3D materials because the depolarization field is effective; while in-plane 2D ferroelectrics inherits the intrinsic "bulk" properties.

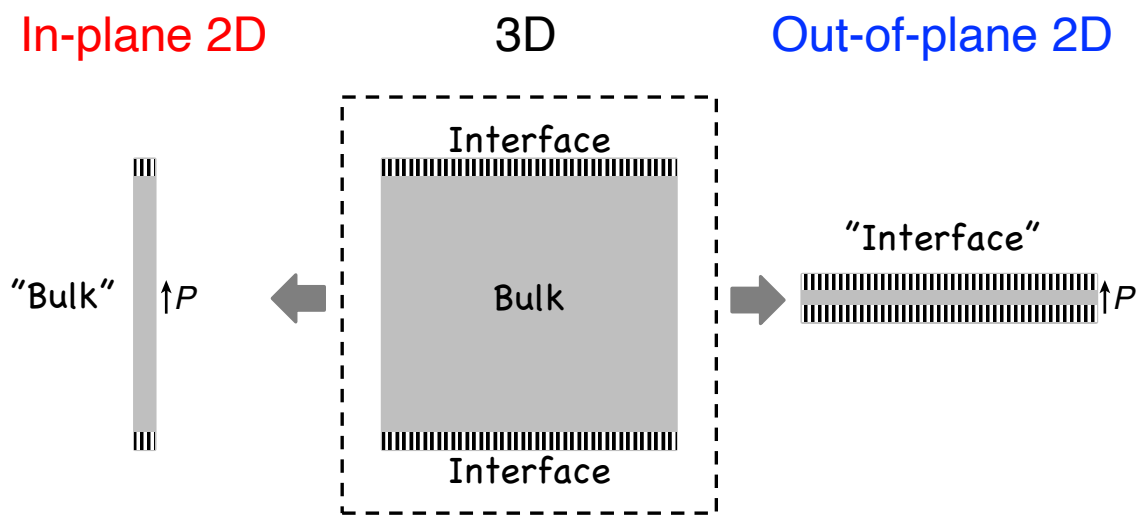

Figure 4-5: Conceptual illustration of downscaling of in-plane and out-of-plane ferroelectrics.

4.1.3 Depolarization Field at Metal/Ferroelectric Interface

The origin of depolarization field has been described in the previous works, for example, in Ref. [15, 205]. When the charge q is induced in the parallel capacitance in vacuum, the electric field is $E = q/\varepsilon_0$. When a dielectric is inserted between the electrodes, E is $E = q/k\varepsilon_0$, where k is the relative permittivity of the dielectric. This can be regarded that the surface charge decrease from q to q/k: a part of the surface charge $(1 - 1/k)q$ is used to screen the polarization charge, and the rest of charge generate the internal electric field in the dielectric. These two types of charges are called as "polarization charge" and "free charge", respectively. For the ferroelectric, the polarization charges are released when a coercive electric field is applied to switch the polarization, which can be detected as displacement current. Assuming that the remnant polarization in ferroelectric is 16 $\mu C/cm^2$, the surface density of electrons is necessary to be over 10^{14} cm^{-2} to screen the polarization charge [205]. If the electron density of contact metal is not enough, the dielectric flux into the metal, resulting in the decrease of ferroelectric polarization.

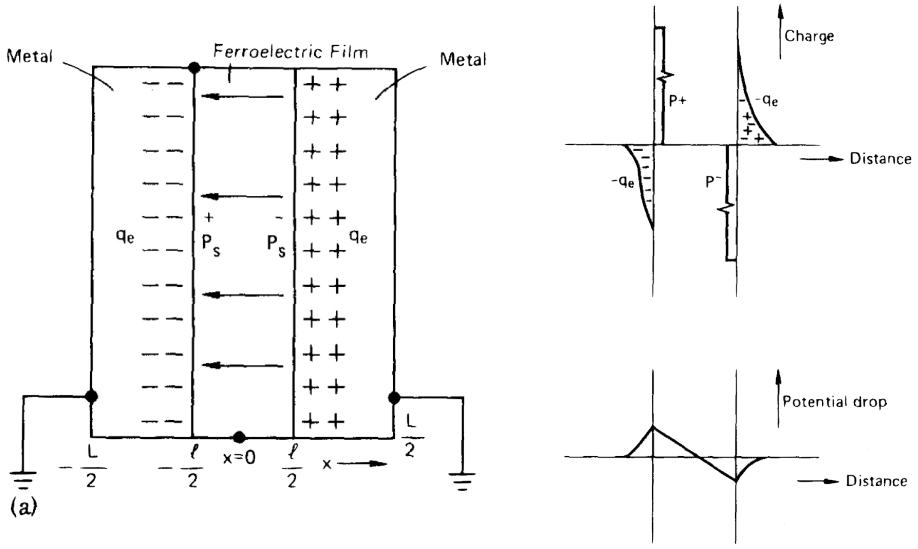

Figure 4-6: Schematic illustration of the origin of depolarization field [15].

4.1.4 Overcoming the Depolarization Field

A great deal of effort has been devoted to overcome the depolarization field [30, 206, 80, 207, 208, 209, 210, 73, 211, 192, 212]. For example, Sai *et al.* has investigated a theoretical calculation to achieve a ferroelectricity for 1 nm thick $PbTiO_3$ by using Pt electrode with a short screening length of 0.1 Å [208]; Liu *et al.* has demonstrated ∼4 nm $CuInP_2S_6$ with using the ferrielectric ordering, which can reduce the polarization [200]. Despite of these contributions, there has not been any established approach to escape from the depolarization field. As a novel approach, the in-plane ferroelectrics are attracting much attention because it should be free from the out-of-plane perturbations. Already in-plane ferroelectricity has been demonstrated in the monolayer SnTe, however, the Currie temperature of it is below room temperature and it also has a out-of-plane polarization: not a purely in-plane ferroelectric [212].

4.1.5 Schottky Barrier Height Modulation for Ferroelectrics

A Schottky barrier height (SBH) modulation is important for the metal/ferroelectric structure as similar with piezoelectric devices, as discussed in Chapter 3. A direct proof for the ferroelectricity is to observe the displacement current at the coercive

Table 4.1: Literature review of the strategy to overcome the depolarization field in a ferroelectric system.

Materials	Methods	P_s (μC cm^{-2})	OOP/IP	T_c (K)	d (nm)	Ref.
Group-IV monochalcogenides	In-plane polarization^T	36.2–96.8	IP	>RT	0.5	[30, 206]
$BaTiO_3$	$SrRuO_3$ electrode^T	NA	OOP	>RT	2.4	[80]
$BaTiO_3$	Pt electrode^T	NA	OOP	>RT	1.2	[207]
$PbTiO_3$	Pt electrode^T	NA	OOP	>RT	0.4	[208]
$PbTiO_3$	Chemical absorbate^E	NA	OOP	>700	1.2	[209]
$PbTiO_3$	180° stripe domain^E	NA	OOP	>700	1.2	[209]
$YMnO_3$	Improper ferroelectricity^T	6.2	OOP	NA	2.3	[213]
$BaZrO_3$	$SrRuO_3$ electrode^T	NA	OOP	NA	0.4	[210]
Monolayer SnTe	In-plane polarization^E	NA	IP	270	0.63	[73]
1T-MoS_2	Improper ferrielectricity^T	0.28	OOP	NA	0.63	[211]
$CuInP_2S_6$	Ferrielectric ordering^T	4	OOP	>RT	4	[192]
Monolayer $AgNiO_2Se_6$	Ferrielectric ordering^T	0.2	OOP	>RT	0.6	[212]

P_s: Polarization; OOP/IP: Polarization direction of out-of-plane and in-plane; T_c: Currie temperature; d: thickness; T: Theoretical; and E: Experimental.

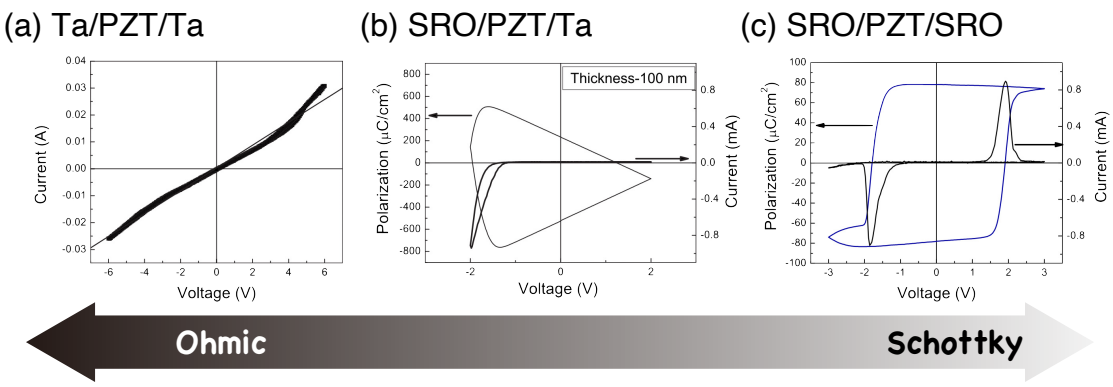

Figure 4-7: I–V characteristic for PZT with different metal contacts.

electric field. As an analogous of SnS, a conductive PZT is considered here. Figs. 4-7 shows a series of I_{D}–V_{D} curves for n-type PZT with different conbination of electrode (Ta or $SrRuO_3$) [182]. When the PZT is sandwiched with double $SrRuO_3$, a normal displacement current and ferroelectric hysteresis are observed, though with using the ohmic contact of Ta electrode, it becomes leaky and difficult to detect the displacement current. In order to efficiently detect the small signal of displacement current, Schottky contacts are necessary to prevent the carrier injection from metal to ferroelectric channel.

4.2 Second Harmonic Generation from 2D SnS

Second harmonic generation (SHG) is a nonlinear optical phenomenon that an excitation light, whose frequency is ω, generates a new photon with a frequency of 2ω [214], as shown in Fig. 4-8. The existence of SHG guarantees the non-centrosymmetry in the piezoelectric and ferroelectric materials. In this works, SHG measurement is used for a direct evidence for the structural non-centrosymmetry in monolayer SnS. In this section, a theoretical backgrounds and experimental setup will be briefly summarized.

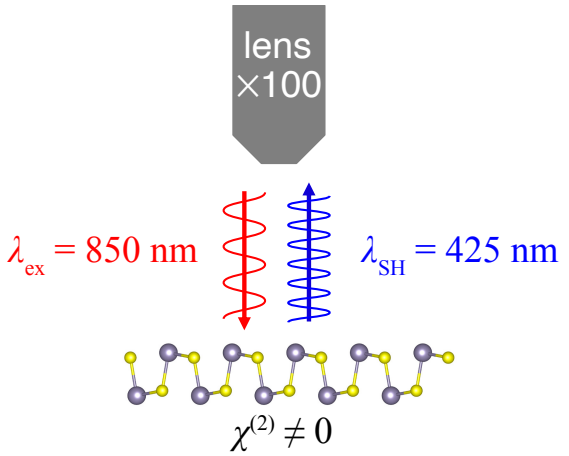

Figure 4-8: Schematic illustration of SHG measurement.

4.2.1 Theory and Experiments of SHG

To understand the difference between centrosymmetric and non-centrosymmetic materials, discussion will start from the relationship between an optical polarization and potential energy of electrons [214]. Assuming a centrosymmetric material, the potential energy of electron can be written as,

$$V(x) = V(-x) = \frac{m}{2}\omega_0^2 x^2 + \frac{m}{4}Bx^4 + \cdots \tag{4.10}$$

where ω_0^2 and B are constants and m is the electron mass. The equation $V(x) = V(-x)$ is reflecting the crystal symmetry. The restoring force on an electron is written

as,

$$F = -\frac{\partial V}{\partial x} = -m\omega_0^2 x - mbx^3 \tag{4.11}$$

Considering a low frequency electric field $E(t)$, its Fourier components are smaller than ω_0^2. The excursion $x(t)$ induced by the field is shown by equation the total force on the electron to be zero:

$$-eE(t) - m\omega_0^2 x(x) = 0 \tag{4.12}$$

Thus,

$$x(t) = -\frac{e}{m\omega_0^2} E(t) \tag{4.13}$$

This means the induced optical polarization is proportional to the external electric field (Fig. 4-9a).

For non-centrosymmetric materials, the relationship $V(x) = V(-x)$ is no longer correct, then the potential energy of electron now include the odd powers as follows:

$$V(x) = \frac{m\omega_0^2}{2} x^2 + \frac{m}{3} Dx^3 \tag{4.14}$$

where D is a constant. The restoring force on electrons can be written as,

$$F = -\frac{\partial V(x)}{\partial x} = -(m\omega_0^2 x + mDx^2 + \cdots) \tag{4.15}$$

Assuming $D > 0$, the relation between the optical polarization and the external electric field are shown in Fig. 4-9b.

As a results, the optical polarization under an electric field $E^{(\omega)} cos\omega t$ will be like as Fig. 4-9. A Fourier analysis on the nonlinear polarization wave in the non-centrocymmetric material, will contain the SHG. The optical polarization P in non-centrosymmetric material can be written with electric susceptibility $\chi^{(n)}$ as follows:

$$P^{(2)} = \frac{1}{2}\chi^(2) E^2 cos^2 \omega t \tag{4.16}$$

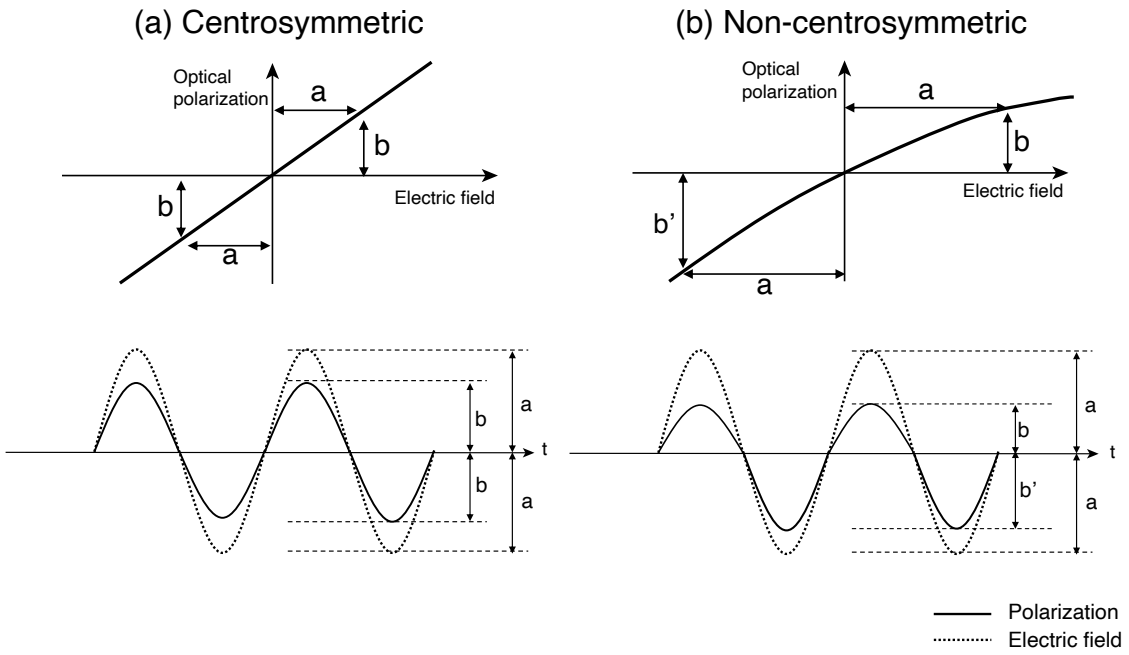

Figure 4-9: Relation between polarization and the external electric field.

which means that the SHG intensity is to the squared electric field. Thus, especially for the thin material such as 2D materials, very strong excitation laser is necessary to detect the SHG signal. Usually for the SHG measurement of few-to-monolayer sample, a pulsed laser is used to prevent the degradation during the measurement [215, 216].

4.3 Demonstration of Ferroelectricity in SnS

Nanoscale ferroelectrics have been explored for decades in areas such as nonvolatile memories, sensors, and nonlinear optoelectronics. For 3D ferroelectrics, only a few successes have been reported in downscaling the film thickness: ∼1 nm $BaTiO_3$ [217, 218] and 1.2 nm $PbTiO_3$ [209]. Otherwise, ferroelectricity disappears in the nanoscale owing to the depolarization field or interfacial effects [15, 80, 81]. In contrast to the 3D materials, 2D layered materials have a dangling-bond-free surface with van der Waals (vdW) gap, and hence, they maintain the intrinsic properties even at an ultrathin thickness. Recent intensive works on 2D ferroelectrics [192, 193, 194, 195, 196, 197, 198, 199, 73, 200, 201, 202, 203, 204] have experimentally demonstrated stable ferroelectricity down to the ultimate monolayer thickness for out-of-plane ferroelectrics ($MoTe_2$ [192] and WTe_2 [193]) and in-plane/out-of-plane intercorrelated ferroelectrics (α-In2Se3 [198, 199] and SnTe [73]). Even in 2D ferroelectrics, however, the spontaneous polarization is also degraded with decreasing thickness when the 2D ferroelectric layer is vertically sandwiched with metals, owing to the depolarization field at metal/ferroelectric interfaces [83], as in 3D ferroelectrics. Therefore, in-plane ferroelectrics are superior to the out-of-plane and intercorrelated ferroelectrics in terms of preventing the depolarization field, given that the in-plane device structure enables a large gap between the electrodes.

The orthorhombic group-IV monochalcogenide (MX; M = Sn/Ge and X = S/Se), a purely in-plane 2D ferroelectric, has attracted considerable interest [30, 206, 219, 220, 51, 135] because ferroelasticity and ferroelectricity have been predicted as multiferroicity with a larger spontaneous polarization (P_s = 1.81–4.84×10^{-10} C/m) [30, 206], compared with the above-mentioned 2D ferroelectrics. Moreover, the existence of spontaneous polarization guarantees piezoelectricity, and a remarkable piezoelectric coefficient of $d \sim$ 75–251 pm/V has also been predicted [206], which is much larger than that of MoS_2 ($d \sim$ 4 pm/V) [28] and comparable to that of $Pb(Zr_xTi_{1-x})O_3$ (d ∼ 300 pm/V). These properties dominantly originate from a puckered structure along the armchair direction as a strong anisotropy analogue of black phosphorus. Given

that MX is not a typical insulator for 3D ferroelectrics but a semiconductor, these properties will provide multifunctionalities in nanoscale devices. Among the MXs, SnS is the best because SnX is more chemically stable than GeX [71, 92] and the Curie temperature of SnS is higher than that of SnSe [135]. Very recently, Bao et al. reported a ferroelectric device of bulk SnS (∼15 nm), breaking the centrosymmetry by applying an external electric field [159]. As the few-to-monolayer SnS has been investigated only by piezoresponse force microscopy (PFM) owing to its small size of several tens of nanometers, the demonstration of a ferroelectric device for monolayer SnS has been challenging. Ferroelectricity in SnS has the odd–even effect owing to the stacking sequence of the centrosymmetric AB staking, as shown in Fig. 4-10a. The centrosymmetry exists in the even-number layers so that ferroelectricity is expected only in the odd-number layers and becomes prominent in few-to-monolayer SnS [30, 51, 159]. However, the synthesis of a high-quality monolayer SnS in the micrometer-size scale suitable for device fabrication has not been achieved [109, 86, 107], because the interlayer interaction is strong due to the lone pair electrons in the Sn atoms, which generate a large electron distribution and electronic coupling between adjacent layers [87, 161].

Here, we report an in-plane ferroelectric device of a micrometer-size monolayer SnS grown by physical vapor deposition (PVD), where the growth conditions are precisely controlled to balance the adsorption/desorption of SnS. The Raman spectrum for monolayer SnS indicates high crystalline quality and strong anisotropy. Second harmonic generation (SHG) spectroscopy reveals that, unlike bulk SnS, monolayer SnS is non-centrosymmetric. Ferroelectric switching is successfully demonstrated for the monolayer device at room temperature (RT). Remarkably, for thin SnS below a critical thickness (∼15 layers, L), the SHG signal and ferroelectric switching are also observed in the even-number SnS, thus overcoming the odd–even effect, which suggests that ultrathin SnS is grown in an unusual stacking sequence lacking centrosymmetry.

4.3.1 Experimental Methods

PVD growth. SnS crystals were grown by a home-built PVD growth furnace with three heating zones (Fig. 2-23). A commercially available SnS powder was used as a source. To promote lateral growth, we used a freshly cleaved mica substrate sized 1 cm × 1 cm × 0.5 mm, whose surface is atomically flat. N_2 carrier gas was introduced into the furnace through the mass flow controller and the growth pressure was reduced to 10 Pa by a vacuum system to enhance the SnS desorption during the growth.

Optical characterizations. μ-Raman spectra were measured using a 488 nm excitation laser, whose penetration depth is ∼20 nm in SnS. The nominal $1/e^2$ spot diameter and laser power on the sample surface were 2.5 μm and 0.5 mW, respectively. To avoid degradation of SnS during the measurement, the samples were measured in the vacuum. The SHG measurements were conducted using a mode-locking Ti:sapphire laser (wavelength: 850 nm, pulse width: ∼150 fs and repetition rate: 80 MHz) in a home-built optical microscope under the backscattering configuration. The laser pulse was focused to a spot size ∼1.1 μm on the sample by a 100× objective lens. The backscattered SHG signals were sent into a 0.75-m monochromator and detected by a nitrogen-cooled CCD camera. For polarization-resolved SHG, the sample was mounted on a motorized rotational stage. The linear polarization of the excitation laser and SHG signals was selected and analyzed separately by polarizers and half-wave plates.

Ab initio Simulation. We have used the Vienna ab initio simulation package (VASP) to perform first-principles calculations based on density functional theory to study geometric and electric properties [221]. The exchange and correlation potentials are the Perdew-Burke-Ernzerhof (PBE) functional and is treated using the generalized gradient approximation (GGA) [222]. We employed the Monkhorst-Pack scheme to sample reciprocal space with Γ-centered 16 × 16 × 1 grid for geometry relaxations of 2D systems and 16 × 16 × 4 grids for that of bulk system. The plane-wave basis cutoff energy is set to be 500 eV. The convergence criterion is set to be 10-5 eV for energy in SCF cycles. And the full relaxation is continued until the residual force is less than

0.01 eVÅ^{-1}. We set 25 Åvacuum perpendicular to the 2D plane is used to avoid the interaction between replaced atoms. In addition, Grimme's DFT-D2 [223] method implemented in VASP is invoked to correct the vdW-like interaction existing in these systems. Moreover, we calculated phonon dispersion at Γ-point based on density functional perturbation theory. In addition, the calculation of phonon dispersion and irreducible representation has been implemented using phonopy [224].

Device fabrication and transport characterization. Two-terminal devices were fabricated with electrode pattering using standard electrode beam lithography. Electrode metals (In, Al, Ag, Cu, Ni, Pd, and Au) were deposited *via* thermal evaporation, followed by additional Au deposition as passivation for the source/drain metals. The electrical transport characteristics were measured in vacuum to avoid sample degradation. The Q–E curves were measured by a ferroelectric evaluation system (FCE-1A, Toyo corporation) with samples set in vacuum.

4.3.2 Growth of few-to-monolayer SnS

SnS has the puckered structure along the armchair direction distorted from the NaCl structure (Figs. 4-10a and b), leaving the lone pair electrons in the Sn atoms. The lone pair electrons contributes to the strong interlayer force [87, 161]. Therefore, the in-situ observation of SnS growth has confirmed a very high growth rate in the perpendicular direction [162]. Thus, monolayer SnS has been realized by molecular beam epitaxy growth, although only with a limited crystal size of several tens of nanometers [159]. Otherwise, the minimum thickness was 5.5 nm *via* PVD growth [86]. To suppress the perpendicular growth rate, SnS desorption during the PVD growth was precisely controlled with growth pressure and temperature (Fig. 2-23). Consequently, a thickness controllable PVD process was realized from bulk to monolayer thickness (Fig. 4-10c and 4-11). Fig. 4-10d and Fig. 2-26 show atomic force microscopy (AFM) topographic images of SnS grown on mica substrates. For bulk SnS thicker than ∼16 nm, the SnS crystal has a sharply defined diamond shape that reflects the thermodynamically stable crystal facets (Fig. 4-10b). With decreasing temperatures of the SnS source powder (T_{source}) and substrate (T_{sub}), the SnS thickness decreased

and the corner became rounded. The typical temperatures (T_{source}, T_{sub}) for the SnS crystals with thicknesses of ∼36 nm and ∼3-4 nm were (590°C, 530°C) and (530°C, 410°C), respectively. Finally, at T_{source} = 470°C and T_{sub} = 410°C, monolayer-thick SnS was realized with micrometer size of up to ∼5 Âţm, which is a reasonable size for the device fabrication. Note that monolayer-thick SnS has an atomically flat surface without wedding cake morphology owing to the Stranski–Krastanov growth mode [159] or spiral growth assisted by a screw dislocation [162]. The rounded shape could be caused by the SnS desorption during the growth and an insufficient growth time to reach the thermodynamic equilibrium state for thin SnS [107, 162].

The small "holes" found in the AFM image of monolayer-thick SnS are probably etch pits created during the growth. When a post-growth annealing was performed for the SnS crystals, aligned square-shaped etch pits were created, indicating a single crystalline nature (Fig. 2-28). Moreover, a lattice matching of SnS with the mica substrate was detected by the in-plane X-ray diffraction (XRD) measurement, suggesting a strong SnS/mica interaction (Fig. 4-12) [225]. Fig. 4-12a shows in-plane XRD Φ-scan for PVD grown SnS on mica measured with the samples tilted at an angle of $\chi = 23.3°$, which corresponds to the angle between SnS(016) and (001) planes [225]. The growth time was changed from 2 to 15 min. The 15-min grown sample was full covered with >20 nm SnS crystals, whereas the 2-min grown sample has small coverage with isolated multi-layer SnS crystals. As a reference, the Φ-scan of intrinsic mica substrate is shown at the bottom. For mica, six peaks were observed with an interval of 60°. The fluctuation of diffraction intensity is probably owing to an inhomogeneous distribution of SnS crystals on mica substrate. Fig. 4-12b shows a Φ-scan for few-layer SnS with the selected region as shown in 4-12a. The Φ-scan of SnS(016) plane indicates 12 peaks with an interval of 30° for few-layer and >20 nm SnS, which agrees well with the reported data for SnS on mica [225]. These results indicate a strong interaction between SnS and mica probably due to a lattice matching. Although the crystallographic interaction between SnS/mica may disappear with increasing the SnS thickness, there is still a preferred orientation for SnS growth as long as the thickness is several-tens nanometers.

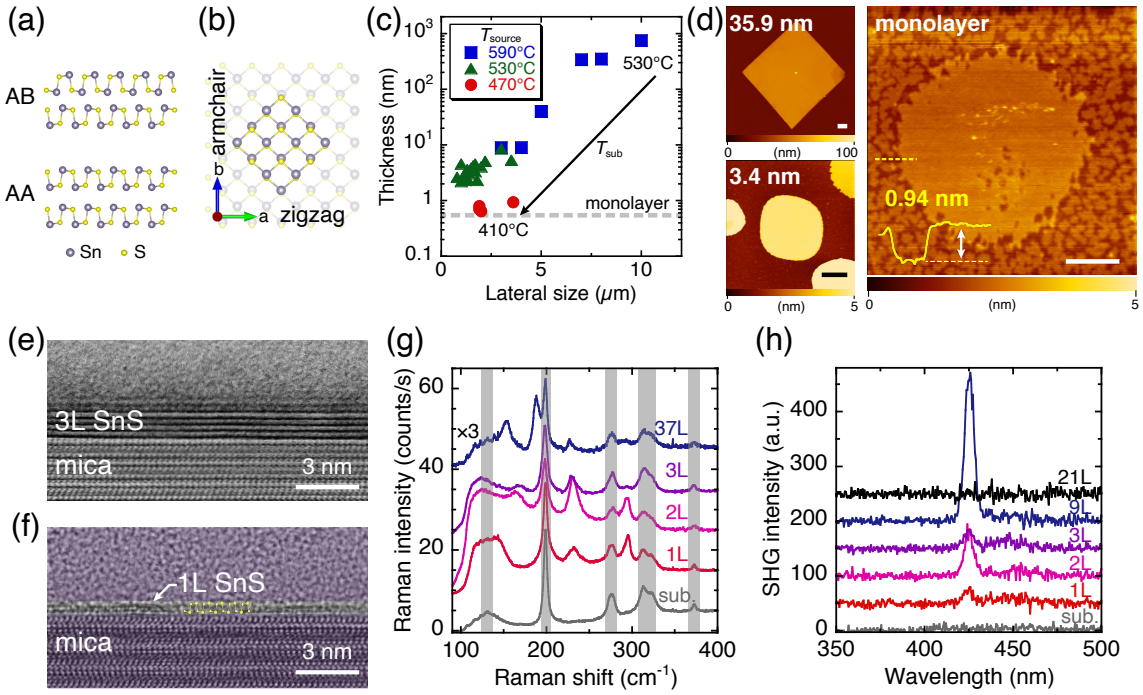

Figure 4-10: Characterization of few-to-monolayer SnS. (a) Cross-sectional crystal structures of SnS along the armchair direction with different stacking sequences: noncentrosymmetric AA and centrosymmetric AB staking. (b) Top view of crystal structure of monolayer SnS, whose two-fold axis is along the armchair direction. Highlighted area shows thermodynamically stable facets. (c) Thickness versus lateral size of PVD grown SnS with changing T_{source} and T_{sub}. (d) AFM topographic images of SnS crystals with different thicknesses from bulk to monolayer. The scale bars represent 1 μm. (e) Cross-sectional STEM image of trilayer SnS. (f) Cross-sectional TEM image of monolayer SnS along the armchair direction. As guide to the eye, all of the region except the SnS crystal is shaded, and the atomic model is overlaid on the TEM image. (g) Thickness dependence of Raman spectrum for SnS at 3 K. The peaks in the hatch come from the mica substrate. (h) SHG spectra for SnS with different thicknesses from bulk to monolayer at RT.

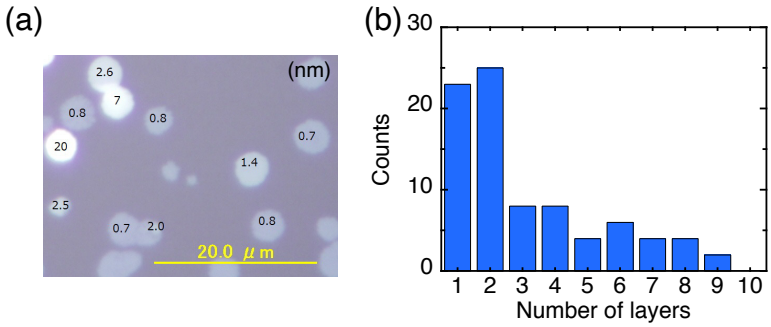

Figure 4-11: Thickness distribution of PVD grown SnS. (a) Typical optical image and (b) thickness distribution histogram of SnS on mica with different thickness obtained via the same substrate and growth conditions (Fig. 2-23).

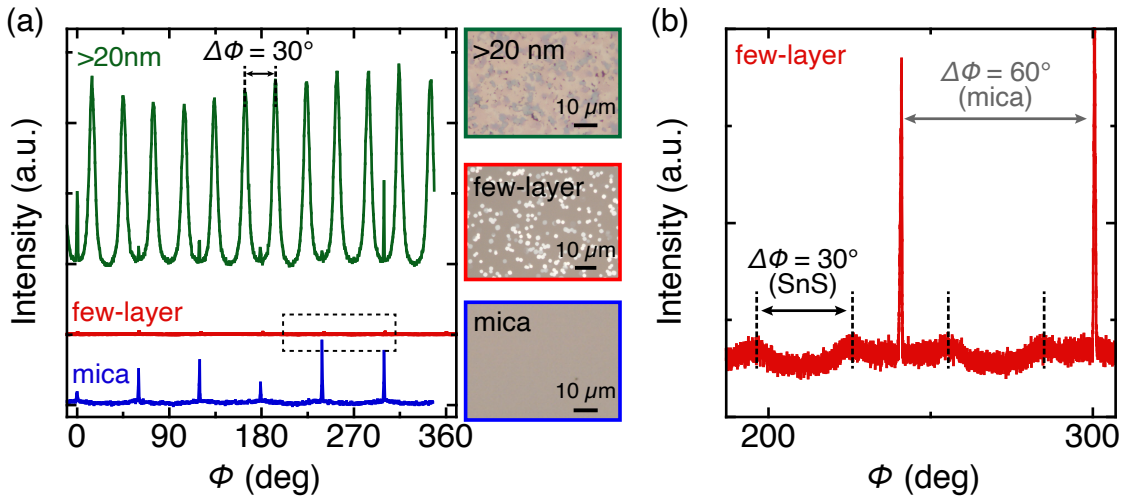

Figure 4-12: XRD analysis of SnS grown on mica.

Fig. 4-10e shows a cross-sectional bright-field scanning transmission electron microscopy (STEM) image of trilayer SnS. For trilayer SnS, the composition ratio Sn : S was 1 : 0.8 from energy-dispersive X-ray spectroscopy (EDS) (Fig. 2-30a), indicating the absence of other S rich phases (e.g., SnS_2 and Sn_2S_3). Interestingly, from the TEM image of trilayer SnS, the monolayer thickness d_{1L} was determined to be 5.8 Å, larger than that of the mechanically exfoliated bulk sample ($d_{1L} \sim 5.4$ Å[161]). This expansion suggests the possibility of an unusual stacking sequence rather than the AB stacking. From an ab initio simulation, the AA stacked bilayer SnS (Fig. 4-10a) indicates $d_{1L} = 6.34$ Å, larger than $d_{1L} = 5.85$ Åfor the AB stacking. For the TEM observation of monolayer SnS, the crystal orientation was determined beforehand by polarized Raman spectroscopy, as discussed later, because the TEM image of monolayer SnS is much more indistinct than that of the bulk crystals owing to the degradation during the sample preparation by the focused ion beam (FIB) process and the TEM observation itself. By adjusting the zone axis, it can be observed that two sub-layers have a monolayer structure, which matches well with the configuration along the armchair direction (Fig. 4-10f).

Fig. 4-10g shows Raman spectra for PVD grown SnS with different thicknesses from bulk to monolayer, measured at 3K. For a bulk SnS (∼37 L), specific peaks were observed at 153.7, 188.3, 227.6, and 291.8 cm^{-1} in addition to the peaks from mica substrate at ∼131, 198.9, 276.0, 312.8, 322.9, and 372.5 cm^{-1}. These peak positions are well consistent with those of bulk SnS *via* mechanical exfoliation or PVD [109, 86, 107, 161]. With a decreased thickness from trilayer to monolayer, the Raman peak positions at approximately 230 and 293 cm^{-1} almost coincided with each other, while those between 140 and 190 cm^{-1} changed significantly. For monolayer SnS, a Raman peak was observed at ∼145 cm^{-1}, and also at 232.4 and 295.0 cm^{-1}. A similar trend was also obtained at RT (Fig. 2-34). Those values will be discussed later with the results of polarized Raman spectroscopy and the phonon mode calculation.

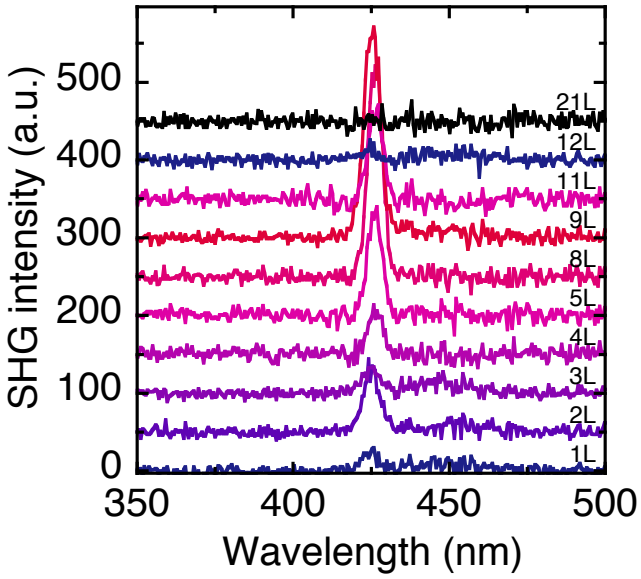

Figure 4-13: Typical RT SHG spectra for SnS with different thicknesses.

4.3.3 Non-centrosymmetry in Monolayer SnS

To determine the non-centrosymmetry, which is required for ferroelectricity, μ-SHG spectroscopy [226, 215] was carried out for different thicknesses, from bulk to monolayer (Fig. 4-10h). An 850-nm laser was used as the excitation source. The bulk SnS, thicker than ∼21L, showed no SHG signal, while SnS under the critical thickness of ∼15L showed SHG signal at $\lambda = 425$ nm. Although the odd–even effect was expected for the AB stacked SnS, it was found that all the ultrathin SnS flakes, including the even-number layers, showed SHG signals below the critical thickness (Fig. 4-13). For confirmation, mica substrate was measured under the same conditions. Although it is known that a weak SHG signal can be generated even for the centrosymmetric material due to the surface SHG effect [226], no SHG signal was detected from the mica surface (Fig. 4-10h). These results suggest an unusual stacking sequence of the PVD grown SnS, along with the results of interlayer distance from the TEM image.

Fig. 4-14 shows the result of SHG measurement for 9L SnS after the annealing at 410°C. As shown in the inset AFM image, a square-shaped etch pit were formed near the crystal edge. Even though no other etch pits were found in much of the SnS surface region, SHG signal was undetectable for the annealed sample probably due to

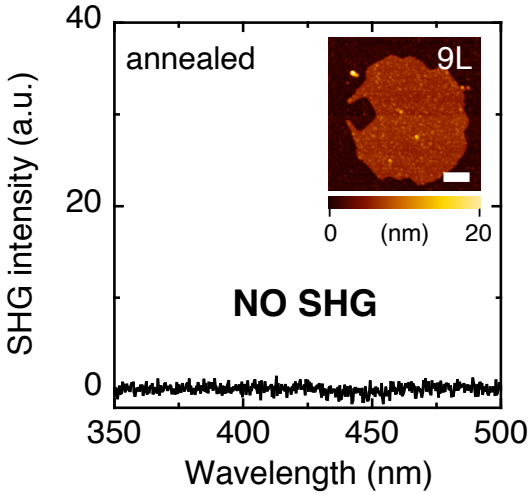

Figure 4-14: SHG measurement for 9L SnS after the annealing at 410°C. The scale bars represent 500 nm.

the introduction of extrinsic defects. This result confirms that non-centrosymmetry and ferroelectricity are very sensitive to the crystalline quality.

4.3.4 Optical Anisotropy in SnS

In monolayer SnS, the dipole moment along the armchair direction leads to spontaneous polarization [30, 206]. Different from the thick SnS, it is difficult to identify the orientation of the present few-to-monolayer crystals from their shape, as mentioned above. To characterize the in-plane anisotropy, the angular dependences of both Raman and SHG have been investigated (Fig. 4-15a). Fig. 4-16a shows the polarization dependence of the Raman spectrum for monolayer SnS under the parallel polarization configuration at 3 K. Specific peaks were observed at approximately 234 and 294 cm^{-1}, which are consistent with the results of the unpolarized Raman measurement, although it was difficult to determine the precise peak position between 100 and 200 cm^{-1} because of the overlaps with peaks from the substrate. To investigate the relationship between the Raman active modes and stacking sequences for SnS, an ab initio calculation was carried out using the Vienna ab initio simulation package (VASP) [221]. Fig. 4-17a shows a typical example of phonon dispersion along the path passing through the main high-symmetry k-points in the irreducible Brillouin zone of

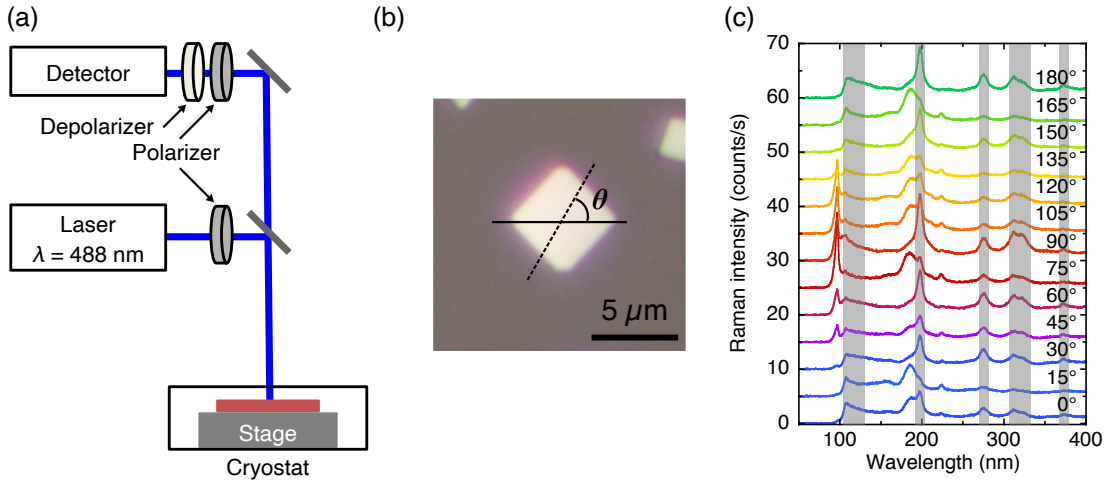

Figure 4-15: (a) Schematic diagram of polarized Raman spectroscopy. The polarization angle was changed through rotating the polarizers. The second polarizer was set to be parallel or perpendicular to the polarized incident light for Raman measurement. (b,c) Polarized Raman spectroscopy for bulk SnS at 3K under the parallel polarization.

monolayer SnS. Fig. 4-17b and Fig. 4-18 summarize the Raman active phonon modes for the AB and AA stacked SnS with different number of layers. For bulk SnS, the experimental results almost agree with the calculated results, whereas there are large differences between experiments and calculation for the few-to-monolayer SnS. The origin of this difference is probably the strain incorporated through the interaction with the mica substrate, as discussed above. By comparing the calculated Raman active modes and experimental results, the Raman signals of the monolayer at 234 cm^{-1} is attributed to the A_1 mode of the C_{2v} point group (Fig. 4-18). As expected, the Raman peak intensity at 234 cm^{-1} shows a significant change as a function of the rotation angle (Fig. 4-16a). The Raman tensor R for the A_1 mode of C_{2v} point group can be written as [227]

$$R(A_1) = \begin{pmatrix} |A|e^{i\varphi_A} & 0 & 0 \\ 0 & |B|e^{i\varphi_B} & 0 \\ 0 & 0 & |C|e^{i\varphi_C} \end{pmatrix} \tag{4.17}$$

which is the same as the A_g mode of bulk SnS (D_{2h} point group) that shows

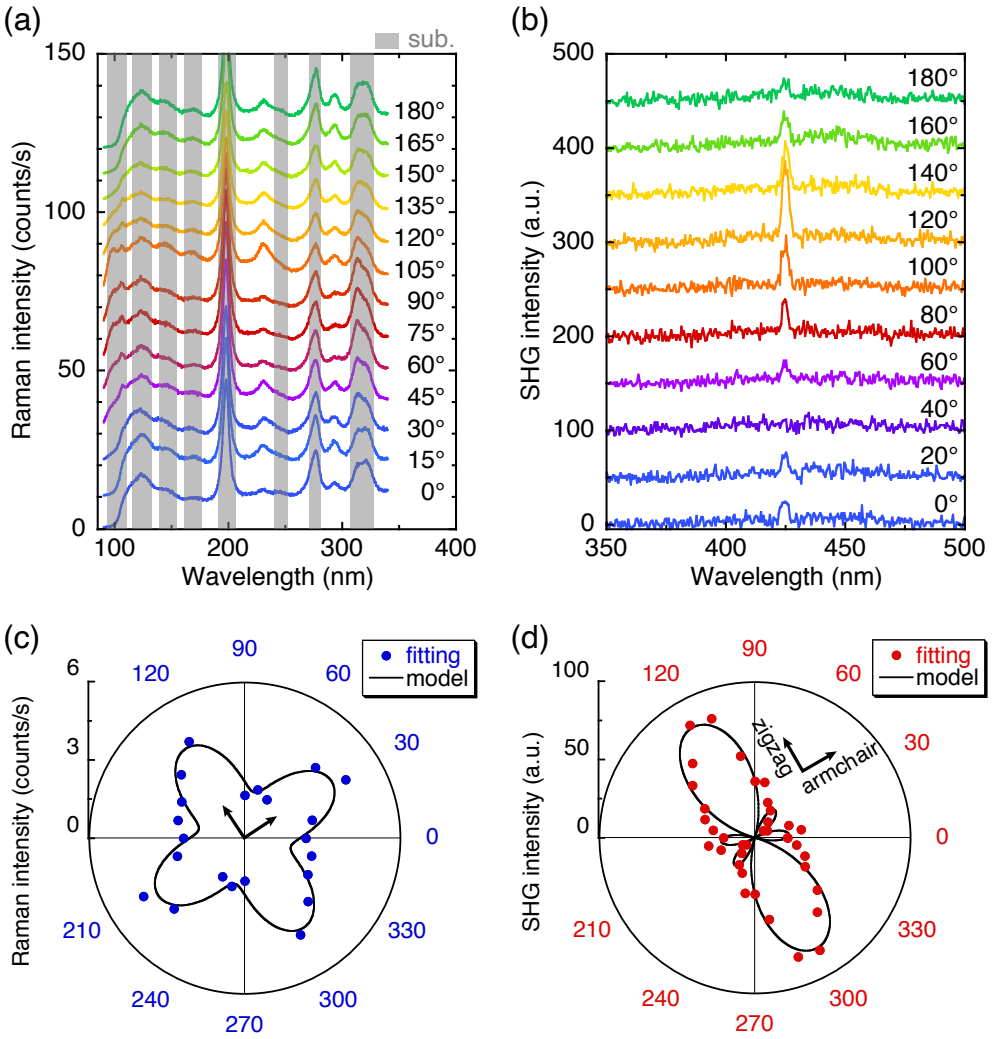

Figure 4-16: Optical anisotropies of monolayer SnS. (a,b) Polarization dependences of Raman (3 K) and SHG (RT) spectrum of monolayer SnS, with parallel and perpendicular polarization, respectively. The gray shaded region of Raman spectra represents Raman peak from mica substrate. (c,d) Polar plots of Raman intensity at ∼234.0 cm^{-1} and SHG intensity at 425 nm, respectively. The inset axes show the armchair and zigzag directions.

a strong anisotropy [109, 86, 107]. The unitary vector of incident light is $e_i = (cos\theta, sin\theta, 0)$, where θ is the polarization angle defined as the angle between the incident light and the zigzag direction of SnS crystal. The unitary vector of scattered light is $e_s = (cos\theta, sin\theta, 0)$ and $(sin\theta, cos\theta, 0)$ for the parallel ($\|$) and perpendicular ($\perp$) polarization, respectively. For the polarized Raman intensity of the A_1 peak, the angular dependences can be calculated using the following equations [107]:

$$I_{\|} \propto |A|^2 cos^4\theta + |B|^2 sin^4\theta + 2|A||B| cos^2\theta sin^2\theta cos\varphi_{BA} \quad (4.18)$$

$$I_{\perp} \propto \frac{|A|^2 + |B|^2 - 2|A||B| cos\varphi_{BA}}{4} sin^2 2\theta \quad (4.19)$$

where $\varphi_{BA} = |\varphi_B - \varphi_A|$ is the phase difference between the Raman tensor elements $|A|e^{i\varphi_A}$ and $|B|e^{i\varphi_B}$. By fitting the experimental data with Eq. 4.18, the crystal orientation was revealed (Fig. 4-16c). As in the polarized Raman spectroscopy, Fig. 4-16b shows a strong angular dependence of SHG for monolayer SnS with perpendicular polarization configuration. For the polarized SHG intensity under parallel and perpendicular polarization, the angular dependence in the C_{2v} point group is written as [228]

$$\chi^{(2)}_{\|} = \left(\chi^{(2)}_{xyx} + \chi^{(2)}_{yxx}\right) sin\theta cos^2\theta + \chi^{(2)}_{yyy} sin^3\theta \quad (4.20)$$

$$\chi^{(2)}_{\perp} = \chi^{(2)}_{yxx} cos^3\theta \left(\chi^{(2)}_{yyy} - \chi^{(2)}_{xyx}\right) cos\theta sin^2\theta \quad (4.21)$$

where $\chi^{(2)}_{ijk}$ is the SHG susceptibility tensor element along the different directions. We fitted the experimental data based on Eq. (5) to determine the zigzag/armchair orientation, as shown in Fig. 4-16d. The measured patterns agree well with the theoretical model. The anisotropy revealed from the polarized Raman and SHG spectra indicates again the high crystallinity of monolayer SnS.

To compare the angular dependence for bulk with the monolayer, polarized optical measurements were performed for 10L SnS, as shown in Fig. 4-19. Note that

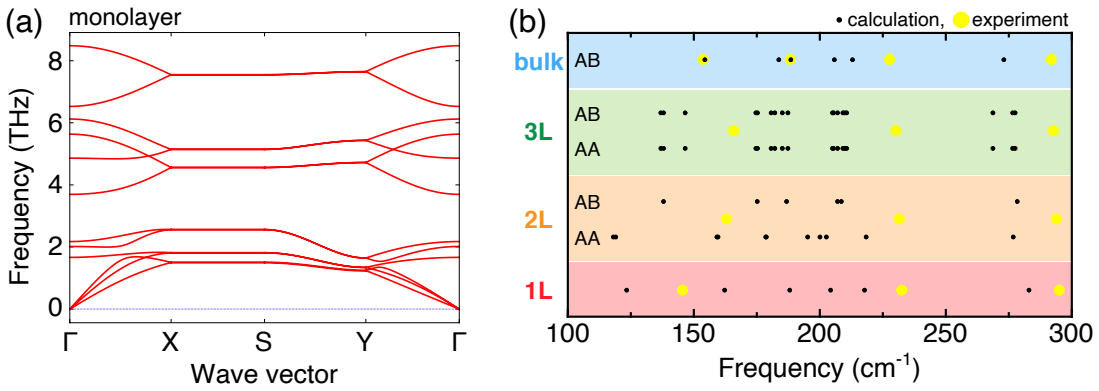

Figure 4-17: Theoretical calculation of phonon dispersion and Raman active modes. (a) Phonon dispersion of the monolayer SnS. (b) Comparison of calculated Raman active modes and experimental Raman peak positions for SnS with different thicknesses (monolayer, bilayer, trilayer, and bulk) and stacking sequences (AA and AB).

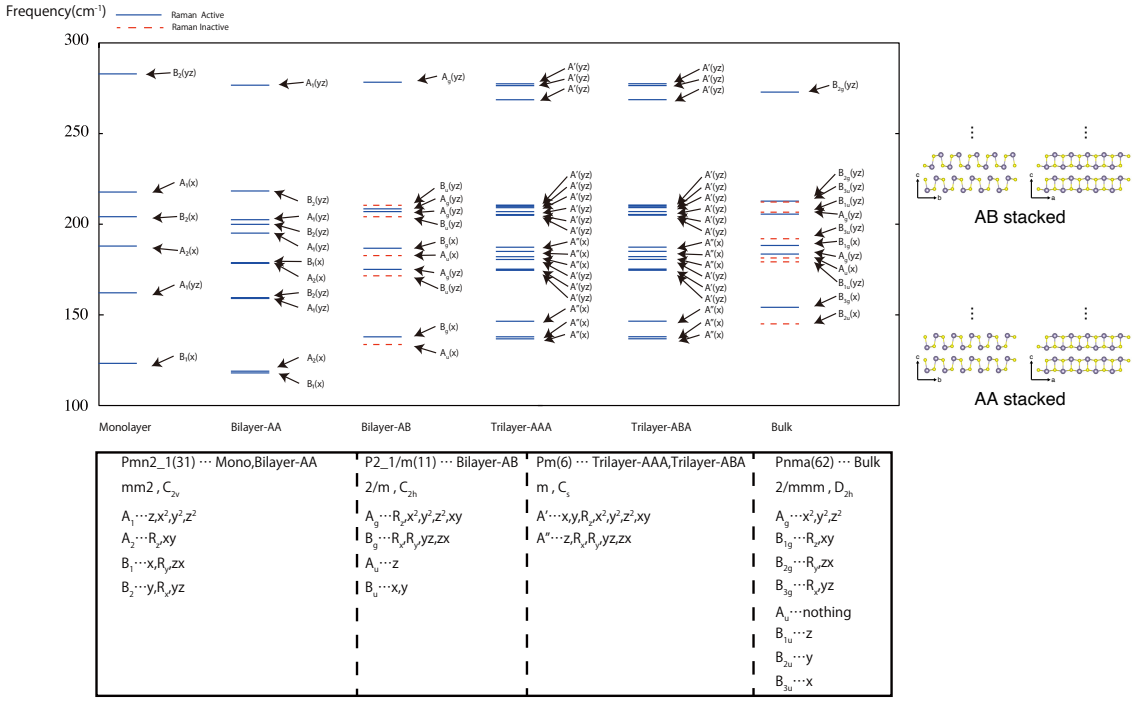

Figure 4-18: Calculated Raman active/inactive phonon modes for monolayer, AA/AB-bilayer, AA/AB-trilayer, and AB-bulk SnS. The point group, irreducible representation of phonon modes, and vibration direction are summarized.

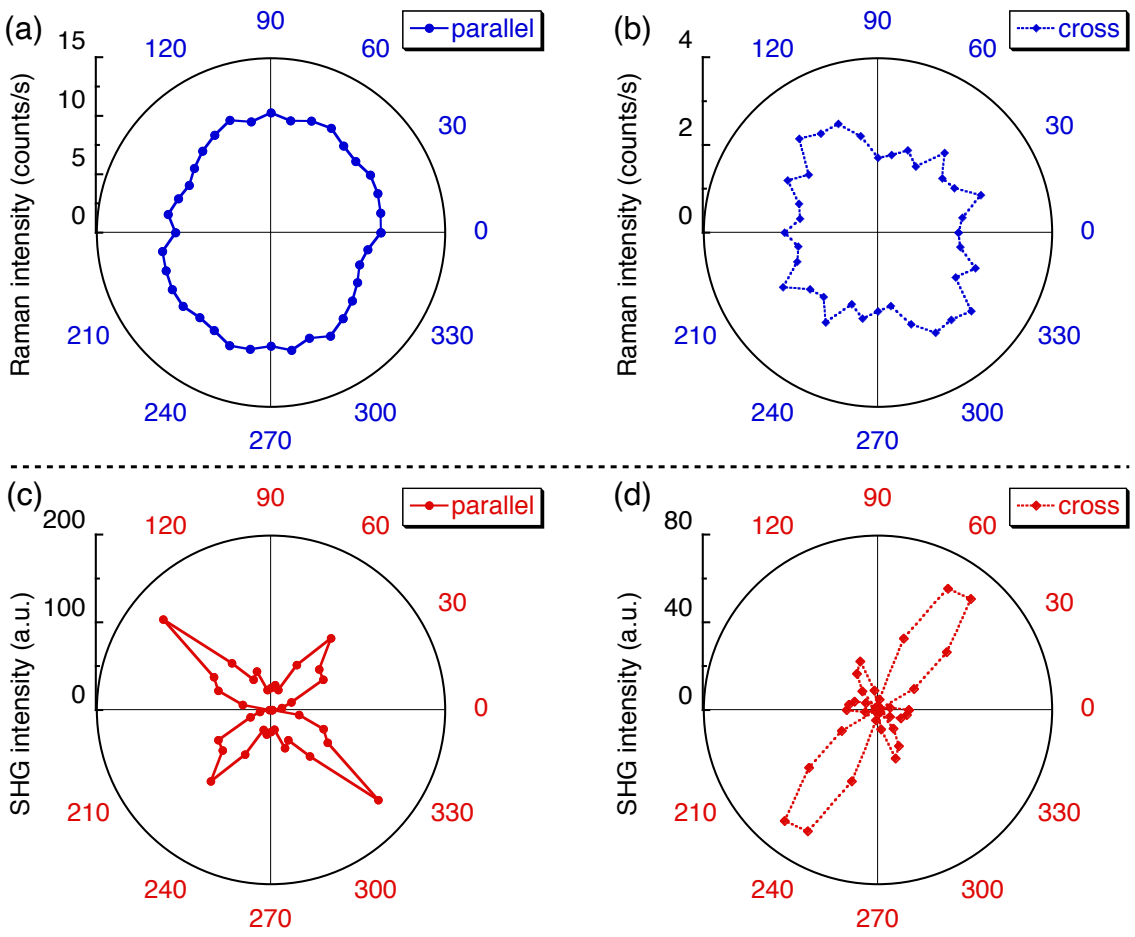

Figure 4-19: Angular dependence of optical measurements for 10L SnS: Raman intensity at ~226 cm^{-1} under (a) parallel and (b) perpendicular polarization, and SHG intensity under (c) parallel and (d) perpendicular polarization.

different 10L SnS samples were used for each measurement. A strong anisotropy was confirmed for the SHG intensity, though angular dependence were slight for the Raman measurements. This discrepancy is probably due to the difference of crystalline quality, which also resulted in the large distribution of SHG intensity even for the same thickness, as discussed later (Fig. 4-29)

4.3.5 Metal Selection for Schottky Contact

Switching of the spontaneous polarization and SHG is required to prove the ferroelectricity in SnS. A tip poling experiment by using scanning probe microscopy is an effective way to observe the polarization switching for the local area. However,

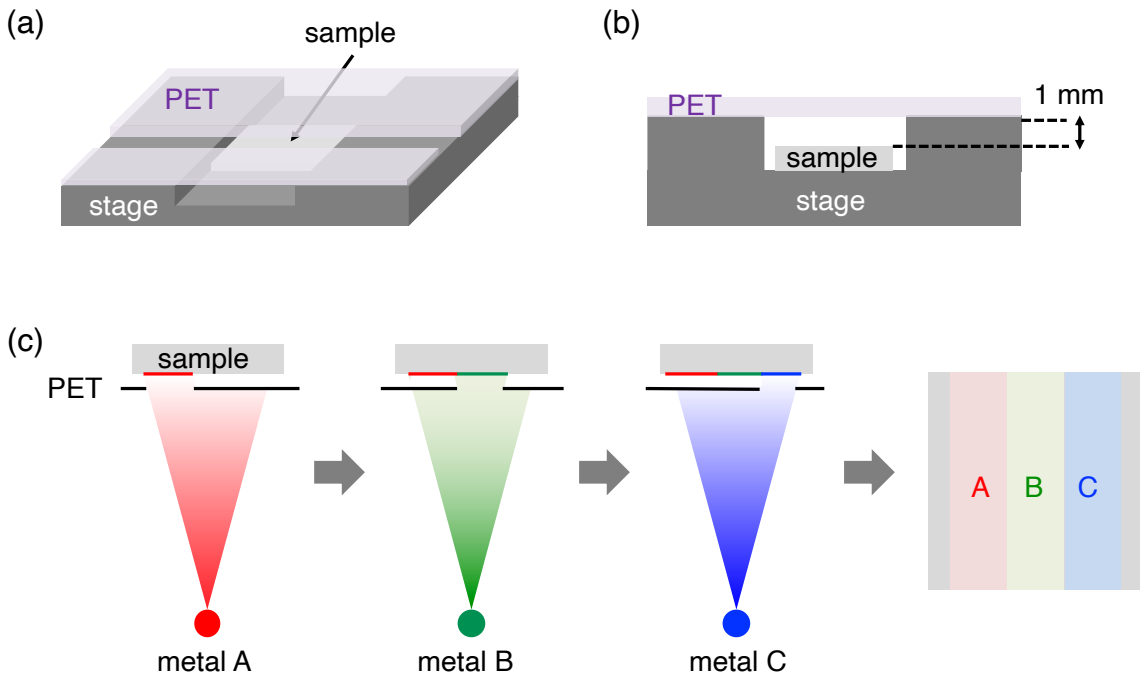

Figure 4-20: Fabrication method of multiple metal depositions. (a) Bird's-eye view and (b) cross-sectional view of sample stage with PET shield. (c) Step-by-step deposition of multiple metals.

it is more difficult to detect the trace of spontaneous polarization in SnS than that in out-of-plane ferroelectrics because in-plane ferroelectricity does not respond to the out-of-plane electric field applied by the probe tip. To demonstrate the in-plane polarization switching, in-plane two-terminal devices with source/drain electrodes on SnS crystals were fabricated (Fig. 4-20 and 4-21). After the EB lithography for the electrodes, the sample was set on a home-made stage with hollow (Fig. 4-20a,b). The sample surface was partially covered with the PET shield, which was placed approximately 1 mm apart from the sample. Each metal was deposited step-by-step with changing the position of the PET shield by using a standard thermal evaporator (Fig. 4-20c). Finally, SnS devices with different electrode metals were obtained on the same wafer, as shown in Fig. 4-21a. During the fabrication process, the exact locations of SnS crystals were captured by optical images so that only one crystal were contacted by two adjacent electrodes. Note again that SnS is a semiconductor with energy gaps of 1.5 eV for monolayer and 1.1 eV for bulk [52], where channel conductance makes it difficult to identify the very small displacement current. To

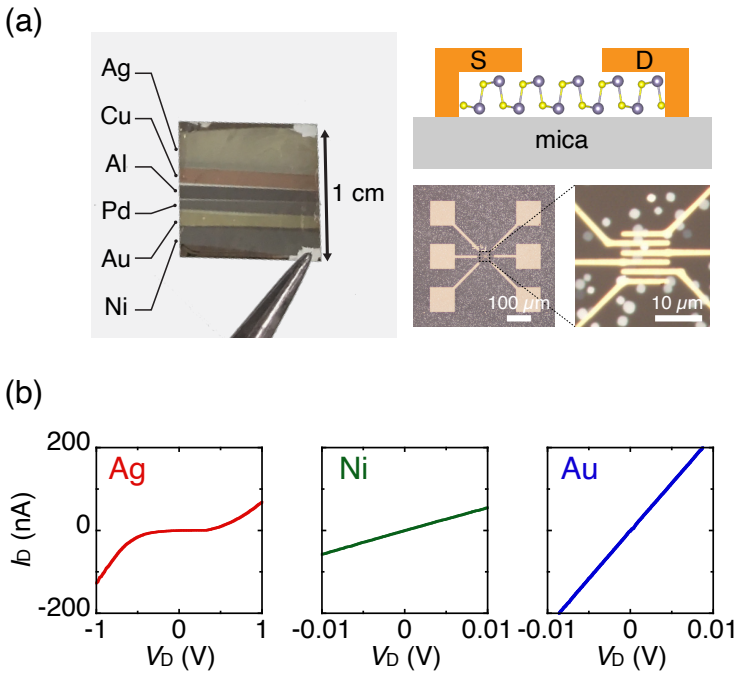

Figure 4-21: (a) Left: Photograph of mica substrate after the deposition of various metals with different work functions. Right: Cross-sectional schematic and optical images of two-terminal SnS devices. Typical channel length l_{ch} and width w_{ch} were l_{ch} = 0.4–0.8 μm and w_{ch} = 3–5 μm, respectively. (b) I_D–V_D curves for bulk SnS with different metal contacts: Ag, Ni, and Au.

prevent the channel conductance by forming an insulator-like interface, the Schottky barrier height (SBH) has been investigated by changing the metal work function (Φ_m). After bulk SnS (∼20 nm) was grown on the mica substrate, a standard electron beam lithography was performed followed by multiple metal depositions with a series of metals (In, Al, Ag, Cu, Ni, Pd, and Au), as shown in Fig. 4-21. Assuming that the metal/SnS interface is ideal and free from Fermi level pinning [176], the SBH will strongly depend on Φ_m. In such a case, the metal with smaller Φ_m is preferable to increase the SBH for the *p*-type semiconductor SnS [109, 161, 67, 150]. At RT, ohmic I_D–V_D curves were obtained for bulk SnS with metals of In, Cu, Ni, Pd, and Au, while Schottky I_D–V_D with Al and Ag (Fig. 4-21, and Fig. 4-22).

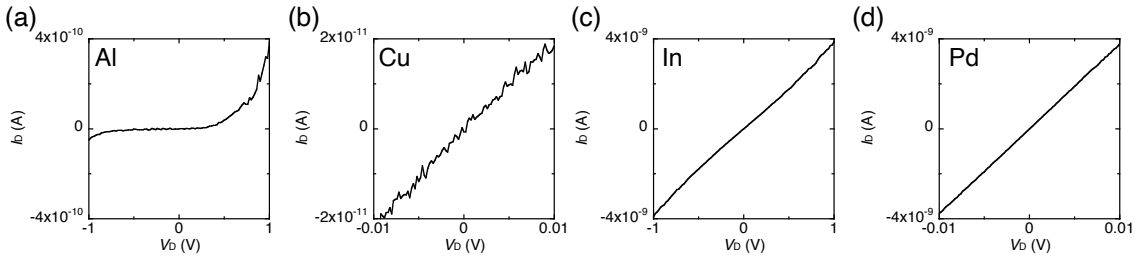

Figure 4-22: Typical I_{D}–V_{D} curves for bulk SnS with different contact metals: (a) Al, (b) Cu, (c) In, and (d) Pd.

4.3.6 Ferroelectric Switching in Few-layer SnS

Fig. 4-23 shows I_{D}–V_{D} curves for 9L SnS with the Ag contact measured by increasing the V_{D} sweep range at RT. Unlike the I_{D}–V_{D} curve without hysteresis for the ohmic Ni metal contact (Fig. 4-24), the Schottky Ag contact exhibited a well-reproducible hysteresis (Fig. 4-25). Although it is known that Ag could give memristor behavior owing to its high diffusivity [229, 230], no significant Ag diffusion was confirmed from the AFM images at the low resistive state (Fig. B-4). Moreover, the larger drain bias led to a larger window of hysteresis loop, distinguishing a maximum conductivity at approximately $V_{\mathrm{D}} = \pm 1V$.

To confirm that this hysteresis originates from the ferroelectric switching, a double-wave measurement was performed [231]. When V_{D} was applied from 0 to 2 V for two times, a current peak was observed only in the first sweep and it turned to be a highly resistive state in the second sweep (Fig. 4-26). Similarly, a negative V_{D} sweep (0 to -2 V) showed a current peak only once in the first sweep. This is because polar switching results in the current peak in the first sweep, but never in the second sweep because the direction of polarization is steady. Therefore, this result of double-wave measurement is strong evidence for the switching of spontaneous polarization, that is, ferroelectricity. It should be emphasized that that the crystal orientation of SnS was not determined before the electrode fabrication. Despite the fact that spontaneous polarization exists along the armchair direction, the I_{D}–V_{D} hysteresis loop was observed regardless of the initial crystal orientation that the external electric field is applied. This result suggests that the more flexible polarization switching due

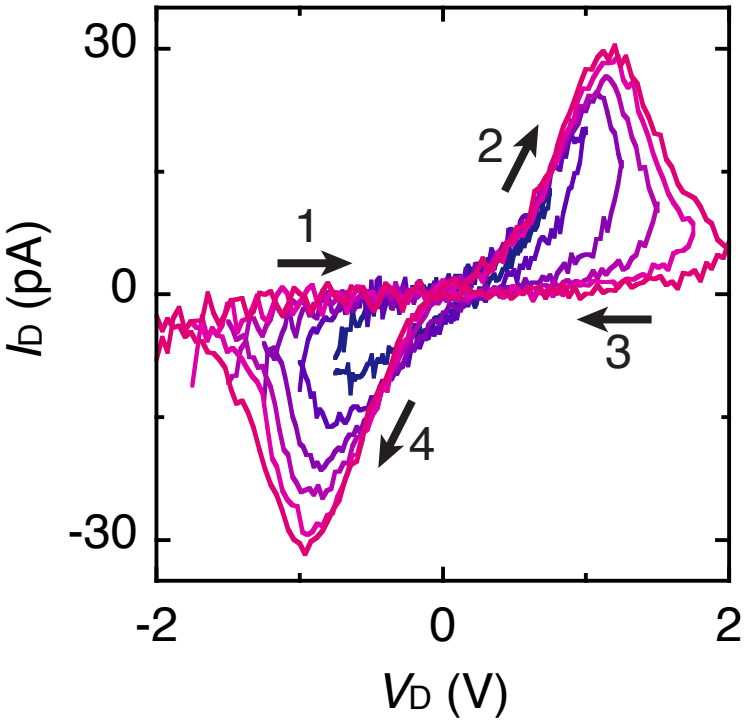

Figure 4-23: Ferroelectric switching behaviors of few-layer SnS.

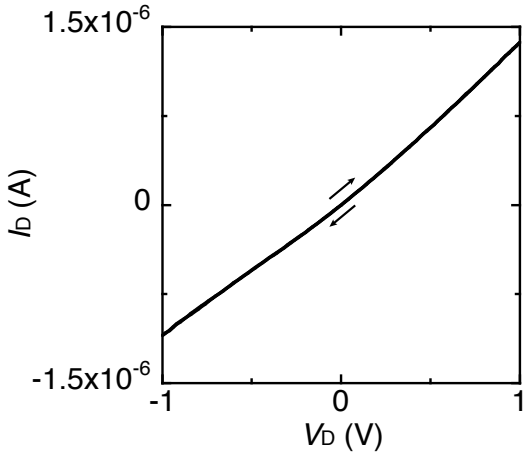

Figure 4-24: Typical I_D–V_D curve with Ni contact for few-layer SnS below the critical thickness for ferroelectricity.

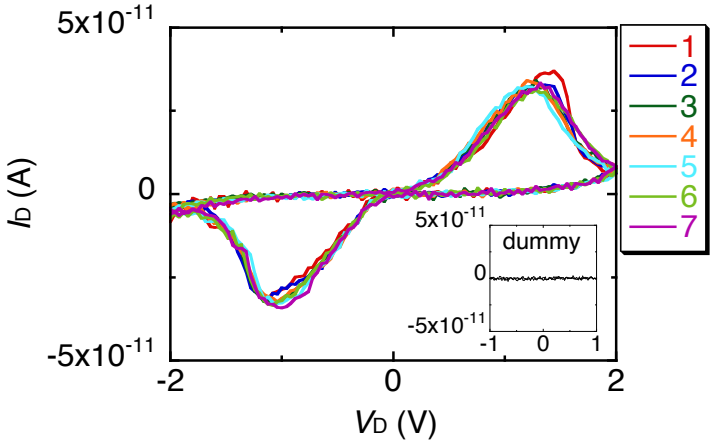

Figure 4-25: Ferroelectric switching characteristic of I_D–V_D for Ag/9L-SnS cycled 7 times at RT. Inset: I_D–V_D for a dummy sample without SnS. Ferroelectric hysteresis was absent for the dummy device without SnS. The reproducible switching characteristic was observed in the multiple measurements, indicating the stability of ferroelectricity.

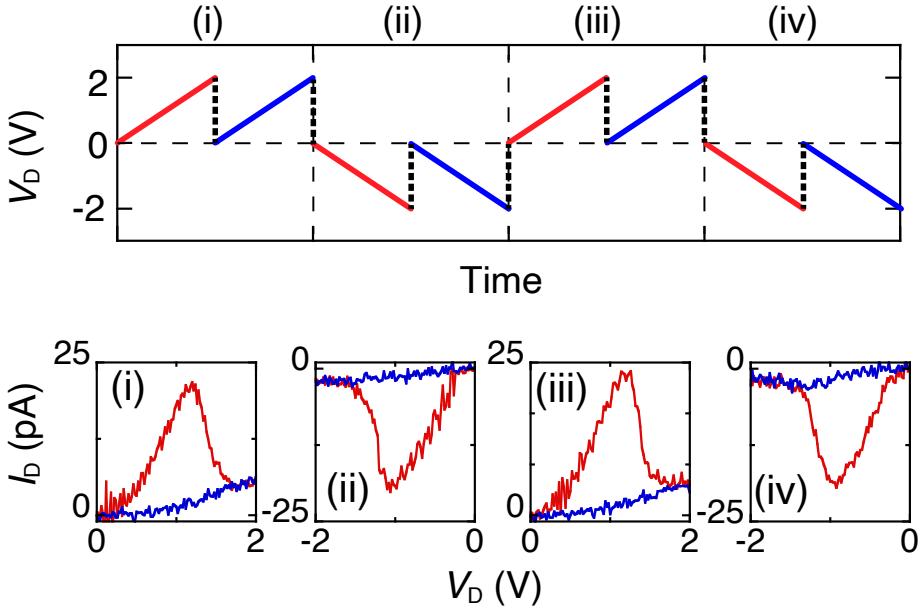

Figure 4-26: Double-wave measurement from 0 to 2 and 0 to −2 V. Top: applied voltage along time. The voltage was applied two times at the positive and negative bias repeatedly. Bottom: I_D–V_D curves for different sweeps (i)–(iv). The red and blue lines represent the first and second sweep, respectively.

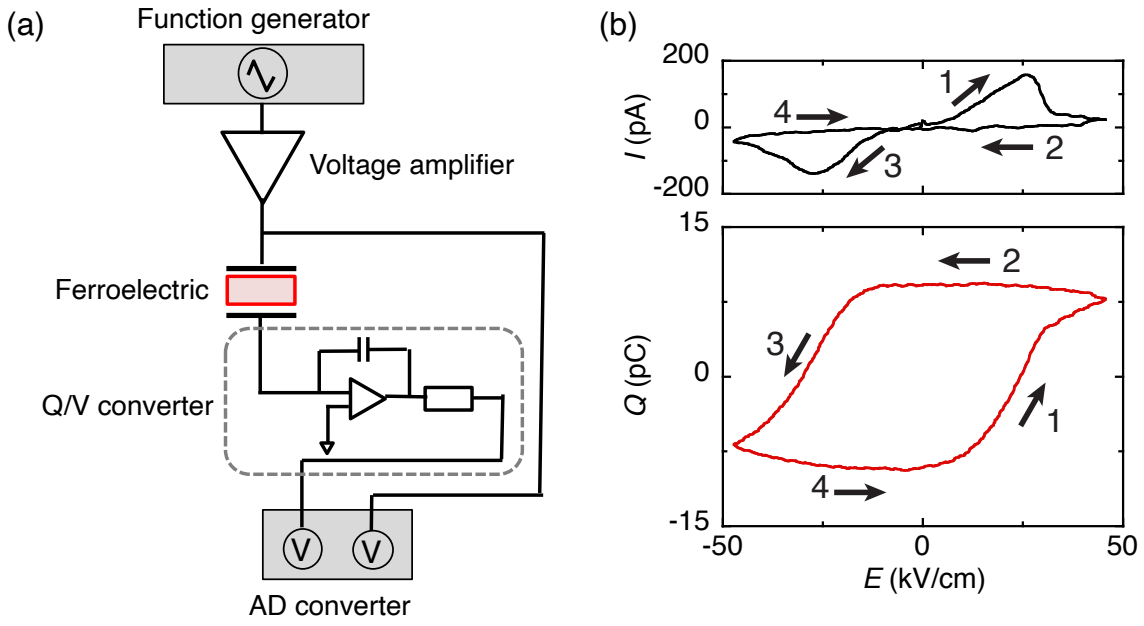

Figure 4-27: (a) Ferroelectric measurement system. (b) Ferroelectric resistive switching for Ag/SnS: current and charge versus nominal electric field measured by ferroelectric measurement system at 1 Hz and RT.

to the possible existence of the domain structure. Furthermore, even an external electric field along the non-ferroelectric zigzag direction could induce ferroelectricity with structural rearrangement into the armchair structure[232] in a similar way as ferroelasticity [30, 206].

To further analyze this switching behavior quantitatively, Q–E (Q is charge, and E is electric field) curve was measured using a ferroelectric evaluation system. When the AC bias at 1 Hz was applied ($0 \rightarrow +2 \rightarrow -2 \rightarrow 0$ V), an I–E curve drew a hysteresis loop very similar to the I_{D}–V_{D} curve under DC bias (Fig. 4-27). Here, E is assumed to be V_D/l_{ch}, where lch is the channel length, which should overestimate E because there is also a voltage drop at the Schottky contact. The Q–E loop corresponding to the I–E loop is shown at the bottom of Fig. 4-27. A distinct hysteresis loop was obtained with the charge of ∼9 pC, which is a characteristic of ferroelectrics in general when the external electric field switches the polarization to generate the displacement current. However, the remnant polarization $P_{\mathrm{r}} = Q/w_{ch}$, where w_{ch} is channel width, was determined to be $P_{\mathrm{r}} \sim 3$ μC/m, which is almost four orders of magnitude larger than the theoretical value of $P_{\mathrm{r}} = 260$ pC/m [206], as shown in Fig. 4-28. This

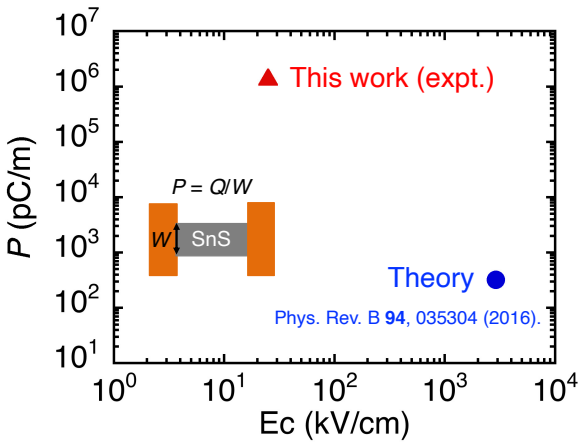

Figure 4-28: Comparison between theoretically [219] and experimentally (this work) determined spontaneous polarization and conceive electric field of SnS.

discrepancy suggests that the hysteresis loop is not mainly due to the displacement current. The hysteresis loop can be dominantly caused by the contribution of other factors in addition to the displacement current, as discussed below.

Considering it has been suggestively pointed out that the closed Q–E loop can be artificially obtained even for non-ferroelectric materials when they are lossy or leaky [233, 234], the large discrepancy on the remnant polarization for SnS is carefully discussed as follows. One possible case is for films with a large concentration of traps near the metal/film interface [234]. The number of traps required to reproduce the Q–E loop in Fig. 4-27 was estimated. As it corresponds to one in three of the total number of atoms in the SnS channel material, the traps are not the origin for the large P (see details in Chap B). The other case is the resistive switching [235], where a hysteresis loop similar to that in Fig. 4-27 has been discussed as an effect of SBH modulation at the metal/ferroelectric interface owing to the reversed polarization for the previous works on ferroelectric 2D materials ($MoTe_2$ [192], WTe_2 [193], α-In2Se3 [198, 199, 202, 203], SnTe [73], and $CuInP_2S_6$ [200, 201]). In the present study, the current flowing through the SnS channel was drastically suppressed by selecting the strong Schottky contact metal. Nevertheless, the present ferroelectric Q–E hysteresis loop is considered to be owing to the resistive change at the metal/SnS Schottky interface accompanied with polar switching because the displacement cur-

rent level for in-plane 2D devices is negligibly small. Moreover, the coercive electric field Ec, which originates this switching, was found to be ∼25 kV/cm for 9L SnS. This value is comparable to the experimental value for bulk SnS with gate-induced non-centrosymmetry (∼10.7 kV/cm) [159], whereas it is much smaller than the theoretical value for monolayer (1.8×10^3 kV/cm) [219]. This discrepancy between the experiment and calculation is probably related to the existence of a mobile domain wall or lattice strain in SnS caused by the difference in thermal expansion coefficients between SnS and the mica substrate in the real system [206].

4.3.7 Mechanism of Broken Odd–even Effect

For further understanding the dependences of SHG and ferroelectric switching on the number of layers, the SnS thickness was systematically changed. Fig. 4-29a shows I_{D}–V_{D} curves measured in the same way as that in Fig. 4-23. For the monolayer, bilayer, and trilayer, the ferroelectric switching was realized as in 9L SnS, as discussed above. For SnS thicker than 15L, the current leakage through the SnS channel dramatically increased and it was difficult to observe the ferroelectric hysteresis loop. To quantify the effect of polar switching on the resistivity, the conductivity ratio for the low resistive state (ON) and high resistive state (OFF) at Ec was calculated. Fig. 4-29b shows the dependence of the ON/OFF ratio on the number of layers together with the SHG intensity. A large distribution was found in the SHG intensity for each number of layers, which is probably caused by the variation of crystalline quality due to the desorption-controlled PVD growth. This heterogeneity was also found when a different batch of SnS powder source was used. That is, the maximum SHG intensity for SnS grown via one batch exceeded that grown via the other batch. This result suggests the possibility of further increase in the SnS crystalline quality with the improvement of the SnS powder source. Despite of these dispersions, the SHG intensity tends to increase with a number of layers up to ∼10L, then it decreases, and finally quenches above 21L. The ferroelectric switching only occurs below this critical thickness. These results indicate that there is a change in the stacking sequence from the AA to AB stacking, which determines the existence of ferroelectricity.

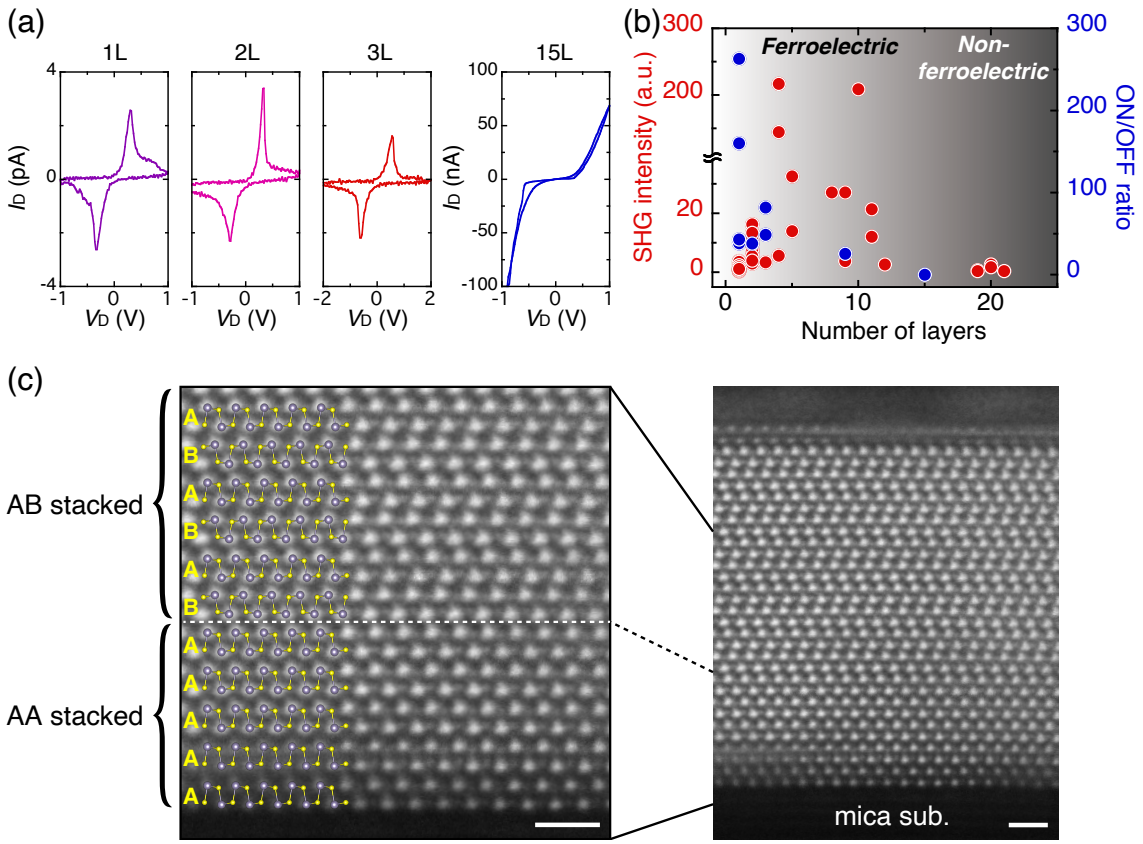

Figure 4-29: Layer number dependences of SHG and ferroelectricity of SnS. (a) Ferroelectric resistive switching for SnS with different thicknesses: monolayer, bilayer, trilayer, and 15L. (b) Thickness dependences of the SHG intensity and ON/OFF ratio for different thicknesses. The ON/OFF ratio was determined at the coercive electric field of I_D–V_D for Ag/SnS device. (c) Cross-sectional HAADF-STEM image of 16L SnS along the armchair direction. The scale bars represent 1 nm

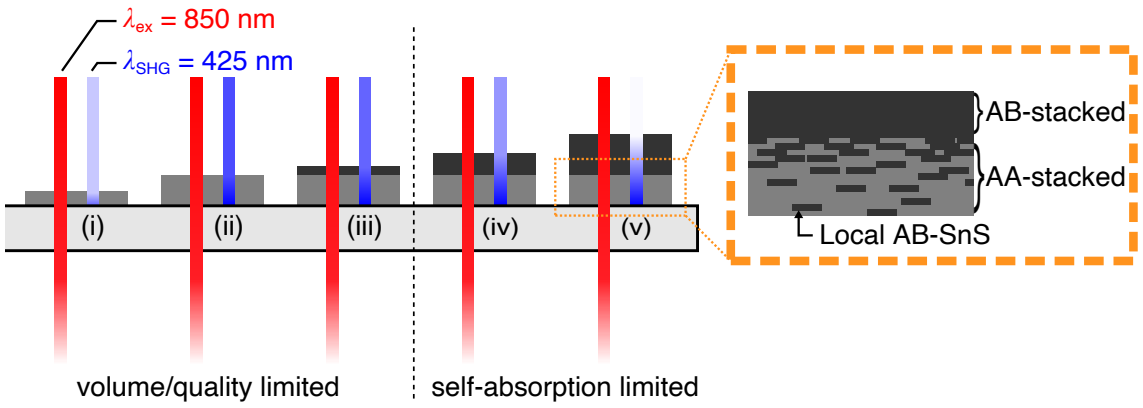

Figure 4-30: Schematic illustration of a model for interlayer coupling in multilayer SnS. The red and blue lines indicate the excitation laser (λ = 850 nm) and SHG signal (λ = 425 nm), respectively.

Fig. 4-30 shows a possible model for the thickness dependence for SHG intensity and ferroelectric resistive switching. In this model, for the thin SnS crystals, the stacking sequence is dominated by AA stacking probably due to the effect of strain introduced through the interaction with the mica substrate. In contrast, above the critical thickness of ∼15L, the stacking sequence is gradually changed to AB stacking, which is a thermodynamically stable state. In the SHG measurements, an 850-nm excitation laser, whose penetration depth in SnS is at least of several-hundred-nm [236, 237], was used to generate the SH signals. Thus, in the case of SnS thinner than ∼20L as discussed in this work, the whole region is excited. When the SnS thickness reaches the critical thickness at (iii), the SHG signal is maximized. Above the critical thickness, although the volume of noncentrosymmetric region does not change, the self-absorption of the SHG signal at 425 nm becomes effective because its penetration depth is much shorter than 850 nm [236, 237]. As a result, the SHG intensity decreases with increasing SnS thickness and is finally annihilated.

In order to prove the stacking transition, cross-sectional structure was further investigated for 16L SnS by TEM observation. For this sample, the crystal orientation was determined from the diamond-shaped-like crystal structure so that we can observe the atomic configuration along the armchair direction, where AA and AB stackings can be identified (Fig. 4-29c and 4-31). Fig. 4-29c shows high-angle an-

nular dark-field (HAADF) STEM image of 16L SnS along the armchair direction. The stacking transition from AA to AB is clearly observed at the thickness of 6L. Even though this transition plane was steeply continuous through a selected region of several tens of nanometers, it can be possible that the transitions occur at different thicknesses in a micrometer scale and from sample to sample, resulting in the discrepancy between critical thicknesses determined from TEM and SHG measurements. This unusual growth mode is probably due to the substrate effect, such as lattice strain and electrostatic surface charges. In the previous work on bulk SnS ($\sim$15 nm) [159], an I_{D}–V_{D} hysteresis loop similar to that in the present work was observed for in-plane two-terminal Au contact devices, where the ferroelectricity in bulk SnS was achieved by extrinsically breaking the inversion symmetry through the perpendicular electric field from the back gate. It should be emphasized that the intrinsic ferroelectricity is observed for monolayer SnS in this study.

In conclusion, monolayer SnS with micrometer size is grown by precisely controlling the growth pressure and temperature in PVD. The lack of the centrosymmetry and a strong anisotropy rooted from the puckered structure is confirmed based on polarized Raman and SHG spectroscopies. After the current flowing through the SnS channel in two-terminal devices was suppressed by selecting the strong Schottky Ag contact, RT in-plane ferroelectric switching was realized by the double-wave method. Remarkably, the robust RT ferroelectricity was identified in SnS below the critical thickness of $\sim$15L, probably due to the interaction with the substrate. This result suggests a possibility of controlling the stacking sequence of multilayer SnS, going beyond the limit of ferroelectricity in monolayer SnS. Given that SnS is the semiconductor with multiferroicity [30, 206], innately exhibiting pyroelectricity and piezoelectricity, this work will open up possibilities of providing novel multifunctionalities in vdW heterostructure devices.

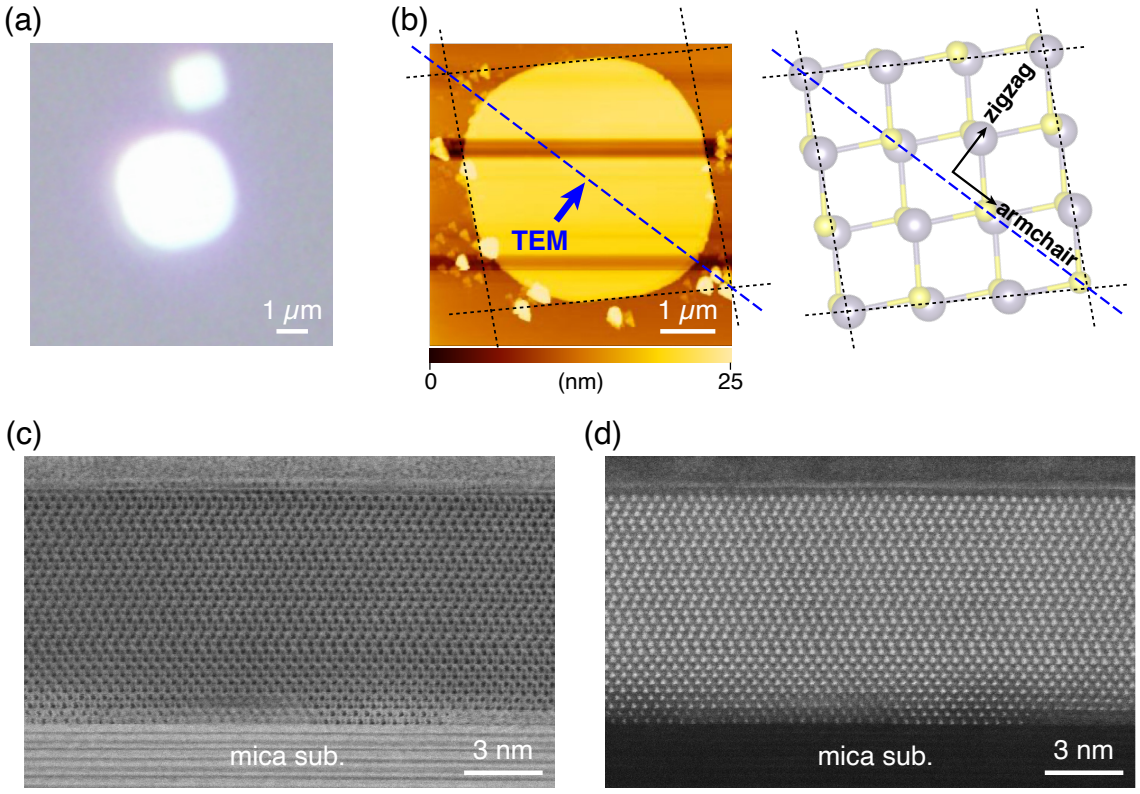

Figure 4-31: Cross-sectional TEM observation of PVD grown SnS on mica. (a) Optical and (b) AFM topographic images of 16L SnS. The sample was cut along the armchair direction, as shown in a dashed blue line. (c) Bright-field STEM and d HAADF-STEM images of 16L SnS.

Chapter 5

Summary and Outlook

5.1 Summary

The piezoelectricity and ferroelectricity in the non-centrosymmetric 2D materials have been explored in this thesis. As a promising material platform, this work has focused on monolayer SnS especially.

In Chapter 2, the origin of strong interlayer forces in SnS was discussed starting from its structural configuration. The significant role of lone pair electrons in Sn atoms were portrayed to explain the structural distortion, interlayer interaction, and chemical/thermal stabilities of 2D SnS. Fabrication methods of monolayer SnS have been investigated from a top-down thinning to bottom-up crystal growth. Comparing each fabrication procedures, structural, optical, and electrical characterizations will be discussed to evaluate the crystalline quality. The micrometer sized monolayer SnS has been, *for the first time*, achieved *via* surface oxidation thinning method, with forming a robust self-passivation of SnO_x. Also, bottom-up crystal growth was studied with physical vapor deposition (PVD). The PVD grown monolayer SnS exhibited higher crystalline quality and less extrinsic defects than monolayer *via* top-down thinning. As a key technology of monolayer growth, important roles in mica substrate has been discussed.

In Chapter 3, fundamentals and experimental results for the piezoelectric devices was described. Modulation of Schottky barrier height at the interface between metal

and SnS was found to be critical, for applying it to the piezoelectric and ferroelectric devices. The fundamental mechanism for the piezoelectric effect in the 2D materials has been investigated with using 2D MoS_2 as a model material. The important techniques in the device fabrication, metal transfer method to create the van der Waals gap between metal/MoS_2 free from Fermi level pinning, was discussed in detail. The origin and of piezoelectricity in 2D materials were found to be an asymmetric modulation of Schottky barrier height at the 2D/metal interface. Furthermore, an electromechanical response of 2D SnS was investigated, under both static and dynamic external strains. As an analogy of the piezoelectric effect, the piezoresistive effect has been precisely distinguished from the piezoelectricity. Piezoresistive and piezoelectric effects were characterized with a symmetric and asymmetric change of Schottky barrier height at source and drain. The novel approach in characterizing piezoelectric charge at the 2D/metal interface, transport measurement of top-gated field effect transistor under the strains, was describes. As a key finding, the piezo-charge was unveiled by modulating channel property.

In Chapter 4, the first demonstration of room temperature (RT) ferroelectricity was described. As a prerequisite property for ferroelectricity, the structural non-centrosymmetry was confirmed for the monolayer by second harmonic generation (SHG) measurement. The angular resolved SHG and Raman measurements were also performed to reveal a strong anisotropy in SnS. Also, the dependence of SHG intensity on the number of layers was investigated. The remarkable finding for the layer number dependence that the intrinsic property of odd–even effect in 2D SnS is broken for the few-to-monolayer SnS PVD grown on mica substrate, has been discussed in detail. The electrical transport characterization of a two-probe device with modulating the Schottky barrier height was described, as a direct proof for the ferroelectricity in SnS. The ferroelectric resistive switching under the external electric field has been demonstrated at RT and 1 Hz. The purely in-plane ferroelectric down to monolayer limit is highly motivated because it can preserve the ferroelectricity free from the out-of-plane perturbation. All other 2D ferroelectrics, which have been experimentally demonstrated at the moment, includes the out-of-plane polarization,

as shown in Fig. 5-1. The first observation of purely in-plane ferroelectricity of SnS in this work will pave the way for vdW heterostructure with novel functionalities.

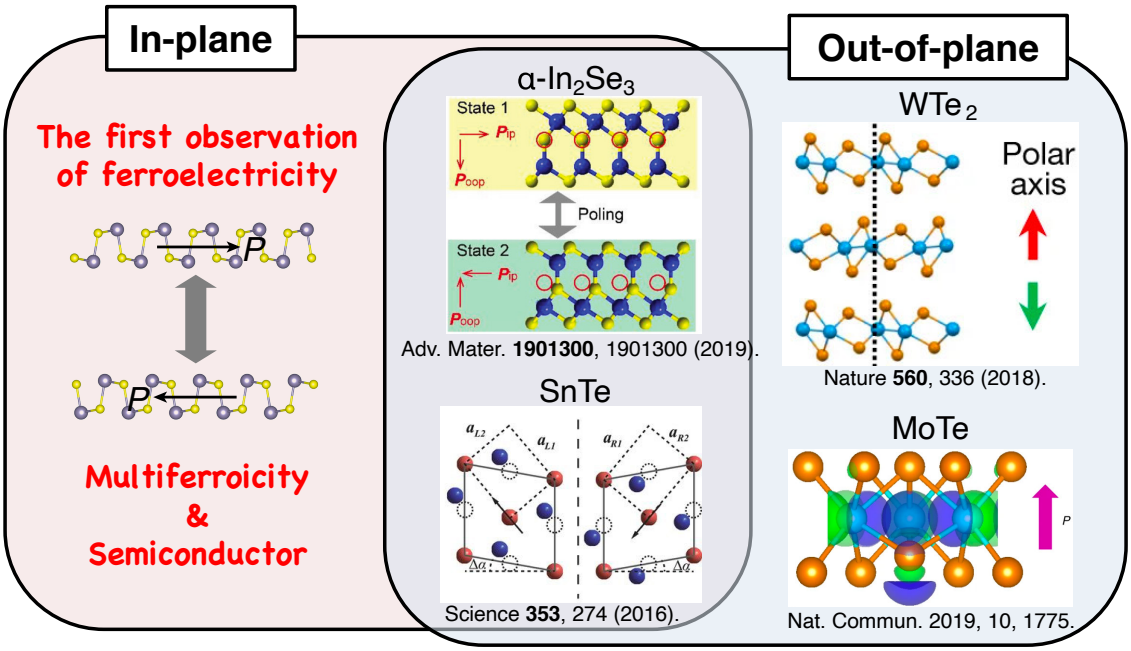

Figure 5-1: Summary of 2D ferroelectrics: SnS and other materials from this work and Ref. [73, 192, 193, 202].

5.2 Outlook

Fig. 5-2 shows potential applications of SnS with novel functionalities: piezoelectricity, ferroelectricity, and ferroelasticity. Firstly, the discovery of broken odd–even effect in the SnS will pave the way for further improvement of piezoelectric generators based on non-centrosymmetric 2D materials. In this work, the broken odd–even number effect was found to be limited up to ∼15 layers. In order to control the stacking sequences of the 2D materials, screw dislocation assisted spiral growth will be effective [238, 239, 240, 241]. With using the spiral growth in the manner of AA-stacking, the out-put power can increase with increasing the number of layers, beyond the monolayer limit. When the thickness increase, the mechanical properties such as elastic stiffness will change. Thus, there should be a tradeoff between the amount of polarization charge and mechanical flexibility. Analyses on the figure of merit for the flexible generator are also significant.

Secondly, given that SnS is ferroelectric and semiconductor, nonvolatile memories such as ferroelectric RAMs (FeRAMs) and ferroelectric tunnel junctions (FTJs) are possible applications for SnS. Recently, not a few works have been reported on in-plane FeRAM and FTJs [74]. H. Shen *et al*. has proposed a device structure for in-plane FTJs based on the group-IV monochalcogenides (Fig. 5-2), which has an advantage of a faster reading operation and a nondestructive reading process [74]. In this work, non-centrosymmetric SnS was realized on mica substrate. To demonstrate the in-plane FTJ device, as shown in Fig. 5-2, transfer techniques on to the conductive substrate will be necessary.

Finally, as an analogy of ferroelectricity, theoretical works have predicted ferroelasticity [30, 206], which enable polarization switching with external strain, instead of electric field for ferroelectricity. For SnS, the spontaneous polarization direction can be rotated by 90°: the atomic configuration as zigzag transform in to the armchair structure under a moderate tensile strain. Together with the electrical and optical anisotropies that have been demonstrated in this work, the ferroelasticity will open up possibilities for an opto/electrically readable shape memory toward the soft-robotics

applications.

In conclusion, this work on the exploration of the piezoelectric and ferroelectric characteristics in the non-centrosymmetric 2D materials indicates their promising potential for the novel optical, electrical, and mechanical applications.

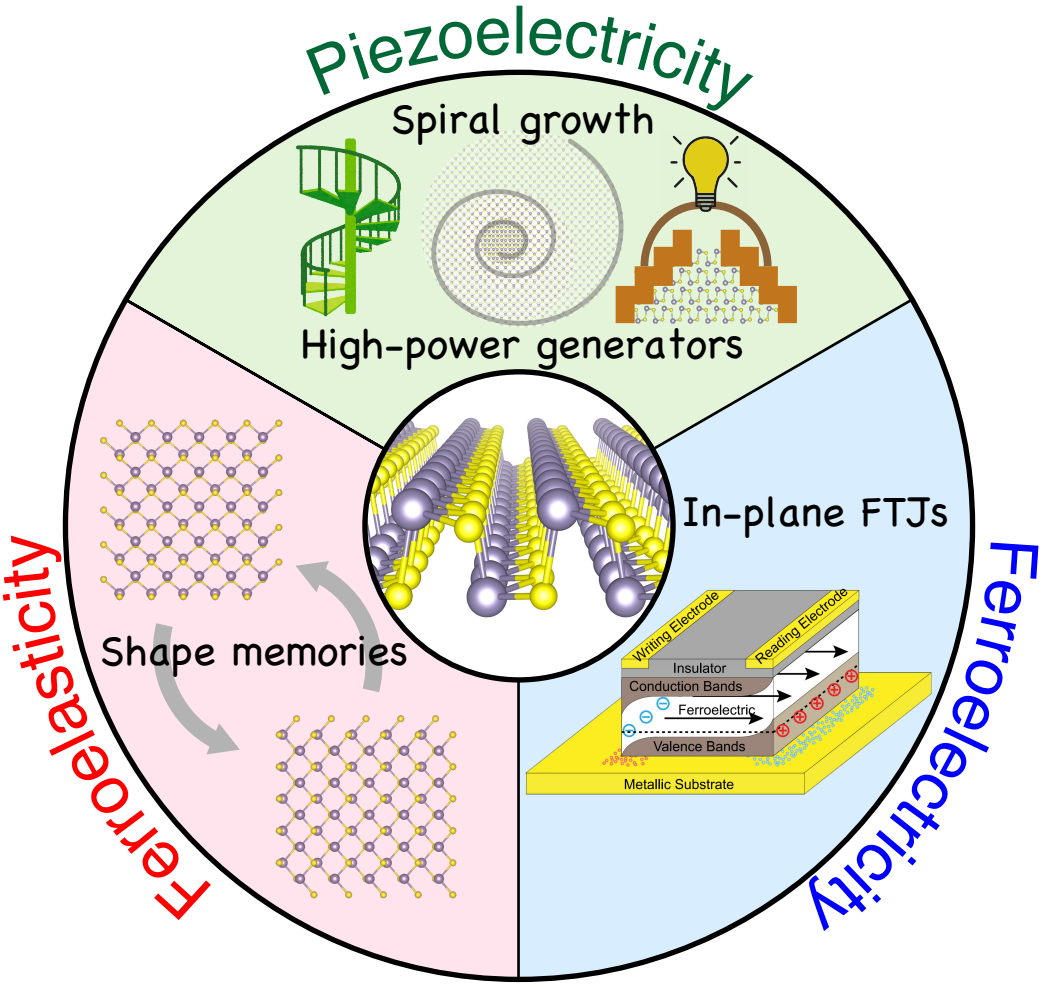

Figure 5-2: Potential applications of SnS with novel functionalities [30, 74, 206].

Appendix A

Post-oxidation methods

A.1 Oxygen Plasma

Bulk SnS was prepared *via* Au-mediated mechanical exfoliation on SiO_2/Si substrate. A high frequency oxygen plasma was used to oxide and physically etch the bulk surface. The RF power and oxygen pressure was fixed at 300 W and 50 Pa, respectively. In order to investigate the crystalline quality of SnS before and after the oxygen plasma, μ-Raman was used. The excitation wavelength and laser power was 488 nm and 0.1 mW, respectively.

In Fig. A-1a, an atomic force microscopy (AFM) images of SnS surface before and after the oxygen plasma treatment for 300 sec. Even after the oxidation, the RMS roughness is stable at around 0.2–0.4 nm, and the SnS thickness decreased by 2.6 nm. This is a result of surface oxidation and physical etching of SnO_x surface (Fig. A-1b). Fig. A-2 shows the time evolution of optical contrast of SnS along with the oxygen plasma. The optical contrast decreased with time, while the SnS thickness increased initially increased up to 60 sec, and then turned to decrease. This is probably caused by a following process. In the early time of oxidation, the formation of transparent SnO_x exceed the decrease of thickness by physical etching. After the enough time, forming a SnO_x layer, the oxidation rate is dominated by the oxygen diffusion in SnO_x layer, and the system reach to the equilibrium of oxidation and etching. At the equilibrium phase (>60 sec), the etching rate was 30 sec/layer, which is easy to

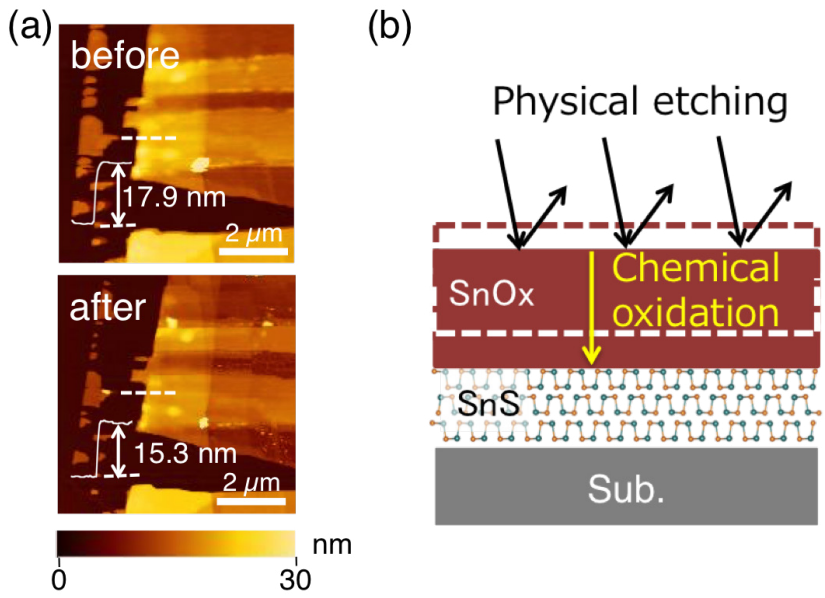

Figure A-1: (a) AFM images of SnS before/after O_2 plasma treatment for 300 sec. (b) Schematic view of self-passivated SnS layer.

control the thickness.

In order to investigate the effect of the plasma treatment on the crystalline quality, Raman spectra were measured. To eliminate the volume effect, the thick SnS flake was used: $\sim$ 130 nm, SnS, which is enough tchicker that the penetration depth of 488-nm laser in SnS ($\sim$ 20 nm). In Fig. A-3, Raman spectra before/after the oxidation for 30 sec. For the as-exfoliated SnS, specific Raman peaks were observed at 95, 164, 192, and 219 cm^{-1}, but other peaks of SnO_x or SiO_2/Si substrate were not observed. After the oxidation, there was no significant change in the intensity or peak shape, thus the quality of SnS just under the SnO_x layer is probaly preserved.

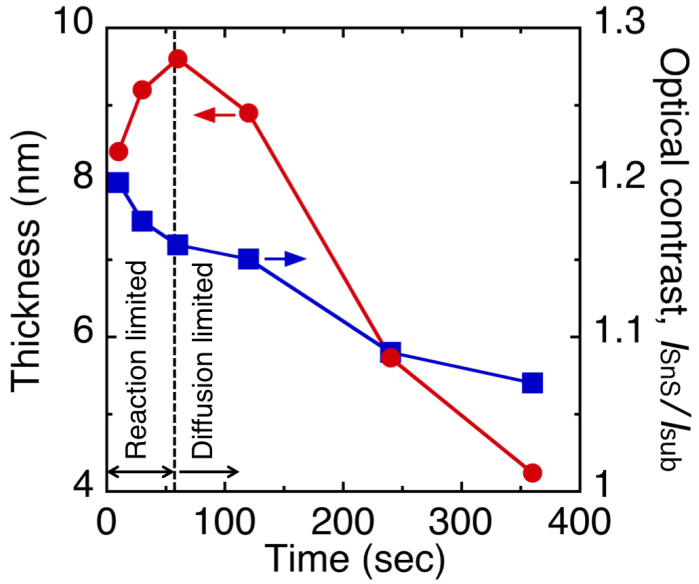

Figure A-2: Time dependence of flake thickness and optical contrast.

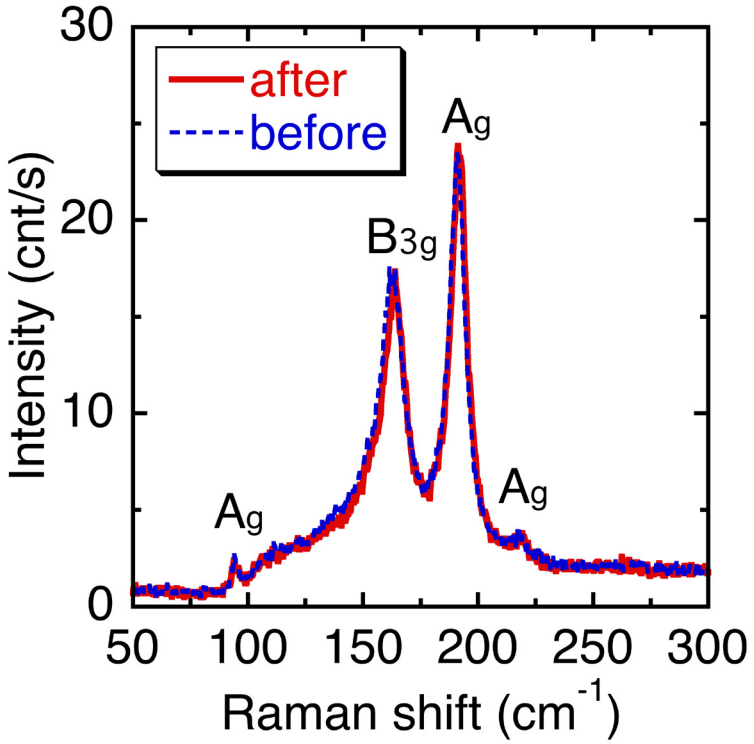

Figure A-3: Raman spectrum from thick SnS layer before/after plasma treatment for 300 sec.x-Raman

A.2 Ozone

In spite of the robust features in bulk SnS, the oxygen plasma method was found to be unacceptable for its damage. As shown in Fig. A-4a,b, for the thin SnS, the oxygen plasma treatment resulted in the surface roughness. This is probably owing to a localized oxidation [90].

In order to decrease the localized oxidation, more mild method of ozone treatment was tries. In Fig. A-4, the optical image before and after the ozone treatment at 200°C for 1 h is shown. Similar with the oxygen plasma treatment, the surface roughness was apparently observed. These features indicate the oxygen favorable nature of thin SnS, and the requirement for the careful treatment for top-down thinning or device fabrication. As shown in the Section 2.3, the oxygen annealing was found to be the most reliable post-thinning method.

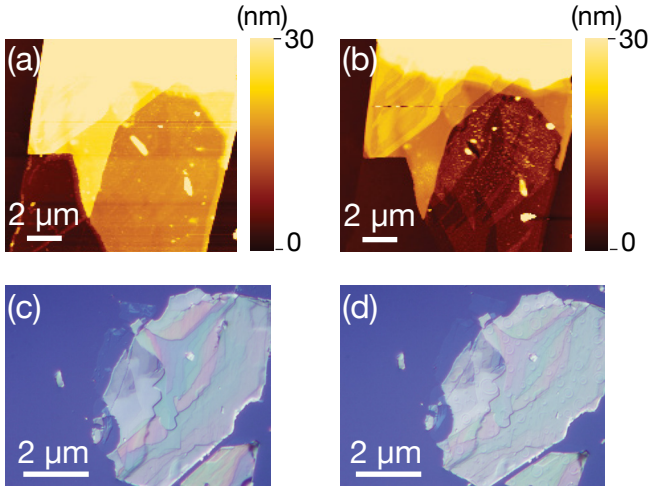

Figure A-4: (a,b) AFM topographic images of SnS flakes (a) before and (b) after O_2 plasma treatment at RT with the radio frequency power of 300 W for 450 sec. (c,d) Optical images with Normarski interference contrast of SnS flakes (c) before and (d) after ozone treatment at 200°C for 1 h.

Appendix B

Quasi-ferroelectricity in Non-ferroelectric systems

B.1 Carrier Emission from Trapping Sites

False ferroelectricity in nonferroelectric systems has been theoretically investigated based on the carrier trapping model [234]. In this model, the following properties are assumed; 1) the sample is a semiconductor with Schottky contacts on both the source and drain contacts, 2) a large concentration of trap sites is located over a finite thickness w_t at the semiconductor/metal interfaces, 3) the normal leakage current is neglected and the carrier emission from the traps is dominant, and 4) the displacement current due to the space charge near the contacts produced by the trapping/detrapping is neglected. Based on this model, the carrier emission from the traps I_{tr} can be written as

$$I_{tr} = \frac{qAw_tN}{\tau} exp\left(-\frac{V}{4\tau V_a f}\right) \tag{B.1}$$

where A is the area of the electrode, N is the initial concentration of occupied traps, τ is the emission time constant from the traps, V is the applied source–drain voltage, V_a is the amplitude of the applied signal (Fig. B-1a), and f is its frequency.

To exclude the possibility that the present ferroelectric switching behavior is due

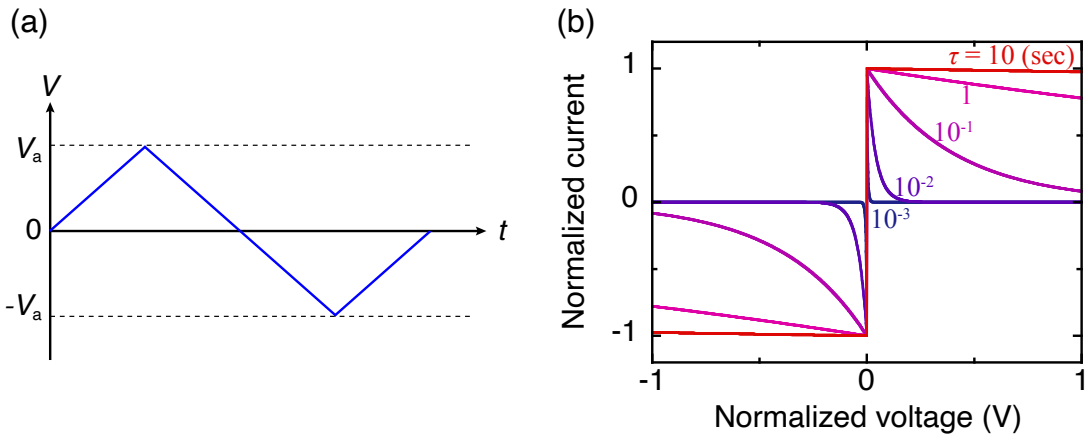

Figure B-1: Theoretical analysis of I–V hysteresis loop based on the carrier trapping model. (a) The schematic diagram of applied voltage. (b) Calculated relationship between voltage and current from carrier emission. The emission time constant τ was changed from 1 ms to 10 s.

to the carrier emission from the traps, we discuss the suitability of carrier trapping models assuming that the present device is not ferroelectric. When the relationship of current and voltage is calculated based on Eq. B.1, the shape of the I–V curve strongly depends on τ, as shown in Fig. B-1b. Comparing the I–V shapes of the calculated and experimental results (Figs. 4-26, 4-27 and 4-29), the value of τ is approximately estimated to be in the order of 100 ms. The maximum current I_{max} can be obtained when the voltage is close to zero. Substituting $V = 0$ V into Eq. B.1, the total number of traps Aw_tN can be expressed as follows,

$$Aw_tN = \frac{\tau}{q} I_{max} \tag{B.2}$$

From the experimental results, I_{max} is ranged up to 150 pA (Fig. 4-27e). When we substitute $\tau = 100$ ms and $I_{max} = 150$ pA, the total number of traps is determined to be 9×10^7 states near the Ag/SnS interface in the SnS channel (the channel thickness, length, and width are 5.4 nm, 0.4 µm, and 3.0 µm, respectively). In this case, the number of traps corresponds to one in three of the total number of atoms in the SnS channel, which is too large intuitively. From these results, the effect of carrier emission from the traps can be neglected for the present ferroelectric I–V hysteresis loops.

B.2 Excluding the Effect of Ag diffusion

It is well-known that Ag have a high reactivity with sulfides, and easy to diffuse. These characteristics can show a memristor behavior. For example, in a Ag/SnO_x system, a memristor property has been observed [242]. In this memristor, firstly an Ag filament is formed with applying the electric field, then there is a transition from high-resistive state to low-resistive state. This switching is similar with the present data in this work, however, these hysteresis trace different curves with each other. For Ag/SnO_x memristor, the hysteresis draws a crossed 8-shape, while Ag/SnS ferroelectric switching hysteresis shows non-crossed 8-shape. This difference is one of the supporting data to exclude the quasi-ferro from silver's properties.

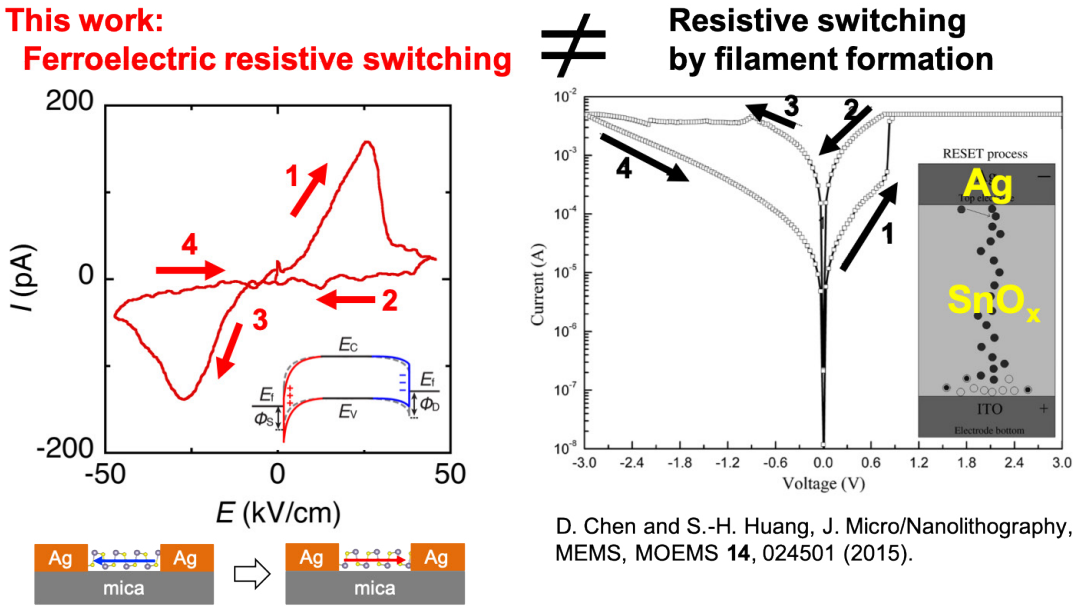

Figure B-2: Comparison between ferroelectric and ReRAM behaviors.

Formation of conductive filament has been reported in the Ag/2D-material structures, as shown in Fig. B-3 [230]. In this work, AFM topographic image was observed after the I_D–V_D measurement. In order to observe the SnS surface at the low resistive state (LRS), the drain voltage was swept from −1 V to 800 mV just before the AFM measurement (Fig. B-4a). No significant Ag diffusion was confirmed in the channel region at the LRS compared with the AFM image before the electrical measurement

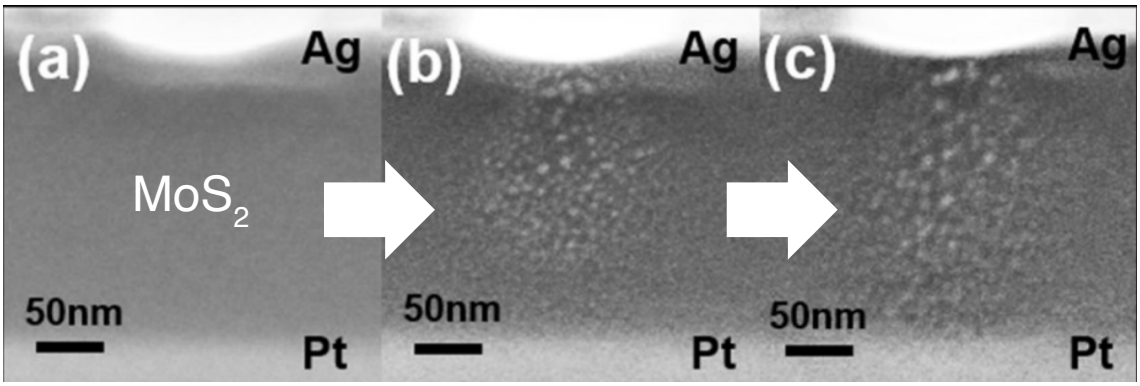

Figure B-3: Formation of conducting Ag filament in $Ag/MoS_2/Pt$ planar device [230].

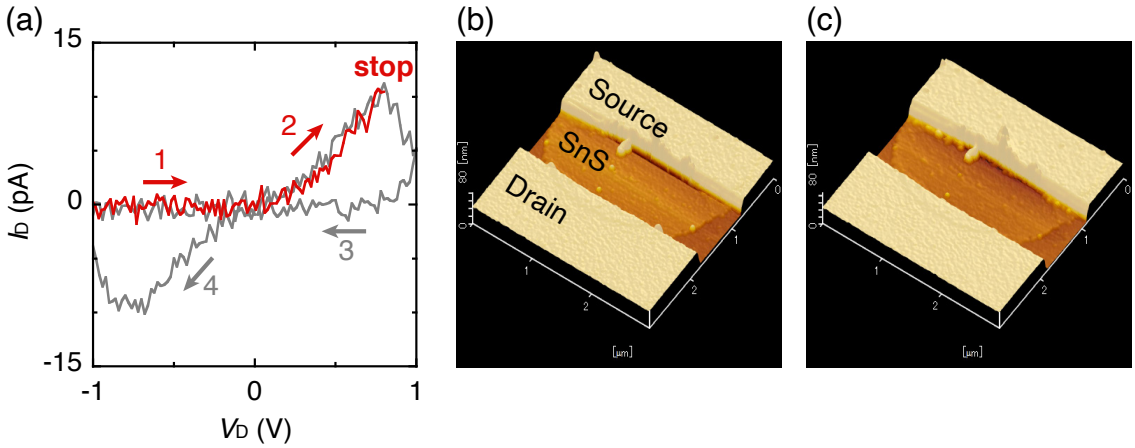

Figure B-4: Exclusion of Ag diffusion into SnS. (a) I_D–V_D curves for 2.6 nm (∼4L) SnS with Ag electrodes. A single sweep from −1 V to 800 mV stopped at the low resistive state is shown in a red line. For comparison, (b) double sweep is shown in a gray line. AFM topographic images a before and (c) after applying the external electric field. The scale bars represent 500 nm.

(Fig. B-4b,c).

In conclusion, the effect of Ag diffusion and filament formation are not dominant for the experiments on Ag/SnS.

Bibliography

[1] Lional C. Kimerling. The Economics of Science: from Photons to Products. *Opt. Photonics News*, 9(10):19, 1998.

[2] Kevin Ashton. That 'Internet of Things' Thing. In the real world, things matter more than ideas. *RFID Jounal*, 2009.

[3] Qian Zhu, Ruicong Wang, Qi Chen, Yan Liu, and Weijun Qin. IOT Gateway: Bridging Wireless Sensor Networks into Internet of Things. In *2010 IEEE/IFIP Int. Conf. Embed. Ubiquitous Comput.*, pages 347–352. IEEE, 2010.

[4] Antonio Iera, Christian Floerkemeier, Jin Mitsugi, and Giacomo Morabito. The Internet of things. *IEEE Wirel. Commun.*, 17(6):8–9, 2010.

[5] K. E. Skouby and P. Lynggaard. Smart home and smart city solutions enabled by 5G, IoT, AAI and CoT services. In *2014 Int. Conf. Contemp. Comput. Informatics*, volume 35, pages 874–878. IEEE, 2014.

[6] Liang Xiao, Xiaoyue Wan, Xiaozhen Lu, Yanyong Zhang, and Di Wu. IoT Security Techniques Based on Machine Learning: How Do IoT Devices Use AI to Enhance Security? *IEEE Signal Process. Mag.*, 35(5):41–49, 2018.

[7] J. Bryzek. Emergence of a $Trillion Mems Sensor Market. In *SensorSon*, 2012.

[8] Janusz Bryzek. The Trillion Foundation for the Sensors (TSensors) IoT. In *TSensors Summit*, 2014.

[9] Kazuyoshi Itagaki. EnOcean energy harvester wireless switch & sensor and foresight of future IoT. In *66th JSAP Spring Meet.*, pages 10p–M121–2, 2019.

[10] Simone Bertolazzi, Paolo Bondavalli, Stephan Roche, Tamer San, Sung-Yool Choi, Luigi Colombo, Francesco Bonaccorso, and Paolo Samorì. Nonvolatile Memories Based on Graphene and Related 2D Materials. *Adv. Mater.*, 31(10):1806663, 2019.

[11] Tetsuo Endoh, Hiroki Koike, Shoji Ikeda, Takahiro Hanyu, and Hideo Ohno. An Overview of Nonvolatile Emerging Memories –Spintronics for Working Memories. *IEEE J. Emerg. Sel. Top. Circuits Syst.*, 6(2):109–119, 2016.

[12] Peter Maksymovych, Mark Huijben, Minghu Pan, Stephen Jesse, Nina Balke, Ying-Hao Chu, Hye Jung Chang, Albina Y. Borisevich, Arthur P. Baddorf, Guus Rijnders, Dave H. A. Blank, Ramamoorthy Ramesh, and Sergei V. Kalinin. Ultrathin limit and dead-layer effects in local polarization switching of $BiFeO_3$. *Phys. Rev. B*, 85(1):014119, 2012.

[13] D. Lee, H. Lu, Y. Gu, S.-Y. Choi, S.-D. Li, S. Ryu, T. R. Paudel, K. Song, E. Mikheev, S. Lee, S. Stemmer, D. A. Tenne, S. H. Oh, E. Y. Tsymbal, X. Wu, L.-Q. Chen, A. Gruverman, and C. B. Eom. Emergence of room-temperature ferroelectricity at reduced dimensions. *Science*, 349(6254):1314–1317, 2015.

[14] C. H. Ahn, K. M. Rabe, and J.-M. Triscone. Ferroelectricity at the Nanoscale: Local Polarization in Oxide Thin Films and Heterostructures. *Science*, 303(5657):488–491, 2004.

[15] R. R. Mehta, B. D. Silverman, and J. T. Jacobs. Depolarization fields in thin ferroelectric films. *J. Appl. Phys.*, 44(8):3379–3385, 1973.

[16] Shad Roundy, Paul K. Wright, and Jan Rabaey. A study of low level vibrations as a power source for wireless sensor nodes. *Comput. Commun.*, 26(11):1131–1144, 2003.

[17] W. S. N. Trimmer. Microbots and micromechnical systems. *Sensors and Actuators*, 19:267–287, 1989.

[18] J. C. Maxwell. On physical lines of force part I to IV. *London, Edinburgh, Dublin Philos. Mag. J. Sci. Ser.*, 4(21):139, 1861.

[19] Zhong Lin Wang. On Maxwell's displacement current for energy and sensors: the origin of nanogenerators. *Mater. Today*, 20(2):74–82, 2017.

[20] Chen Xu, Xudong Wang, and Zhong Lin Wang. Nanowire Structured Hybrid Cell for Concurrently Scavenging Solar and Mechanical Energies. *J. Am. Chem. Soc.*, 131(16):5866–5872, 2009.

[21] Shuhua Wang, Zhong Lin Wang, and Ya Yang. A One-Structure-Based Hybridized Nanogenerator for Scavenging Mechanical and Thermal Energies by Triboelectric-Piezoelectric-Pyroelectric Effects. *Adv. Mater.*, 28(15):2881–2887, 2016.

[22] Zhong Lin Wang. On the first principle theory of nanogenerators from Maxwell's equations. *Nano Energy*, (October):104272, 2019.

[23] G. A. Maugin. *Continuum Mechanics of Electromagnetic Solids*, volume 33. Elsevier Science Ltd., Amsterdam, North-Holland, 1988.

[24] K. S. Novoselov, A. K. Geim, S. V. Morozov, D. Jiang, Y. Zhang, S. V. Dubonos, I. V. Grigorieva, and A. A. Firsov. Electric Field Effect in Atomically Thin Carbon Films. *Science*, 306(5696):666–669, 2004.

[25] B. Radisavljevic, A. Radenovic, J. Brivio, V. Giacometti, and A. Kis. Single-layer MoS_2 transistors. *Nat. Nanotechnol.*, 6(3):147–150, 2011.

[26] M.R. Hilton and P.D. Fleischauer. Applications of solid lubricant films in spacecraft. *Surf. Coatings Technol.*, 54-55(I 992):435–441, 1992.

[27] Wenzhuo Wu, Lei Wang, Yilei Li, Fan Zhang, Long Lin, Simiao Niu, Daniel Chenet, Xian Zhang, Yufeng Hao, Tony F Heinz, James Hone, and Zhong Lin Wang. Piezoelectricity of single-atomic-layer MoS_2 for energy conversion and piezotronics. *Nature*, 514(7523):470–474, 2014.

[28] Karel-Alexander N. Duerloo, Mitchell T. Ong, and Evan J. Reed. Intrinsic Piezoelectricity in Two-Dimensional Materials. *J. Phys. Chem. Lett.*, 3(19):2871–2876, 2012.

[29] Ruixiang Fei, Wenbin Li, Ju Li, and Li Yang. Giant piezoelectricity of monolayer group IV monochalcogenides: SnSe, SnS, GeSe, and GeS. *Appl. Phys. Lett.*, 107(17):173104, 2015.

[30] Menghao Wu and Xiao Cheng Zeng. Intrinsic Ferroelasticity and/or Multiferroicity in Two-Dimensional Phosphorene and Phosphorene Analogues. *Nano Lett.*, 16(5):3236–3241, 2016.

[31] S. F. Wang, W. Wang, W. K. Fong, Y. Yu, and C. Surya. Tin Compensation for the SnS Based Optoelectronic Devices. *Sci. Rep.*, 7:39704, 2017.

[32] S. V. Morozov, K. S. Novoselov, M. I. Katsnelson, F. Schedin, D. C. Elias, J. A. Jaszczak, and A. K. Geim. Giant Intrinsic Carrier Mobilities in Graphene and Its Bilayer. *Phys. Rev. Lett.*, 100(1):016602, 2008.

[33] Tao Chen and Rebecca Cheung. Mechanical properties of graphene. *Graphene Sci. Handb. Mech. Chem. Prop.*, pages 3–15, 2016.

[34] I. W. Frank, D. M. Tanenbaum, A. M. van der Zande, and P. L. McEuen. Mechanical properties of suspended graphene sheets. *J. Vac. Sci. Technol. B Microelectron. Nanom. Struct.*, 25(6):2558, 2007.

[35] M. S. Dresselhaus and G. Dresselhaus. Intercalation compounds of graphite. *Adv. Phys.*, 51(1):1–186, 2002.

[36] Yuanbo Zhang, Tsung-Ta Tang, Caglar Girit, Zhao Hao, Michael C. Martin, Alex Zettl, Michael F. Crommie, Y. Ron Shen, and Feng Wang. Direct observation of a widely tunable bandgap in bilayer graphene. *Nature*, 459(7248):820–823, 2009.

[37] Yuan Cao, Valla Fatemi, Ahmet Demir, Shiang Fang, Spencer L. Tomarken, Jason Y. Luo, Javier D. Sanchez-Yamagishi, Kenji Watanabe, Takashi Taniguchi, Efthimios Kaxiras, Ray C. Ashoori, and Pablo Jarillo-Herrero. Correlated insulator behaviour at half-filling in magic-angle graphene superlattices. *Nature*, 556(7699):80–84, 2018.

[38] Sunkook Kim, Aniruddha Konar, Wan-Sik Hwang, Jong Hak Lee, Jiyoul Lee, Jaehyun Yang, Changhoon Jung, Hyoungsub Kim, Ji-Beom Yoo, Jae-Young Choi, Yong Wan Jin, Sang Yoon Lee, Debdeep Jena, Woong Choi, and Kinam Kim. High-mobility and low-power thin-film transistors based on multilayer MoS_2 crystals. *Nat. Commun.*, 3(1):1011, 2012.

[39] Jason K. Ellis, Melissa J. Lucero, and Gustavo E. Scuseria. The indirect to direct band gap transition in multilayered MoS_2 as predicted by screened hybrid density functional theory. *Appl. Phys. Lett.*, 99(26):261908, 2011.

[40] Hee Sung Lee, Sung-Wook Min, Youn-Gyung Chang, Min Kyu Park, Taewook Nam, Hyungjun Kim, Jae Hoon Kim, Sunmin Ryu, and Seongil Im. MoS_2 Nanosheet Phototransistors with Thickness-Modulated Optical Energy Gap. *Nano Lett.*, 12(7):3695–3700, 2012.

[41] Sujay B Desai, Surabhi R Madhvapathy, Angada B Sachid, Juan Pablo Llinas, Qingxiao Wang, G. H. Ahn, Gregory Pitner, Moon J Kim, Jeffrey Bokor, Chenming Hu, H.-S. P. Wong, and Ali Javey. MoS_2 transistors with 1-nanometer gate lengths. *Science*, 354(6308):99–102, 2016.

[42] Xiaoxue Song, Fei Hui, Theresia Knobloch, Bingru Wang, Zhongchao Fan, Tibor Grasser, Xu Jing, Yuanyuan Shi, and Mario Lanza. Piezoelectricity in two dimensions: Graphene vs. molybdenum disulfide. *Appl. Phys. Lett.*, 111(8):083107, 2017.

[43] Non-Centrosymmetric. In Dongqing Li, editor, *Encycl. Microfluid. Nanofluidics*, page 1457. Springer US, Boston, MA, 2008.

[44] Gowoon Cheon, Karel-Alexander N. Duerloo, Austin D. Sendek, Chase Porter, Yuan Chen, and Evan J. Reed. Data Mining for New Two- and One-Dimensional Weakly Bonded Solids and Lattice-Commensurate Heterostructures. *Nano Lett.*, 17(3):1915–1923, 2017.

[45] Junjie Qi, Yann-Wen Lan, Adam Z Stieg, Jyun-Hong Chen, Yuan-Liang Zhong, Lain-Jong Li, Chii-Dong Chen, Yue Zhang, and Kang L Wang. Piezoelectric effect in chemical vapour deposition-grown atomic-monolayer triangular molybdenum disulfide piezotronics. *Nat. Commun.*, 6(1):7430, 2015.

[46] Hanyu Zhu, Yuan Wang, Jun Xiao, Ming Liu, Shaomin Xiong, Zi Jing Wong, Ziliang Ye, Yu Ye, Xiaobo Yin, and Xiang Zhang. Observation of piezoelectricity in free-standing monolayer MoS_2. *Nat. Nanotechnol.*, 10(2):151–155, 2015.

[47] Ju-Hyuck Lee, Jae Young Park, Eun Bi Cho, Tae Yun Kim, Sang A. Han, Tae-Ho Kim, Yanan Liu, Sung Kyun Kim, Chang Jae Roh, Hong-Joon Yoon, Hanjun Ryu, Wanchul Seung, Jong Seok Lee, Jaichan Lee, and Sang-Woo Kim. Reliable Piezoelectricity in Bilayer WSe_2 for Piezoelectric Nanogenerators. *Adv. Mater.*, 29(29):1606667, 2017.

[48] Jiabin Li, Ting Zhao, Chaoyu He, and Kai-Wang Zhang. Surface oxidation: an effective way to induce piezoelectricity in 2D black phosphorus. *J. Phys. D. Appl. Phys.*, 51(12):12LT01, 2018.

[49] Jiabin Li, Chaoyu He, Kai-Wang Zhang, and Jianxin Zhong. First-principles prediction of a new ground state for surface-oxidized phosphorene with remarkable piezoelectricity. *J. Phys. D. Appl. Phys.*, 2019.

[50] Mitchell T. Ong and Evan J. Reed. Engineered Piezoelectricity in Graphene. *ACS Nano*, 6(2):1387–1394, 2012.

[51] Alexander I Lebedev. Ferroelectricity and piezoelectricity in monolayers and nanoplatelets of SnS. *J. Appl. Phys.*, 124(16):164302, 2018.

[52] Yongfu Sun, Zhihu Sun, Shan Gao, Hao Cheng, Qinghua Liu, Fengcai Lei, Shiqiang Wei, and Yi Xie. All-Surface-Atomic-Metal Chalcogenide Sheets for High-Efficiency Visible-Light Photoelectrochemical Water Splitting. *Adv. Energy Mater.*, 4(1):1300611, 2014.

[53] Chao Xin, Jiaxin Zheng, Yantao Su, Shuankui Li, Bingkai Zhang, Yancong Feng, and Feng Pan. Few-Layer Tin Sulfide: A New Black-Phosphorus-Analogue 2D Material with a Sizeable Band Gap, Odd-Even Quantum Confinement Effect, and High Carrier Mobility. *J. Phys. Chem. C*, 120(39):22663–22669, 2016.

[54] Otfried Madelung. *Semiconductors: Data Handbook*. Springer-Verlag Berlin Heidelberg, Berlin, Heidelberg, 2004.

[55] Jack R. Brent, David J. Lewis, Tommy Lorenz, Edward A. Lewis, Nicky Savjani, Sarah J. Haigh, Gotthard Seifert, Brian Derby, and Paul O'Brien. Tin(II) Sulfide (SnS) Nanosheets by Liquid-Phase Exfoliation of Herzenbergite: IV-VI Main Group Two-Dimensional Atomic Crystals. *J. Am. Chem. Soc.*, 137(39):12689–12696, 2015.

[56] W. Albers, C. Haas, and F. van der Maesen. The preparation and the electrical and optical properties of SnS crystals. *J. Phys. Chem. Solids*, 15(3-4):306–310, 1960.

[57] Vera Steinmann, R. Jaramillo, Katy Hartman, Rupak Chakraborty, Riley E. Brandt, Jeremy R. Poindexter, Yun Seog Lee, Leizhi Sun, Alexander Polizzotti, Helen Hejin Park, Roy G. Gordon, and Tonio Buonassisi. 3.88% Efficient Tin Sulfide Solar Cells Using Congruent Thermal Evaporation. *Adv. Mater.*, 26(44):7488–7492, 2014.

[58] M.M. Nassary. Temperature dependence of the electrical conductivity, Hall effect and thermoelectric power of SnS single crystals. *J. Alloys Compd.*, 398(1-2):21–25, 2005.

[59] Sukrit Sucharitakul, U. Rajesh Kumar, Raman Sankar, Fang-Cheng Chou, Yit-Tsong Chen, Chuhan Wang, Cai He, Rui He, and Xuan P. A. Gao. Screening limited switching performance of multilayer 2D semiconductor FETs: the case for SnS. *Nanoscale*, 8(45):19050–19057, 2016.

[60] Kachirayil J. Saji, Kun Tian, Michael Snure, and Ashutosh Tiwari. 2D Tin Monoxide–An Unexplored *p*-Type van der Waals Semiconductor: Material Characteristics and Field Effect Transistors. *Adv. Electron. Mater.*, 2(4):1500453, 2016.

[61] Weihao Wang, Tao Zhang, Aleksandr Seliverstov, Huihui Zhang, Yichen Wang, Fengzhi Wang, Xiaoli Peng, Qiaoqi Lu, Chao Qin, Xinhua Pan, Yu-jia Zeng, Chris Van Haesendonck, and Zhizhen Ye. Layer-Dependent Optoelectronic Properties of 2D van der Waals SnS Grown by Pulsed Laser Deposition. *Adv. Electron. Mater.*, 1901020:1901020, 2019.

[62] Zafer Mutlu, Ryan J. Wu, Darshana Wickramaratne, Sina Shahrezaei, Chueh Liu, Selcuk Temiz, Andrew Patalano, Mihrimah Ozkan, Roger K. Lake, K. A. Mkhoyan, and Cengiz S. Ozkan. Phase Engineering of 2D Tin Sulfides. *Small*, 12(22):2998–3004, 2016.

[63] Jonathan M. Skelton, Lee A. Burton, Fumiyasu Oba, and Aron Walsh. Chemical and Lattice Stability of the Tin Sulfides. *J. Phys. Chem. C*, 121(12):6446–6454, 2017.

[64] R. E. Abutbul, E. Segev, L. Zeiri, V. Ezersky, G. Makov, and Y. Golan. Synthesis and properties of nanocrystalline π-SnS –a new cubic phase of tin sulphide. *RSC Adv.*, 6(7):5848–5855, 2016.

[65] Joachim Breternitz, René Gunder, Hannes Hempel, Silvia Binet, Ibbi Ahmet, and Susan Schorr. Facile Bulk Synthesis of π-Cubic SnS. *Inorg. Chem.*, 56(19):11455–11457, 2017.

[66] Zhengtao Deng, Di Cao, Jin He, Su Lin, Stuart M Lindsay, and Yan Liu. Solution Synthesis of Ultrathin Single-Crystalline SnS Nanoribbons for Photodetectors *via* Phase Transition and Surface Processing. *ACS Nano*, 6(7):6197–6207, 2012.

[67] Julien Vidal, Stephan Lany, Mayeul D'Avezac, Alex Zunger, Andriy Zakutayev, Jason Francis, and Janet Tate. Band-structure, optical properties, and defect physics of the photovoltaic semiconductor SnS. *Appl. Phys. Lett.*, 100(3):032104, 2012.

[68] Dimitri D. Vaughn, Romesh J. Patel, Michael A. Hickner, and Raymond E. Schaak. Single-Crystal Colloidal Nanosheets of GeS and GeSe. *J. Am. Chem. Soc.*, 132(43):15170–15172, 2010.

[69] Georgios A. Tritsaris, Brad D. Malone, and Efthimios Kaxiras. Optoelectronic properties of single-layer, double-layer, and bulk tin sulfide: A theoretical study. *J. Appl. Phys.*, 113(23):233507, 2013.

[70] Xing Zhou, Qi Zhang, Lin Gan, Huiqiao Li, Jie Xiong, and Tianyou Zhai. Booming Development of Group IV-VI Semiconductors: Fresh Blood of 2D Family. *Adv. Sci.*, 3(12):1600177, 2016.

[71] Naoki Higashitarumizu, Hayami Kawamoto, Keiji Ueno, and Kosuke Nagashio. Fabrication and Surface Engineering of Two-Dimensional SnS Toward Piezoelectric Nanogenerator Application. *MRS Adv.*, 3(45-46):2809–2814, 2018.

[72] U. V. Waghmare, N. A. Spaldin, H. C. Kandpal, and R. Seshadri. First-principles indicators of metallicity and cation off-centricity in the IV-VI rocksalt chalcogenides of divalent Ge, Sn, and Pb. *Phys. Rev. B*, 67(12):125111, 2003.

[73] Kai Chang, Junwei Liu, Haicheng Lin, Na Wang, Kun Zhao, Anmin Zhang, Feng Jin, Yong Zhong, Xiaopeng Hu, Wenhui Duan, Qingming Zhang, Liang Fu, Qi Kun Xue, Xi Chen, and Shuai Hua Ji. Discovery of robust in-plane ferroelectricity in atomic-thick SnTe. *Science*, 353(6296):274–278, 2016.

[74] Huitao Shen, Junwei Liu, Kai Chang, and Liang Fu. In-Plane Ferroelectric Tunnel Junction. *Phys. Rev. Appl.*, 11(2):024048, 2019.

[75] Fangyuan Lu, Juehan Yang, Renxiong Li, Nengjie Huo, Yongtao Li, Zhongming Wei, and Jingbo Li. Gas-dependent photoresponse of SnS nanoparticles-based photodetectors. *J. Mater. Chem. C*, 3(6):1397–1402, 2015.

[76] Chandan Rana, Swades Ranjan Bera, and Satyajit Saha. Growth of SnS nanoparticles and its ability as ethanol gas sensor. *J. Mater. Sci. Mater. Electron.*, 30(3):2016–2029, 2019.

[77] M. F. Afsar, M. A. Rafiq, and A. I. Y. Tok. Two-dimensional SnS nanoflakes: synthesis and application to acetone and alcohol sensors. *RSC Adv.*, 7(35):21556–21566, 2017.

[78] Hongyu Tang, Yutao Li, Huaiyu Ye, Fafei Hu, Chenshan Gao, Lu-Qi Tao, Tao Tu, Guangyang Gou, Xianping Chen, Xuejun Fan, Tian-Ling Ren, and Guoqi (Kouchi) Zhang. High-performance humidity sensor using Schottky-contacted SnS nanoflakes for noncontact healthcare monitoring. *Nanotechnology*, 31(5):055501, 2019.

[79] Zhongjian Xie, Dou Wang, Taojian Fan, Chenyang Xing, Zhongjun Li, Wei Tao, Liping Liu, Shiyun Bao, Dianyuan Fan, and Han Zhang. Black phosphorus analogue tin sulfide nanosheets: synthesis and application as near-infrared photothermal agents and drug delivery platforms for cancer therapy. *J. Mater. Chem. B*, 6(29):4747–4755, 2018.

[80] Javier Junquera and Philippe Ghosez. Critical thickness for ferroelectricity in perovskite ultrathin films. *Nature*, 422(6931):506–509, 2003.

[81] Massimiliano Stengel and Nicola A. Spaldin. Origin of the dielectric dead layer in nanoscale capacitors. *Nature*, 443(7112):679–682, 2006.

[82] Wenzhuo Wu, Gang Qiu, Yixiu Wang, Ruoxing Wang, and Peide Ye. Tellurene: its physical properties, scalable nanomanufacturing, and device applications. *Chem. Soc. Rev.*, 47(19):7203–7212, 2018.

[83] Fei Xue, Junwei Zhang, Weijin Hu, Wei-ting Hsu, Ali Han, Siu-fung Leung, Jing-kai Huang, Yi Wan, Shuhai Liu, Junli Zhang, Jr-hau He, Wen-hao Chang, Zhong Lin Wang, Xixiang Zhang, and Lain-jong Li. Multidirection Piezoelectricity in Mono- and Multilayered Hexagonal α-In_2Se_3. *ACS Nano*, 12(5):4976–4983, 2018.

[84] Satoru Konabe and Takahiro Yamamoto. Piezoelectric coefficients of bulk 3R transition metal dichalcogenides. *Jpn. J. Appl. Phys.*, 56(9):098002, 2017.

[85] Dan Tan, Morten Willatzen, and Zhong Lin Wang. Prediction of strong piezoelectricity in 3R-MoS_2 multilayer structures. *Nano Energy*, 56:512–515, 2019.

[86] Jing Xia, Xuan-Ze Li, Xing Huang, Nannan Mao, Dan-Dan Zhu, Lei Wang, Hua Xu, and Xiang-Min Meng. Physical vapor deposition synthesis of two-dimensional orthorhombic SnS flakes with strong angle/temperature-dependent Raman responses. *Nanoscale*, 8(4):2063–2070, 2016.

[87] Hong-Yue Song and Jing-Tao Lü. Density functional theory study of inter-layer coupling in bulk tin selenide. *Chem. Phys. Lett.*, 695:200–204, 2018.

[88] Jeremy K Burdett and Timothy J McLarnan. A study of the arsenic, black phosphorus, and other structures derived from rock salt by bond-breaking processes. I. Structural enumeration. *J. Chem. Phys.*, 75(12):5764–5773, 1981.

[89] Wolfgang Tremel and Roald Hoffmann. Tin sulfide, tellurium iodide ($(Te_2)_2I_2$), and related compounds: symmetry-controlled deformations in solid-state materials. *Inorg. Chem.*, 26(1):118–127, 1987.

[90] Joshua D. Wood, Spencer A. Wells, Deep Jariwala, Kan-Sheng Chen, Eunkyung Cho, Vinod K. Sangwan, Xiaolong Liu, Lincoln J. Lauhon, Tobin J. Marks, and Mark C. Hersam. Effective Passivation of Exfoliated Black Phosphorus Transistors against Ambient Degradation. *Nano Lett.*, 14(12):6964–6970, 2014.

[91] Sangik Lee, Chansoo Yoon, Ji Hye Lee, Yeon Soo Kim, Mi Jung Lee, Wondong Kim, Jaeyoon Baik, Quanxi Jia, and Bae Ho Park. Enhanced Performance of Field-Effect Transistors Based on Black Phosphorus Channels Reduced by Galvanic Corrosion of Al Overlayers. *ACS Appl. Mater. Interfaces*, 10(22):18895–18901, 2018.

[92] Yu Guo, Si Zhou, Yizhen Bai, and Jijun Zhao. Oxidation Resistance of Monolayer Group-IV Monochalcogenides. *ACS Appl. Mater. Interfaces*, 9(13):12013–12020, 2017.

[93] Han Liu, Adam T. Neal, Zhen Zhu, Zhe Luo, Xianfan Xu, David Tománek, and Peide D. Ye. Phosphorene: An Unexplored 2D Semiconductor with a High Hole Mobility. *ACS Nano*, 8(4):4033–4041, 2014.

[94] Thomas J. Whittles, Lee A. Burton, Jonathan M. Skelton, Aron Walsh, Tim D. Veal, and Vin R. Dhanak. Band Alignments, Valence Bands, and Core Levels in the Tin Sulfides SnS, SnS_2, and Sn_2S_3: Experiment and Theory. *Chem. Mater.*, 28(11):3718–3726, 2016.

[95] Mehrshad Mehboudi, Alex M. Dorio, Wenjuan Zhu, Arend van der Zande, Hugh O. H. Churchill, Alejandro A. Pacheco-Sanjuan, Edmund O. Harriss, Pradeep Kumar, and Salvador Barraza-Lopez. Two-Dimensional Disorder in Black Phosphorus and Monochalcogenide Monolayers. *Nano Lett.*, 16(3):1704–1712, 2016.

[96] K Prabhakaran, F Maeda, Y Watanabe, and T Ogino. Thermal decomposition pathway of Ge and Si oxides: observation of a distinct difference. *Thin Solid Films*, 369(1-2):289–292, 2000.

[97] Koji Kita, Choong Hyun Lee, Toshiyuki Tabata, Tomonori Nishimura, Kosuke Nagashio, and Akira Toriumi. Desorption kinetics of GeO from GeO_2/Ge structure. *J. Appl. Phys.*, 108(5):054104, 2010.

[98] Sujay B. Desai, Surabhi R. Madhvapathy, Matin Amani, Daisuke Kiriya, Mark Hettick, Mahmut Tosun, Yuzhi Zhou, Madan Dubey, Joel W. Ager, Daryl Chrzan, and Ali Javey. Gold-Mediated Exfoliation of Ultralarge Optoelectronically-Perfect Monolayers. *Adv. Mater.*, 28(21):4053–4058, 2016.

[99] H. R. Chandrasekhar, R. G. Humphreys, U. Zwick, and M. Cardona. Infrared and Raman spectra of the IV-VI compounds SnS and SnSe. *Phys. Rev. B*, 15(4):2177–2183, 1977.

[100] J. D. Wiley, W. J. Buckel, and R. L. Schmidt. Infrared reflectivity and Raman scattering in GeS. *Phys. Rev. B*, 13(6):2489–2496, 1976.

[101] C. Maurel, T. Cardinal, P. Vinatier, L. Petit, K. Richardson, N. Carlie, F. Guillen, M. Lahaye, M. Couzi, F. Adamietz, V. Rodriguez, F. Lagugné-Labarthet, V. Nazabal, A. Royon, and L. Canioni. Preparation and characterization of germanium oxysulfide glassy films for optics. *Mater. Res. Bull.*, 43(5):1179–1187, 2008.

[102] Wayne E. Morgan and John R. Van Wazer. Binding energy shifts in the x-ray photoelectron spectra of a series of related Group IVa compounds. *J. Phys. Chem.*, 77(7):964–969, 1973.

[103] David R. Lide. *CRC Handbook of Chemistry and Physics, Internet Version*. CRC press, Boca Raton, 2005.

[104] Jiajie Pei, Xin Gai, Jiong Yang, Xibin Wang, Zongfu Yu, Duk-Yong Choi, Barry Luther-Davies, and Yuerui Lu. Producing air-stable monolayers of phosphorene and their defect engineering. *Nat. Commun.*, 7(1):10450, 2016.

[105] Mahito Yamamoto, Sudipta Dutta, Shinya Aikawa, Shu Nakaharai, Katsunori Wakabayashi, Michael S. Fuhrer, Keiji Ueno, and Kazuhito Tsukagoshi. Self-Limiting Layer-by-Layer Oxidation of Atomically Thin WSe_2. *Nano Lett.*, 15(3):2067–2073, 2015.

[106] A. Ziletti, A. Carvalho, D. K. Campbell, D. F. Coker, and A. H. Castro Neto. Oxygen Defects in Phosphorene. *Phys. Rev. Lett.*, 114(4):046801, 2015.

[107] Mingling Li, Yiming Wu, Taishen Li, Yulin Chen, Huaiyi Ding, Yue Lin, Nan Pan, and Xiaoping Wang. Revealing anisotropy and thickness dependence of Raman spectra for SnS flakes. *RSC Adv.*, 7(77):48759–48765, 2017.

[108] Yoshihiko Kanemitsu, Hiroshi Uto, Yasuaki Masumoto, Takahiro Matsumoto, Toshiro Futagi, and Hidenori Mimura. Microstructure and optical properties of free-standing porous silicon films: Size dependence of absorption spectra in Si nanometer-sized crystallites. *Phys. Rev. B*, 48(4):2827–2830, 1993.

[109] Zhen Tian, Chenglei Guo, Mingxing Zhao, Ranran Li, and Jiamin Xue. Two-Dimensional SnS: A Phosphorene Analogue with Strong In-Plane Electronic Anisotropy. *ACS Nano*, 11(2):2219–2226, 2017.

[110] Masaru Nakamura, Hiroaki Nakamura, Masataka Imura, Shigeki Otani, Kiyoshi Shimamura, and Naoki Ohashi. SnS crystal grown using horizontal gradient freeze method and its electrical properties. *J. Alloys Compd.*, 591:326–328, 2014.

[111] S. Del Bucchia, J. C. Jumas, and Maurice Maurin. Contribution à l'étude de composés sulfurés d'étain(II): affinement de la structure de SnS. *Acta Crystallogr. Sect. B*, 37(10):1903–1905, 1981.

[112] Li-Chuan Zhang, Guangzhao Qin, Wu-Zhang Fang, Hui-Juan Cui, Qing-Rong Zheng, Qing-Bo Yan, and Gang Su. Tinselenidene: a Two-dimensional Auxetic Material with Ultralow Lattice Thermal Conductivity and Ultrahigh Hole Mobility. *Sci. Rep.*, 6(1):19830, 2016.

[113] Saptarshi Das, Hong-Yan Chen, Ashish Verma Penumatcha, and Joerg Appenzeller. High Performance Multilayer MoS_2 Transistors with Scandium Contacts. *Nano Lett.*, 13(1):100–105, 2013.

[114] Ashish V. Penumatcha, Ramon B. Salazar, and Joerg Appenzeller. Analysing black phosphorus transistors using an analytic Schottky barrier MOSFET model. *Nat. Commun.*, 6(1):8948, 2015.

[115] Nan Fang and Kosuke Nagashio. Accumulation-Mode Two-Dimensional Field-Effect Transistor: Operation Mechanism and Thickness Scaling Rule. *ACS Appl. Mater. Interfaces*, 10(38):32355–32364, 2018.

[116] Hyeongsu Choi, Jeongsu Lee, Seokyoon Shin, Juhyun Lee, Seungjin Lee, Hyunwoo Park, Sejin Kwon, Namgue Lee, Minwook Bang, Seung-Beck Lee, and Hyeongtag Jeon. Fabrication of high crystalline SnS and SnS_2 thin films, and their switching device characteristics. *Nanotechnology*, 29(21):215201, 2018.

[117] Lídia C. Gomes and A. Carvalho. Phosphorene analogues: Isoelectronic two-dimensional group-IV monochalcogenides with orthorhombic structure. *Phys. Rev. B*, 92(8):085406, 2015.

[118] David Avellaneda, M. T. S. Nair, and P. K. Nair. Polymorphic Tin Sulfide Thin Films of Zinc Blende and Orthorhombic Structures by Chemical Deposition. *J. Electrochem. Soc.*, 155(7):D517, 2008.

[119] Lee A Burton, Diego Colombara, Ruben D Abellon, Ferdinand C Grozema, Laurence M Peter, Tom J Savenije, Gilles Dennler, and Aron Walsh. Synthesis, Characterization, and Electronic Structure of Single-Crystal SnS, Sn_2S_3, and SnS_2. *Chem. Mater.*, 25(24):4908–4916, 2013.

[120] M. Ristov, Gj Sinadinovski, I. Grozdanov, and M. Mitreski. Chemical deposition of tin(II) sulphide thin films. *Thin Solid Films*, 173(1):53–58, 1989.

[121] Ganbat Duvjir, Taewon Min, Trinh Thi Ly, Taehoon Kim, Anh-Tuan Duong, Sunglae Cho, S. H. Rhim, Jaekwang Lee, and Jungdae Kim. Origin of *p*-type characteristics in a SnSe single crystal. *Appl. Phys. Lett.*, 110(26):262106, 2017.

[122] Jingli Wang, Qian Yao, Chun-Wei Huang, Xuming Zou, Lei Liao, Shanshan Chen, Zhiyong Fan, Kai Zhang, Wei Wu, Xiangheng Xiao, Changzhong Jiang, and Wen-Wei Wu. High Mobility MoS_2 Transistor with Low Schottky Barrier Contact by Using Atomic Thick *h*-BN as a Tunneling Layer. *Adv. Mater.*, 28(37):8302–8308, 2016.

[123] Changsik Kim, Inyong Moon, Daeyeong Lee, Min Sup Choi, Faisal Ahmed, Seunggeol Nam, Yeonchoo Cho, Hyeon-Jin Shin, Seongjun Park, and Won Jong Yoo. Fermi Level Pinning at Electrical Metal Contacts of Monolayer Molybdenum Dichalcogenides. *ACS Nano*, 11(2):1588–1596, 2017.

[124] N. Koteeswara Reddy, K. Ramesh, R. Ganesan, K.T. Ramakrishna Reddy, K.R. Gunasekhar, and E.S.R. Gopal. Synthesis and characterisation of co-evaporated tin sulphide thin films. *Appl. Phys. A*, 83(1):133–138, 2006.

[125] Zhihao Yu, Yiming Pan, Yuting Shen, Zilu Wang, Zhun-Yong Ong, Tao Xu, Run Xin, Lijia Pan, Baigeng Wang, Litao Sun, Jinlan Wang, Gang Zhang, Yong Wei Zhang, Yi Shi, and Xinran Wang. Towards intrinsic charge transport in monolayer molybdenum disulfide by defect and interface engineering. *Nat. Commun.*, 5(9):5290, 2014.

[126] Nan Fang and Kosuke Nagashio. Band tail interface states and quantum capacitance in a monolayer molybdenum disulfide field-effect-transistor. *J. Phys. D. Appl. Phys.*, 51(6):065110, 2018.

[127] Branimir Radisavljevic and Andras Kis. Mobility engineering and a metal-insulator transition in monolayer MoS_2. *Nat. Mater.*, 12(9):815–820, 2013.

[128] S. Kurabayashi and K. Nagashio. Transport properties of the top and bottom surfaces in monolayer MoS_2 grown by chemical vapor deposition. *Nanoscale*, 9(35):13264–13271, 2017.

[129] T. Chattopadhyay, J. Pannetier, and H.G. Von Schnering. Neutron diffraction study of the structural phase transition in SnS and SnSe. *J. Phys. Chem. Solids*, 47(9):879–885, 1986.

[130] L. Makinistian and E. A. Albanesi. On the band gap location and core spectra of orthorhombic IV-VI compounds SnS and SnSe. *Phys. status solidi*, 246(1):183–191, 2009.

[131] Ruiqiang Guo, Xinjiang Wang, Youdi Kuang, and Baoling Huang. First-principles study of anisotropic thermoelectric transport properties of IV-VI semiconductor compounds SnSe and SnS. *Phys. Rev. B*, 92(11):115202, 2015.

[132] Tengfei Pei, Lihong Bao, Ruisong Ma, Shiru Song, Binghui Ge, Liangmei Wu, Zhang Zhou, Guocai Wang, Haifang Yang, Junjie Li, Changzhi Gu, Chengmin Shen, Shixuan Du, and Hong-Jun Gao. Epitaxy of Ultrathin SnSe Single Crystals on Polydimethylsiloxane: In-Plane Electrical Anisotropy and Gate-Tunable Thermopower. *Adv. Electron. Mater.*, 2(11):1600292, 2016.

[133] Aron Walsh and Graeme W Watson. Influence of the Anion on Lone Pair Formation in Sn(II) Monochalcogenides: A DFT Study. *J. Phys. Chem. B*, 109(40):18868–18875, 2005.

[134] Li-Dong Zhao, Shih-Han Lo, Yongsheng Zhang, Hui Sun, Gangjian Tan, Ctirad Uher, C. Wolverton, Vinayak P. Dravid, and Mercouri G. Kanatzidis. Ultralow thermal conductivity and high thermoelectric figure of merit in SnSe crystals. *Nature*, 508(7496):373–377, 2014.

[135] Ruixiang Fei, Wei Kang, and Li Yang. Ferroelectricity and Phase Transitions in Monolayer Group-IV Monochalcogenides. *Phys. Rev. Lett.*, 117(9):097601, 2016.

[136] Lun Li, Zhong Chen, Ying Hu, Xuewen Wang, Ting Zhang, Wei Chen, and Qiangbin Wang. Single-Layer Single-Crystalline SnSe Nanosheets. *J. Am. Chem. Soc.*, 135(4):1213–1216, 2013.

[137] Jizhou Jiang, Calvin Pei Yu Wong, Jing Zou, Shisheng Li, Qixing Wang, Jianyi Chen, Dianyu Qi, Hongyu Wang, Goki Eda, Daniel H C Chua, Yumeng Shi,

Wenjing Zhang, and Andrew Thye Shen Wee. Two-step fabrication of single-layer rectangular SnSe flakes. *2D Mater.*, 4(2):021026, 2017.

[138] Hongquan Zhao, Yuliang Mao, Xin Mao, Xuan Shi, Congshen Xu, Chunxiang Wang, Shangmin Zhang, and Dahua Zhou. Band Structure and Photoelectric Characterization of GeSe Monolayers. *Adv. Funct. Mater.*, 28(6):1704855, 2018.

[139] I. Lefebvre, M. A. Szymanski, J. Olivier-Fourcade, and J. C. Jumas. Electronic structure of tin monochalcogenides from SnO to SnTe. *Phys. Rev. B*, 58(4):1896–1906, 1998.

[140] Chih-Hsien Cheng, Yu-Chieh Chi, Chung-Lun Wu, Chun-Jung Lin, Ling-Hsuan Tsai, Jung-Hung Chang, Mu Ku Chen, Min-Hsiung Shih, Chao-Kuei Lee, Chih-I. Wu, Din Ping Tsai, and Gong-Ru Lin. Catalytically solid-phase self-organization of nanoporous SnS with optical depolarizability. *Nanoscale*, 8(8):4579–4587, 2016.

[141] K. S. Hazra, J Rafiee, M. A. Rafiee, A. Mathur, S. S. Roy, J. McLauhglin, N. Koratkar, and D. S. Misra. Thinning of multilayer graphene to monolayer graphene in a plasma environment. *Nanotechnology*, 22(2):025704, 2011.

[142] Wanglin Lu, Haiyan Nan, Jinhua Hong, Yuming Chen, Chen Zhu, Zheng Liang, Xiangyang Ma, Zhenhua Ni, Chuanhong Jin, and Ze Zhang. Plasma-assisted fabrication of monolayer phosphorene and its Raman characterization. *Nano Res.*, 7(6):853–859, 2014.

[143] Yulu Liu, Haiyan Nan, Xing Wu, Wei Pan, Wenhui Wang, Jing Bai, Weiwei Zhao, Litao Sun, Xinran Wang, and Zhenhua Ni. Layer-by-Layer Thinning of MoS_2 by Plasma. *ACS Nano*, 7(5):4202–4209, 2013.

[144] Hui Zhu, Xiaoye Qin, Lanxia Cheng, Angelica Azcatl, Jiyoung Kim, and Robert M. Wallace. Remote Plasma Oxidation and Atomic Layer Etching of MoS_2. *ACS Appl. Mater. Interfaces*, 8(29):19119–19126, 2016.

[145] Jumiati Wu, Hai Li, Zongyou Yin, Hong Li, Juqing Liu, Xiehong Cao, Qing Zhang, and Hua Zhang. Layer Thinning and Etching of Mechanically Exfoliated MoS_2 Nanosheets by Thermal Annealing in Air. *Small*, 9(19):3314–3319, 2013.

[146] Xin Lu, Muhammad Iqbal Bakti Utama, Jun Zhang, Yanyuan Zhao, and Qihua Xiong. Layer-by-layer thinning of MoS_2 by thermal annealing. *Nanoscale*, 5(19):8904–8908, 2013.

[147] A. Castellanos-Gomez, M. Barkelid, A. M. Goossens, V. E. Calado, H. S. J. van der Zant, and G. A. Steele. Laser-Thinning of MoS_2 : On Demand Generation of a Single-Layer Semiconductor. *Nano Lett.*, 12(6):3187–3192, 2012.

[148] P.K. Nair, M.T.S. Nair, Ralph A. Zingaro, and Edward A. Meyers. XRD, XPS, optical and electrical studies on the conversion of SnS thin films to SnO_2. *Thin Solid Films*, 239(1):85–92, 1994.

[149] Keiji Ueno. Introduction to the Growth of Bulk Single Crystals of Two-Dimensional Transition-Metal Dichalcogenides. *J. Phys. Soc. Jpn.*, 84(12):121015, 2015.

[150] Jenifer R. Hajzus, Adam J. Biacchi, Son T. Le, Curt A. Richter, Angela R. Hight Walker, and Lisa M. Porter. Contacts to solution-synthesized SnS nanoribbons: dependence of barrier height on metal work function. *Nanoscale*, 10(1):319–327, 2017.

[151] Robert Summitt, James A. Marley, and Nicholas F. Borrelli. The ultraviolet absorption edge of stannic oxide (SnO_2). *J. Phys. Chem. Solids*, 25(12):1465–1469, 1964.

[152] F.J. Arlinghaus. Energy bands in stannic oxide (SnO_2). *J. Phys. Chem. Solids*, 35(8):931–935, 1974.

[153] David R. Penn. Electron mean-free-path calculations using a model dielectric function. *Phys. Rev. B*, 35(2):482–486, 1987.

[154] S. Tanuma, C. J. Powell, and D. R. Penn. Calculations of electron inelastic mean free paths. V. Data for 14 organic compounds over the 50-2000 eV range. *Surf. Interface Anal.*, 21(3):165–176, 1994.

[155] P. S. Peercy and B. Morosin. Pressure and Temperature Dependences of the Raman-Active Phonons in SnO_2. *Phys. Rev. B*, 7(6):2779–2786, 1973.

[156] E. L. Peltzer y Blancá, A. Svane, N. E. Christensen, C. O. Rodríguez, O. M. Cappannini, and M. S. Moreno. Calculated static and dynamic properties of β-Sn and Sn-O compounds. *Phys. Rev. B*, 48(21):15712–15718, 1993.

[157] Bianca Eifert, Martin Becker, Christian T. Reindl, Marcel Giar, Lilan Zheng, Angelika Polity, Yunbin He, Christian Heiliger, and Peter J. Klar. Raman studies of the intermediate tin-oxide phase. *Phys. Rev. Mater.*, 1(1):014602, 2017.

[158] Lídia C. Gomes, A. Carvalho, and A. H. Castro Neto. Vacancies and oxidation of two-dimensional group-IV monochalcogenides. *Phys. Rev. B*, 94(5):054103, 2016.

[159] Yang Bao, Peng Song, Yanpeng Liu, Zhihui Chen, Menglong Zhu, Ibrahim Abdelwahab, Jie Su, Wei Fu, Xiao Chi, Wei Yu, Wei Liu, Xiaoxu Zhao, Qing-Hua Xu, Ming Yang, and Kian Ping Loh. Gate-Tunable In-Plane Ferroelectricity in Few-Layer SnS. *Nano Lett.*, 19(8):5109–5117, 2019.

[160] Hui Kyung Park, Jaeseung Jo, Hee Kyeung Hong, Gwang Yeom Song, and Jaeyeong Heo. Structural, optical, and electrical properties of tin sulfide thin films grown with electron-beam evaporation. *Curr. Appl. Phys.*, 15(9):964–969, 2015.

[161] Naoki Higashitarumizu, Hayami Kawamoto, Masaru Nakamura, Kiyoshi Shimamura, Naoki Ohashi, Keiji Ueno, and Kosuke Nagashio. Self-passivated ultra-thin SnS layers *via* mechanical exfoliation and post-oxidation. *Nanoscale*, 10(47):22474–22483, 2018.

[162] Peter Sutter and Eli Sutter. Growth Mechanisms of Anisotropic Layered Group IV Chalcogenides on van der Waals Substrates for Energy Conversion Applications. *ACS Appl. Nano Mater.*, 1(6):3026–3034, 2018.

[163] N. Takahashi, K. Watanabe, T. Taniguchi, and K. Nagashio. Atomic layer deposition of Y_2O_3 on *h*-BN for a gate stack in graphene FETs. *Nanotechnology*, 26(17):175708, 2015.

[164] Seong-Jun Jeong, Yeahyun Gu, Jinseong Heo, Jaehyun Yang, Chang-Seok Lee, Min-Hyun Lee, Yunseong Lee, Hyoungsub Kim, Seongjun Park, and Sungwoo Hwang. Thickness scaling of atomic-layer-deposited HfO_2 films and their application to wafer-scale graphene tunnelling transistors. *Sci. Rep.*, 6(1):20907, 2016.

[165] Yunseong Lee, Woojin Jeon, Yeonchoo Cho, Min-Hyun Lee, Seong-Jun Jeong, Jongsun Park, and Seongjun Park. Mesostructured $Hf_xAl_yO_2$ Thin Films as Reliable and Robust Gate Dielectrics with Tunable Dielectric Constants for High-Performance Graphene-Based Transistors. *ACS Nano*, 10(7):6659–6666, 2016.

[166] T. Uwanno, Y. Hattori, T. Taniguchi, K. Watanabe, and K. Nagashio. Fully dry PMMA transfer of graphene on *h*-BN using a heating/cooling system. *2D Mater.*, 2(4):041002, 2015.

[167] K. Maruyama and K. Nagahsio. High-k Er_2O_3 top gate deposition on 2D channel at room temperature by P_{O2} controlled thermal evaporation. In *2018 Int. Conf. Solid State Devices Mater.*, pages 761–762, 2018.

[168] Eiichi Fukada and Iwao Yasuda. On the Piezoelectric Effect of Bone. *J. Phys. Soc. Jpn.*, 12(10):1158–1162, 1957.

[169] Thanh D. Nguyen, Sheng Mao, Yao-Wen Yeh, Prashant K. Purohit, and Michael C. McAlpine. Nanoscale Flexoelectricity. *Adv. Mater.*, 25(7):946–974, 2013.

[170] Qian Deng, Mejdi Kammoun, Alper Erturk, and Pradeep Sharma. Nanoscale flexoelectric energy harvesting. *Int. J. Solids Struct.*, 51(18):3218–3225, 2014.

[171] Kenji Uchino. *Ferroelectric Devices*. Morikita Publishing Co., Ltd., Tokyo, Japan, 2005.

[172] Longfei Pan, Bingsuo Zou, and Li-Jie Shi. Electric field modulation of the band gap, dielectric constant and polarizability in SnS atomically thin layers. *Phys. Lett. A*, 380(27-28):2227–2232, 2016.

[173] Takeshi Morita. *Piezoelectric Phenomena*. Morikita Publishing Co., Ltd., Tokyo, Japan, 2017.

[174] Mikio Umeda, Kentaro Nakamura, and Sadayuki Ueha. Analysis of the transformation of mechanical impact energy to electric energy using piezoelectric vibrator. *Japanese J. Appl. Physics, Part 1 Regul. Pap. Short Notes Rev. Pap.*, 35(5 B):3267–3273, 1996.

[175] Zhong Lin Wang. Piezotronics and Piezo-Phototronics of theThird Generation of Semiconductors. In *Tutor. ES 21 Nanogenerators Piezotronics –Principles, Mater. Devices Nanosyst.*, pages 1–42. MRS Spring Meeting and Exhibit, 2019.

[176] Yuan Liu, Jian Guo, Enbo Zhu, Lei Liao, Sung-joon Lee, Mengning Ding, Imran Shakir, Vincent Gambin, Yu Huang, and Xiangfeng Duan. Approaching the Schottky-Mott limit in van der Waals metal-semiconductor junctions. *Nature*, 557(7707):696–700, 2018.

[177] Tomonori Nishimura, Koji Kita, and Akira Toriumi. Evidence for strong Fermi-level pinning due to metal-induced gap states at metal/germanium interface. *Appl. Phys. Lett.*, 91(12):123123, 2007.

[178] Hideki Hasegawa. Unified disorder induced gap state model for insulator-semiconductor and metal-semiconductor interfaces. *J. Vac. Sci. Technol. B Microelectron. Nanom. Struct.*, 4(4):1130, 1986.

[179] Winfried Mönch. Chemical trends of barrier heights in metal-semiconductor contacts: On the theory of the slope parameter. *Appl. Surf. Sci.*, 92(95):367–371, 1996.

[180] Le Huang, Fugen Wu, and Jingbo Li. Structural anisotropy results in strain-tunable electronic and optical properties in monolayer GeX and SnX (X = S, Se, Te). *J. Chem. Phys.*, 144(11):114708, 2016.

[181] Lídia C. Gomes, A. Carvalho, and A. H. Castro Neto. Enhanced piezoelectricity and modified dielectric screening of two-dimensional group-IV monochalcogenides. *Phys. Rev. B*, 92(21):214103, 2015.

[182] Lucian Pintilie, Viorica Stancu, L. Trupina, and Ioana Pintilie. Ferroelectric Schottky diode behavior from a $SrRuO_3$-$Pb(Zr_{0.2}Ti_{0.8})O_3$-Ta structure. *Phys. Rev. B*, 82(8):085319, 2010.

[183] L. Pintilie and M. Alexe. Metal-ferroelectric-metal heterostructures with Schottky contacts. I. Influence of the ferroelectric properties. *J. Appl. Phys.*, 98(12):124103, 2005.

[184] Zhong Lin Wang. Piezoelectric Nanogenerators Based on Zinc Oxide Nanowire Arrays. *Science*, 312(5771):242–246, 2006.

[185] Wei Liu, Aihua Zhang, Yan Zhang, and Zhong Lin Wang. Density functional studies on edge-contacted single-layer MoS_2 piezotronic transistors. *Appl. Phys. Lett.*, 107(8):083105, 2015.

[186] Wei Liu, Yongli Zhou, Aihua Zhang, Yan Zhang, and Zhong Lin Wang. Theoretical study on the top- and enclosed-contacted single-layer MoS_2 piezotronic transistors. *Appl. Phys. Lett.*, 108(18):181603, 2016.

[187] Antonio Di Bartolomeo, Alessandro Grillo, Francesca Urban, Laura Iemmo, Filippo Giubileo, Giuseppe Luongo, Giampiero Amato, Luca Croin, Linfeng Sun, Shi-Jun Liang, and Lay Kee Ang. Asymmetric Schottky Contacts in Bilayer MoS_2 Field Effect Transistors. *Adv. Funct. Mater.*, 28(28):1800657, 2018.

[188] J. R. Rumble. *CRC Handbook of Chemistry and Physics*. CRC Press, Taylor & Francis Group, Boca Raton, FL, 98 edition, 2017.

[189] Andriy Borodin and Michael Reichling. Characterizing TiO_2(110) surface states by their work function. *Phys. Chem. Chem. Phys.*, 13(34):15442, 2011.

[190] Sang A. Han, Tae-Ho Kim, Sung Kyun Kim, Kang Hyuck Lee, Hye-Jeong Park, Ju-Hyuck Lee, and Sang-Woo Kim. Point-Defect-Passivated MoS_2 Nanosheet-Based High Performance Piezoelectric Nanogenerator. *Adv. Mater.*, 30(21):1800342, 2018.

[191] A.F. Devonshire. Theory of ferroelectrics. *Adv. Phys.*, 3(10):85–130, 1954.

[192] Shuoguo Yuan, Xin Luo, Hung Lit Chan, Chengcheng Xiao, Yawei Dai, Maohai Xie, and Jianhua Hao. Room-temperature ferroelectricity in $MoTe_2$ down to the atomic monolayer limit. *Nat. Commun.*, 10(1):1775, 2019.

[193] Zaiyao Fei, Wenjin Zhao, Tauno A. Palomaki, Bosong Sun, Moira K. Miller, Zhiying Zhao, Jiaqiang Yan, Xiaodong Xu, and David H. Cobden. Ferroelectric switching of a two-dimensional metal. *Nature*, 560(7718):336–339, 2018.

[194] Lu You, Yang Zhang, Shuang Zhou, Apoorva Chaturvedi, Samuel A. Morris, Fucai Liu, Lei Chang, Daichi Ichinose, Hiroshi Funakubo, Weijin Hu, Tom Wu, Zheng Liu, Shuai Dong, and Junling Wang. Origin of giant negative piezoelectricity in a layered van der Waals ferroelectric. *Sci. Adv.*, 5(4):eaav3780, 2019.

[195] Yu Zhou, Di Wu, Yihan Zhu, Yujin Cho, Qing He, Xiao Yang, Kevin Herrera, Zhaodong Chu, Yu Han, Michael C. Downer, Hailin Peng, and Keji Lai. Out-of-Plane Piezoelectricity and Ferroelectricity in Layered α-In_2Se_3 Nanoflakes. *Nano Lett.*, 17(9):5508–5513, 2017.

[196] Changxi Zheng, Lei Yu, Lin Zhu, James L. Collins, Dohyung Kim, Yaoding Lou, Chao Xu, Meng Li, Zheng Wei, Yupeng Zhang, Mark T. Edmonds, Shiqiang Li,

Jan Seidel, Ye Zhu, Jefferson Zhe Liu, Wen Xin Tang, and Michael S. Fuhrer. Room temperature in-plane ferroelectricity in van der Waals In_2Se_3. *Sci. Adv.*, 4(7):eaar7720, 2018.

[197] Jun Xiao, Hanyu Zhu, Ying Wang, Wei Feng, Yunxia Hu, Arvind Dasgupta, Yimo Han, Yuan Wang, David A. Muller, Lane W. Martin, Pingan Hu, and Xiang Zhang. Intrinsic Two-Dimensional Ferroelectricity with Dipole Locking. *Phys. Rev. Lett.*, 120(22):227601, 2018.

[198] Chaojie Cui, Wei-Jin Hu, Xingxu Yan, Christopher Addiego, Wenpei Gao, Yao Wang, Zhe Wang, Linze Li, Yingchun Cheng, Peng Li, Xixiang Zhang, Husam N. Alshareef, Tom Wu, Wenguang Zhu, Xiaoqing Pan, and Lain-Jong Li. Intercorrelated In-Plane and Out-of-Plane Ferroelectricity in Ultrathin Two-Dimensional Layered Semiconductor In_2Se_3. *Nano Lett.*, 18(2):1253–1258, 2018.

[199] Fei Xue, Weijin Hu, Ko Chun Lee, Li Syuan Lu, Junwei Zhang, Hao Ling Tang, Ali Han, Wei Ting Hsu, Shaobo Tu, Wen Hao Chang, Chen Hsin Lien, Jr Hau He, Zhidong Zhang, Lain Jong Li, and Xixiang Zhang. Room-Temperature Ferroelectricity in Hexagonally Layered α-In_2Se_3 Nanoflakes down to the Monolayer Limit. *Adv. Funct. Mater.*, 28(50):1–7, 2018.

[200] Fucai Liu, Lu You, Kyle L. Seyler, Xiaobao Li, Peng Yu, Junhao Lin, Xuewen Wang, Jiadong Zhou, Hong Wang, Haiyong He, Sokrates T. Pantelides, Wu Zhou, Pradeep Sharma, Xiaodong Xu, Pulickel M. Ajayan, Junling Wang, and Zheng Liu. Room-temperature ferroelectricity in $CuInP_2S_6$ ultrathin flakes. *Nat. Commun.*, 7:12357, 2016.

[201] Mengwei Si, Pai-Ying Liao, Gang Qiu, Yuqin Duan, and Peide D. Ye. Ferroelectric Field-Effect Transistors Based on MoS_2 and $CuInP_2S_6$ Two-Dimensional van der Waals Heterostructure. *ACS Nano*, 12(7):6700–6705, 2018.

[202] Fei Xue, Xin He, José Ramón Durán Retamal, Ali Han, Junwei Zhang, Zhixiong Liu, Jing Kai Huang, Weijin Hu, Vincent Tung, Jr Hau He, Lain Jong Li, and Xixiang Zhang. Gate-Tunable and Multidirection-Switchable Memristive Phenomena in a Van Der Waals Ferroelectric. *Adv. Mater.*, 1901300:1901300, 2019.

[203] Siyuan Wan, Yue Li, Wei Li, Xiaoyu Mao, Wenguang Zhu, and Hualing Zeng. Room-temperature ferroelectricity and a switchable diode effect in two-dimensional α-In_2Se_3 thin layers. *Nanoscale*, 10(31):14885–14892, 2018.

[204] A. Belianinov, Q. He, A. Dziaugys, P. Maksymovych, E. Eliseev, A. Borisevich, A. Morozovska, J. Banys, Y. Vysochanskii, and S. V. Kalinin. $CuInP_2S_6$ Room Temperature Layered Ferroelectric. *Nano Lett.*, 15(6):3808–3814, 2015.

[205] Akira Toriumi. Ferroelectric properties of thin HfO_2 films. *Oyo Butsuri*, 88(9):586–596, 2019.

[206] Hua Wang and Xiaofeng Qian. Two-dimensional multiferroics in monolayer group IV monochalcogenides. *2D Mater.*, 4(1):015042, 2017.

[207] G. Gerra, A. K. Tagantsev, N. Setter, and K. Parlinski. Ionic Polarizability of Conductive Metal Oxides and Critical Thickness for Ferroelectricity in $BaTiO_3$. *Phys. Rev. Lett.*, 96(10):107603, 2006.

[208] Na Sai, Alexie M. Kolpak, and Andrew M. Rappe. Ferroelectricity in ultrathin perovskite films. *Phys. Rev. B*, 72(2):020101, 2005.

[209] D. D. Fong, G. Brian Stephenson, Stephen K. Streiffer, Jeffrey A. Eastman, Orlando Auciello, Paul H. Fuoss, and Carol Thompson. Ferroelectricity in Ultrathin Perovskite Films. *Science*, 304(5677):1650–1653, 2004.

[210] Yajun Zhang, Gui-Ping Li, Takahiro Shimada, Jie Wang, and Takayuki Kitamura. Disappearance of ferroelectric critical thickness in epitaxial ultrathin $BaZrO_3$ films. *Phys. Rev. B*, 90(18):184107, 2014.

[211] Sharmila N. Shirodkar and Umesh V. Waghmare. Emergence of Ferroelectricity at a Metal-Semiconductor Transition in a 1T Monolayer of MoS_2. *Phys. Rev. Lett.*, 112(15):157601, 2014.

[212] Bo Xu, Hui Xiang, Yidong Xia, Kun Jiang, Xiangang Wan, Jun He, Jiang Yin, and Zhiguo Liu. Monolayer $AgBiP_2Se_6$: an atomically thin ferroelectric semiconductor with out-plane polarization. *Nanoscale*, 9(24):8427–8434, 2017.

[213] Bas B. Van Aken, Thomas T.M. Palstra, Alessio Filippetti, and Nicola A. Spaldin. The origin of ferroelectricity in magnetoelectric $YMnO_3$. *Nat. Mater.*, 3(3):164–170, 2004.

[214] Amnon Yariv. *Introduction to optical electronics*. Holt, Rinehart and Winston, United Kingdom, 2nd edition, 1976.

[215] Wei-Ting Hsu, Zi-Ang Zhao, Lain-Jong Li, Chang-Hsiao Chen, Ming-Hui Chiu, Pi-Shan Chang, Yi-Chia Chou, and Wen-Hao Chang. Second Harmonic Generation from Artificially Stacked Transition Metal Dichalcogenide Twisted Bilayers. *ACS Nano*, 8(3):2951–2958, 2014.

[216] Xu Zhou, Jingxin Cheng, Yubing Zhou, Ting Cao, Hao Hong, Zhimin Liao, Shiwei Wu, Hailin Peng, Kaihui Liu, and Dapeng Yu. Strong Second-Harmonic Generation in Atomic Layered GaSe. *J. Am. Chem. Soc.*, 137(25):7994–7997, 2015.

[217] Seung Ran Lee, Lkhagvasuren Baasandorj, Jung Won Chang, In Woong Hwang, Jeong Rae Kim, Jeong-Gyu Kim, Kyung-Tae Ko, Seung Bo Shim, Min Woo Choi, Mujin You, Chan-Ho Yang, Jinhee Kim, and Jonghyun Song. First Observation of Ferroelectricity in $\sim$1 nm Ultrathin Semiconducting $BaTiO_3$ Films. *Nano Lett.*, 19(4):2243–2250, 2019.

[218] Dianxiang Ji, Songhua Cai, Tula R. Paudel, Haoying Sun, Chunchen Zhang, Lu Han, Yifan Wei, Yipeng Zang, Min Gu, Yi Zhang, Wenpei Gao, Huaixun Huyan, Wei Guo, Di Wu, Zhengbin Gu, Evgeny Y. Tsymbal, Peng Wang, Yuefeng Nie, and Xiaoqing Pan. Freestanding crystalline oxide perovskites down to the monolayer limit. *Nature*, 570(7759):87–90, 2019.

[219] Paul Z. Hanakata, Alexandra Carvalho, David K. Campbell, and Harold S. Park. Polarization and valley switching in monolayer group-IV monochalcogenides. *Phys. Rev. B*, 94(3):035304, 2016.

[220] Salvador Barraza-Lopez, Thaneshwor P. Kaloni, Shiva P. Poudel, and Pradeep Kumar. Tuning the ferroelectric-to-paraelectric transition temperature and dipole orientation of group-IV monochalcogenide monolayers. *Phys. Rev. B*, 97(2):024110, 2018.

[221] G. Kresse and J. Furthmüller. Efficient iterative schemes for ab initio total-energy calculations using a plane-wave basis set. *Phys. Rev. B*, 54(16):11169–11186, 1996.

[222] John P. Perdew, Kieron Burke, and Matthias Ernzerhof. Generalized Gradient Approximation Made Simple. *Phys. Rev. Lett.*, 77(18):3865–3868, 1996.

[223] Stefan Grimme. Semiempirical GGA-type density functional constructed with a long-range dispersion correction. *J. Comput. Chem.*, 27(15):1787–1799, 2006.

[224] Atsushi Togo and Isao Tanaka. First principles phonon calculations in materials science. *Scr. Mater.*, 108:1–5, 2015.

[225] S.F. Wang, W.K. Fong, W. Wang, and C. Surya. Growth of highly textured SnS on mica using an SnSe buffer layer. *Thin Solid Films*, 564:206–212, 2014.

[226] Yilei Li, Yi Rao, Kin Fai Mak, Yumeng You, Shuyuan Wang, Cory R. Dean, and Tony F. Heinz. Probing symmetry properties of few-layer MoS_2 and h-BN by optical second-harmonic generation. *Nano Lett.*, 13(7):3329–3333, 2013.

[227] R. Loudon. The Raman effect in crystals. *Adv. Phys.*, 13(52):423–482, 1964.

[228] Hua Wang and Xiaofeng Qian. Giant Optical Second Harmonic Generation in Two-Dimensional Multiferroics. *Nano Lett.*, 17(8):5027–5034, 2017.

[229] F. Longnos, E. Vianello, C. Cagli, G. Molas, E. Souchier, P. Blaise, C. Carabasse, G. Rodriguez, V. Jousseaume, B. De Salvo, F. Dahmani, P. Verrier, D. Bretegnier, and J. Liebault. On the impact of Ag doping on performance and reliability of GeS_2-based conductive bridge memories. *Solid. State. Electron.*, 84:155–159, 2013.

[230] Siqi Yin, Zhaochu Luo, Qian Li, Chengyue Xiong, Yunlong Liu, Rajan Singh, Fei Zeng, Yi Zhong, and Xiaozhong Zhang. Emulation of Learning and Memory Behaviors by Memristor Based on Ag Migration on 2D MoS_2 Surface. *Phys. status solidi*, 216(14):1900104, 2019.

[231] Mamoru Fukunaga and Yukio Noda. New Technique for Measuring Ferroelectric and Antiferroelectric Hysteresis Loops. *J. Phys. Soc. Jpn.*, 77(6):064706, 2008.

[232] Xin-Wei Shen, Wen-Yi Tong, Shi-Jing Gong, and Chun-Gang Duan. Electrically tunable polarizer based on 2D orthorhombic ferrovalley materials. *2D Mater.*, 5(1):011001, 2017.

[233] J. F. Scott. Ferroelectrics go bananas. *J. Phys. Condens. Matter*, 20(2):021001, 2008.

[234] L. Pintilie and M. Alexe. Ferroelectric-like hysteresis loop in nonferroelectric systems. *Appl. Phys. Lett.*, 87(11):112903, 2005.

[235] Atsushi Tsurumaki, Hiroyuki Yamada, and Akihito Sawa. Impact of Bi Deficiencies on Ferroelectric Resistive Switching Characteristics Observed at p-type Schottky-Like Pt/$Bi_{1-\delta}FeO_3$ Interfaces. *Adv. Funct. Mater.*, 22(5):1040–1047, 2012.

[236] Rona E. Banai, Hyeonseok Lee, Michael A. Motyka, Ramprasad Chandrasekharan, Nikolas J. Podraza, J. R. S. Brownson, and Mark W. Hom. Optical Properties of Sputtered SnS Thin Films for Photovoltaic Absorbers. *IEEE J. Photovoltaics*, 3(3):1084–1089, 2013.

[237] M.M El-Nahass, H.M Zeyada, M.S Aziz, and N.a El-Ghamaz. Optical properties of thermally evaporated SnS thin films. *Opt. Mater. (Amst).*, 20(3):159–170, 2002.

[238] Liang Chen, Bilu Liu, Ahmad N. Abbas, Yuqiang Ma, Xin Fang, Yihang Liu, and Chongwu Zhou. Screw-Dislocation-Driven Growth of Two-Dimensional Few-Layer and Pyramid-like WSe_2 by Sulfur-Assisted Chemical Vapor Deposition. *ACS Nano*, 8(11):11543–11551, 2014.

[239] Xiaopeng Fan, Yuzhou Zhao, Weihao Zheng, Honglai Li, Xueping Wu, Xuelu Hu, Xuehong Zhang, Xiaoli Zhu, Qinglin Zhang, Xiao Wang, Bin Yang, Jianghua Chen, Song Jin, and Anlian Pan. Controllable Growth and Formation Mechanisms of Dislocated WS_2 Spirals. *Nano Lett.*, 18(6):3885–3892, 2018.

[240] R. Suzuki, M. Sakano, Y. J. Zhang, R. Akashi, D. Morikawa, A. Harasawa, K. Yaji, K. Kuroda, K. Miyamoto, T. Okuda, K. Ishizaka, R. Arita, and Y. Iwasa. Valley-dependent spin polarization in bulk MoS_2 with broken inversion symmetry. *Nat. Nanotechnol.*, 9(8):611–617, 2014.

[241] Liming Zhang, Kaihui Liu, Andrew Barnabas Wong, Jonghwan Kim, Xiaoping Hong, Chong Liu, Ting Cao, Steven G. Louie, Feng Wang, and Peidong Yang. Three-Dimensional Spirals of Atomic Layered MoS_2. *Nano Lett.*, 14(11):6418–6423, 2014.

[242] Da Chen and Shi-Hua Huang. Investigation of resistive switching behavior of Ag/SnO_x/ITO device. *J. Micro/Nanolithography, MEMS, MOEMS*, 14(2):024501, 2015.

Publications

This thesis is based on the following publications:

1. **N. Higashitarumizu**, H. Kawamoto, C.-J., B.-H. Lin, F.-H. Chu, I. Yonemori, T. Nishimura, K. Wakabayashi, W.-H. Chang, K. Nagashio. Purely in-plane ferroelectricity in monolayer SnS at room temperature. (in revision)

2. **N. Higashitarumizu**, H. Kawamoto, M. Nakamura, K. Shimamura, N. Ohashi, K. Ueno, and K. Nagashio. Self-passivated ultra-thin SnS layers *via* mechanical exfoliation and post-oxidation. *Nanoscale* 10, 22474–22483, 2018.

3. **N. Higashitarumizu**, H. Kawamoto, K. Ueno, and K Nagashio. Fabrication and surface engineering of two-dimensional SnS toward piezoelectric nanogenerator application. *MRS Adv.* 3, 2809–2814, 2018.

The following publications are not directly related to this thesis:

4. M. Yako, **N. Higashitarumizu**, and Y. Ishikawa. Impact of interface recombination on direct-gap photoluminescence from Ge epitaxial layers on Si. *Jpn.J. Appl. Phys.* 58, SBBE08, 2019.

5. A.Z. Al-Attili, D. Burt, Z. Li, **N. Higashitarumizu**, F.Y. Gardes, K. Oda, Y. Ishikawa, and S. Saito. Germanium vertically light-emitting micro-gears generating orbital angular momentum. *Opt. Express* 26, 34675–34688, 2018.

6. **N. Higashitarumizu** and Y. Ishikawa. Enhanced direct-gap light emission from Si-capped n^+-Ge epitaxial layers on Si after post-growth rapid cyclic an-

nealing: impact of non-radiative interface recombination toward Ge/Si double heterostructure lasers. *Opt. Express*, 25, 21286–21300, 2017.

7. D. Burt, A. Al-Attili, Z. Li, F. Gardès, M. Sotto, **N. Higashitarumizu**, Y. Ishikawa, K. Oda, O.M. Querin, S. Saito, and R. Kelsall. Enhanced light emission from improved homogeneity in biaxially suspended Germanium membranes from curvature optimization. *Opt. Express* 25, 22911, 2017.

8. A.Z. Al-Attili, S. Kako, M.K. Husain, F.Y. Gardes, **N. Higashitarumizu**, S. Iwamoto, Y. Arakawa, Y. Ishikawa, H. Arimoto, K. Oda, T. Ido, and S. Saito. Whispering Gallery Mode Resonances from Ge Micro-Disks on Suspended Beams. *Front. Mater.* 2, 1, 2015.

9. A.Z. Al-Attili, S. Kako, M.K. Husain, F.Y. Gardes, H. Arimoto, **N. Higashitarumizu**, S. Iwamoto, Y. Arakawa, Y. Ishikawa, and S. Saito. Spin-on doping of germanium-on-insulator wafers for monolithic light sources on silicon. *Jpn. J. Appl. Phys.* 54, 052101, 2015.

Awards

1. Research Fellowship for Young Scientists (DC2), Japan Society for the Promotion of Science, 2019–present.

2. The 47th JSAP Young Scientist Presentation Award, The Japan Society of Applied Physics, 2019.

3. 52nd SSDM Young Researcher Award, International Conference on Solid State Devices and Materials (SSDM), 2019.

4. EMS Award, The 37th Electronics Materials Symposium, 2018.